

DTIC FILE COPY

(2)

Unclassified /
SECURITY CLASSIFICATION OF THIS PAGE

AD-A221 050

REPORT DOCUMENTATION PAGE

Form Approved
OMB No. 0704-0188

1a. REPORT SECURITY CLASSIFICATION Unclassified			1b. RESTRICTIVE MARKINGS		
2a. SECURITY CLASSIFICATION AUTHORITY DTIC ELECTE APR 30 1990			3. DISTRIBUTION/AVAILABILITY OF REPORT Approved for public release; distribution is unlimited.		
2b. DECLASSIFICATION/DOWNGRADING SCHEDULE			5. MONITORING ORGANIZATION REPORT NUMBER(S) AFOSR-TR- 90-0500		
4. PERFORMING ORGANIZATION REPORT NUMBER(S) B Co			7a. NAME OF MONITORING ORGANIZATION AFOSR/NA		
6a. NAME OF PERFORMING ORGANIZATION JET PROPULSION LABORATORY CALIFORNIA INSTITUTE OF TECH.			7b. ADDRESS (City, State, and ZIP Code) Building 410, Bolling AFB DC 20332-6448		
6b. OFFICE SYMBOL (If applicable)			8a. NAME OF FUNDING/SPONSORING ORGANIZATION AFOSR/NA		
8b. OFFICE SYMBOL (If applicable) NA			9. PROCUREMENT INSTRUMENT IDENTIFICATION NUMBER ISSA 87-0025		
8c. ADDRESS (City, State, and ZIP Code) Building 410, Bolling AFB DC 20332-6448			10. SOURCE OF FUNDING NUMBERS		
			PROGRAM ELEMENT NO. 61102F	PROJECT NO. 2308	TASK NO. A2
			WORK UNIT ACCESSION NO.		
11. TITLE (Include Security Classification) (U) THE MODELING OF DROP-CONTAINING TURBULENT EDDIES					
12. PERSONAL AUTHOR(S) DR. JOSETTE BELLAN					
13a. TYPE OF REPORT FINAL		13b. TIME COVERED FROM 10/1/86 TO 9/30/89		14. DATE OF REPORT (Year, Month, Day) NOVEMBER 1989	
15. PAGE COUNT 231					
16. SUPPLEMENTARY NOTATION					
17. COSATI CODES			18. SUBJECT TERMS (Continue on reverse if necessary and identify by block number)		
FIELD	GROUP	SUB-GROUP	TURBULENCE, EVAPORATION, DENSE SPRAYS		
19. ABSTRACT (Continue on reverse if necessary and identify by block number)					
<p>Formulations are presented both for spherical clusters of evaporating drops in axial flows, and for cylindrical clusters of evaporating drops in vortical flows. In both situations the formulation is valid for dense and dilute clusters of drops. -- It is shown that the evaporation of dense, spherical clusters of drops is substantially influenced by turbulence. Dense clusters of drops embedded in low turbulence surroundings initially contract due to evaporative cooling; modest expansion follows due to hot gas eventually entering the cluster. Dense clusters of drops embedded in high turbulence surroundings experience a short initial period of evaporative cooling which is followed by substantial cluster expansion. In contrast, the evaporation of dilute clusters of drops is not sensitive to turbulence: minimal cooling of the gas results in a minimal contraction with no expansion to follow.</p> <p style="text-align: right;">(CONTINUED ON BACK)</p>					
20. DISTRIBUTION/AVAILABILITY OF ABSTRACT <input checked="" type="checkbox"/> UNCLASSIFIED/LIMITED <input checked="" type="checkbox"/> SAME AS RPT <input checked="" type="checkbox"/> DTIC USERS			21. ABSTRACT SECURITY CLASSIFICATION Unclassified		
22a. NAME OF RESPONSIBLE INDIVIDUAL Julian M Tishkoff			22b. TELEPHONE (Include Area Code) (202) 767-0465		22c. OFFICE SYMBOL AFOSR/NA

19.

The evaporation time of dense, cylindrical clusters of drops in vortical flows is mainly controlled by the initial solid body rotation of the drops. The evaporation time is a strong decreasing function of the air/fuel mass ratio in the dense cluster regime and asymptotically levels off in the dilute cluster regime. As the drops evaporate they move out radially forming a cylindrical shell around the center of the vortex. Both the final to initial volume ratio and the final to initial shell thickness ratio are decreasing functions of the initial air/fuel mass ratio.

It is shown that whereas the evaporation time does not correlate with the initial Stokes number in the dense cluster regime, both the volume ratio and the shell thickness ratio correlate very well with the initial Stokes number. In the small Stokes number regime, the correlation is insensitive to the initial air/fuel mass ratio.

Additionally, it is found that the evaporation time of both dense spherical clusters of drops in axial flows, and dense cylindrical clusters of drops in vortical flows can be substantially decreased by reducing the size of the cluster. In both cases, substantial fuel vapor loss was seen to occur through the boundary(ies) of the cluster. The ratio of the mass of fuel vapor lost from the cluster by the initial mass of the fuel increases substantially with decreasing cluster size.

Accession For	
NTIS GFA&I	<input checked="checked" type="checkbox"/>
DTIC TAB	<input type="checkbox"/>
Unannounced	<input type="checkbox"/>
Justification	
By	
Distribution/	
Availability Codes	
Dist	Avail and/or Special
A-1	

THE MODELING OF DROP CONTAINING
TURBULENT EDDIES

FINAL REPORT

BY

JOSETTE BELLAN

JET PROPULSION LABORATORY
CALIFORNIA INSTITUTE OF TECHNOLOGY
4800 OAK GROVE DRIVE
PASADENA, CA 91109

90 04 27 064

TABLE OF CONTENTS

A.	SUMMARY.....	1
B.	INTRODUCTION.....	3
C.	OBJECTIVE.....	3
D.	APPROACH.....	3
E.	RESULTS.....	3
APPENDIX 1:	An Analytical Study of Transport, Mixing and Chaos.....	6
APPENDIX 2:	Transport, Mixing and Stretching in Chaotic Stokes Flows: The Two-Row Mill.....	99
APPENDIX 3:	Turbulence Effects During Evaporation of Drops in Clusters.....	115
APPENDIX 4:	Transport-Related Phenomena for Clusters of Drops.....	129
APPENDIX 5:	Liquid Drop Behavior in Dense and Dilute Clusters.....	142
APPENDIX 6:	The Dynamics of Dense and Dilute Clusters of Drops in Large, Coherent Vortices.....	211

A . SUMMARY

- I. AFOSR PROPOSAL NUMBER 81-2672
- II. PERIOD COVERED BY REPORT: 1 October, 1986 - 30 September, 1989
- III. TITLE OF PROPOSAL: The Modeling of Drop-Containing Turbulent Eddies
- IV. CONTRACT or GRANT NUMBER: NAS 7-918 Task Order RE 182 Amendment 480
- V. NAME OF INSTITUTION: California Institute of Technology
- VI. AUTHOR OF REPORT: J. Bellan
- VII. LIST OF PRESENTATIONS AND MANUSCRIPTS SUBMITTED OR PUBLISHED UNDER FULL OR PARTIAL AFOSR SPONSORSHIP, INCLUDING JOURNAL REFERENCES:
 - (1) "Dispersion During Evaporation of Drops in Clusters", J. Bellan and K. Harstad, SIAM Conference on Numerical Combustion, March, 1987, San Francisco, CA.
 - (2) "On the Behavior of Droplet Clusters," J. Bellan and K. Harstad, ILASS Meeting, June, 1987, Madison, WI.
 - (3) "Turbulence Effects During Evaporation of Drops in Clusters", J. Bellan and K. Harstad, Int. J. Heat Mass Transfer, 31, 8, pp 1655-1663, 1988
 - (4) "An Analytical Study of Transport, Mixing and Chaos in an Unsteady Vortical Flow," V. Rom-Kedar, A. Leonard and S. Wiggins, presented at the 40th Anniversary Meeting of the Division of Fluid Dynamics of the American Physical Society, August 1987; accepted for publication Journal of Fluid Mechanics
 - (5) "Chaotic Mixing in a Stokes Flow Between Eccentric Rotating Cylinders," T. Kaper and S. Wiggins, presented at the 40th Anniversary Meeting of the Division Fluid Dynamics of the American Physical Society, August 1987; also invited lecture at the Dynamics Days Conference, Houston, Texas, January 1988
 - (6) "Transport-Related Phenomena for Clusters of Drops", J. Bellan and K. Harstad, presented at the 4th ICLASS, 1988; in press Int. J. Heat Mass Transfer
 - (7) "Liquid Drop Behavior in Dense and Dilute Clusters", J. Bellan, chapter to appear in Numerical Approaches to Combustion Modeling (E. Oran and J. Boris, eds.) in the AIAA Progress Series (M. Summerfield, ed. in chief)

- (8) "Some Aspects of Liquid Dispersion and Evaporation in Swirling Flows", J. Bellan and K. Harstad, paper 89-61, presented at the Fall Meeting of the Western States Section/The Combustion Institute, October 23-24, 1989, Livermore, CA
- (9) "The Dynamics of Dense and Dilute Clusters of Drops Evaporating in Large, Coherent Vortices", J. Bellan and K. Harstad, submitted for publication 23rd Symp. (Int.) on Combustion, July 1990, Orleans, France
- (10) "Transport, Mixing and Stretching in a Chaotic Stokes Flow; The Two-Row Mill. "T. Kaper and S. Wiggins; paper published in the Proc. of the 3rd joint ASCE-ASME Mechanics Conference, La Jolla, CA, July 9-12, 1989

VIII. SCIENTIFIC PERSONNEL SUPPORTED BY THE PROJECT AND DEGREES AWARDED DURING THE CONTRACT PERIOD.

J. Bellan
 K. G. Harstad
 A. Leonard
 K. Aaron
 V. Rom-Kedar, Ph.D., June 1989, Caltech
 T. Kaper, 3rd year, graduate student Ph.D., Caltech

IX. INTERACTIONS ASSOCIATED WITH THIS RESEARCH:

- 1. Caltech (A. Leonard)
- 2. ONR
- 3. Wright Patterson Air Force Base (T. Jackson)
- 4. ARO
- 5. DOE
- 6. Keio University, Osaka University, Toyokashi Institute of Technology, Japan
- 7. University of Sydney (R.W. Bilger and associates)
- 8. Stanford University (R. Hanson)
- 9. Carnegie Mellon University (N.A. Chigier)
- 10. U.S.C. (J. Lasheras)
- 11. U.C. Irvine (group directed by W. A. Sirignano and S. Samuelsen)
- 12. Sandia National Laboratory, Livermore (group directed by B. Sanders)
- 13. Washington State University, Pullman, WA (C.T. Crowe)

Josette Bellan
 Jet Propulsion Laboratory
 California Institute of Technology
 4800 Oak Grove Drive
 MS 125-214
 Pasadena, CA 91109

B. INTRODUCTION

This report describes research performed during FY'87-FY'89 at the Jet Propulsion Laboratory on the Modeling of Drop Containing Turbulent Eddies.

C. OBJECTIVES

The objective of this effort was to develop a model of the behavior of a single drop-containing turbulent eddy.

D. APPROACH

The approach was characterized by a step-wise progression towards our objective in order to insure that the simplest model capturing the crucial aspects of the drop-eddy interaction was developed. In this manner enough realism is embedded into the model to qualitatively describe the physical picture, while the simplicity makes this model a good candidate for further development in order to develop quantitative capabilities.

E. RESULTS

Initially, the idea was to use contour dynamics methods to describe the vortex motion and to couple to this the particle behavior. For this reason, Caltech was issued a subcontract to look into transport and mixing in vortical flows. Two publications (see Appendix 1 and Appendix 2) and three conference presentations, including an invited presentation, were the results of this work [see items VII (4) and VII (5) in the Summary].

However, it turns out that preliminary work (see Appendix 3) focussing on heat and mass transfer across the surface of a cluster embedded in a turbulent flow showed that instead of the cluster volume evolving at a rate consistent with evaporation such that all new vapor stays inside the cluster, there is substantial mass transfer across the cluster surface. The situation where the cluster volume evolution is such that all evaporated mass stays within the cluster is amenable to a contour dynamics description because the contour lines are streamlines, however if mass crosses the cluster boundary this description is no longer valid. This preliminary model showed that transport across the cluster boundary is important and that other alternatives to the contour dynamics methods must be found.

Additionally, this model showed that, in absence of vortical motion inside the cluster, a cluster of evaporating drops always contracts initially due to heat transfer from the gas phase to the liquid phase. For dilute clusters of drops, there is little contraction because there is not much liquid mass, and after this initial contraction the cluster volume stays basically constant. In contrast, for dense clusters of drops there is strong contraction and a recovery ensues. This recovery is due to transport of surrounding hot gas to the cluster, across its boundary. The amount of recovery increases as turbulence levels in the surrounding gas increase and also as the initial radius of the cluster decreases. It was also shown that the evaporation time is a strong function of both turbulence levels and initial relative velocity between drops and gas in the dense cluster, regime, whereas the evaporation time is not a function of either turbulence or relative velocity in the dilute cluster regime.

Just as important, it was found that the evaporation time is a strong decreasing function of the initial cluster radius in the dense cluster regime and independent of the initial cluster radius in the dilute regime. Thus, turbulence is seen to be important in two ways: First it can break the spray into clusters and the smaller is the cluster, the shorter is the evaporation time. Second it brings hot, unvitiated (by fuel) vapor from the surroundings, thereby promoting evaporation. The present results show that evaporation control should be envisaged near the atomizer, where the spray is dense, because it is precisely in this regime that turbulence has the greatest effect.

Based upon the above results it was decided that since transport processes across the cluster boundary were so important, the model describing the radial motion of the drops, and thus the cluster boundary motion, must be improved. With this new, improved model comparisons were made (see Appendix 4) between four models based upon combinations of two different turbulence models (transport to the cluster) and two different models of drop radial motion (transport from the cluster). The results (see Appendix 4) showed that the evaporation time is insensitive to the models in the dilute cluster regime; that all models have same qualitative behavior in the dense cluster regime; and that the quantitative predictions are different for the four models in the dense cluster regime.

All models show that the evaporation time is an increasing function of the initial cluster radius, with a strong dependence in the small cluster radius regime, however quantitatively the evaporation time is a function of the model. It was also found that the ratio of fuel mass lost to the initial fuel mass is a decreasing function of cluster radius because for smaller clusters the surface to volume ratio is larger thus enhancing evaporation. These results were qualitatively the same, independent of the turbulence levels, however, for larger turbulence levels the ratio was larger. In contrast, the ratio of the total mass lost from the cluster to the initial mass was shown to be insensitive to the initial cluster radius, except for very small clusters. These results show that in order to evaluate and improve models, experimentalists must make measurements in the dense cluster regime and for small clusters, where the sensitivity of the results is highest.

All the above results were obtained for clusters of drops moving axially in a flow. Thus both drops and gas in the cluster had an axial and a radial velocity component, the radial component accounting for cluster expansion or contraction. The pertinent points of the studies of drops in such spherical clusters are described in Appendix 5.

In order to describe the behavior of collections of drops in large, coherent vortices such as have been observed in the shear layer between the spray and the surrounding gas^(1,2), another configuration was studied. In this new configuration, a single longitudinally infinite vortex with an infinitely thin viscous core contains a cluster of drops. Uniformity is assumed in the longitudinal direction and thus the model is formulated for a section across the longitudinal axis. The cluster of drops has also a cylindrical geometry with an inner radius and an outer radius both located within the free part of the vortex. Thus the drops form a cylindrical shell inside the vortex with the inner surface of the shell being initially located either at a finite location or infinitesimally close to the vortex center. In this new configuration both

drops and gas have radial and azimuthal velocities which are functions of time and the radial coordinate from the vortex center. The drag force incorporates blowing effects from the drop surface as the drop evaporates. The model is described in detail in Appendix 6. Results obtained with this model show that the evaporation time is a strong function of the initial solid body rotation of drops and a weaker function of the initial solid body rotation of the gas in the dense cluster regime. In the dilute cluster regime the reverse is true. The initial irrotational drop motion and initial gas solid body rotation affect evaporation in both dense and dilute regimes. It is also found that the ratio of the final (when the drop residual radius is 5%) to initial volume ratio is a decreasing function of the initial air/fuel mass ratio because for denser clusters the centrifugal force is higher due to the larger amount of mass in the cluster. The volume ratio was shown to be highest for largest initial solid body rotation of the drops. The ratio of the final to initial shell thickness of the cluster was also shown to be a decreasing function of the initial air/fuel mass ratio. This was explained by the fact that irrotational motion tends to pack the cluster, whereas solid body rotation tends to pull the cluster apart. Since the initial irrotational gas motion was taken higher than that of the drops, as the drops move out radially they lose solid body rotation and acquire irrotational motion. Since the same momentum is transferred to more mass as the air/fuel mass ratio decreases, the irrotational drop motion will increase less. Thus solid body rotation will be more important yielding a thicker shell.

One of the most important results of this study was the finding that although the evaporation time does not correlate with the initial Stokes number, in the dense cluster regime both the volume ratio and the shell thickness ratio do correlate with the initial Stokes number. The reasons for this are explained in detail in Appendix 5, and thus will not be repeated here. The important conclusion is that this correlation provides a way of qualitatively checking this theory without necessarily needing a precise measurement of the drop number density providing that one makes the measurements in the dense cluster regime and that one can distinguish between two clusters which one is denser.

Parametric variations with the initial cluster radius show that the evaporation time can be substantially reduced by decreasing the initial cluster radius in the small cluster-radius regime. Details on the parametric variation are given in Appendix 6.

REFERENCES

1. Lazaro, B. J. and Lasheras, J. C., "Droplet Dispersion and Transport Mechanism in a Turbulent, Free Shear-Layer", 22nd Symp. (Int.) on Combustion, pp 1991-1198, 1988
2. Lazaro, B. J., and Lasheras, J. C., "Particle Dispersion in a Turbulent, Plane, Free Shear Layer", Phys. Fluids A, 1, 6, pp 1035-1044, 1989.

AN ANALYTICAL STUDY OF TRANSPORT, MIXING AND CHAOS IN AN UNSTEADY VORTICAL FLOW

By V. ROM-KEDAR*,
Applied Mathematics

A. LEONARD
Graduate Aeronautical Laboratories

and S. WIGGINS
Applied Mechanics
California Institute of Technology, Pasadena CA 91125

We examine the transport properties of a particular two dimensional, inviscid incompressible flow using dynamical systems techniques. The velocity field is time periodic and consists of the field induced by a vortex pair plus an oscillating strain-rate field. In the absence of the strain-rate field the vortex pair moves with a constant velocity and carries with it a constant body of fluid. When the strain-rate field is added the picture changes dramatically: fluid is entrained and detrained from the neighborhood of the vortices and chaotic particle motion occurs. We investigate the mechanism for this phenomena and study the transport and mixing of fluid in this flow. Our work consists of both numerical and analytical studies. The analytical studies include the interpretation of the invariant manifolds as the underlying structure which govern the transport. For small values of strain-rate amplitude we use Melnikov's technique to investigate the behavior of the manifolds as the parameters of the problem change and to prove the existence of a horseshoe map and thus the existence of chaotic particle paths in the flow. Using the Melnikov technique once more we develop an analytical estimate of the flux rate into and out of the vortex neighborhood. We then develop a technique for determining the residence time distribution for fluid particles near the vortices that is valid for arbitrary strain-rate amplitudes. The technique involves an understanding of the geometry of the tangling of the stable and unstable manifolds and results in a dramatic reduction in computational effort required for the determination of the residence time distributions. Additionally, we investigate the total stretch of material elements while they are in the vicinity of the vortex pair, using this quantity as a measure of the effect of the horseshoes on trajectories passing through this region. The numerical work verifies the analytical predictions regarding the structure of the invariant manifolds, the mechanism for entrainment and detrainment, and the flux rate.

*Present address: The James Franck Institute, The University of Chicago, Chicago IL 60637

1. Introduction

In most fluid flows of interest, transport and mixing are dominated by convective processes so that the relative motions of fluid particles are all important. Unfortunately particle motion is generally more complex than the underlying fluid dynamics. For example, while the motion of three point vortices in an unbounded domain is integrable, particle motion in this flow can be chaotic (Aref [1983]) and certain simple steady, spatially periodic solutions to the Euler equations in three dimensions, known as ABC (Arnold, Beltrami and Childress) flows yield chaotic particle motion (Dombre et al. [1986]).

Of course, if the fluid dynamics is sufficiently simple then particle motions are integrable and a direct analytical attack on the problem may be fruitful. An example in this class is the analysis of a diffusion flame by Marble [1985], involving the rolling up of an initially plane interface in the flow of a viscous line vortex in two dimensions. At the other end of the scale, when the flow is turbulent, direct numerical integration of the Navier-Stokes equations plus convective equations for passive scalars (Kerr [1985], Pope [1987]) is a computational approach to mixing problems, whereas a theoretical approach might consist of constructing reasonable physical models for mixing processes (Broadwell [1987], Dimotakis [1987], Kerstein and Ashurst [1984]). In this paper we consider an intermediate case, one in which the flow is relatively simple but the particle motion is chaotic. We show that the recent rapid development in the theory of nonlinear dynamical systems and chaotic phenomena gives much hope for a rather extensive analysis of particle motion in such flows. Indeed, the dynamical systems approach to the study of fluid flows is very similar in spirit to the flow visualization techniques utilized in the experimental study of coherent structures in the sense that dynamical systems theory is concerned with the global topology of the flow from a Lagrangian point of view. Since to good approximation temperature and mass move with the fluid velocity, understanding the structures governing particles motion in fluid flows is necessary for interpretations of flow visualizations (the visualization of motion of mass particles) and predictions of mass and heat transfer in technological applications.

The application of dynamical systems theory to the study of the global topology of fluid particle motions is not new. The first work appears to be that of Hénon [1966] who, acting on a suggestion of Arnold [1965], numerically studied the fluid particle motions in ABC flow. Hénon showed that the flow contained KAM tori as well as chaotic motions of the Smale horseshoe type. This flow has recently been the subject of more extensive study by Dombre et al. [1986]. Chaotic particle motions in the ABC flows also have relevance to the kinematic dynamo problem, see Arnold and Korkine [1983], Galloway and Frisch [1986], and Moffatt and Proctor [1985]. Aref [1984] made the first explicit connection between particle motions in two-dimensional incompressible flow and two-dimensional Hamiltonian dynamical systems.

Since the study of fluid particle motions involves only kinematical considerations, the application, and hence, results of dynamical systems theory are independent of Reynolds number. For example, Aref and Balachandar [1986] showed that unsteady Stokes flow between eccentric rotating cylinders, in which the rotation rate is modulated periodically in time, can exhibit chaotic particle motions of the

Smale horseshoe type. Thus this particular Stokes flow is effectively nonreversible. This same flow has also been studied experimentally as well as theoretically by Chaiken et al. [1986], [1987]. Ottino and coworkers (see Chien et al. [1986], Khakar et al. [1986], and Ottino et al. [1988]) studied chaotic fluid particle motions in a variety of flows, both at small and large Reynolds numbers with particular emphasis on using dynamical systems techniques as a theoretical basis for the discussion of mixing processes. Broomhead and Rytie [1988] study fluid particle motions in the velocity field of Taylor vortices close to the onset of the wavy instability and demonstrate the chaotic transference of fluid between neighboring vortices. Feingold et al. [1988] study models for particle motion in three dimensional time dependent flows. Additional references applying dynamical systems techniques to the study of fluid particle trajectories are Suresh [1985] and Arter [1983].

In this paper we study fluid particle motions in the velocity field induced by two counter-rotating point vortices of equal strength subject to a time periodic strain field. This is a fundamental type of flow which is relevant to a wide variety of applications as, for example, in the study of oscillatory flows in wavy walled tubes (see Ralph [1986], Sobey [1985], and Appendix 1), in the study of trailing vortices, and in the study of perturbed vortex rings (Shariff [1989]).

The main difference in our analysis of the topology of a fluid flow via dynamical systems techniques as opposed to previous analyses is that rather than just using the framework of dynamical systems theory to give a description of the topology and indicate the presence of chaotic fluid particle trajectories we use the framework in order to calculate physically measurable quantities such as fluxes and the distribution of volumes via residence times. We do this by first identifying the structures in the flow responsible for these physical processes and then by using the dynamics of these structures to predict these physical quantities. Thus in some sense we realize the goal of the study of coherent structures for our problem. Additionally, in this paper we introduce two new concepts that play an important role in the study of mixing and transport processes due to chaotic fluid particle motions. They are:

1. *Tangle Dynamics.* In section 3 we review how the study of particle motions in two-dimensional incompressible time-periodic fluid flows can be reduced to the study of a two-dimensional map. It is well known in the dynamical systems literature that such maps may possess *resonance bands* consisting of alternating hyperbolic and elliptic periodic points. This has fluid dynamical significance in the sense that the stable and unstable manifolds of the hyperbolic points create partial barriers to transport in the flow. Additionally, these stable and unstable manifolds may intersect many times resulting in a complicated geometrical structure that dramatically influences the stretching and deformation of fluid elements. We develop analytical and computational techniques which we refer to as *tangle dynamics* that allow us to compute the rate of transport of fluid between regions separated by these partial barriers. From this information we can compute residence time distributions and, more generally, determine the effect of a resonance band on a fluid element. We

develop these ideas in the context of the specific flow considered in this paper, however recently the methods have been generalized to apply to any two-dimensional time-periodic fluid flow, see Rom-Kedar and Wiggins [1989].

2. *Finite Time Stretch.* Ottino [1988] has shown the relationship between the notion of a Liapunov exponent from dynamical systems theory and the stretching of fluid elements. However, the Liapunov exponent is a quantity computed for a single fluid particle trajectory which is time averaged in an asymptotic sense. Thus there is a practical limitation of this quantity in that, for many open flows, most fluid particles spend only a finite time in the chaotic zone rendering the classical theory of Liapunov exponents inappropriate. This is so because the asymptotic time average for such trajectories would give a zero exponent. However, using tangle dynamics and proof of the existence of chaotic particle motions, we are able to determine which particles should experience exponential stretching and the finite time interval over which most of this stretching will take place. We then quantify the stretching by considering the total stretch suffered during this finite period of time.

This paper is organized as follows: In section 2 we derive the velocity field for the oscillating vortex pair and in section 3 we begin our analysis of the velocity field by introducing the Poincaré map. In section 4 we discuss three qualitatively distinct regions which arise in our flow: the free flow region, the core, and the mixing region. We discuss tangle dynamics and the associated mechanism for mass transport in the flow in section 5 and we consider mass transport in detail and give precise definitions to the concepts of entrainment and detrainment in terms of tangle dynamics in section 6, along with the results of numerical computations. In section 7 we discuss the concept of chaos and show how it arises in our flow, and in section 8 we discuss mixing and the total stretch of fluid elements as they pass through regions containing localized chaos. Summary and conclusions are given in section 9.

2. Oscillating Vortex Pair

We examine the flow governed by a vortex pair in the presence of an oscillating external strain-rate field. The vortices have circulations $\pm \Gamma$ and are separated by a nominal distance $2d$ in the y -direction. The stream function for the flow in a frame moving with the average velocity of the vortices is

$$\Psi = -\frac{\Gamma}{4\pi} \log \left[\frac{(x - x_v)^2 + (y - y_v)^2}{(x - x_v)^2 + (y + y_v)^2} \right] - V_v y + \varepsilon xy \sin(\omega t) \quad (2.1)$$

where $(x_v(t), \pm y_v(t))$ are the vortex positions, ε is the strain rate and V_v is the average velocity of the vortex pair. If $\varepsilon = 0$ then $(x_v, y_v) = (0, d)$ and $V_v = \frac{\Gamma}{4\pi d}$. The equations of particle motion are

$$\frac{dx}{dt} = \frac{\partial \Psi}{\partial y} \quad \frac{dy}{dt} = -\frac{\partial \Psi}{\partial x} \quad (2.2)$$

We show, as an example, in Appendix 1 that this flow approximates the flow induced by a vortex pair in a wavy-wall channel. We obtain dimensionless variables as follows:

$$x/d \rightarrow x, y/d \rightarrow y, \frac{\Gamma t}{2\pi d^2} \rightarrow t, \frac{\varepsilon}{\omega} \rightarrow \varepsilon, \frac{2\pi d V_v}{\Gamma} \rightarrow v_v, \frac{\Gamma}{2\pi \omega d^2} \rightarrow \gamma, \frac{2\pi \Psi}{\Gamma} \rightarrow \Psi$$

Then (2.1) and (2.2) become

$$\frac{dx}{dt} = - \left[\frac{(y - y_v)}{(x - x_v)^2 + (y - y_v)^2} - \frac{y + y_v}{(x - x_v)^2 + (y + y_v)^2} \right] - v_v + \frac{\varepsilon x}{\gamma} \sin(t/\gamma) \quad (2.3a)$$

$$\frac{dy}{dt} = (x - x_v) \left[\frac{1}{(x - x_v)^2 + (y - y_v)^2} - \frac{1}{(x - x_v)^2 + (y + y_v)^2} \right] - \frac{\varepsilon y}{\gamma} \sin(t/\gamma) \quad (2.3b)$$

Using the fact that a point vortex is convected with the flow but does not induce self velocity we obtain the following equations for the vortex position locations:

$$\frac{dx_v}{dt} = \frac{1}{2y_v} - v_v + \frac{\varepsilon x_v}{\gamma} \sin(t/\gamma) \quad (2.4a)$$

$$\frac{dy_v}{dt} = - \frac{\varepsilon y_v}{\gamma} \sin(t/\gamma) \quad (2.4b)$$

The resulting motion of the vortices is relatively simple. Equation (2.4) with the initial conditions $x_v(0) = 0, y_v(0) = 1$, are easily integrated to give

$$x_v(t) = \frac{\gamma}{2} e^{-\varepsilon(\cos(t/\gamma)-1)} \int_0^{t/\gamma} \left[1 - 2v_v e^{\varepsilon(\cos(s)-1)} \right] ds \quad (2.5a)$$

$$y_v(t) = e^{\varepsilon(\cos(t/\gamma)-1)} \quad (2.5b)$$

The requirement that the mean velocity of the vortex pair be zero in the moving frame yields $v_v = \frac{e^t}{2I_0(\varepsilon)}$, where I_0 is the modified Bessel function of order zero. From (2.5) it is clear that the vortices oscillate in orbits near the points $(0, \pm 1)$. Thus we term the resulting flow given by (2.3) the Oscillating Vortex Pair (OVP) flow.

Equations (2.3) together with (2.5) give the equations of particle motion as a function of two dimensionless parameters γ and ε , proportional to vortex strength and strain rate, respectively. For most of the analysis that follows ε can take on arbitrary values. However for the perturbation calculations we shall assume that ε is small and will require an expansion of the right hand side of (2.3) in powers of ε . This expansion yields equations of motion for fluid particles which are of the form of a periodically

perturbed integrable Hamiltonian system:

$$\frac{dx}{dt} = f_1(x, y) + \epsilon g_1(x, y, t/\gamma, \gamma) + O(\epsilon^2) \quad (2.6a)$$

$$\frac{dy}{dt} = f_2(x, y) + \epsilon g_2(x, y, t/\gamma, \gamma) + O(\epsilon^2) \quad (2.6b)$$

The functions f_i, g_i are given in Appendix 2.

For $\epsilon = 0$ the phase portrait of the integrable Hamiltonian system, or equivalently the streamlines of the flow induced by a vortex pair in the frame moving with the vortices, appears in figure 2.1. Note that for this case, there are two hyperbolic stagnation points p_-, p_+ connected by three limiting streamlines Ψ_+, Ψ_0 and Ψ_- defined by $\Psi(x, y)|_{\epsilon=0} = 0, |x| \leq \sqrt{3}$, with $y > 0, y = 0$, and $y < 0$ respectively. Thus a fixed, closed volume of fluid or "bubble" is bounded by the limiting streamlines and moves with the vortex pair for all times. As we shall see below, this picture changes dramatically when $\epsilon \neq 0$. Note also that for any ϵ , the flow is symmetric about the x axis and thus we need only study the flow in the upper half plane. Such symmetry would be present in axisymmetric flows. If the strain-rate field is not aligned with the $x - y$ axes the straight line connecting the two vortices also rotates periodically, but the qualitative behavior of the particle motion is the same as that discussed in the following.

Figure 2.1 Streamlines of the Unperturbed Flow.

3. Analysis: The Poincaré Map

We are interested in the structure of the flow generated by the velocity field (2.3) and how the structure varies as the parameters γ and ϵ are varied. A brute force method for achieving this goal would be to numerically integrate (2.3) for a large number of initial conditions for the range of γ and ϵ values of interest. Although this would be an efficient means for generating a large list of numbers, it is not at all clear how one would extract information concerning the structure of the flow from this list of numbers. One might try plotting the trajectories of a large number of fluid particles in space, however, because the velocity field is unsteady, these trajectories may intersect themselves as well as others many times leading to a complicated topological structure which might obscure relatively simple structures whose dynamics essentially govern the flow. In order to better understand the dynamics of the unsteady flow generated by (2.3) we will study the associated *Poincaré map*.

Roughly speaking, the Poincaré map of the flow is constructed by associating to a fluid particle at a fixed phase of the external strain-rate field its location under evolution by the flow after one period of the strain-rate field. More mathematically, we rewrite the unsteady two dimensional velocity field (2.3) as a steady three dimensional velocity field by introducing the phase of the strain-rate field as a new dependent variable. We do this by defining the function

$$\theta(t) = t/\gamma \quad \text{mod } 2\pi$$

in which case (2.3) and (2.5) can be written as:

$$\begin{aligned} x &= \frac{\partial \Psi}{\partial y}(x, y, \theta; \varepsilon, \delta) \\ y &= -\frac{\partial \Psi}{\partial x}(x, y, \theta; \varepsilon, \delta) \\ \theta &= 1/\gamma. \end{aligned} \tag{3.1}$$

and for small ε (2.6) becomes:

$$\begin{aligned} \dot{x} &= f_1(x, y) + \varepsilon g_1(x, y, \theta; \gamma) + O(\varepsilon^2) \\ \dot{y} &= f_2(x, y) + \varepsilon g_2(x, y, \theta; \gamma) + O(\varepsilon^2) \\ \dot{\theta} &= 1/\gamma. \end{aligned} \tag{3.2}$$

A two dimensional *cross-section* of the three dimensional phase space of (3.1) or (3.2) is given by:

$$\Sigma^{\bar{\theta}} = \left\{ (x, y, \theta) \mid \theta = \bar{\theta} \in (0, 2\pi] \right\}$$

and the Poincaré map of $\Sigma^{\bar{\theta}}$ into $\Sigma^{\bar{\theta}}$ is defined as:

$$\begin{aligned} T_{\bar{\theta}} : \Sigma^{\bar{\theta}} &\rightarrow \Sigma^{\bar{\theta}} \\ (x(\bar{\theta}), y(\bar{\theta})) &\mapsto (x(\bar{\theta} + 2\pi), y(\bar{\theta} + 2\pi)). \end{aligned}$$

So studying the flow via the Poincaré map is equivalent to sampling fluid particle trajectories at time intervals equal to the period of the strain-rate field.

The main advantage obtained from using the Poincaré map to study unsteady, time-periodic velocity fields is that the technique tends to filter out redundant dynamical phenomena and reveal the underlying structures which govern various properties of the flow such as mixing and transport. For example, a periodic particle trajectory in the flow which may have a very complicated topological structure is manifested as a finite, discrete set of points for the Poincaré map. Many more examples will follow throughout the rest of the paper. Also, in Appendix 5 we collect several useful properties of Poincaré maps.

Our goal is to study properties of the orbit structure of the Poincaré map in order to discover the structures necessary to predict mixing and transport properties of the flow.

4. Three Qualitatively Distinct Flow Regions

Let us recall the structure of the unperturbed velocity field now in the context of the Poincaré map. In this case the velocity field is steady and fluid particles follow the streamlines defined by the level curves of the stream function. Thus orbits of the Poincaré map are sequences of discrete points lying on the streamlines. The streamlines are examples of *invariant curves or manifolds* of the Poincaré map meaning that particles which start on such a curve must thereafter remain on that curve under all iterations of the Poincaré map. The stagnation points p_- and p_+ are fixed points of the Poincaré map. Orbits of fluid particles on Ψ_u and Ψ_l approach p_+ asymptotically in positive time and p_- asymptotically in negative time. In the terminology of dynamical systems theory, Ψ_u and Ψ_l are referred to as the stable manifold of p_+ , denoted W_+^s , and Ψ_0 plus $(-\infty, p_-)$ is the unstable manifold of p_+ , denoted W_+^u . Similarly, Ψ_u and Ψ_l are referred to as the unstable manifold of p_- , denoted W_-^u , and Ψ_0 plus (p_-, ∞) is the stable manifold of p_- , denoted W_-^s . Orbits of fluid particles starting on Ψ_u , Ψ_0 , and Ψ_l are referred to as *heteroclinic orbits* and $\Psi_u \cup \Psi_0 \cup (p_+) \cup (p_-)$ and $\Psi_l \cup \Psi_0 \cup (p_+) \cup (p_-)$ are said to form *heteroclinic cycles*. For brevity we shall simply refer to the closed curve $\Psi_u \cup \Psi_l \cup (p_+) \cup (p_-)$ as the *limiting streamlines*.

Notice that fluid particle motions outside the region bounded by the limiting streamlines are qualitatively different than those inside this region. We now want to discuss more fully the different possible fluid particle motions and how they are constrained by structures in the flow.

The Free Flow Region. Under the influence of the unperturbed velocity field fluid particles outside the region bounded by the limiting streamlines move from right to left along the unbounded streamlines. We refer to this as the *free flow region*. Under the influence of the externally strained velocity field fluid particles which are sufficiently far from the limiting streamlines behave in the same manner as those in the unperturbed velocity field. Particles move from right to left as before now with vertical oscillations but their trajectories never encircle a vortex.

The Core. We refer to the region of fluid which is permanently trapped and hence moves with the vortex pair for all time as the *core*. For the unperturbed flow the core is the fluid within the limiting streamlines and it contains two separate cells with boundaries $C_u = \Psi_u \cup \Psi_0 \cup (p_+) \cup (p_-)$ and $C_l = \Psi_l \cup \Psi_0 \cup (p_+) \cup (p_-)$. Fluid particles in the interior of C_u and C_l move in closed paths along the streamlines of the unperturbed velocity field. We can uniquely label each closed streamline in C_u and C_l by the area which it encloses. We label this area by I (note: in the context of Hamiltonian mechanics I is called the *action*, see Arnold [1978]). Associated with each closed streamline is a period

$T(I)$ which is the time needed for a particle starting on the streamline to make one complete circuit along the streamline. The period goes to zero as the point vortices are approached and to ∞ as C_u and C_l are approached.

We now interpret this extremely simple motion of fluid particles in the unperturbed case inside C_u and C_l in terms of orbits of the Poincaré map. The streamlines in this case are examples of *invariant curves* of the Poincaré map. That is, orbits of fluid particles which start on the streamlines must always stay on the streamlines. There are two types of orbits depending on whether or not the number $\frac{T(I)}{2\pi\gamma}$ is rational or irrational (note: in the context of dynamical systems theory the number $\frac{T(I)}{2\pi\gamma}$ is referred to as a *rotation number*). These two types of orbits behave very differently under the influence of the time periodic strain-rate field.

$T(I)/2\pi\gamma = p/q$: p, q , integers. In this case, every fluid particle on the invariant circle in the Poincaré map in the unperturbed case returns to its original position after q cycles of the Poincaré map. However, in the process it makes p complete revolutions around the invariant circle. Thus all fluid particles on the invariant circle move periodically with period q .

In general, this situation can be expected to change dramatically under the influence of the time periodic strain-rate field. The invariant circle is destroyed and a finite even number of periodic orbits of alternating stability type will be preserved in the externally strained case. Half of the periodic orbits will be stable and half will be unstable of saddle type. The stable and unstable manifolds of the saddle type motions may intersect transversely, yielding chaotic fluid particle motions. The resulting structure is known as a *p/q resonance band* or *stochastic layer*, see Arnold and Avez [1968] for more details.

$T(I)/2\pi\gamma = \omega$: ω irrational. In the unperturbed velocity field every fluid particle starting on an invariant circle of the Poincaré map rotates around the circle, never returning to its initial position. Two possibilities for the behavior of these orbits under external strain are as follows:

KAM tori. If ω is sufficiently poorly approximated by rational numbers, i.e. it satisfies a diophantine condition (see Arnold and Avez [1968] or Moser [1973]), then, for sufficiently small amplitude strain-rates ε , the invariant circle is preserved in the perturbed Poincaré map. This invariant circle is referred to as a *KAM torus* after Kolmogorov, Arnold, and Moser who first proved the result (known as the KAM theorem). KAM tori are extremely important since they represent total barriers to fluid motion and hence strongly influence transport.

Cantori. If ω fails to satisfy the number theoretic hypotheses of the KAM theorem then the work of Percival [1980], Aubry and LeDaeron [1983], and Mather [1984] implies that the invariant circle may break down under the time periodic strain-rate field into an invariant cantor set or *cantorus*. The dynamics on the cantor set are similar to the dynamics on the KAM torus. However, the cantor set

contains gaps which permit the (possibly very slow) passage of fluid.

We refer the reader to figure 4.1 for an illustration of resonance bands, KAM tori, and cantori in the core. Our primary concern is with particle motion in the mixing region defined below. Thus we only remark that these three structures govern the fluid transport within the core. In the parameter range we are studying there exists the largest KAM torus which serves as a complete barrier to the flow, and therefore will prevent the mixing of outer fluid with the fluid in the core. An interesting question is whether the core region is composed of a single region bounded by a KAM torus or if there are islands outside the largest KAM torus in which the motion is bounded. During the numerical experiments, described in Section 6, we observed that for $\gamma = 0.5$ there is only one observable core region while for $\gamma = 1.38$ there are at least two (see figure 6.10).

Figure 4.1. Resonance Bands and KAM Tori.

The Mixing Region. We now want to focus our attention on p_+ and p_- and their stable and unstable manifolds. In the unperturbed flow W_+^s and W_-^u coincide along the streamlines Ψ_+ and Ψ_- to create a boundary separating the core from the free flow region. With the addition of external strain we can make the following assertions:

1. For sufficiently small amplitude strain fields (i.e. for ε sufficiently small) p_+ and p_- persist as fixed points of the Poincaré map. We shall denote them by $p_{+, \varepsilon}$ and $p_{-, \varepsilon}$, respectively.
2. The stable and unstable manifolds of p_+ and p_- persist to become the stable and unstable manifolds of $p_{+, \varepsilon}$ and $p_{-, \varepsilon}$. We denote them by $W_{+, \varepsilon}^s$, $W_{+, \varepsilon}^u$, $W_{-, \varepsilon}^s$, and $W_{-, \varepsilon}^u$, respectively.

These two results follow from general theorems regarding the persistence of invariant manifolds which can be found in Fenichel [1971] or Hirsch, Pugh, and Shub [1977] and they are independent of the specific analytical form of the time periodic strain-rate field (note: these results would also apply to quasiperiodic strain rates, See Wiggins [1987], [1988]).

We will see in section 6 that for arbitrary ε , (1) persistence of invariant manifolds for arbitrary values may be decided by computation, (2) particle transport is governed by the invariant manifolds, and (3) that the unstable manifold is the observable structure in a broad class of flow visualizations.

From our discussion of the symmetry of the velocity field in section 3, it follows that $y = 0$ is always an invariant manifold for both the perturbed and unperturbed velocity field. This implies that $\Psi_0 = W_+^u \cup W_-^s = W_{+, \varepsilon}^u \cup W_{-, \varepsilon}^s$ persists as an invariant streamline. However, the interpretation of $W_{+, \varepsilon}^s$ and $W_{-, \varepsilon}^u$ is more subtle since they need not coincide as in the unperturbed case. Now $W_{+, \varepsilon}^s$ and $W_{-, \varepsilon}^u$ are smooth invariant curves and a fluid particle path starting on these curves in the continuous time flow is represented as an infinite set of discrete points on these curves in the Poincaré section. As such it is possible for $W_{-, \varepsilon}^u$ and $W_{+, \varepsilon}^s$ to intersect in an isolated point as shown in figure 4.2. Note that

figure 4.2 could not hold in the unperturbed case because, for steady flows, particle paths must coincide with streamlines and streamlines cannot intersect in isolated points without violating uniqueness of solutions of ordinary differential equations. If we consider the orbit of this point of intersection under the Poincaré map, then by invariance of $W_{+, \varepsilon}^s$ and $W_{-, \varepsilon}^s$ it must forever remain on both $W_{+, \varepsilon}^s$ and $W_{-, \varepsilon}^s$ resulting in a geometrical shape similar to that shown in figure 4.2. This splitting of the stable manifold of p_+ and the unstable manifold of p_- results in a mechanism for the transference of fluid between the vicinity of the core and the vicinity of the free flow region. It also provides the mechanism for chaotic particle motion. For this reason, we refer to region bounded roughly by the envelopes of $W_{+, \varepsilon}^s$ and $W_{-, \varepsilon}^s$ as the *mixing region*. A precise definition of the mixing region is given in section 6. The mixing region of course, does not exist for the unperturbed case. One characterization that distinguishes the free flow region, the mixing region, and the core is that they consist of particle trajectories that encircle a vortex zero, a finite, and an infinite number of times, respectively.

Figure 4.2. The Homoclinic Tangle in the Mixing Region.

The Melnikov Technique

An analytical technique which allows us to predict the behavior of $W_{+, \varepsilon}^s$ and $W_{-, \varepsilon}^s$ for small ε was developed by Melnikov [1963] and consists of a measurement of the distance between $W_{+, \varepsilon}^s$ and $W_{-, \varepsilon}^s$. Up to a known normalization factor, the first order term of the Taylor series expansion about $\varepsilon = 0$ of the distance between $W_{+, \varepsilon}^s$ and $W_{-, \varepsilon}^s$ can be computed without solving (2.3) explicitly. This first order term is known as the *Melnikov function*. In Appendix 3, we discuss the geometry of the Melnikov function as well as some of the relevant technical points behind its derivation. In this section, we state the results of the calculations for our problem.

The distance between $W_{+, \varepsilon}^s$ and $W_{-, \varepsilon}^s$ is given by

$$d(t_0, \varepsilon) = \varepsilon \frac{M(t_0)}{\|f(q_u(-t_0))\|} + O(\varepsilon^2) \quad (4.1)$$

where $q_u(t)$ is a heteroclinic fluid particle trajectory of the unperturbed velocity field lying in Ψ_u , t_0 parametrizes distance along Ψ_u , and

$$\|f(q_u(-t_0))\| = \sqrt{(f_1(q_u(-t_0)))^2 + (f_2(q_u(-t_0)))^2}.$$

The Melnikov function $M(t_0)$ is defined to be

$$M(t_0) = \int_{-\infty}^{\infty} \left[f_1(q_u(t))g_2(q_u(t), t+t_0) - f_2(q_u(t))g_1(q_u(t), t+t_0) \right] dt. \quad (4.2)$$

and Melnikov's theorem (see Appendix 3) shows us that simple zeros of $M(t_0)$ (i.e. $M(t_0) = 0$,

$\frac{\partial M}{\partial t_0} \neq 0$) imply simple zeros of $d(t_0, \varepsilon)$ for ε sufficiently small. We remark that $d(t_0, \varepsilon)$ may be either positive or negative as it is actually the *signed* distance between $W_{+, \varepsilon}^s$ and $W_{-, \varepsilon}^u$. In Appendix 3, we show that the sign of $d(t_0, \varepsilon)$ gives us information concerning the relative orientation of $W_{+, \varepsilon}^s$ and $W_{-, \varepsilon}^u$. Also note that $\|f(q_u(-t_0))\| \rightarrow 0$ exponentially fast as $t_0 \rightarrow \pm \infty$ which implies that $|d(t_0, \varepsilon)| \rightarrow \infty$ as $t_0 \rightarrow \pm \infty$. This just reflects the fact that $W_{+, \varepsilon}^s$ and $W_{-, \varepsilon}^u$ oscillate unboundedly near $p_{-, \varepsilon}$ and $p_{+, \varepsilon}$ respectively.

We numerically calculate the Melnikov function for the velocity field (2.3) and obtain

$$M(t_0) = \frac{F(\gamma)}{\gamma} \sin(t_0/\gamma) \quad (4.3)$$

where $F(\gamma)$ is plotted in figure 4.3. Note that for fixed γ , $M(t_0)$ has an infinite number of isolated zeros at which $\frac{\partial M}{\partial t_0} \neq 0$. As discussed in Appendix 3, these correspond to transverse intersections of $W_{+, \varepsilon}^s$ and $W_{-, \varepsilon}^u$ and therefore we obtain a direct analytical confirmation of figure 4.2. At $\gamma = 1.78$, $F(\gamma)$ changes sign, which corresponds to a change in the orientation of the intersection of $W_{+, \varepsilon}^s$ and $W_{-, \varepsilon}^u$. For $\gamma = 1.78$, $M(t_0) = 0$ implying that $d(t_0, \varepsilon) = O(\varepsilon^2)$. In figure 4.4 we present the manifolds computed numerically for several values of γ confirming the change of orientation of the intersection.

Figure 4.3 Graph of $F(\gamma)$.

Figure 4.4 Numerical Computations of the Invariant Manifolds for Various Parameter Values.

5. Tangle Dynamics

We now describe the dynamics associated with the tangling of the stable and unstable manifolds of $p_{+, \varepsilon}$ and $p_{-, \varepsilon}$. Specifically, we will describe the essential dynamical mechanisms for fluid transport within the mixing region. We will see that the properties of invariance of the stable and unstable manifolds as well as the orientation preserving property of the Poincaré map render a temporal simplicity to the geometrically complex structure associated with the tangling of the manifolds. This allows us to obtain a quantitative hold on the dynamics in the mixing region. In much of what follows there will be no restriction on the amplitude of ε .

Lobe Motion. We begin with two definitions:

Definition 5.1. Consider a point $q \in W_{+, \varepsilon}^s \cap W_{-, \varepsilon}^u$ and let $p_{+, \varepsilon} q$ denote the segment of $W_{+, \varepsilon}^s$ from $p_{+, \varepsilon}$ to q and let $p_{-, \varepsilon} q$ denote the segment of $W_{-, \varepsilon}^u$ from $p_{-, \varepsilon}$ to q . Then q is called a *primary intersection point* (pip) if $p_{+, \varepsilon} q$ and $p_{-, \varepsilon} q$ intersect only in q , i.e. $p_{+, \varepsilon} q \cap p_{-, \varepsilon} q = \{q\}$. See figure 5.1.

Definition 5.2. Let q_1 and q_2 be two adjacent pip, i.e. there are no pip on the segments of $W_{+, \varepsilon}^s$ and $W_{-, \varepsilon}^u$ which connect q_1 and q_2 . We refer to the region bounded by the segments of $W_{+, \varepsilon}^s$ and $W_{-, \varepsilon}^u$ which connect q_1 and q_2 as a *lobe*. See figure 5.1.

The spatial structure of the manifolds provides a natural ordering by time which is useful when we discuss the flux as well as entrainment and detrainment. To describe this ordering we need the following definitions:

Definition 5.3. Let q_1 and q_2 be pip's. Then we say that $q_1 < q_2$ if q_1 is closer than q_2 to $p_{-\varepsilon}$ in terms of distance along $W_{-, \varepsilon}^u$.

Definition 5.4. Suppose that L_1 and L_2 are lobes. Then we say that $L_1 < L_2$ if each of the pip's defining L_1 are less than or equal to each of the pip's defining L_2 .

Figure 5.1. q_1, q_2, q_3, q_4 are pip's, q_5 is not a pip. L_1, L_2, L_3 are lobes with $L_1 < L_2 < L_3$.

Now let q be a particular pip and consider the region bounded by $p_{+, \varepsilon} q \cup p_{-, \varepsilon} q \cup [W_{+, \varepsilon}^u \cap W_{-, \varepsilon}^s]$. We refer to this as region A. We will describe the motion of fluid across the boundary of A. There is no restriction on the choice of q . In figure 5.2 we choose q rather arbitrarily for illustrative purposes. Later we choose q so that A corresponds as much as possible to the unperturbed core. See figure 5.5.

Figure 5.2. The E_i and D_i for $F(\gamma) > 0$.

Definition 5.5. A lobe is called an *exterior lobe* if no part of its interior is contained in A. A lobe that is not an exterior lobe is called an *interior lobe*.

Now consider figure 5.2. The lobes E_i are exterior lobes for $i \leq 0$ and interior lobes for $i > 0$. Similarly, the lobes D_i are exterior lobes for $i > 0$ and interior lobes for $i \leq 0$. The following is our main result concerning the dynamics of the lobes.

Suppose that the lobes are defined so that for some $n \geq 1$:

1. $T(E_i) = E_{i+n}$
2. $T(D_i) = D_{i+n}$

For small ε , n is just one-half the number of simple zeroes of the Melnikov function in one cycle, $\tau = 2\pi\gamma$. (See Appendix 4.) For arbitrary ε we construct $W_{+, \varepsilon}^s$ and $W_{-, \varepsilon}^u$ numerically and simply track the progression of a pip during one cycle to determine n .

The concise observation above belies its many underlying implications:

1. After one cycle of the time periodic strain-rate field (i.e. one iterate of the Poincaré map) E_0, \dots, E_{-n+1} enter region A. Similarly, after one cycle D_{-1}, \dots, D_{-n} leave region A.
2. The lobes E_i, D_i maintain their ordering throughout their evolution in time under the action of the Poincaré map, i.e.

$$E_i < E_j \text{ implies } T^k(E_i) < T^k(E_j)$$

$$D_i < D_j \text{ implies } T^k(D_i) < T^k(D_j)$$

$$E_i < D_j \text{ implies } T^k(E_i) < T^k(D_j)$$

for all k . This is a consequence of the fact that the Poincaré map preserves orientation and therefore the relative ordering of points along $W_{-,\varepsilon}^u$ is preserved.

Lobe Area. Knowledge of the total area of the n lobes, E_0, \dots, E_{-n+1} , would tell us the amount of fluid entering A per cycle. We show that the Melnikov function gives this information for small ε .

Consider figure 5.3 and the lobe L defined by the pip's q_1 and q_2 . Let us denote the infinitesimal element of arclength along $W_{-,\varepsilon}^u$ by ds and let $l(s)$ denote the perpendicular distance between $W_{+,\varepsilon}^s$ and $W_{-,\varepsilon}^u$. Then the area of L , denoted $\mu(L)$, is given by

$$\mu(L) = \int_{q_1}^{q_2} l(s) ds. \quad (5.1)$$

figure 5.3 Geometry of the Area of the Lobes.

Now $W_{+,\varepsilon}^s$ and $W_{-,\varepsilon}^u$ can be approximated uniformly on semi-infinite time intervals (see Guckenheimer and Holmes [1983]) and because these manifolds move only an $O(\varepsilon)$ amount from the unperturbed manifolds on these time intervals the angle between the line along which $d(t_0, \varepsilon)$ is measured (see Appendix 3) and the line along which $l(s)$ is measured is $O(\varepsilon)$. Thus we can write

$$l(s) = |d(t_0, \varepsilon)| + O(\varepsilon^2) \quad (5.2)$$

$$= \frac{\varepsilon |M(t_0)|}{\|f(q_u(-t_0))\|} + O(\varepsilon^2) \quad (5.3)$$

and

$$ds = \frac{ds}{dt_0} dt_0 = \left[\|f(q_u(-t_0))\| + O(\epsilon) \right] dt_0.$$

Substituting (5.2) and (5.3) into (5.1) gives

$$\begin{aligned} \mu(L) &= \int_{t_{01}}^{t_{02}} \left[\frac{\epsilon |M(t_0)|}{\|f(q_u(-t_0))\|} + O(\epsilon^2) \right] \left[\|f(q_u(-t_0))\| + O(\epsilon) \right] dt_0 \\ &= \epsilon \int_{t_{01}}^{t_{02}} |M(t_0)| dt_0 + O(\epsilon^2) \end{aligned} \quad (5.4)$$

where $q_u(-t_{01}) = q_1$ and $q_u(-t_{02}) = q_2$. Thus we see that the integral of the Melnikov function between two adjacent pip's gives an $O(\epsilon)$ approximation to the area of the lobe defined by the pip's. Several comments are now in order.

1. The validity of (5.4) relies heavily on the validity of the approximation of the perturbed manifolds via regular perturbation theory which is rigorous only on semi-infinite time intervals. Thus (5.4) is only valid for lobes defined by pip's which are outside of sufficiently small neighborhoods of $p_{+, \epsilon}$ and $p_{-, \epsilon}$. However, in our case, the Poincaré map preserves area, so knowing the area of one lobe implies that we know the area of all the images of that lobe under the Poincaré map.
2. For our problem, substituting (4.3) into (5.4) gives the following expression for the area of the n lobes

$$\mu(L) = 2\epsilon |F(\gamma)| + O(\epsilon^2). \quad (5.5)$$

This gives us the explicit dependence of the area of the lobes on the parameter γ . A comparison between the numerical calculation of lobe area and the analytical result (5.5) gives good agreement as seen in figure 5.4.

Figure 5.4 Comparison Between Theoretical and Numerical Calculations of Lobe Areas.

Now let us return to our specific problem. We choose the region A to be defined by the pip which lies on the y axis. As mentioned above, this is so that the resulting shape of the region is very similar to the region of trapped fluid in the unperturbed velocity field, see figure 5.5.

Figure 5.5. The Geometry of Region A.

From (4.3), $M(t_0) = (F(\gamma) / \gamma) \sin t_0 / \gamma$ and, therefore, for small ϵ , one lobe enters and one lobe leaves the region A during each cycle with the area of the lobes equal to $2\epsilon |F(\gamma)| + O(\epsilon^2)$. Notice

from figure 5.4 that for $\gamma = 0.93$, $F(\gamma)$ obtains its maximum, thus the volume of fluid entrained per cycle is maximal at this γ . The volume entrained per unit time is maximum at $\gamma = 0.7$ when $F(\gamma)/\gamma$ is maximum. For $\gamma = 1.78$ the Melnikov function vanishes identically. Hence the $O(\epsilon^2)$ terms in the formula for the distance between the manifolds become important. For example, for $\epsilon = 0.1$, we see in figure 4.4c that the manifolds are nearly tangent for $\gamma = 1.38$ rather than for 1.78. Numerically, we observe also that near the γ for which the Melnikov function vanishes two lobes enter and leave the region A per cycle. (See figure 4.4c, d, e.)

Finally we note that the observed behavior of $F(\gamma)$ as γ increases from zero, i.e. rising to a maximum and then decreasing through zero to negative values, may be explained as follows. The horizontal oscillations of the vortex pair have amplitude $O(\epsilon\gamma)$ while the vertical oscillations have amplitude $O(\epsilon)$ independent of γ . Thus for small γ the predominantly vertical oscillations of the vortices and the phase of the oscillations are such that a particle positioned near the top of the unperturbed core a quarter of the way through a cycle is "pulled" into region A. As a result lobe E_1 progresses to lobe E_2 as shown in figures 5.2 and 4.4a. On the other hand, for large γ , the predominantly horizontal oscillations of the vortices and their phase conspire to "push" similarly positioned particles away from A as in figure 4.4f. At $\gamma = 1.38$ (and $\epsilon = 0.1$) these opposing effects cancel to first order as seen in figure 4.4c.

6. Particle Transport

In this section we discuss particle transport - the flow into and out of region A. The time spent in A depends on the particle's initial conditions and we define this time as the *residence time*. A volume of fluid therefore has an associated *residence time distribution*.

The notion of a residence time distribution is an important concept in mixing systems. For example, if fluid is injected into a catalytic reactor, the amount of product will be primarily influenced by the time spent by the fluid in the reactor. Other processes such as chemical reaction and heat or mass transfer have similar dependencies on the residence time distribution. Danckwerts [1953] discussed the importance and the application of this notion for steady flows through vessels (such as a pipe or tank) and the work presented here is similar to his in spirit. Both works rely on the simple observation that in order to determine the residence time distribution of the fluid initially in the vessel or in A, one needs to know the future of entering fluid only. Though developed separately, the method described here can be thought of as a discretization of Danckwert's work to maps, where again the advantage of working with the Poincaré map instead of the time dependent flow is apparent.

We refer to the motion of fluid into A as *entrainment* and the motion of fluid out of A as *detrainment*. For our problem the Melnikov function has 2 simple zeros per period and therefore (at least for sufficiently small ϵ) one lobe is entrained and one lobe is detrained per cycle. We denote these lobes by E and D, respectively, see figure 6.1. This implies that the volume of fluid entrained into region A during each cycle is the area of lobe E or $\mu(E)$. Also, the amount detrained from region A

during each cycle is the area of lobe D or $\mu(D)$ and by incompressibility it must be equal to $\mu(E)$ and, in general,

$$\mu(T^l D) = \mu(T^k E) \quad (6.1)$$

for all $l, k = 0, \pm 1, \pm 2, \dots$

In this section we discuss more detailed questions of particle transport which can be answered by applying the following rules:

R1. Fluid entering region A on cycle k must be in E on cycle $k-1$.

R2. Fluid leaving region A on cycle k must be in D on cycle $k-1$.

R3. $T^l(E)$ cannot intersect $T^k(E)$ and $T^l(D)$ cannot intersect $T^k(D)$ for any $k, l = 0, \pm 1, \pm 2, \dots$

Regarding R3, we note that it is possible for $T^l(E)$ to intersect $T^k(D)$ for some integers l and k .

The questions we wish to address are:

1. How long does it take fluid to escape A given that it started in A?

Remarkably, it will turn out that answering this question is equivalent to answering the following question:

2. How long does it take fluid to escape from A given that it is in lobe E initially?

More specifically we wish to determine the residence time distributions for the two initial conditions mentioned above. The answer to question 1 may be obtained by brute force calculations, where a large number of initial conditions in A are integrated and the number escaping each cycle are counted. The results of such calculations for two γ values are presented in figure 6.10a,b. The similarity to the manifold's shape as seen in figure 4.2 and demonstrated in figure 6.10c is not accidental, it is a manifestation of the lobe dynamics as described in section 5. Using the lobe dynamics enables us to reduce the problem to the computation of the residence time distribution for lobe E only.

Escape Rates

We consider first fluid that is in lobe E initially (at cycle 0). As discussed previously, after one cycle the fluid in E enters A. However, at some later time, say cycle $k-1$, a portion of the original fluid may be found in lobe D and therefore will escape A on the next cycle. We define e_k to be that portion, i.e.,

e_k = volume of fluid in lobe E at cycle 0 that escapes A on the k^{th} cycle.

clearly,

$$e_k = \mu(T^{k-1}E \cap D) \quad k = 1, 2, \dots \quad (6.2a)$$

and

$$e_k = 0 \quad k \leq 0 \quad (6.2b)$$

Note that the corresponding distribution of escape times is given by $e_k/\mu(E)$. Using incompressibility (6.2a) can alternately be written

$$e_k = \mu(E \cap T^{-k+1}D) \quad k=1, 2, \dots \quad (6.3)$$

Figure 6.1 illustrates the geometry associated with (6.2a) and (6.3)

$$\text{Figure 6.1 a) } e_3 = \mu(T^2E \cap D) \quad \text{b) } e_3 = \mu(E \cap T^{-2}D)$$

Note that replacing E with $T^{-l}E$ in (6.2a) and (6.3) gives the volume of fluid in lobe $T^{-l}E$ at cycle 0 that escapes A on the k^{th} cycle. This is clearly equal to e_{k-l} . In fact, the e_k 's contain information concerning all possible intersections of any E_i lobe with any D_j because

$$e_k = \mu(T^{k+m-1}E \cap T^mD) \quad m = 0, \pm 1, \pm 2, \dots$$

In figure 6.2 we illustrate the case $m = -k+1$ by displaying the sets $E \cap T^{-k+1}D$ for several values of k and $\gamma \approx 0.5, 0.9$.

Figure 6.2. Geometry of $E \cap T^{-k+1}D$ for Various Values of k . a) $\gamma \approx 0.5$. b) $\gamma \approx 0.9$.

Now we consider the escape distribution for region A and define escape volumes as follows:

a_k = volume of fluid in region A on cycle 0 that escapes on cycle k .

From previous discussions it follows that fluid leaving A on the k^{th} cycle must be in the lobe $T^{-k+1}D$ at cycle 0. However not all of $T^{-k+1}D$ was in A at cycle 0 since portions of $T^{-k+1}D$ may intersect $T^{-l}E$, $0 \leq l \leq k$, and should not be counted. So it follows that

$$a_k = \mu(T^{-k+1}D) - \sum_{l=0}^k \mu(T^{-k+1}D \cap T^{-l}E). \quad (6.4)$$

where the sum in (6.4) represents the volume of $T^{-k+1}D$ that is also in some $T^{-l}E$ for $0 \leq l \leq k$. By

incompressibility we have

$$\mu(T^{k+1}D) = \mu(D) = \mu(E) \quad (6.5)$$

and from (6.3) we have

$$e_{k+1} = \mu(T^{k+1}D \cap T^{-1}E) \quad (6.6)$$

Using (6.6) and (6.5) allows us to simplify (6.4) as follows

$$a_k = \mu(E) - \sum_{i=0}^k e_{k-i}$$

or

$$a_k = \mu(E) - \sum_{i=1}^k e_i \quad (6.8)$$

Thus, to compute a_k , we need only information concerning the dynamics of lobe E, namely the e_k . We find e_k numerically by computing the escape cycle for each member of a regular array of grid points in lobe E. To verify the relation between the e_k and the a_k given by (6.8), we have also computed the a_k for one particular choice of the parameters ε and γ by a "brute force" calculation using an array of grid points in region A. The results are shown in figure 6.3 and confirm (6.8).

Figure 6.3 Comparison of the Brute Force Calculation and the Reduced Calculation for $\gamma = 0.5$.

We note that with little effort we can obtain other quantities which are of physical interest in terms of the e_k such as:

$$r_k = \text{volume of fluid initially in A that remains in A after } k \text{ cycles.}$$

clearly,

$$r_k = r_{k-1} - a_k \quad (6.9)$$

or

$$r_k = \mu(A) - \sum_{i=1}^k a_i \quad (6.10)$$

Using (6.8) we obtain:

$$r_k = \mu(A) - k\mu(E) + \sum_{i=1}^k (k-i+1)e_i \quad (6.11)$$

Since e_k and r_k are finite and positive and $\sum_{i=1}^k e_i \leq \mu(E)$, we deduce that

$$\sum_{i=1}^{\infty} e_i = \mu(E) \quad (6.12)$$

$$\sum_{i=1}^{\infty} (i-1) e_i = \mu(A) - \mu(C) \quad (6.13)$$

where $r_{\infty} = \mu(C) \leq \mu(A)$ and $\mu(C)$ is the volume of fluid initially in A that never escapes, i.e. the volume of the core of A. The relation (6.12) is also evident from incompressibility. We note also the inversion formula

$$e_k = r_k - 2r_{k-1} + r_{k-2} \quad (6.14)$$

The Mixing Region

We are now in a position where we can precisely define the mixing region. By definition, fluid particles not in either the free flow region or the core must have trajectories on the Poincaré map that enter and leave the region A. Now in order to enter A the fluid particle trajectory must be in $T^{-k}E$, $k=0,1,2,\dots$. In order to leave A the fluid particle trajectory must also be in $T^{-k}D$, $k=0,1,2,\dots$. From (6.12) the lobe E (and, hence, by invariance, all iterates of E) is completely filled with pieces of T^kD , for all k . Hence the mixing region is given by

$$\bigcup_{k=-\infty}^{\infty} D_k \quad (6.15)$$

The significance of this definition is that it allows us to characterize the region of extremely complex fluid motion in terms of the motion of a fluid line element of finite length (i.e. the boundary of the lobes E and D). We note also that (6.15) gives us an additional characterization of the mixing region. Namely, fluid particle trajectories in the mixing region must make *at least* one revolution around a vortex.

The Unstable Manifold as an Attractor

In general one would like to know the residence time distribution associated with any initial shape B of finite area. This seems at the moment too difficult a question. Qualitatively one expects to have similar behavior as obtained for A. Specifically, for any initial shape B which can be regarded as distortion of A (i.e. B includes non-trivial parts of the mixing region, namely it is not contained in one D lobe), the dominant structure which will be visualized and which will control the transport is W_{-k}^u .

This is a result of the motion of lobes which accumulate on W_{ε}^u as $t \rightarrow \infty$, and the assumption that B has finite area. For example, consider the case in which B overlaps A on the upstream side. For large enough k^* , $T^{-k}E$ contains a very small portion of B for all $k > k^*$, which implies that for $k > k^*$, $T^k B$ will have a very narrow layer upstream of W_{ε}^u , see figure 6.4. The above arguments apply to a broad class of flows having similar structure, namely hyperbolic stagnation points with cyclic motion near them, implying that the unstable manifold is the observed structure in many flow visualizations, depending on how the fluid is marked.

Figure 6.4 The Motion of a General Initial Shape B , a) $t=0$ b) $t=2\pi\gamma$ c) $t=4\pi\gamma$.

A remarkable demonstration of the role of the unstable manifold as an attracting set is obtained by comparing the computations of the unstable manifolds for particle motion in the presence of two idealized, leapfrogging vortex rings (Shariff et al. [1988], Shariff [1989]) with flow visualization experiments of two vortex rings by Yamada and Matsui [1978]. These comparisons have been reproduced in Aref and Kambe [1988, figure 8] and the reader is referred to them. In the idealized flow, the motion of the vortex rings and, therefore, the velocity field is periodic in time in a frame moving with the average speed of the rings. Ring motion is computed according to Dyson's [1893] model and consists of (1) an axial self-induced component that is proportional to $(1/R(t) \log(R(t)/\delta(t)))$, where R is the ring radius and δ is the core radius ($R\delta^2 = \text{const}$) plus (2) the velocity contribution of the other ring. In the experiment, a smoke wire was stretched across the diameter of the pipe. Hence tracer is injected not only into the separating boundary layer which rolls-up to form the vortical cores, but also into the irrotational or weakly vortical fluid surrounding the cores. The smoke begins to reveal even the fine scale features of the manifold.

As another example, consider transport in the vicinity of a single unsteady vortex ring. In the case of an ideal, steady axisymmetric ring, limiting streamsurfaces separate the fluid near the vortical core that moves with the ring from fluid in the free flow region and there is no exchange between the two regions. In most cases of interest, where the toroidal radius of the vortical core is not small compared to the ring radius, front and rear stagnation points will exist on the axis. For a turbulent vortex ring, the velocity field is three-dimensional and unsteady corresponding, of course, to the three-dimensional motions of the vorticity field. Thus, three-dimensional lobelike structures continually pierce the ideal streamsurface from both sides and become severely distorted as they encounter the rear stagnation point of the ideal flow. These structures are revealed in the studies of Glezer and Coles [1987] (see figure 6.4) where it is seen that marked fluid that is injected into the ring during formation is deposited into the wake in the form of three-dimensional lobes. Finally, in the case of ideal, unsteady axisymmetric vortex rings, Shariff [1989] has demonstrated computationally the presence of lobe structures in the Poincaré map for the flow in which the time-period perturbations are caused by the ellipticity of the vortex cores.

Figure 6.5 Flow visualization of a turbulent vortex ring. Glezer and Coles [1987].

Numerical Results and Discussion

We now present numerical results for the residence time distributions, (e_k , a_k , and r_k properly normalized) and discuss their dependence on k and the parameter γ . In particular, some characteristics of the numerical results can be readily understood from the manifold structure.

The $e_k = \mu(E \cap T^{-k}D)$ can be computed in one of two ways:

1. Compute the boundaries of the lobes E and $T^{-k}D$ and find the area of their intersection.
2. Track area elements of the interior of lobe E to determine the area that escapes A at each cycle.

Although the first method is theoretically more satisfying, there are two substantial difficulties: (1) the problem of the exponential stretch of the manifolds and thus of the lobe boundary and (2) the determination of the interior of a tangled boundary for large k . We therefore use the second method where the grid mesh on E was chosen to be sufficiently small. In figure 6.2, for large k , it appears as if the escape area is composed of a number of isolated area elements, but this is merely the result of using a finite number of nondeforming area elements. The actual areas in $E \cap T^{-k}D$ must be composed of a finite number of shapes that connect to each other or the boundary of E since $T^{-k}D$ is simply connected. The appearance of isolated computational points for a relatively fine mesh ($dx = dy = 0.005$) shows that the widths of the interior regions of $E \cap T^{-k}D$ become extremely narrow and demonstrates the difficulties one would encounter when using a scheme that tracks the boundary of E or D .

It is interesting to note how the quantities vary according to qualitative features of the manifolds. Figure 6.6 contains plots of e_k for two γ values. The rapid oscillations of e_k with k is typical for all values of γ and is discussed below.

We include log-linear and log-log plots as an aid to identifying possible exponential or power law behavior but, because of the fluctuations of the e_k for small and large k , we will defer the discussion of these possibilities until the a_k are presented. The small k fluctuations consist of two-cycle oscillations with even k maxima and odd k minima. We explain this phenomenon as follows. Note that the invariance of the manifolds gives $e_{2k} = \mu(T^{2k}E \cap D) = \mu(T^kE \cap T^{-k}D)$ and $e_{2k-1} = \mu(T^{k-1}E \cap T^{-k}D)$. Now in the symmetric Poincaré map T^kE and $T^{-k}D$ are mirror images of each other. Since near the x axis both lobes are flat, we will obtain, in general, a larger volume of intersection than is obtained in a "transversal" intersection which occurs in the asymmetric intersection of $T^{k-1}E \cap T^{-k}D$. However, secondary intersections far from the neighborhood of the stagnation point will relax this difference as k increases. Thus the two-cycle oscillation of the e_k decays. For larger k ($k > 20$) the fluctuations observed in figure 6.6 are due to the statistics of the computation. We have verified that a finer mesh will decrease these fluctuations.

Figure 6.6 The e_k .

The a_k are shown in figure. 6.7. Note that for small k the a_k , as a function of γ , increase with γ up to $\gamma = 0.8$ then decrease until $\gamma = 1.3$ then increase again. This behavior is directly related to the entrainment rate or lobe area given by $2\epsilon |F(\gamma)| + O(\epsilon^2)$. (see figure 5.4). Using figures 6.7d-6.7g we can make tentative conclusions regarding the asymptotic behavior of the a_k for large k for $\gamma = 0.5$ and 0.9. Figure 6.7d strongly indicates exponential behavior for $\gamma = 0.5$ or

$$a_k \sim \beta(r_k - r_\infty) \quad \text{as } k \rightarrow \infty,$$

i.e. a constant probability of escape from A-C for large k . For $\gamma < 0.5$, similar exponential behavior is indicated. For $\gamma > 0.5$ there are no strong indications for either exponential or power law behavior with the possible exception of $\gamma = 0.9$. For $\gamma = 0.9$, figure 6.7g suggests a power law behavior for a_k or

$$a_k \sim \frac{\lambda}{k} (r_k - r_\infty)$$

i.e. a decreasing probability of escape as $k \rightarrow \infty$.

Figure 6.7 The a_k .

Fitting an exponential for the a_k by using a least square method for the log-linear plots, we can compute r_∞ using (6.10):

$$r_\infty = r_{k_0} - 1 - \sum_{i=k_0}^{\infty} a_i - 1 - \frac{c}{1 - e^{-\alpha}} e^{-\alpha k_0}$$

where c and α are related to the best linear fit coefficients. The results are presented in figure 6.8 where r_{50} , r_∞ , and the bounds on r_∞ computed via the least square method are presented. The exponents we get are relatively small and therefore the linear fit to the log-linear plots, as well as the results for r_∞ , should be taken with caution.

Figure 6.8 The Core Area.

The core C is not necessarily composed of only one region. In fact, we find that the core splits into at least two separate domains for $\gamma = 1.38$ for example. This is indicated from the photographs of the escape map (figure 6.9a,b), in which the red regions can be approximately identified with the core.

The appearance of a different number of regions with bounded motion for different γ 's is the result of the distinctive resonances associated with each γ value. Recall from section 4 that the streamline associated with a p/q resonance is determined via the relation $T(I)/2\pi\gamma = p/q$. Therefore, as γ increases, the streamline corresponding to the above relation has larger period and hence must be closer

to the mixing region. Therefore, assuming that the largest KAM torus position is approximately independent of γ , we expect that as γ increases more resonance bands are present outside the largest KAM torus and with further increase in γ , they approach the manifolds and become unobservable. The scenario which is shown in figures 6.9 and 6.10 fits the above description as follows:

For $\gamma = 0.3$ the $p = 4$ $q = 1$ resonance band outside the largest KAM torus is manifested as four white spots outside the large white region - the main core. (In figure 6.10c the unstable manifold is plotted, and the white regions are the regions which the manifold cannot penetrate). In figure 6.10a, where the escape map for $\gamma = 0.5$ is plotted we observe only one core region - the $q = 1$ $p = 4$ resonance band disappeared in the vicinity of the manifolds and no other resonance bands appear. As γ increases to $\gamma = 1.38$ the $p = 1$ $q = 1$ resonance band appears outside the largest KAM torus and two core regions are revealed in figure 6.10b.

Figure 6.9 The unstable manifold for $\gamma = 0.3$.

Figure 6.10 Escape map for a) $\gamma = 0.5$, b) $\gamma = 1.38$, c) $\gamma = 0.5$ with the stable manifold of p_+ in white.

7. Chaos

We have seen that transport between the core and the free flow region can be understood by studying the interaction between the stable and unstable manifolds of $p_{+,E}$ and $p_{-,E}$, respectively. Now we want to show that this interaction gives rise to another important dynamical effect, namely chaotic fluid particle motion.

Roughly speaking, chaotic fluid particle motion may result when structures in the flow conspire to strongly stretch, contract and fold a region of fluid. In our flow the tangling of the manifolds provides the folding mechanism and the fixed points $p_{+,E}$ and $p_{-,E}$ provide the stretching and contraction mechanism. The notion of chaos is made unambiguous when we show that this scenario enables us to prove that the Poincaré map possesses *Smale horseshoes* using the Smale-Birkhoff homoclinic theorem, see Guckenheimer and Holmes [1983] or Wiggins [1988]. Consider figure 7.1 and the "rectangular" region of fluid denoted R. Following the evolution of this region under iteration by the Poincaré map T we see that it is folded, stretched, and contracted and eventually mapped back over itself in the shape of a horseshoe.

Figure 7.1. The Geometry of the Horseshoe Map.

We leave out the details but using techniques which can be found in Moser [1973] or Wiggins [1988] one can show that "R" contains an invariant cantor set Λ such that $T^n|_{\Lambda}$, for some $n \geq 1$, has

1. A countable infinity of unstable periodic fluid particle motions of all possible periods.
2. An uncountable infinity of unstable nonperiodic fluid particle motions.
3. A fluid particle whose orbit under T^n eventually approaches every other point in Λ arbitrarily closely.

Λ is called a chaotic invariant set for T^n . We remark that in Moser [1973] and Wiggins [1988] it is shown that by a continuous change of coordinates $T^n|_{\Lambda}$ can be transformed into a Bernoulli process hence making precise the notion of deterministic chaos. The construction shown in figure 7.1 could be repeated near any transverse heteroclinic point hence Smale horseshoes and their associated chaotic dynamics exist throughout that part of the mixing region in Λ .

So the existence of transverse heteroclinic orbits in a heteroclinic cycle give rise to Smale horseshoes and are therefore the underlying mechanism for chaos. The Melnikov function allows us to determine if transverse heteroclinic orbits are present in the flow and hence give a specific criteria for the presence of Smale horseshoes in terms of the system parameters.

It should be apparent that the presence of horseshoes in a fluid flow may have a significant effect on neighboring fluid particle motions. However, it is difficult to quantify this effect. Two things can be said:

1. The unperturbed velocity field is integrable; therefore typical fluid particles may separate at a linear rate at best. However, in the perturbed velocity field, nearby fluid particles may separate at an exponential rate and moreover the presence of horseshoes may cause fluid particle motions in the mixing region to become rapidly uncorrelated. Intuitively, one would believe that horseshoes are desirable in order to enhance mixing. We discuss these issues in the next section.
2. In order to quantify the mixing of fluid between the core and the free flow region one must understand the dynamics of the interface, i.e. the stable manifold of $p_{+,e}$ and the unstable manifold of $p_{-,e}$. This is a topic which we are currently investigating in more detail. However, from our previous description a significant observation can be made. That is, in the unperturbed velocity field the interface separating the core and the free flow region has finite length but in the perturbed velocity field this interface has infinite length.

8. Stretching and Elongation of Material Elements

In this section we investigate the rate of stretching of material elements in the Oscillating Vortex Pair (OVP) flow and its relation to the time spent in the mixing region. The classical measure for quantifying the local stretching of material lines on the average is the Liapunov exponent, see for example Khakhar, Rising and Ottino [1986]. The motivation for computing the Liapunov exponent is

that it quantifies the chaos in some systems; when a positive exponent exists nearby trajectories diverge from each other exponentially. This notion is particularly useful when dealing with dissipative systems with attractors, since then all initial conditions will eventually diverge as much as trajectories on the attractor diverge. In the OVP flow we have proven the existence of chaotic orbits and we therefore have positive Liapunov exponents for those orbits. However, this set of chaotic orbits is of measure zero. Nevertheless, these orbits are responsible for the expansion and contraction in the mixing region: material elements passing through this region will experience the exponential stretching and contraction of the chaotic orbits. Most material points remain in this chaotic zone for only a finite time, which implies that their exponents vanish. Hence, in our application, the Liapunov exponent is not a useful measure of the stretching of material elements. To quantify this phenomenon we consider the total stretch or elongation of a material element due to its motion through the chaotic region. As discussed in section 4, we concentrate on analyzing the behavior in the mixing region.

We start by defining the stretching rate and its relation to the Liapunov exponent following the formulation of Khakhar, Rising, and Omino [1986]. We write (2.3) together with (2.5) in the form:

$$\dot{p} = F(p, t) \quad (8.1)$$

where $p = (x, y)$. The linearized equation about an arbitrary solution of (8.1) is given by

$$\dot{m} = DF(p(t), t)m \quad (8.2)$$

where DF is the matrix of partial derivatives of F .

We define the stretch of an infinitesimal material line dx emanating from p with orientation m at $t=0$ as $\lambda(p, m, t)$. It is clearly given by

$$\lambda(p, m, t) = \frac{|m(t)|}{|m|} \quad (8.3)$$

where $m(t)$ is a solution of (8.2), $m \neq 0$. The Liapunov exponent of the orbit p is defined as

$$\sigma(p, m) = \lim_{t \rightarrow \infty} \frac{1}{t} \ln \lambda(p, m, t) \quad (8.4)$$

We now concentrate on the region of our interest, the mixing region. By (6.15) this region is composed of $\bigcup_{k=-\infty}^{\infty} D_k$; therefore we need to investigate the orbits in the D_k lobes only. While p is in the chaotic region, we expect, by definition, that the instantaneous stretching rate, $\frac{\dot{\lambda}}{\lambda}$, will have a positive average. After p escapes however, we expect stretching to decrease substantially. In fact we have been able to show (Rom-Kedar [1988]) that

$$\ln \lambda(p, m, t) = \beta(p, m) + \chi(p, m, t) + O\left(\frac{1}{t^2}\right) \quad \text{for } t > t_0 \quad (8.5)$$

where t_0 is the time required for p to be entrained and then escape from the chaotic region and $\chi(p, m, t)$ is a periodic function in t with zero mean and is a result of the oscillating strain-rate field that persists far from the vortex pair. This behavior is demonstrated in Figure 8.1 where we show $\ln \lambda$ and $\frac{\dot{\lambda}}{\lambda}$ for a particle initially in the chaotic region and escaping after 12 cycles. Also shown is $\frac{\lambda}{\lambda}$ averaged over each period to filter out the χ component.

Thus the Liapunov exponent given by (8.4) is identically zero for almost all particles and, in OVP flow, β of (8.5) remains as the useful physical quantity which measures the total elongation of a line element. In particular we will concentrate on the maximal elongation of an infinitesimal neighborhood around p with exponent given by

$$\bar{\beta}(p) = \max_m \beta(p, m)$$

Physically, an infinitesimal dye blob of radius $|m|$ placed at p at $t=0$ will have its length amplified by $\exp(\bar{\beta})$ while it is in or near the chaotic region and, from then on, its length will oscillate periodically with mean $\exp(\bar{\beta})|m|$. Note that we need to maximize β over m in contrast with the procedure for finding the largest Liapunov exponent, where almost all vectors will stretch at the same rate event.

This is the result of analyzing the finite time elongation instead of the asymptotic result. The method to obtain $\bar{\beta}$ follows.

Let $M(t)$ be the fundamental solution matrix of equation (8.2) so that

$$\dot{M} = DF(p(t), t)M \quad (8.6)$$

$$M(0) = I$$

Then, a general solution $m(t)$ of equation (8.2) is given by:

$$m(t) = M(t)m$$

Therefore,

$$\max_m \lambda(p, m, t) = \max_m \left[\frac{m^T M^T M m}{m^T m} \right]^{1/2} = \sqrt{\rho(M^T M)}$$

where $\rho(M^T M)$ is the maximal eigenvalue of $M^T M$. (Note that in general $\sqrt{\rho(M^T M)} \neq \rho(M)$, see Goldhirsch et al. [1987]). To compute $\rho(M^T M) = \rho(MM^T)$ we develop an ODE for the components of MM^T , noting that in two dimensions $\rho(M^T M) = \rho(MM^T)$.

Since the OVP flow is irrotational and incompressible the matrix $DF(p(t), t)$ is symmetric and has the form:

$$DF(p(t), t) = \begin{bmatrix} a(t) & b(t) \\ b(t) & -a(t) \end{bmatrix}$$

$$\text{where } a(t) = \frac{\partial u}{\partial x}(p(t), t) \quad b(t) = \frac{\partial u}{\partial y}(p(t), t)$$

Using Eq. (8.6) and the above form of DF we obtain

$$\frac{d}{dt}(MM^T) = \frac{dM}{dt} M^T + M \frac{dM^T}{dt} = (MM^T)DF + DF(MM^T) \quad (8.7)$$

Now MM^T is a symmetric matrix of the form

$$MM^T = \begin{bmatrix} q & r \\ r & s \end{bmatrix}$$

And equation (8.7), written in component form gives a system of three ODE's for the matrix elements q, r, s . Since $\det(MM^T) = 1$ we obtain the following expression for $\rho(MM^T)$:

$$\rho(MM^T) = \frac{q+s+\sqrt{(q+s)^2-4}}{2}$$

The quantity $q + s$ can be obtained either from the ODE's for q, r , and s or by solving the integral equation:

$$(q+s)^2 - 4 = \left[\int_0^t a(t') (q+s)(t') dt' \right]^2 + 4 \left[\int_0^t b(t') (q+s)(t') dt' \right]^2 + 4.$$

Using the former technique we have found $\bar{\beta}$ for a sample of 530 initial conditions in region $A \cap \bigcup_{k=0}^{\infty} D_{-k}$. The results are presented in Figure 8.3 where we plot $\bar{\beta}$ versus the escape cycle of p .

Though $\bar{\beta}$ takes on a range of values for each escape cycle, the general tendency of $\bar{\beta}$ to increase with the escape cycle, as expected, is clear. In Figure 8.4, we show the average of $\bar{\beta}$ over the set of initial conditions having the same escape cycle. The results indicate that the average stretching rate is correlated with residence time, namely, a longer residence time implies a lower average stretching rate.

To summarize, we have shown that the Liapunov exponents vanish in the OVP flow in the mixing region. This is a result of the flow being open with localized chaos, allowing fluid particles to be convected to infinity after a finite amount of stretching. Therefore we use the total stretch, $\exp(\bar{\beta})$, the elongation of a fluid element while in or near the chaotic region, to quantify the chaos. We found that,

on the average, this quantity increases with residence time but that the average stretching rate tends to decrease with residence time.

9. Summary and Conclusions

We have investigated the flow governed by a vortex pair in the presence of an external strain-rate field that oscillates sinusoidally in time. In particular, we studied transport and mixing of passive particles in this flow. The flow depends on two dimensionless parameters - the period of the oscillation divided by the time required for the vortex pair to travel a distance equal to their separation and the strain-rate amplitude divided by the oscillation frequency.

If the amplitude of the external field is zero then, in a frame moving with the vortex pair, the flow is steady. A fixed, closed volume of fluid is trapped and moves with the vortex pair for all time. This volume of fluid or "bubble" is bounded by two limiting streamlines that connect at two hyperbolic stagnation points, one on the upstream side of the bubble and one on the downstream side. No entrainment or detrainment takes place into or out of this volume. Mixing is poor as two particles an infinitesimal distance apart only separate at most linearly in time for large times, i.e. the Liapunov exponent is zero.

If the strain-rate amplitude is nonzero, the flow is time-periodic in a frame moving with the average speed of the vortex pair and each vortex moves on a closed orbit in this frame. However, some particle motions are quite complicated. During each cycle of the oscillation a certain volume of fluid that approaches from the upstream side is entrained into the fluid bubble moving with the vortex pair. A particle within this entrained fluid volume moves chaotically during its time of residence in the comoving bubble. These particles subsequently escape (are detrained) according to a discrete distribution over the number of cycles in residence till escape. Another distribution of residence times, that corresponding to those particles initially in the bubble at cycle zero, is easily computed from the former distribution.

A quantitative understanding of this transport mechanism was best achieved by examining the Poincaré map for the particle motion. In particular, we considered the stable and unstable manifolds of the two hyperbolic fixed points of the map. For the unperturbed flow, the fixed points coincide with the stagnation points in the flow. Similarly, the unstable manifolds of the upstream fixed point and the stable manifolds of the downstream fixed point coincide with the limiting streamlines in the unperturbed flow and, therefore, coincide with each other. For the perturbed flow, these manifolds break apart and intersect each other transversally, forming a tangle. Within this tangle there are two infinite families of lobes with the boundary of each lobe consisting of a segment of the unstable manifold and, the remainder, a segment of the stable manifold. Any given lobe generates all other lobes in the same family by mapping backwards and forwards in time.

One lobe in particular will be entrained during the next cycle and, in the other family, there is a lobe that will be detrained. By incompressibility all lobes have the same volume and it is this amount of fluid therefore that is entrained and detrained during each cycle. Lobes within a given family do not intersect one another. However, lobes from one family intersect members from the other family. The areas or volumes of intersection correspond directly to the residence time distributions mentioned above. Thus we have a tangle dynamics. Namely all information concerning transport or dispersion of particles in this two-space plus time-dependent flow field is generated by one-dimensional objects - the stable and unstable manifolds of the fixed points of the Poincaré map.

The above results do not require that the strain-rate amplitude be small. However, if the amplitude is small we used regular perturbation theory in the form of the Melnikov technique to check for the existence of transversal intersections and to estimate the width of the fluid zone along the original dividing streamline that participates in the exchange process. In addition we have shown that the lobe area is proportional to the integral of the Melnikov function over one cycle. This analysis showed that, as the period of oscillation increases from zero, the entrainment rate rises from zero to a maximum then falls to zero and rises again. This behavior is the result of two competing effects concerning the advection of particles near the limiting streamline at the top of the bubble, one effect is to advect particles into the bubble during one cycle while the other advects particles away from the bubble.

For arbitrary values of the strain-rate amplitude the lobe structure may be computed numerically. This is a relatively simple matter because the unstable manifolds are attractors in forward time and the stable manifolds are attractors integrating backwards in time. Of course, as one attempts to follow a given lobe for a large number of cycles a rapidly increasing number of points is required to define the structure of the lobe boundary because of the chaotic motion of the boundary points that remain in the bubble. Lobe intersection volume may be computed by tracking lobe boundaries as described above but as an alternative method, and the one used in this paper, one can simply track a uniform array of closely-spaced points that initially fill only the lobe that will be entrained during the next cycle.

We have shown that the existence of transverse heteroclinic orbits, i.e. the lobe structures, gives rise to Smale horseshoes as a result of a stretching and folding mechanism present in the Poincaré map. These horseshoes represent the underlying mechanism for chaotic particle motion. To quantify this chaotic motion and, in particular, the rate of stretching of material elements, we investigated the total elongation of an infinitesimal material element and its dependence on time spent within the bubble.

The concepts and analysis discussed in this paper should be useful in a wide variety of applications. Further development might concentrate on (1) extension of the present results for time-periodic flows to quasi-periodic or chaotic fluid flows, (2) connecting the present work to coarse-grained approaches to turbulent transport using convection-diffusion equations, and (3) developing analytical techniques for the lobe intersection problem by, for example, deriving appropriate one-dimensional maps.

This work was supported in part by Caltech's Program in Advanced Technologies, sponsored by Aerojet General, General Motors, and TRW, and by the Air Force Office of Scientific Research through the Jet Propulsion Laboratory. V.R. acknowledges the support of a Zonta Amelia Earhart Fellowship and of a P.E.O. International Peace Scholarship.

Appendix 1: Vortex Pair in a Wavy-Wall Channel

We show that the particle motion given by (2.3) and (2.5) approximates the motion in the vicinity of a vortex pair moving in a wavy-wall channel. Consider the following solution to the Euler equations, given by the streamfunction of a vortex pair, Ψ_v , plus the streamfunction of a potential flow:

$$\Psi = \Psi_v + \Psi'_{pot} \quad (\text{A1.1a})$$

where

$$\Psi'_v = -\frac{\Gamma}{4\pi} \log \frac{(x - x_v)^2 + (y - y_v)^2}{(x - x_v)^2 + (y + y_v)^2} \quad (\text{A1.1b})$$

and

$$\Psi_{pot} = (V + \varepsilon V_1(\varepsilon))y - \frac{\varepsilon}{k^2} \cos(kx) \sinh(ky) \quad (\text{A1.1c})$$

Here $\pm \Gamma$ are the circulations of the vortices whose positions are $(x_v(t), \pm y_v(t))$, $V + \varepsilon V_1(\varepsilon)$ the average fluid velocity in the channel far away from the vortex pair and $\varepsilon V_1(\varepsilon)$ is defined such that the average velocity of the vortex pair is independent of ε (see below). The vortices move with the fluid velocity given by

$$\frac{dx}{dt} = \frac{\partial \Psi}{\partial y}, \quad \frac{dy}{dt} = -\frac{\partial \Psi}{\partial x} \quad (\text{A1.2})$$

For $\varepsilon = 0$, we have

$$x_v(t) = (V + \frac{\Gamma}{4\pi d})t \quad (\text{A1.3})$$

$$y_v(t) = d$$

Setting $\Psi = \Psi_{wall} = \text{const}$ in (A1.1a) and assuming that $\frac{y_v}{y_{wall}} \ll 1$ we find the equation for the wall boundary,

$$y = y_{wall}(x) \quad (A1.4)$$

$$= \frac{\Psi_{wall}}{V} - \frac{\varepsilon V_1(0)\Psi_{wall}}{V^2} + \frac{\varepsilon}{k^2 V} \sinh\left(\frac{k\Psi_{wall}}{V}\right) \cos(kx) + O(\varepsilon^2) + O\left(\frac{y_v}{y_{wall}}\right)$$

confirming that equations (A1.1) represent flow in a wavy-wall channel where the walls are sufficiently far from the vortices.

Now we compute particle motion by (A1.2) and let $x = \tilde{x} + f(t)$, $x_v(t) = \tilde{x}_v(t) + f(t)$. If $k\tilde{x}_v \ll 1$ and we consider the flow field near the vortices with $ky \ll 1$, then we obtain the desired form:

$$\frac{d\tilde{x}}{dt} = -\frac{\Gamma}{2\pi} \left[\frac{(y - y_v)}{(\tilde{x} - \tilde{x}_v)^2 + (y - y_v)^2} - \frac{y + y_v}{(\tilde{x} - \tilde{x}_v)^2 + (y + y_v)^2} \right] \quad (A1.5a)$$

$$- V_v + \varepsilon \tilde{x} \sin(\omega t) + O(\varepsilon^2)$$

$$\frac{dy}{dt} = \frac{\Gamma(\tilde{x} - \tilde{x}_v)}{2\pi} \left[\frac{1}{(\tilde{x} - \tilde{x}_v)^2 + (y - y_v)^2} - \frac{1}{(\tilde{x} - \tilde{x}_v)^2 + (y + y_v)^2} \right] \quad (A1.5b)$$

$$- \varepsilon y \sin(\omega t) + O(\varepsilon^2)$$

if $f(t)$ is the solution to

$$\frac{df}{dt} = -\frac{\varepsilon}{k} \cos(kf(t)) + V + \frac{\Gamma}{4\pi d} + \varepsilon^2 V_2(\varepsilon) \quad (A1.6)$$

where $V_2(\varepsilon)$ is defined such that

$$f(t) = \left(V + \frac{\Gamma}{4\pi d}\right)t + \varepsilon g(t, \varepsilon) \quad (A1.7)$$

where g is periodic in t . We also have that

$$\omega = k\left(V + \frac{\Gamma}{4\pi d}\right) \quad (A1.8)$$

and

$$V_v = \frac{\Gamma}{4\pi d} - \varepsilon V_1(\varepsilon) \quad (A1.9)$$

Appendix 2: Expansion of the Equations of Motion

The nondimensional equations of motion (2.3) have the following expansion in ϵ :

$$\frac{dx}{dt} = f_1(x, y) + \epsilon g_1(x, y, t/\gamma; \gamma) + O(\epsilon^2) \quad (\text{A2.1a})$$

$$\frac{dy}{dt} = f_2(x, y) + \epsilon g_2(x, y, t/\gamma; \gamma) + O(\epsilon^2) \quad (\text{A2.1b})$$

where the f_i are given by:

$$f_1 = -\frac{y-1}{I_-} + \frac{y+1}{I_+} - \frac{1}{2} \quad (\text{A2.2a})$$

$$f_2 = x \left[\frac{1}{I_-} - \frac{1}{I_+} \right] \quad (\text{A2.2b})$$

and the g_i are given by:

$$g_1 = [\cos(t/\gamma) - 1] \left\{ \frac{1}{I_-} + \frac{1}{I_+} - \frac{2(y-1)^2}{I_-^2} - \frac{2(y+1)^2}{I_+^2} \right\} +$$

$$(x/\gamma) \sin(t/\gamma) \left\{ \gamma^2 \left[\frac{y-1}{I_-^2} - \frac{y+1}{I_+^2} \right] + 1 \right\} - \frac{1}{2} \quad (\text{A2.3a})$$

$$g_2 = 2x [\cos(t/\gamma) - 1] \left\{ \frac{y-1}{I_-^2} + \frac{y+1}{I_+^2} \right\} +$$

$$(1/\gamma) \sin(t/\gamma) \left\{ \frac{\gamma^2}{2} \left[\frac{1}{I_-} - \frac{1}{I_+} \right] - x^2 \gamma^2 \left[\frac{1}{I_-^2} - \frac{1}{I_+^2} \right] - y \right\} \quad (\text{A2.3b})$$

The definitions of I_{\pm} are

$$I_{\pm} = x^2 + (y \pm 1)^2 \quad (\text{A2.4})$$

Appendix 3: The Melnikov Function

In this appendix, we want to discuss some aspects of the Melnikov Function. Specifically, how it arises and what it measures. Recall that the perturbed velocity field can be written in the form

$$\begin{aligned}
\dot{x} &= f_1(x, y) + \varepsilon g_1(x, y, \theta; \gamma) + O(\varepsilon^2) \\
\dot{y} &= f_2(x, y) + \varepsilon g_2(x, y, \theta; \gamma) + O(\varepsilon^2) \\
\dot{\theta} &= 1/\gamma
\end{aligned} \tag{A3.1}$$

As a convenient shorthand notation we will often write (A3.1) in the following vector form

$$\begin{aligned}
\dot{q} &= f(q) + \varepsilon g(q, \theta; \gamma) + O(\varepsilon^2) \\
\dot{\theta} &= 1/\gamma
\end{aligned} \tag{A3.2}$$

where $q = (x, y)$, $f = (f_1, f_2)$, and $g = (g_1, g_2)$.

In each case the unperturbed velocity field is obtained by taking $\varepsilon = 0$ in (A3.1) and (A3.2). We study the two dimensional Poincaré map T obtained from the solutions of (A3.2) which is defined as follows:

$$T : \Sigma \rightarrow \Sigma \tag{A3.3}$$

$$(x(0), y(0)) \mapsto (x(2\pi\gamma), y(2\pi\gamma)).$$

Recall that the Poincaré map obtained from the unperturbed velocity field has saddle points at p_+ and p_- which are connected to each other by the three heteroclinic orbits Ψ_+ , Ψ_0 , and Ψ_- (see Figure 2.1). As noted earlier, by symmetry of the unperturbed flow Ψ_0 remains unbroken under the external strain. We use the Melnikov function to determine the behavior of Ψ_+ and Ψ_- . Since the perturbed velocity field is symmetric about the x -axis, for definiteness, we will only draw pictures of the upper half plane in our development of the Melnikov function.

The construction of the Melnikov function consists of four steps:

1. Develop a parametrization of the unperturbed heteroclinic orbit in the Poincaré section.
2. Define a moving coordinate system along the unperturbed heteroclinic orbit in the Poincaré Section.
3. Define the distance between $W_{+, \varepsilon}^s$ and $W_{-, \varepsilon}^u$ in the moving coordinate system at points along the unperturbed heteroclinic orbit.
4. Utilize Melnikov's trick to develop a computable form for the geometrically defined distance between $W_{+, \varepsilon}^s$ and $W_{-, \varepsilon}^u$ on the points along the unperturbed heteroclinic orbit.

We begin with Step 1.

Step 1: Let $q_u(t)$ denote a heteroclinic trajectory of the unperturbed velocity field which lies in Ψ_+ .

Then since the unperturbed velocity field is not time dependent (i.e., it is autonomous) $q_u(t - t_0)$ is also a heteroclinic trajectory of the unperturbed velocity field which lies in Ψ_u for any $t_0 \in \mathbb{R}$ (see Arnold [1973] for a proof of this fact). Thus $q_u(-t_0)$, $t_0 \in \mathbb{R}$ provides a parametrization of Ψ_u where t_0 is the unique time that it takes for a fluid particle on Ψ_u to flow to $q_u(0)$.

Step 2: The vector $f^\perp(q_u(-t_0)) = (-f_2(q_u(-t_0)), f_1(q_u(-t_0)))$ is perpendicular to Ψ_u at each point $q_u(-t_0)$ on Ψ_u . Thus varying t_0 will serve to move $f^\perp(q_u(-t_0))$ along Ψ_u and the distance between $W_{+, \varepsilon}^s$ and $W_{-, \varepsilon}^u$ will be measured along $f^\perp(q_u(-t_0))$.

Step 3: At $\varepsilon = 0$, W_+^s and W_-^u intersect $f^\perp(q_u(-t_0))$ transversely at each $q_u(-t_0) \in \Psi_u$ (see Arnold [1982] for a definition of the transversal intersection of two manifolds). The intersections are preserved under perturbations so that for ε sufficiently small $W_{+, \varepsilon}^s$ and $W_{-, \varepsilon}^u$ intersect $f^\perp(q_u(-t_0))$ transversely in the points q_ε^s and q_ε^u . Thus we define the distance between $W_{+, \varepsilon}^s$ and $W_{-, \varepsilon}^u$ at the point $q_u(-t_0)$ to be

$$\text{distance} = |q_\varepsilon^u - q_\varepsilon^s|. \quad (\text{A3.4})$$

§

See Figure A3.1.

Figure A3.1. The Geometry of the Distance Between $W_{+, \varepsilon}^s$ and $W_{-, \varepsilon}^u$.

The problem with this definition of the distance is that it does not lend itself to an expression which can easily be computed without solving explicitly for fluid particle motions of the perturbed velocity field; a task which would be quite formidable. However following Melnikov [1963], we define the following "signed" distance measurement

$$d(t_0, \varepsilon) = \frac{f^\perp(q_u(-t_0)) \cdot (q_\varepsilon^u - q_\varepsilon^s)}{\|f^\perp(q_u(-t_0))\|} \quad (\text{A3.5})$$

where " \cdot " denotes the usual vector dot product. It should be clear that by the choice of q_ε^u and q_ε^s that $d(t_0, \varepsilon) = 0$ if and only if $q_\varepsilon^u = q_\varepsilon^s$.

Now because $W_{+, \varepsilon}^s$ and $W_{-, \varepsilon}^u$ vary differentiably with respect to parameters (Fenichel [1971], Hirsch, Pugh, and Shub [1977]) we can Taylor expand (A3.5) about $\varepsilon = 0$ to obtain

$$d(t_0, \varepsilon) = \varepsilon \frac{f^\perp(q_u(-t_0)) \cdot \left(\frac{\partial q^u}{\partial \varepsilon} \Big|_{\varepsilon=0} - \frac{\partial q^s}{\partial \varepsilon} \Big|_{\varepsilon=0} \right)}{\|f^\perp(q_u(-t_0))\|} + O(\varepsilon^2) \quad (\text{A3.6})$$

where we have used the fact that $q_0^u = q_0^s$.

The *Melnikov function*, denoted $M(t_0)$, is defined to be:

$$M(t_0) = f^-(q_u(-t_0)) \cdot \left(\frac{\partial q_\varepsilon^u}{\partial \varepsilon} \Big|_{\varepsilon=0} - \frac{\partial q_\varepsilon^s}{\partial \varepsilon} \Big|_{\varepsilon=0} \right) \quad (\text{A3.7})$$

and is (up to the normalization factor $\|f(q_u(-t_0))\|^{-1}$) the leading order term in the Taylor series expansion for the distance between $W_{+,\varepsilon}^s$ and $W_{-,\varepsilon}^u$ at the point $q_u(-t_0)$.

Step 4. Melnikov [1963] was able to derive an expression for (A3.7) without explicitly computing particle paths of the perturbed velocity field. His procedure consisted of the following steps

- a). Prove that the particle paths of the perturbed velocity field through the points q_ε^u and q_ε^s exist on the time intervals $(-\infty, 0]$ and $[0, \infty)$, respectively.
- b). Using a) along with the first variational equation for solutions through q_ε^u and q_ε^s (i.e. regular perturbation theory) derive a linear first order ordinary differential equation for the time dependent Melnikov function

$$M(t, t_0) = f^-(q_u(t - t_0)) \cdot \left(\frac{\partial q_\varepsilon^u(t)}{\partial \varepsilon} \Big|_{\varepsilon=0} - \frac{\partial q_\varepsilon^s(t)}{\partial \varepsilon} \Big|_{\varepsilon=0} \right) \quad (\text{A3.8})$$

where $q_\varepsilon^u(t)$ and $q_\varepsilon^s(t)$ are particle paths of the perturbed velocity field satisfying $q_\varepsilon^u(0) = q_\varepsilon^u$ and $q_\varepsilon^s(0) = q_\varepsilon^s$, respectively. Thus $M(0, t_0) = M(t_0)$.

- c). Solve the linear first order differential equation for $M(t, t_0)$ and obtain the Melnikov function by evaluating at $t = 0$. In the process boundary conditions for the solution at $\pm\infty$ are imposed which were the reason for needing the existence proof of particle paths on semi-infinite time intervals as described in a).

For the full details of these steps see Guckenheimer and Holmes [1983] or Wiggins [1988]. Finally, one obtains the following form for the Melnikov function.

$$M(t_0) = \int_{-\infty}^{\infty} \left[f_1(q_u(t)) g_2(q_u(t), t + t_0) - f_2(q_u(t)) g_1(q_u(t), t + t_0) \right] dt \quad (\text{A3.9})$$

and we have the following key theorem.

Theorem A3.1. Suppose there exists $t_0 = \bar{t}_0$ such that

$$1) \quad M(\bar{t}_0) = 0$$

$$2) \quad \frac{\partial M}{\partial t_0}(\bar{t}_0) \neq 0$$

Then $W_{+, \varepsilon}^s$ and $W_{-, \varepsilon}^u$ intersect transversely near $q_u(-\bar{t}_0)$. If $M(t_0)$ is bounded away from zero for all t_0 , then $W_{+, \varepsilon}^s$ and $W_{-, \varepsilon}^u$ are bounded away from each other.

Proof. See Guckenheimer and Holmes [1983] or Wiggins [1988].

Thus we can determine whether or not $W_{+, \varepsilon}^s$ and $W_{-, \varepsilon}^u$ intersect without solving for fluid particle motions of the perturbed velocity field.

We now want to point out two properties of the Melnikov function which are important.

1. Zero's of $M(t_0)$ Correspond to Primary Intersection Points

The Melnikov function is a first order measure of the distance between $W_{+, \varepsilon}^s$ and $W_{-, \varepsilon}^u$ along the line $f^{\perp}(q_u(-t_0))$. However, it is possible that $W_{+, \varepsilon}^s$ and $W_{-, \varepsilon}^u$ may intersect $f^{\perp}(q_u(-t_0))$ many times as depicted in Figure A3.2. The question arises of which two points on $W_{+, \varepsilon}^s \cap f^{\perp}(q_u(-t_0))$ and $W_{-, \varepsilon}^u \cap f^{\perp}(q_u(-t_0))$ is the distance being measured. The answer to this question comes from the validity of the regular perturbation theory which was used to obtain a computable expression for the Melnikov function (step 4). The fact that we can approximate fluid particle motions of the perturbed velocity field uniformly only on semi-infinite time intervals coupled with the geometry of the time dependent Melnikov function implies that the Melnikov function is a measurement between points in $W_{+, \varepsilon}^s$ and $W_{-, \varepsilon}^u$ along $f^{\perp}(q_u(-t_0))$ which are "closest" to $p_{+, \varepsilon}$ and $p_{-, \varepsilon}$, respectively, in the sense of elapsed time of motion along $W_{+, \varepsilon}^s$ and $W_{-, \varepsilon}^u$. These points are denoted \bar{q}_ε^s and \bar{q}_ε^u in Figure A3.2. From definition 5.1, it follows that \bar{q}_ε^s and \bar{q}_ε^u are primary intersection points. For more details see Wiggins [1988].

Figure A3.2. Intersection of the Manifolds with $f^{\perp}(q_u(-t_0))$

2. The Relative Displacement of $W_{+, \varepsilon}^s$ and $W_{-, \varepsilon}^u$

Since transport in the mixing region is governed by $W_{+, \varepsilon}^s$ and $W_{-, \varepsilon}^u$ it is useful to know their relative positions and, because the Melnikov function is a signed distance measurement it contains this information. From the definition of the distance between $W_{+, \varepsilon}^s$ and $W_{-, \varepsilon}^u$ given in (A3.5), it is simple to show that the geometry of the manifolds shown in Figure (A3.3) holds. For the OVP flow the Melnikov function is given by equation 4.3 and Figures 4.3 and 4.4 confirm the relation between the Melnikov function and the relative positions of the stable and unstable manifolds for this flow.

Figure A3.3. The Melnikov Function and the Relative Orientations of the Manifolds.

3. Periodicity of $M(t_0)$

The Melnikov function is a periodic function of t_0 having the same period as the external strain field (see Guckenheimer and Holmes [1983]). This is an indication that one heteroclinic point implies the existence of a countable infinity of heteroclinic points.

Appendix 4: The Melnikov Function and Lobe Motion

We now give the proof of Theorem 5.1 which is restated below:

Theorem 5.1. Suppose $M(t_0)$ has $2n$ simple zeros in one period τ . Then

- 1) $T(E_i) = E_{i+n}$
- 2) $T(D_i) = D_{i+n}$

Proof: From Appendix 3, simple zeros of the Melnikov function correspond to pip's. We denote the $2n$ zeros of $M(t_0)$ in one period as follows:

$$q_i^E < q_i^D < q_{i+1}^E < \dots < q_{i+n-1}^E < q_{i+n-1}^D$$

where the notation and ordering (see definition 5.3) are chosen such that E_{i+k} is formed by q_{i+k}^E and q_{i+k}^D and D_{i+k} is formed by q_{i+k}^D and q_{i+k+1}^E for $k = 1, \dots, n-1$.

Now by orientation preservation pip's maintain their relative ordering along W_{-2}^u under iteration by T and because the velocity field (and hence the Melnikov function) is periodic in time with period τ we have:

$$T(q_i^E) = q_{i+n}^E$$

and

$$T(q_i^D) = q_{i+n}^D$$

Then by definition it follows that

$$T(E_i) = E_{i+n}$$

and

$$T(D_i) = D_{i+n}$$

□

Appendix 5-Some Properties of Poincaré Maps

In this appendix we will point out some general properties of Poincaré maps which have fluid dynamical consequences and are not usually discussed in standard texts.

1. *Area Preservation.* A consequence of the conservation of mass is that the Poincaré map preserves area.
2. *Orientation Preservation.* Poincaré maps obtained by discretely sampling trajectories of ordinary differential equations have the property of preserving the orientation of area elements. Analytically, this means that the determinant of the Jacobian of the map is strictly positive over its domain of definition (note: by area preservation the determinant of the Jacobian is identically one). Geometrically, orientation preservation can be described as follows. Consider a simply connected area element D with three points denoted a , b , and c on the boundary of D . Suppose that as one walks along the boundary of D in a counterclockwise sense (i.e. with the left arm pointed toward the interior of D) beginning at a so that next b and then c is encountered. Now let $T_{\bar{\theta}}(D) = D'$ with $T_{\bar{\theta}}(a) = a'$, $T_{\bar{\theta}}(b) = b'$, and $T_{\bar{\theta}}(c) = c'$. $T_{\bar{\theta}}$ is orientation preserving if as one walks along the boundary of D' in a counterclockwise sense starting at a' then next b' and then c' is encountered. This implies that the interior of a closed curve is mapped to the interior of its image. See Figure A5.1 for an illustration of the geometry of orientation preservation.

Figure A5.1. Orientation Preservation of $T_{\bar{\theta}}$.

3. *Variation of the Cross-section $\Sigma^{\bar{\theta}}$.* Notice from (3.2) that the Poincaré map depends on the phase of the strain-rate field. The question then arises as to how the Poincaré map changes as the phase of the field is varied? Fortunately, there is no qualitative difference in any of these maps. The technical term is that the different maps are *differentiably equivalent* (see Irwin [1980]) which means that given any two Poincaré maps obtained by fixing two different phases of the strain-rate field there exists a differentiable change of coordinates which transforms one map into the other. In particular, the nature of the stability of a fluid particle trajectory is the same for each Poincaré map. Since there is no qualitative difference in the Poincaré maps we will take $\bar{\theta} = 0$. This choice has the advantage that the Poincaré map on this cross-section is symmetric about the y -axis with time reversed. We refer to the associated Poincaré map as T .
4. *Flow Dynamics via the Poincaré Map.* In studying the motion of fluid particles the concepts of streamlines, pathlines, and streaklines are very natural. However, as mentioned earlier, their use in the study of unsteady flows is limited since their relationship to such dynamical phenomena as mixing and transport properties may be unclear (Ottino [1988]). In fact these concepts may be misleading. For example, Hama[1962] showed that streaklines and pathlines in a time-dependent

laminar flow may look turbulent. In the context of the Poincaré map, the dynamical evolution of fluid particles is expressed in terms of the *orbits* of the Poincaré map. The orbit of a fluid particle is defined as follows: Let p be a fluid particle, then the orbit of p under T is the bi-infinite sequence of points given by:

$$\left\{ \dots, T^{-n}(p), \dots, T^{-1}(p), p, T(p), \dots, T^n(p), \dots \right\}$$

where

$$T^n(p) = \overbrace{T(T(\dots(T(p))\dots))}^{n \text{ factors}}.$$

REFERENCES

- Arnold, V. I. 1965 *Sur La Topologie Des Ecoulements Stationnaires De Fluides Parfaits*, C.R. Acad. Sci. Paris, 261, 17.
- Arnold, V. I. 1978 *Mathematical Methods of Classical Mechanics*, Springer-Verlag, New York.
- Arnold, V. I. 1982 *Geometrical Methods in the Theory of Ordinary Differential Equations*. Springer-Verlag: New York, Heidelberg, Berlin.
- Arnold, V. I. and Avez, A. 1968 *Ergodic Problems of Classical Mechanics*, W.A. Benjamin, New York.
- Arnold, V. I. and Korkine, E. I. 1983 The Growth of a Magnetic Field in a Steady Compressible Flow, *Vestn. Mosk. Univ. Mat. Mekh.*, 3, 43 (in Russian).
- Aref, H. 1983 Integrable, Chaotic, and Turbulent Vortex Motion in Two-Dimensional Flows, *Ann. Rev. Fluid Mech.*, 15, 345.
- Aref, H. 1984 Stirring by Chaotic Advection, *J. Fluid Mech.*, 143, 1.
- Aref, H. and Balachandar S. 1986 Chaotic Advection in a Stokes Flow, *Phys. Fluids*, 29, 3515.
- Aref, H. and Kambe, T. 1988 Report on the IUTAM Symposium: fundamental aspects of vortex motion, *J. Fluid Mech.*, 190, 571.
- Arter, W. 1983 Ergodic Streamlines in Steady Convection, *Phys. Lett.*, No. 97A, 171.
- Aubry, S. and Le Daeron, P. R. 1983 The Discrete Frenkel-Kontorova Model and its Extensions. 1. Exact Results for the Ground States, *Physica 8D*, 381.

- Broadwell, J. E. 1987 A Model For Reactions In Turbulent Jets: Effects of Reynolds, Schmidt, and Damkohler Numbers, to appear in *Turbulent Reactive Flows. Vol. I. Structure: Diagnostic and Analysis*, Springer-Verlag Lectures in Engineering.
- Broomhead, D. S. and Rylie, S. C. 1988 Particle Paths in Wavy Vortices, *Nonlinearity*, 1, 409.
- Chaiken, J., Chevray, R., Tabor, M., and Tan, Q. M. 1986 Experimental Study of Lagrangian Turbulence in Stokes Flow, *Proc. R. Soc. Lond. A*, 408, 105.
- Chaiken, J., Chu, C.K., Tabor, M., and Tan, Q.M. 1987 Lagrangian Turbulence and Spatial Complexity in Stokes Flow, *Phys. Fluids*, 30, 687.
- Chien, W. -L, Rising III, H., and Ottino, J. M. 1986 Laminar and Chaotic Mixing in Several Cavity Flows, *J. Fluid Mech.*, 170, 355.
- Danckwerts, P. V. 1953 Continuous Flow Systems of Residence Times, *Chem. Eng. Sci.*, 2, 1.
- Dimotakis, P. E. 1987 Turbulent Shear Layer Mixing with Fast Chemical Reactions, US - France Workshop on Turbulent Reactive Flows (Rouen, France), 7 - 10 July 1987, Proceedings to appear (Springer Verlag).
- Dombre, T., Frisch, U., Greene, J. M., Henon, M., Mehr, A., and Soward, A. 1986 Chaotic Streamlines in the ABC Flows, *J. Fluid Mech.*, 167, 353.
- Dyson, F.W. 1893 *Phil. Trans. Roy. Soc. London* A184 1041.
- Feingold, M., Kadanoff L. P., and Piro O. 1988 Passive Scalars, 3D Volume Preserving Maps and Chaos, *J. Statis. Phys.*, 50, 529.
- Fenichel, N. 1971 Persistence and Smoothness of Invariant Manifolds for Flows, *Indiana Univ. Math. J.*, 21, 193.
- Galloway, D. and Frisch, U. 1986 Dynamo Action in a Family of Flows with Chaotic Streamlines, *Geophys. Astrophys. Fluid Dynamics*, 36, 53.
- Glezer, A. and Coles, D. 1987 private communication.
- Goldhirsch, I., Sulem, P. L., and Orszag, S. A. 1987 Stability and Lyapunov Stability of Dynamical Systems: A Different Approach and a Numerical Method, *Physica*, 27D, 311.
- Guckenheimer, J. and Holmes, P. 1983 *Non-Linear Oscillations, Dynamical Systems and Bifurcations of Vector Fields*, Springer-Verlag, New York.
- Hama, F. R. 1962 Streaklines in a Perturbed Shear Flow, *Phys. Fluids*, 5, No. 6, 644.
- Henon, M. 1966 Sur la Topologie des Lignes de Courant dans un Cas Particular, *C. R. Acad. Sci. Paris Ser. A* 262, 312.

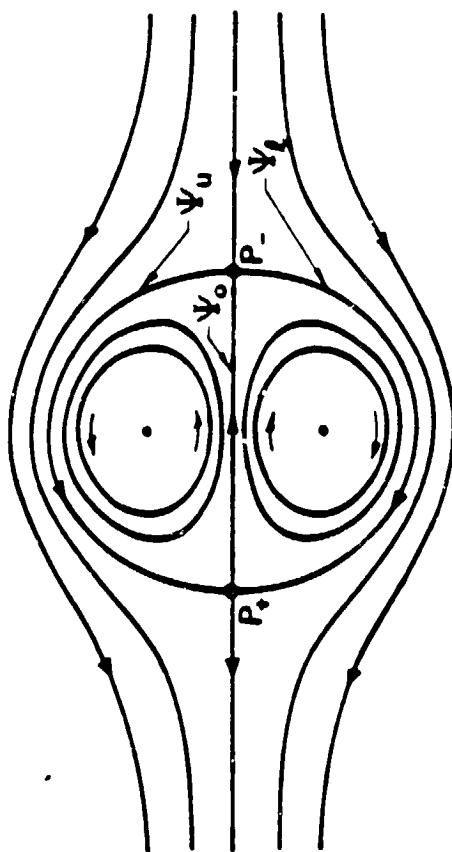
- Hirsch, M. W., Pugh, C. C. and Shub, M. 1977 Invariant Manifolds in "*Springer Lecture Notes in Mathematics*", No. 583, Springer-Verlag, New York.
- Irwin, M. C. 1980 *Smooth Dynamical Systems*, Academic Press, New York.
- Kerr, R. M. 1985 Higher-Order Derivative Correlations and the Alignment of Small-Scale Structures in Isotropic Numerical Turbulence, *J. Fluid Mech.*, **153**, 31.
- Kerstein, A. R. and Ashurst W. T. 1984 Lognormality of Gradients of Diffusive Scalars in Homogeneous, Two Dimensional Mixing Systems, *Phys. Fluids*, **27**, No. 12, 2819.
- Khakhar, D. V., Rising, H. III and Ottino, J. M. 1986 Analysis of Chaotic Mixing in Two Model Systems, *J. Fluid Mech.*, **172**, 419.
- Marble, F. E. 1985 Growth of a Diffusion Flame in the Field of a Vortex, *Recent Advances in the Aerospace Sciences*, pp. 395, C. Casci editor, Plenum Publishing.
- Mather, J. N. 1984 Non-Existence of Invariant Circles, *Ergod. Theory Dyn. Syst.*, **4**, 301.
- Melnikov, V. K. 1963 On the Stability of the Center for Time Periodic Perturbations, *Trans. Moscow Math. Soc.*, **12**, 1.
- Moffatt, H. K. and Proctor, M. R. E. 1985 Topological Constraints Associated with Fast Dynamo Action, *J. Fluid Mech.*, **154**, 493.
- Moser, J. 1973 *Stable and Random Motions in Dynamical Systems*, Princeton University Press, Princeton.
- Ottino, J. M. 1988 *The Kinematics of Mixing: Stretching, Chaos, and Transport*, Cambridge University Press.
- Ottino, J. M., Leong, C. W., Rising, H. and Swanson, P. D. 1988 Morphological Structures Produced by Mixing in Chaotic Flows, *Nature*, **333**, 419.
- Percival, I. C. 1980 Variational Principles For Invariant Tori and Cantori. *AIP Conference Proc., Nonlinear Dynamics and the Beam-Beam Interaction*, **57**, New York. Mouth M. and Herrera J. C. editors.
- Pope, S. B. 1987 Turbulent Premixed Flames, *Ann. Rev. Fluid Mech.*, **19**, 237.
- Ralph, M. E. 1986 Oscillatory Flows in Wavy-Walled Tubes, *J. Fluid Mech.*, **168**, 515.
- Rom-Kedar, V. 1988 *Part I: An Analytical Study of Transport, Mixing and Chaos in an Unsteady Vortical Flow. Part II: Transport in Two Dimensional Maps*. Ph.D Thesis, California Institute of Technology, Pasadena, CA.

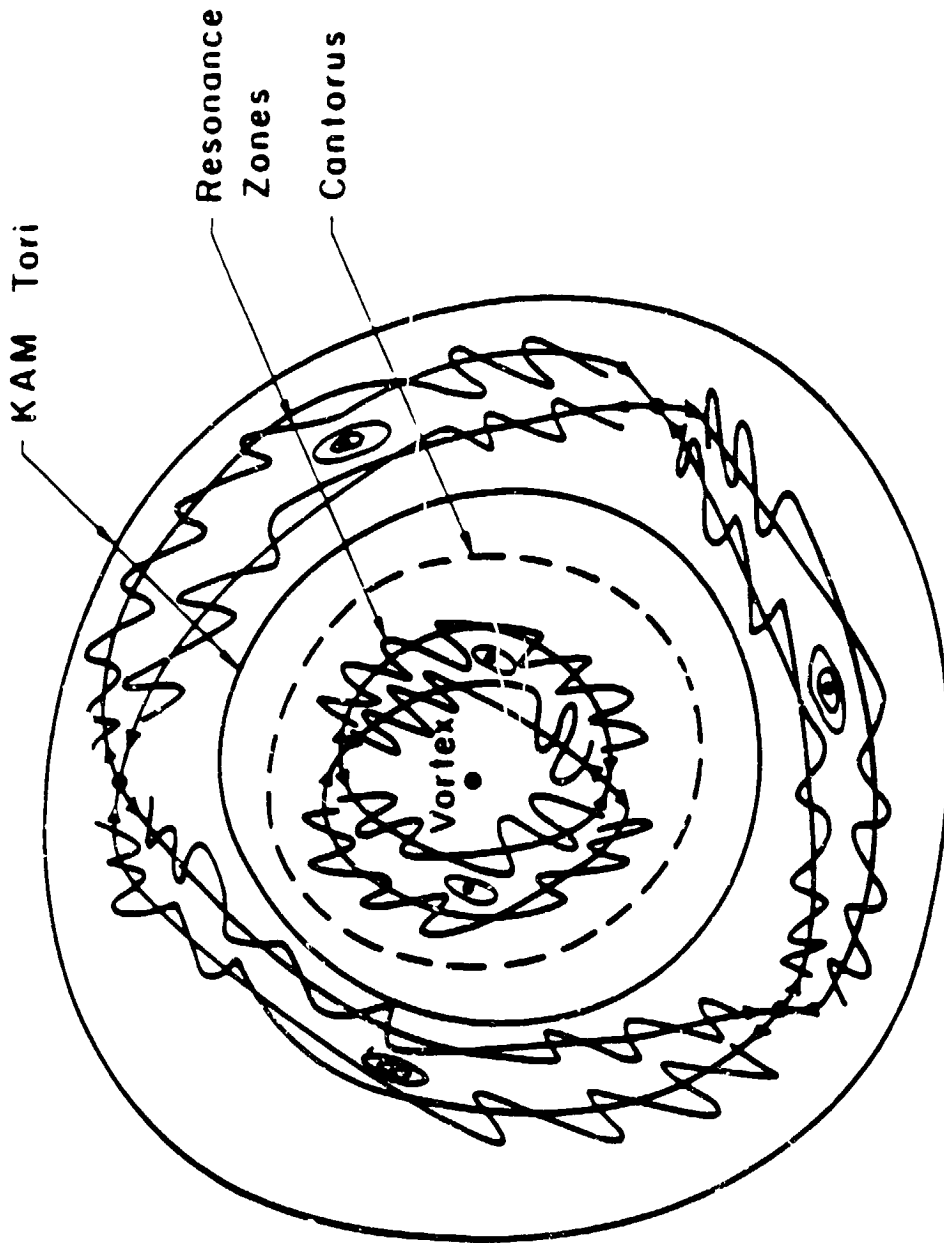
- Rom-Kedar, V. and Wiggins, S. 1989 Transport in Two-Dimensional Maps. *to appear in Arch. Rat. Mech. and Anal.*
- Shariff, K. 1989 Dynamics of a Class of Vortex Rings, Ph.D thesis, Dept. of Mech. Engr., Stanford University.
- Shariff, K., Leonard, A., Zabusky, N. J., and Ferziger, J. H. 1988 Acoustics and Dynamics of Coaxial Interacting Vortex Rings, *Fluid Dyn. Res.*, 3, 337.
- Sobey, I. J. 1985 Dispersion Caused by Separation During Oscillatory Flow Through a Furrowed Channel, *Chem. Eng. Sci.*, 40, 2129.
- Suresh, A. 1985 Point Vortex Interactions, Ph. D thesis, Princeton University.
- Wiggins, S. 1987 Chaos in the Quasiperiodically Forced Duffing Oscillator, *Phy. Lett.*, 124A, 138.
- Wiggins, S. 1988 *Global Bifurcations and Chaos - Analytical Methods*, Springer Verlag: New York, Heidelberg, Berlin.
- Yamada, H. and Matsui, T. 1978 in *An Album of Fluid Motion*, pp. 46, The Parabolic Press, M. Van Dyke editor.

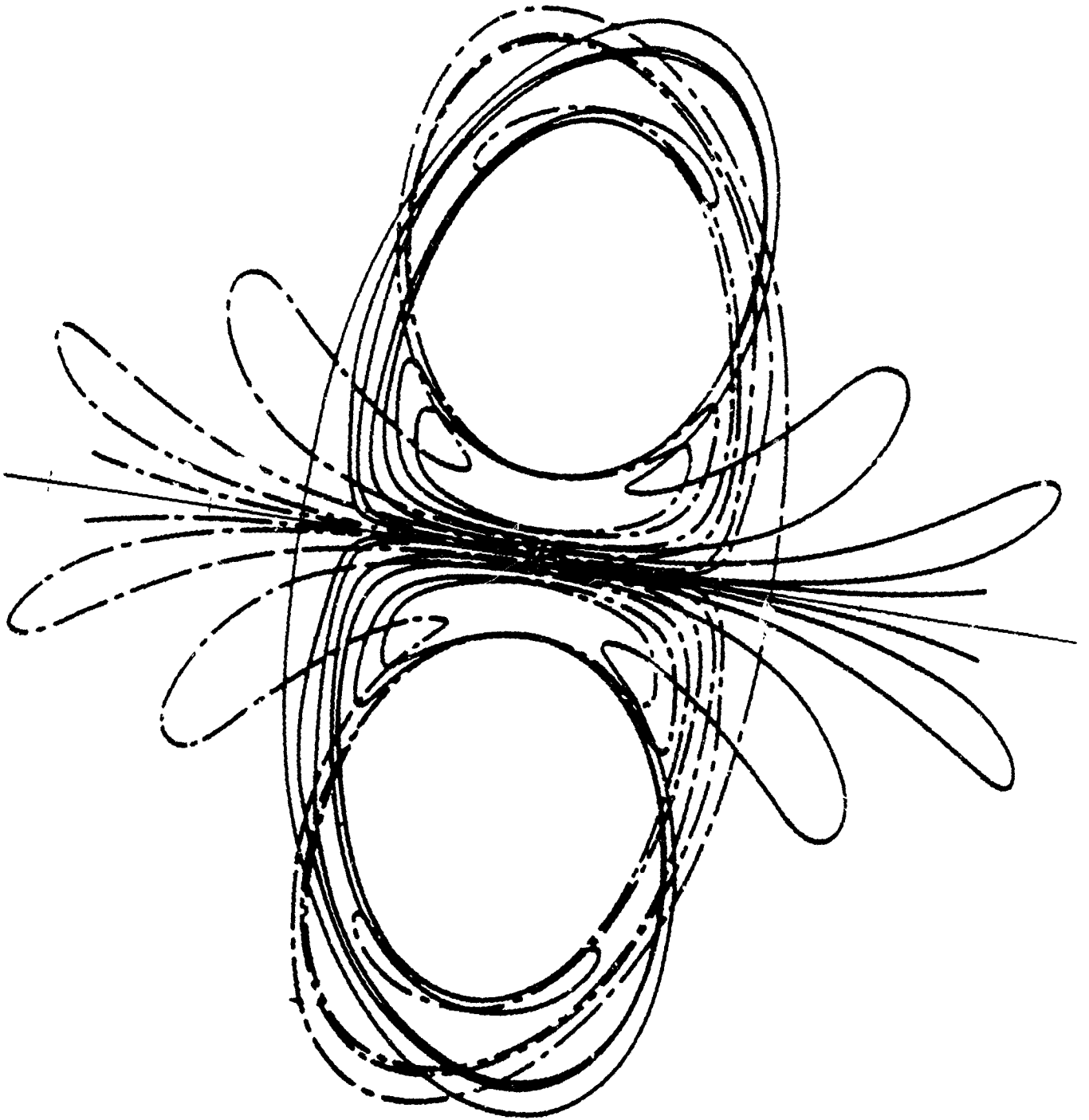
FIGURE CAPTIONS

- Figure2.1 Streamlines of the Unperturbed Flow.
- Figure4.1 Resonance Bands and AM Tori.
- Figure4.2 The Homoclinic Tangle in the Mixing Region.
- Figure4.3 Graph of $F(\gamma)$.
- Figure4.4 Numerical Computations of the Invariant Manifolds for Various Parameter Values, — Unstable Manifold, --- Stable Manifold.
- Figure5.1 q_1, q_2, q_3, q_4 are pip's, q_5 is not a pip. L_1, L_2, L_3 are the lobes with $L_1 < L_2 < L_3$.
- Figure5.2 The E_i and D_i .
- Figure5.3 Geometry of the Area of the Lobes.
- Figure5.4 Comparison Between Theoretical and Numerical Calculations of Lobe Areas, — $F(\gamma)$, *, $\varepsilon = 0.01$, +, $\varepsilon = 0.05$, o, $\varepsilon = 0.1$.
- Figure5.5 The Geometry of Region A, a) unperturbed flow b) perturbed flow.
- Figure6.1 a) $e_3 = \mu(T^2E \cap D)$ b) $e_3 = \mu(E \cap T^{-2}D)$.
- Figure6.2 Geometry of $E \cap T^{-k+1}D$ for Various Values of k . a) $\gamma=0.5$. b) $\gamma=0.9$.
- Figure6.3 Comparison of the Brute Force Calculation and the Reduced Calculation for $\gamma=0.5$,
 ■ brute force calculation with mesh = 0.005,
 □ reduced calculation with mesh = 0.005,
 ◇ brute force calculation with mesh = 0.0075.
- Figure6.4 The Motion of a General Initial Shape B, a) $t=0$ b) $t=2\pi\gamma$ c) $t=4\pi\gamma$.
- Figure6.5 Flow visualization of a turbulent vortex ring. Glezer and Coles [1987].
- Figure6.6 The e_k , a) $\gamma=0.5$, log-linear plot b) $\gamma=0.9$, log linear plot c) $\gamma=0.5$, log-log plot d) $\gamma=0.9$, log-log plot.
- Figure6.7 The a_k , a) $\gamma=0.3, 0.5, 0.7$ b) $\gamma=0.9, 1.1$ c) $\gamma=1.7, 1.9$ d) $\gamma=0.5$, log-linear plot e) $\gamma=0.5$, log-log plot f) $\gamma=0.9$, log-linear plot g) $\gamma=0.9$, log-log plot.
- Figure6.8 The Core Area: ★ $r_{50}/\mu(A)$, ★ $r_{\infty}/\mu(A)$, + upper and lower bounds on $r_{\infty}/\mu(A)$
- Figure6.9 The Unstable Manifold for $\gamma=0.3$.

- Figure6.10 The escape map for a) $\gamma=0.5$ b) $\gamma=1.38$ c) $\gamma=0.5$ with the unstable manifold plotted in white. The initial conditions are colored according to their residence time: the color is graded from blue via green to red with residence time from 0 to 50 cycles.
- Figure7.1 The Geometry of the Horseshoe Map
- Figure8.1 a) $\frac{\dot{\lambda}}{\lambda}$ for an Initial Condition in A-C. b) $\ln \lambda$ for the Same Initial Condition.
- Figure8.2 The Total Stretch $\bar{\beta}$.
- Figure8.3 The Total Stretch Averaged Over a Sample of Initial Conditions With the Same Escape Cycle.
- FigureA3.1 The Geometry of the Distance Between $W_{+,x}^s$ and $W_{-,x}^u$.
- FigureA3.2 Intersection of the Manifolds with $f^{-1}(q_u(-t_0))$
- FigureA3.3 The Melnikov Function and the Relative Orientations of the Manifolds.
- FigureA5.1 Orientation Preservation of $T_{\bar{g}}$.







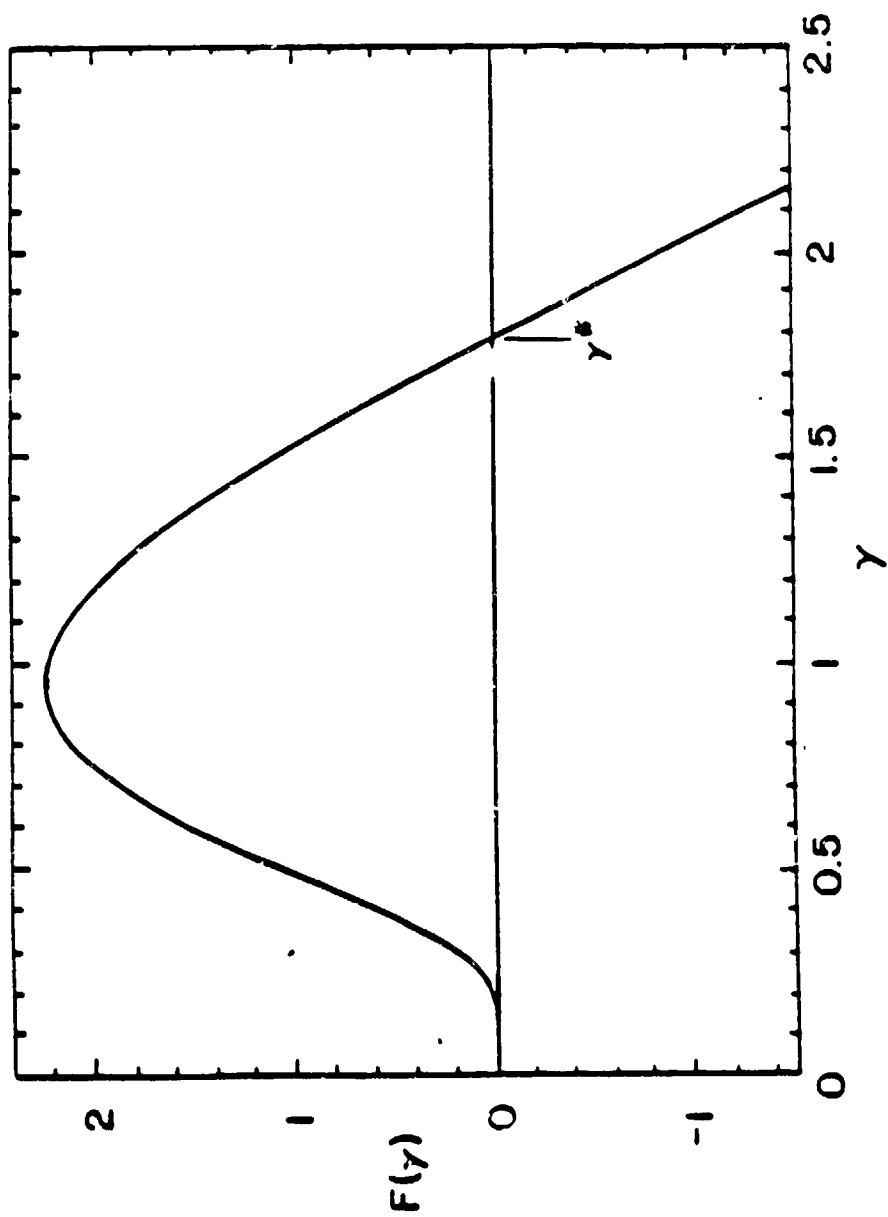
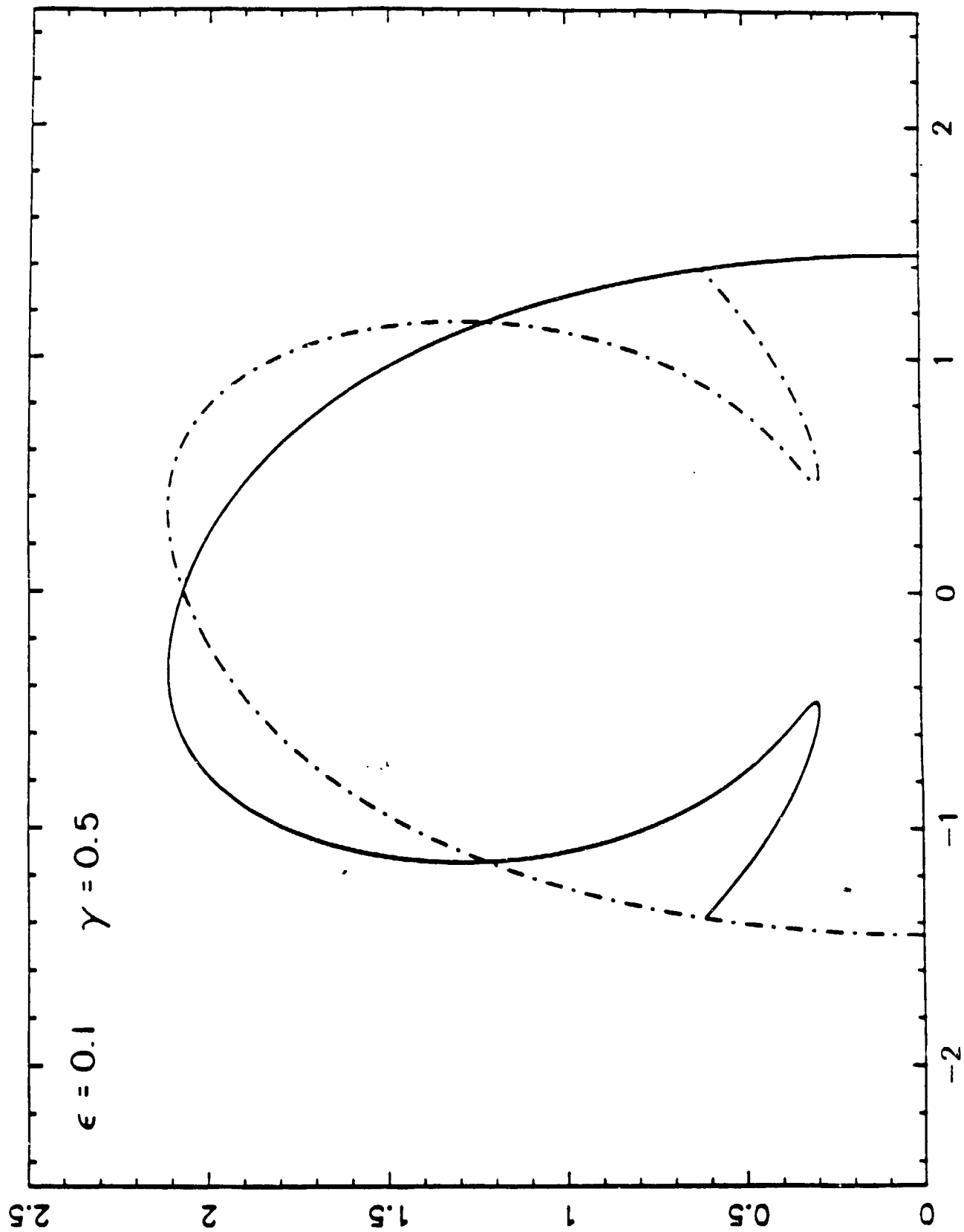
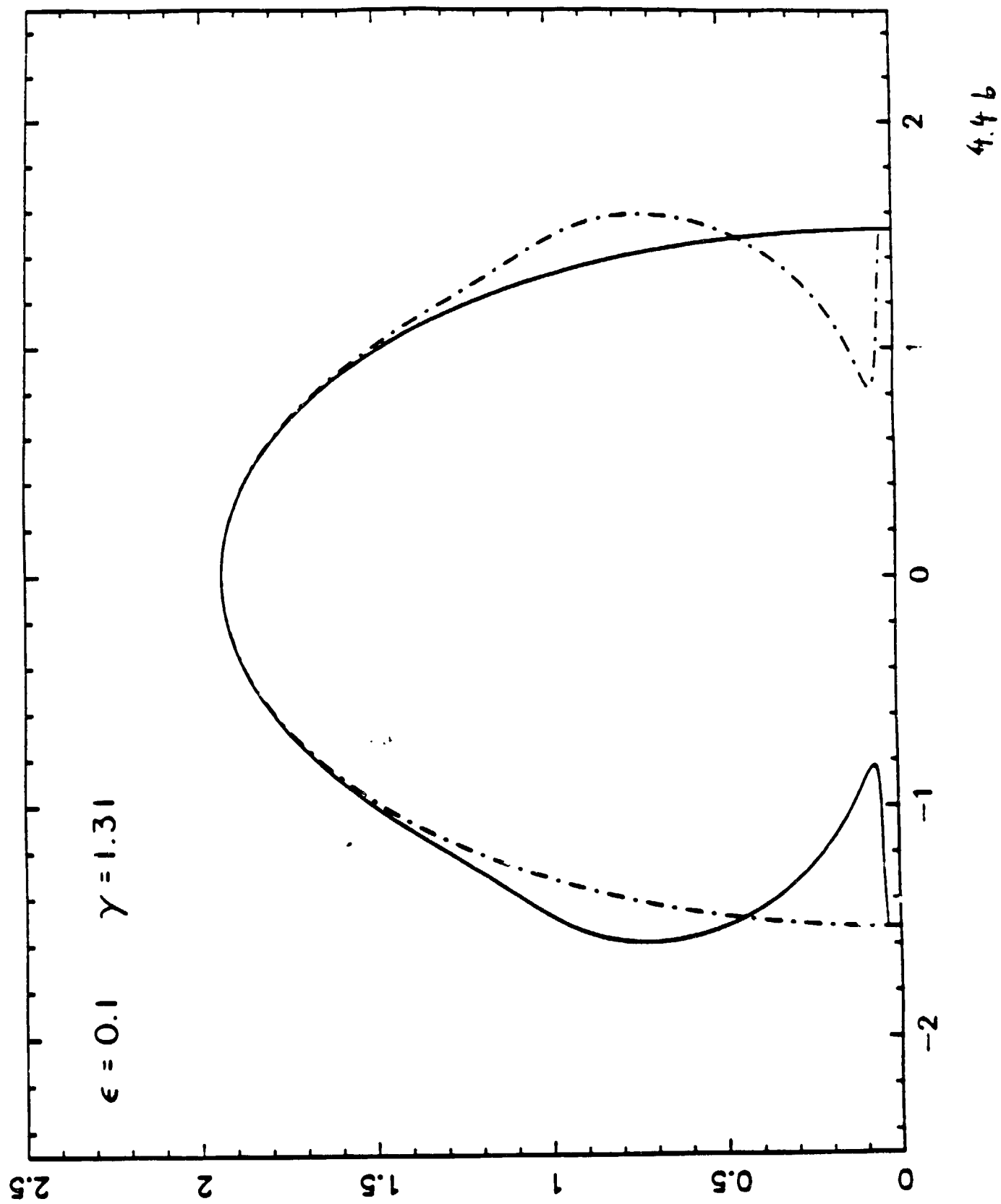
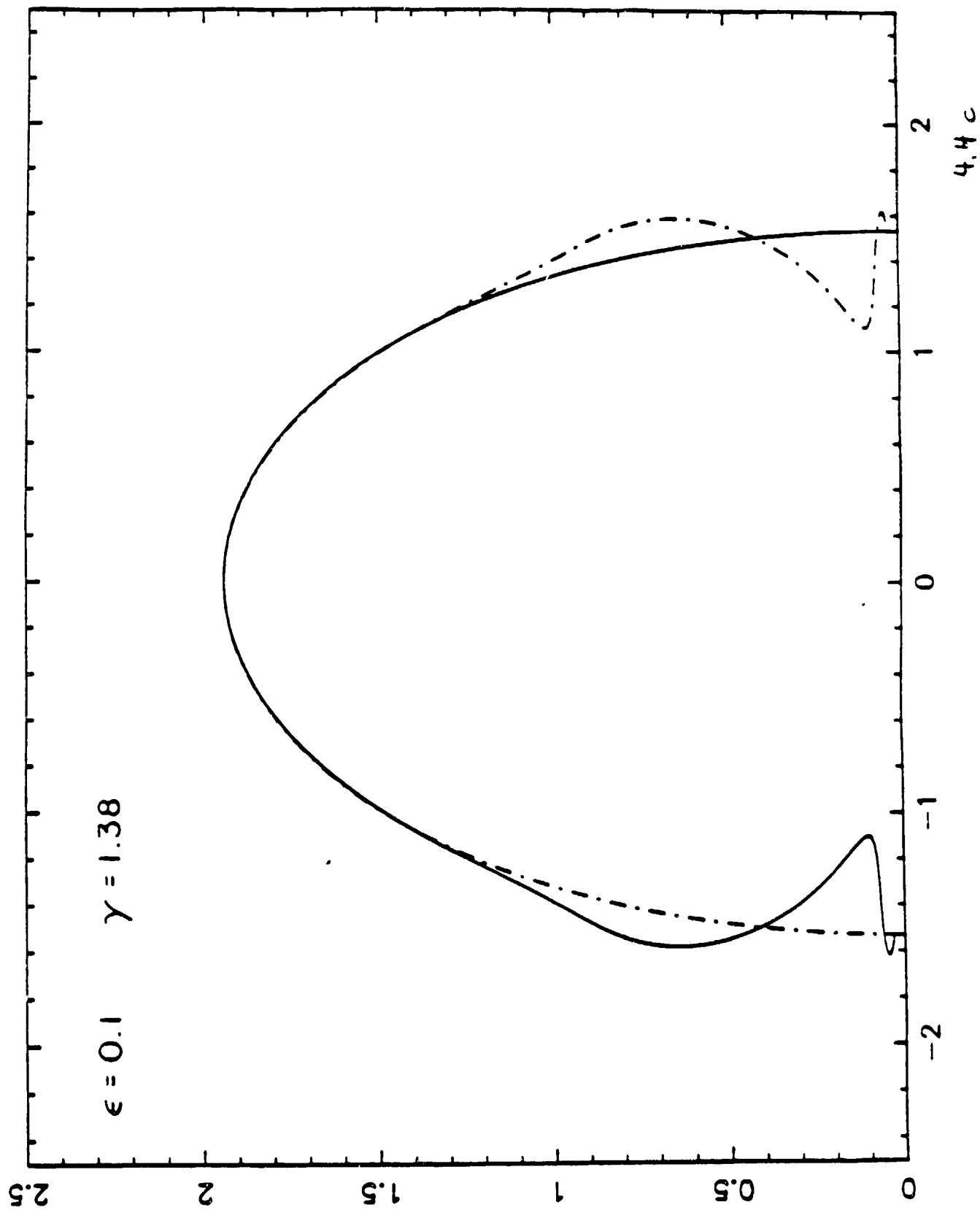
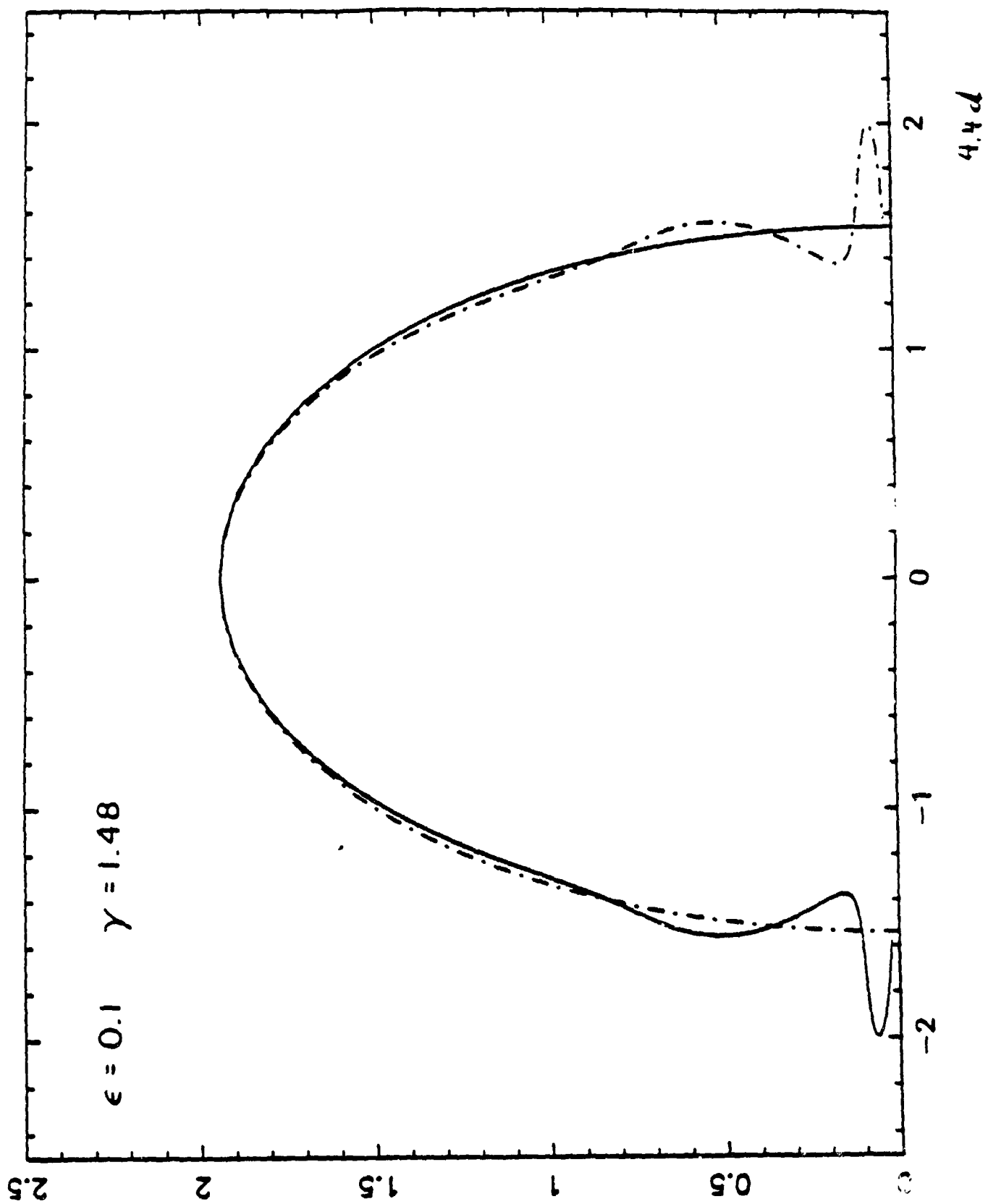


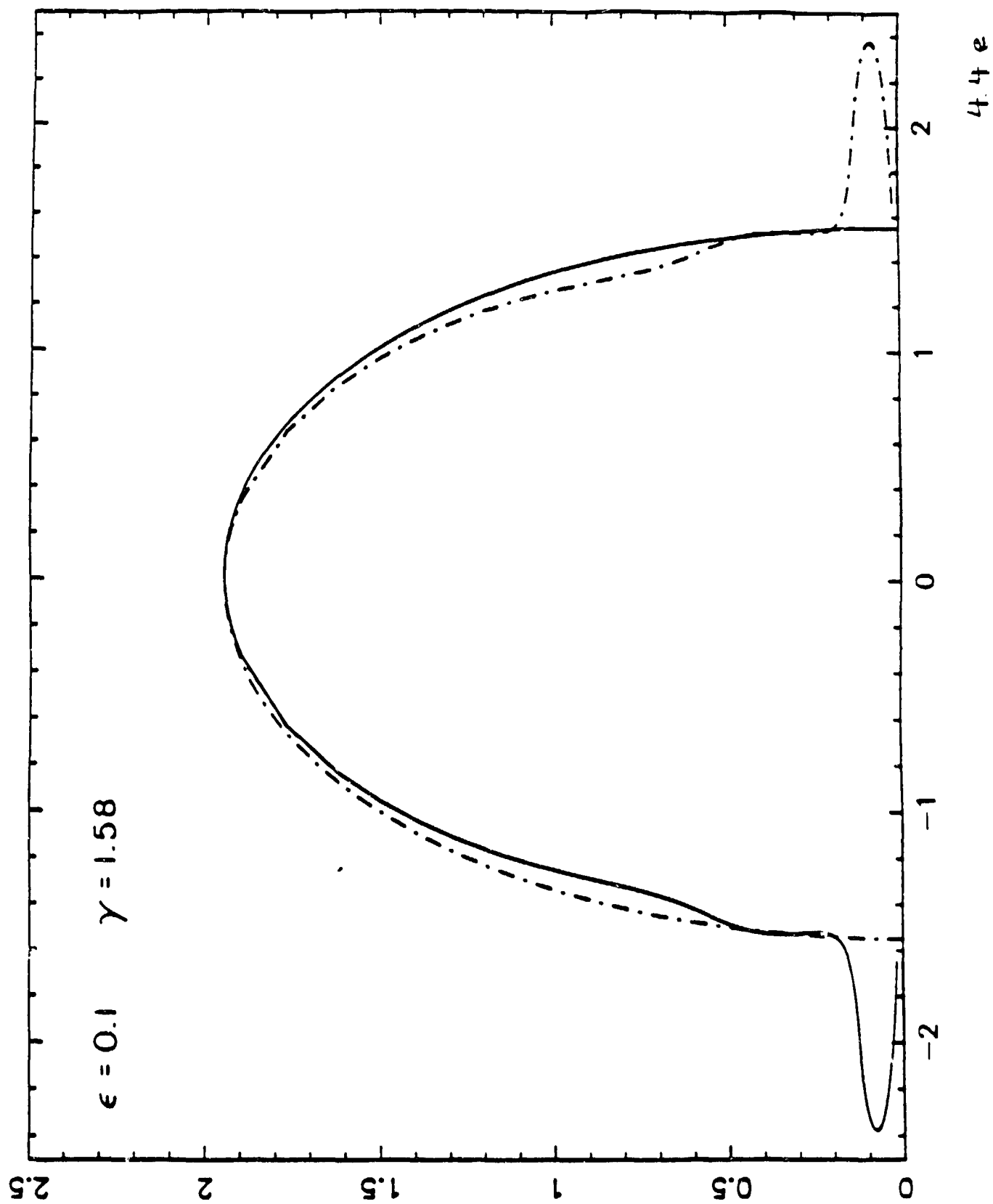
Fig 9.3

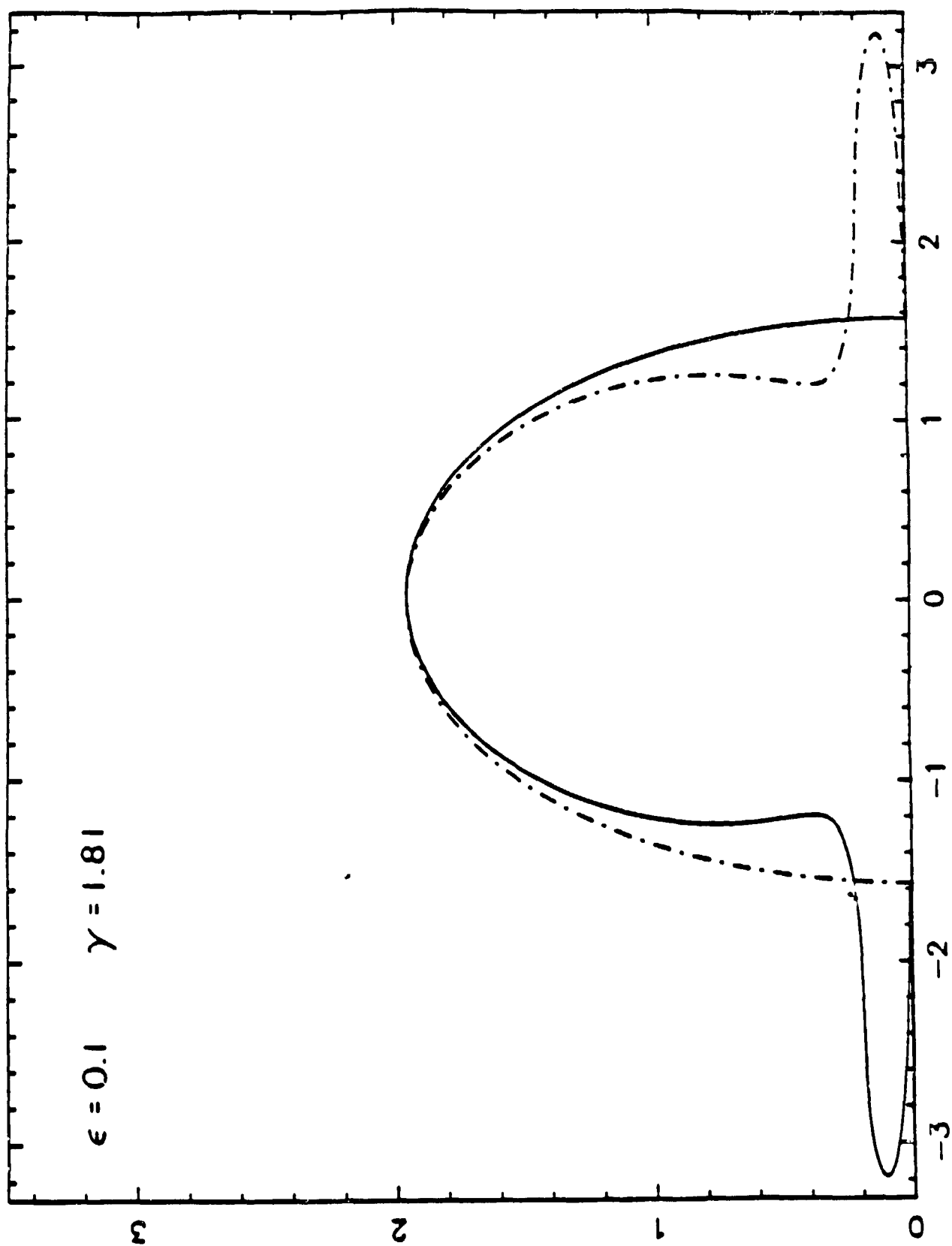




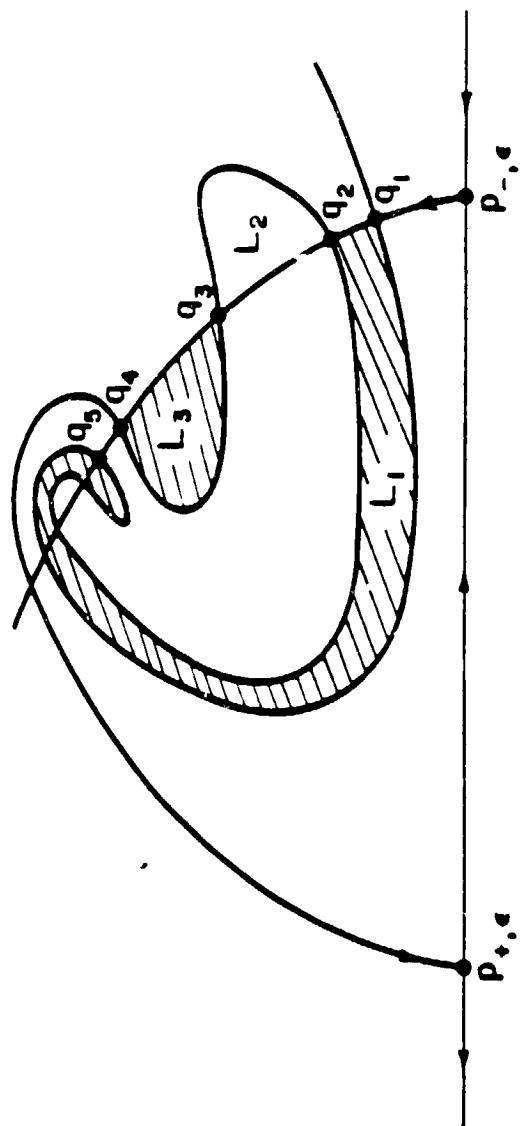


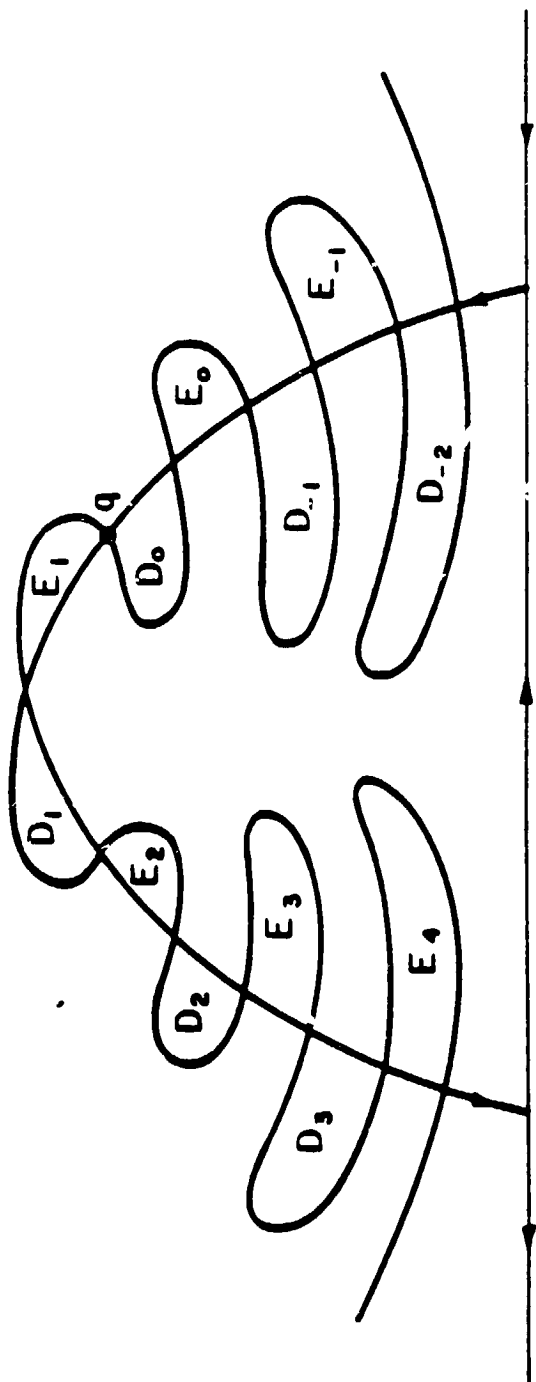


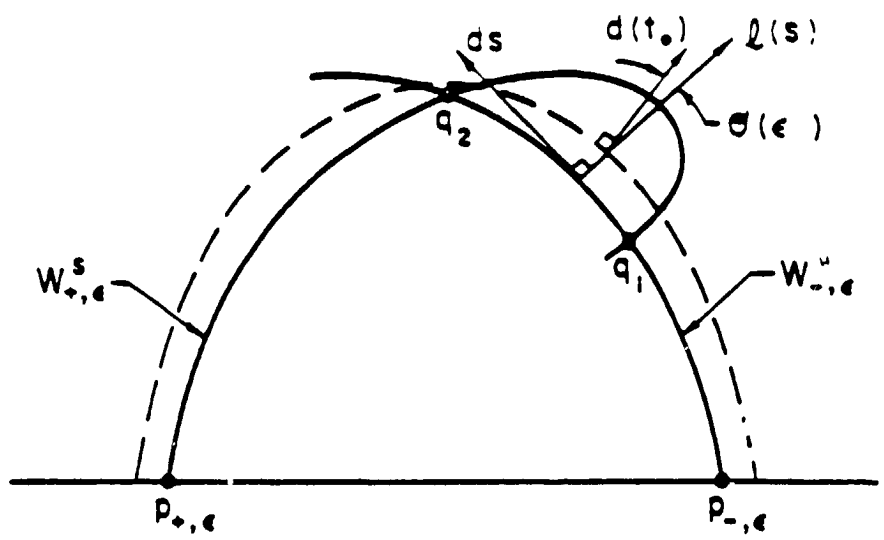


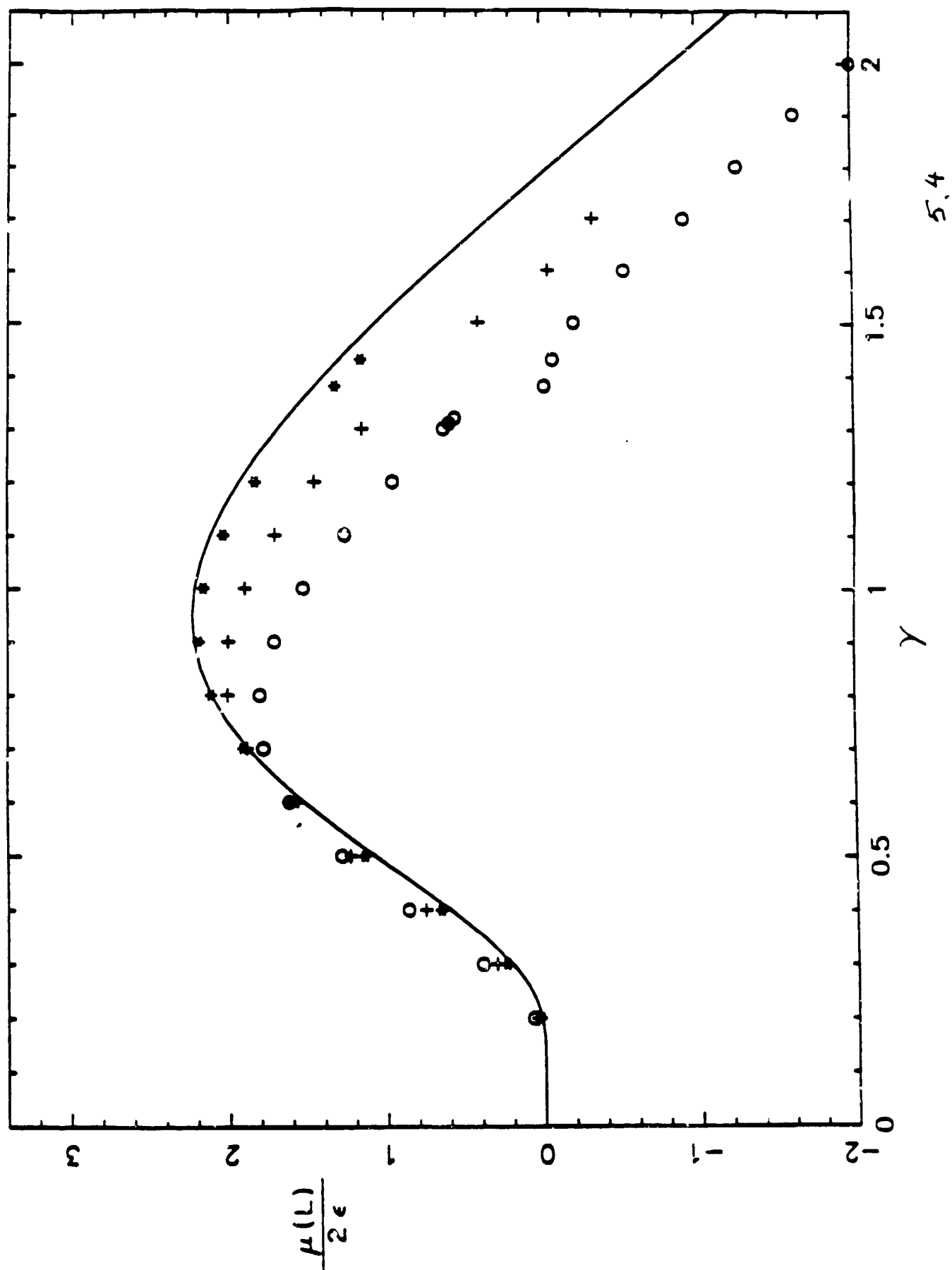


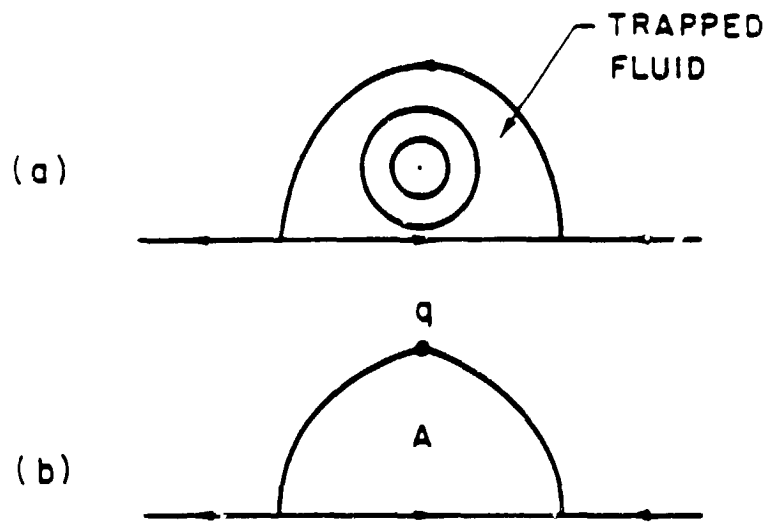
4.4 f

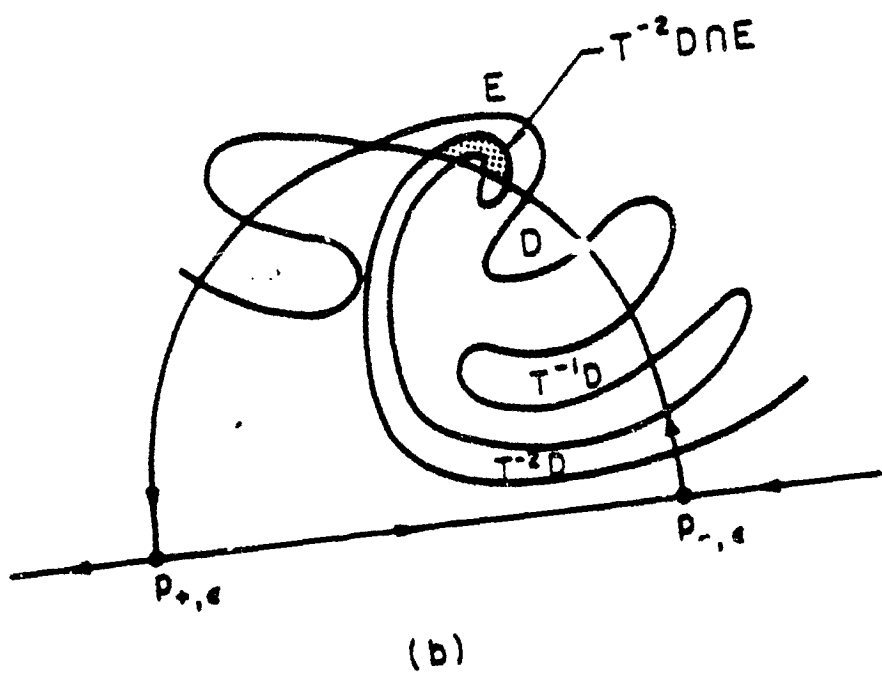
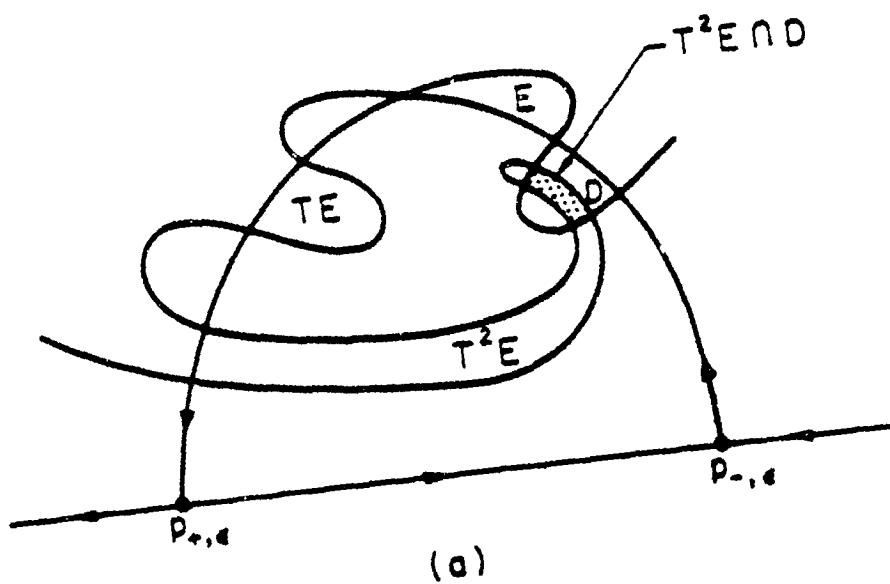


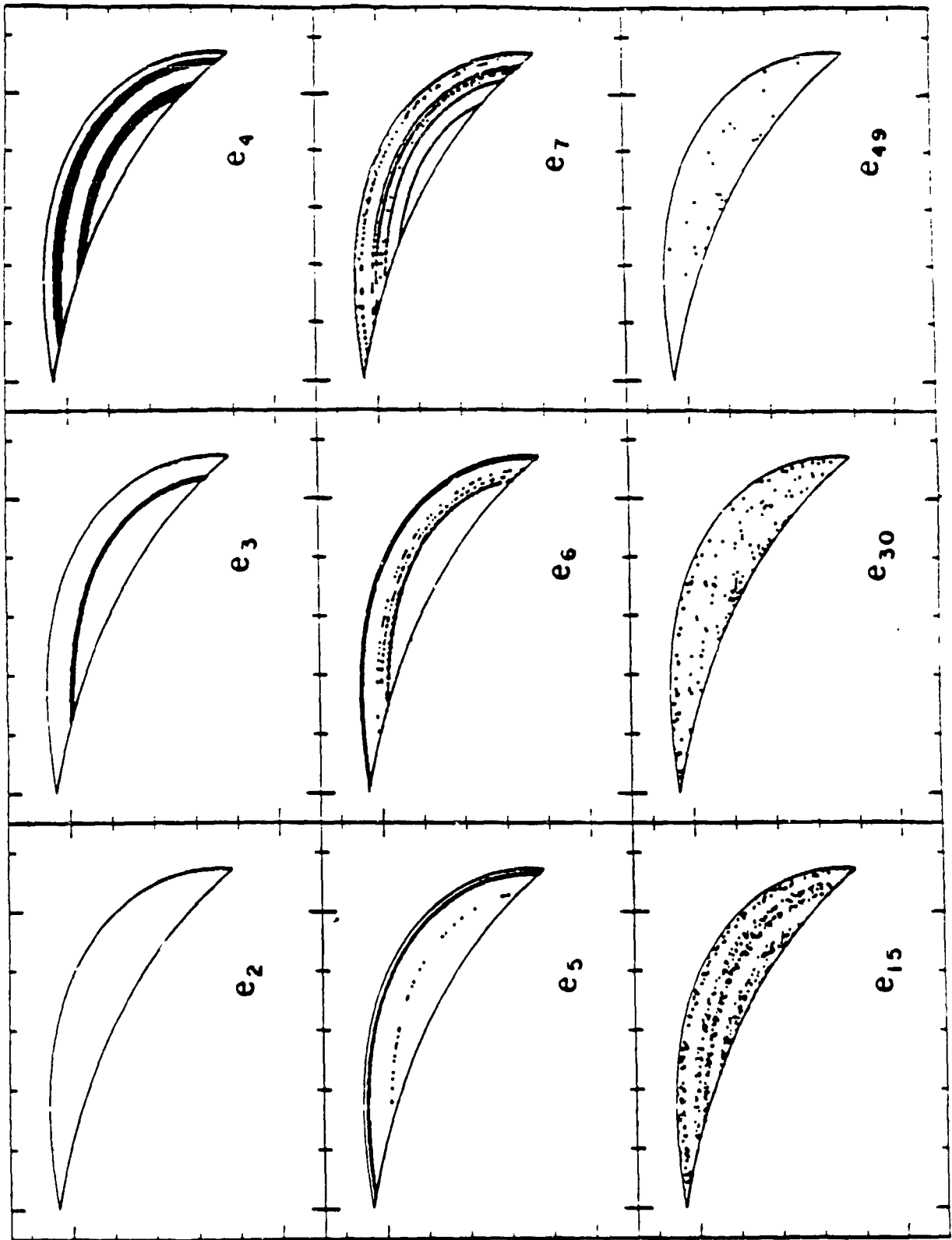




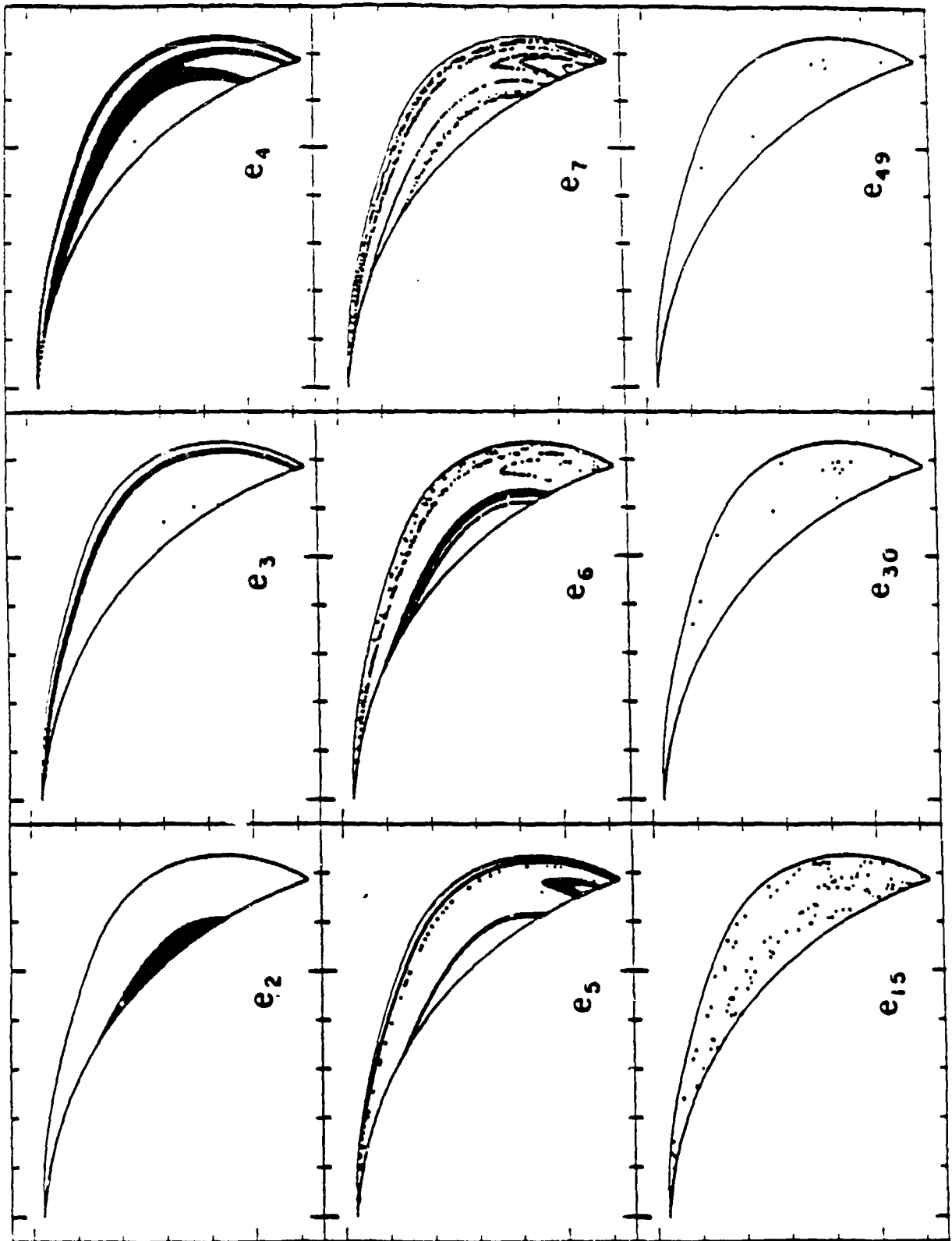




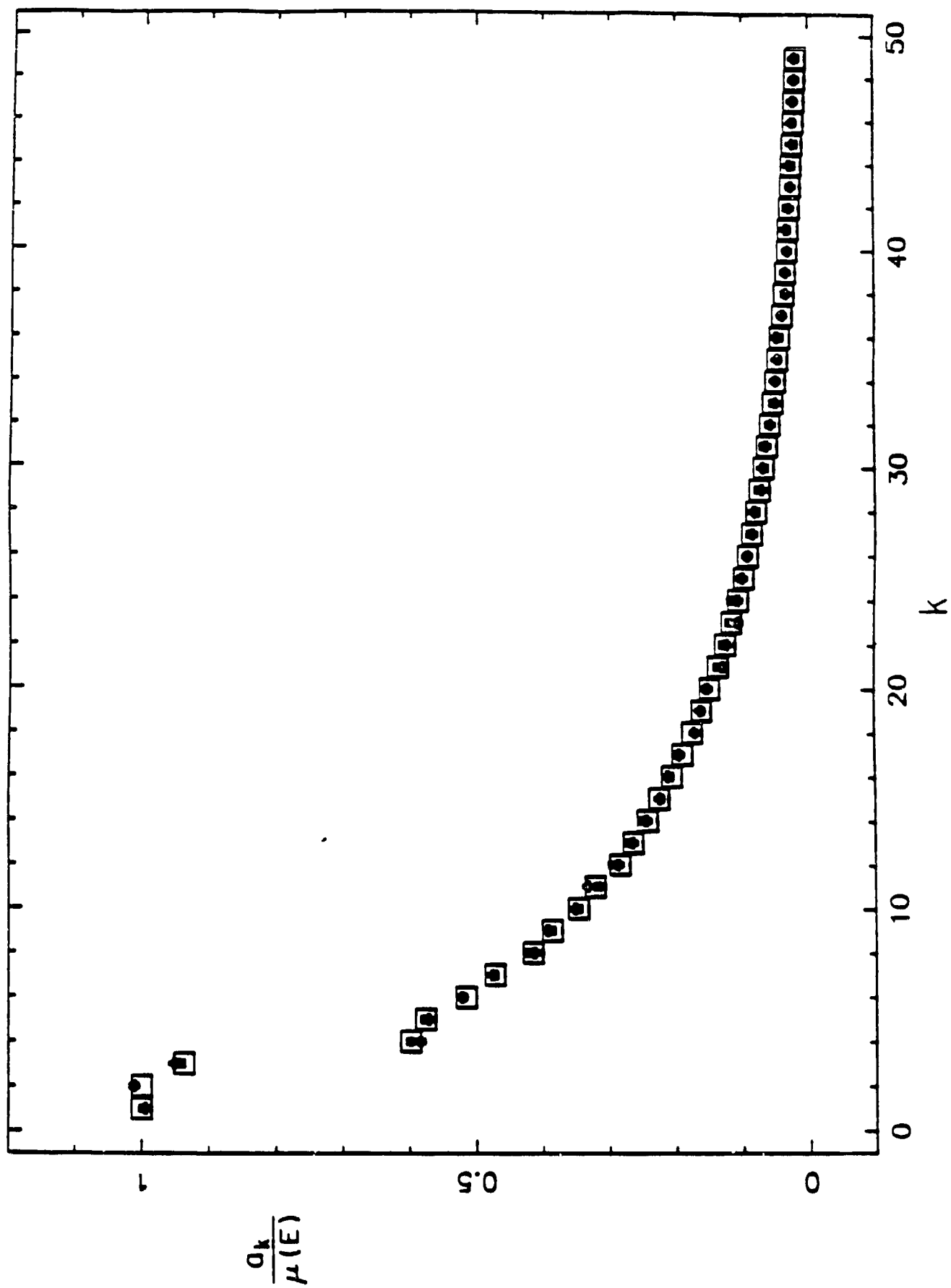


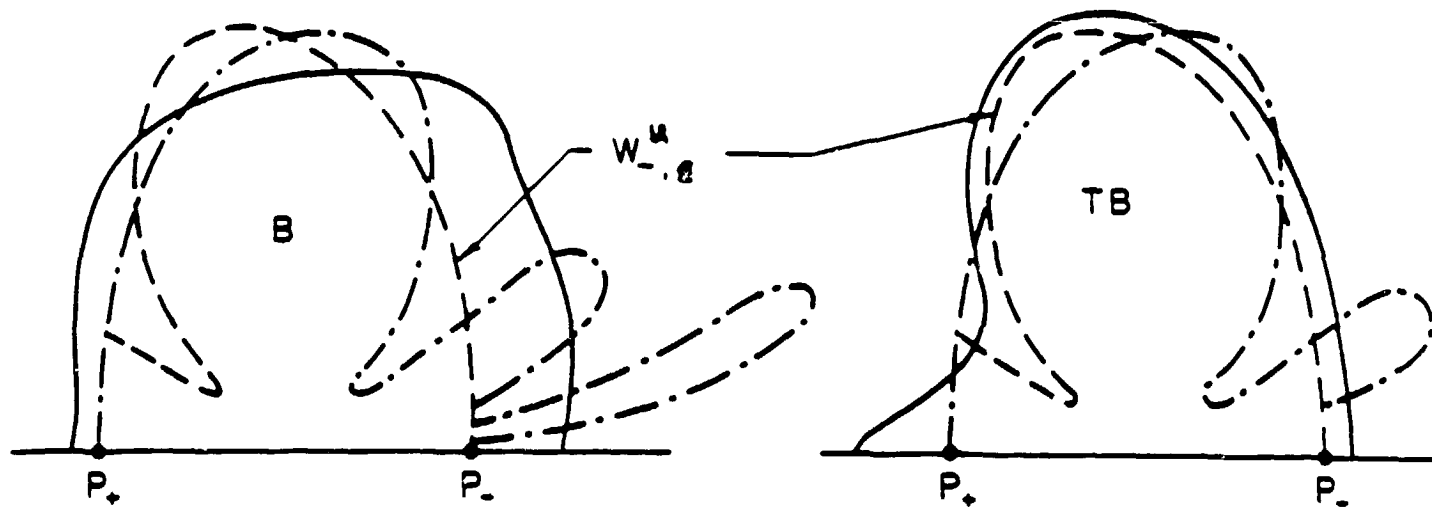

 $\gamma = 0.5$ $\epsilon = 0.1$

6.2a


 $\gamma = 0.9$ $\epsilon = 0.1$

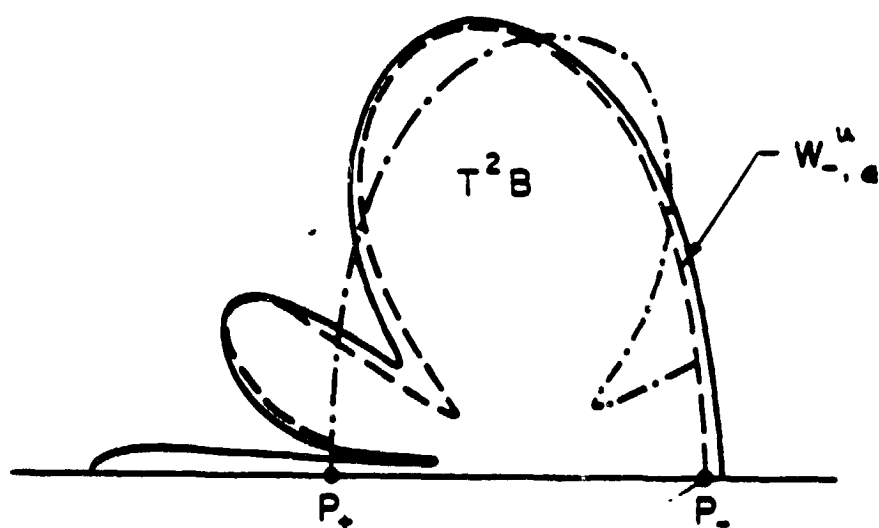
6.2 b





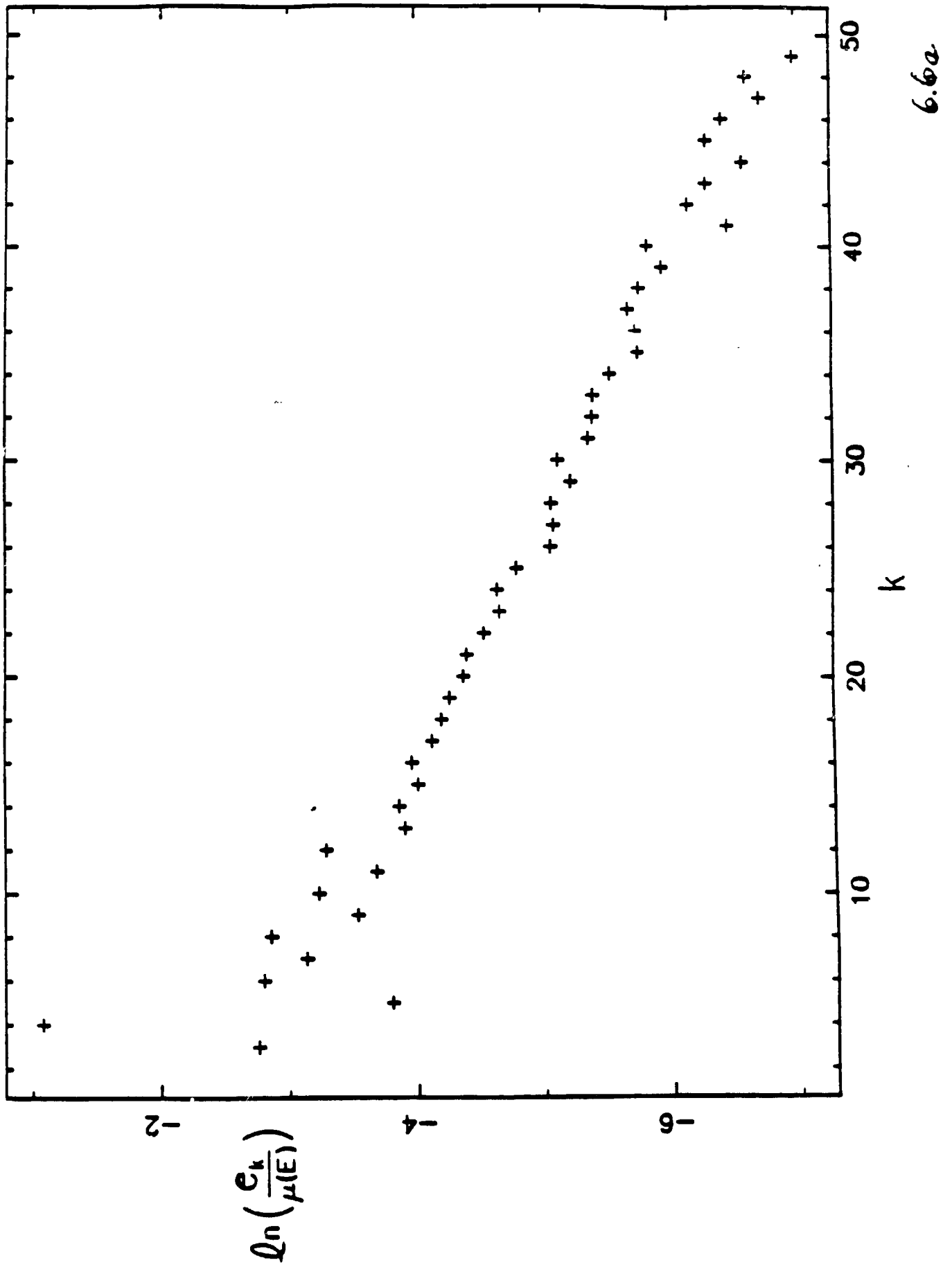
(a)

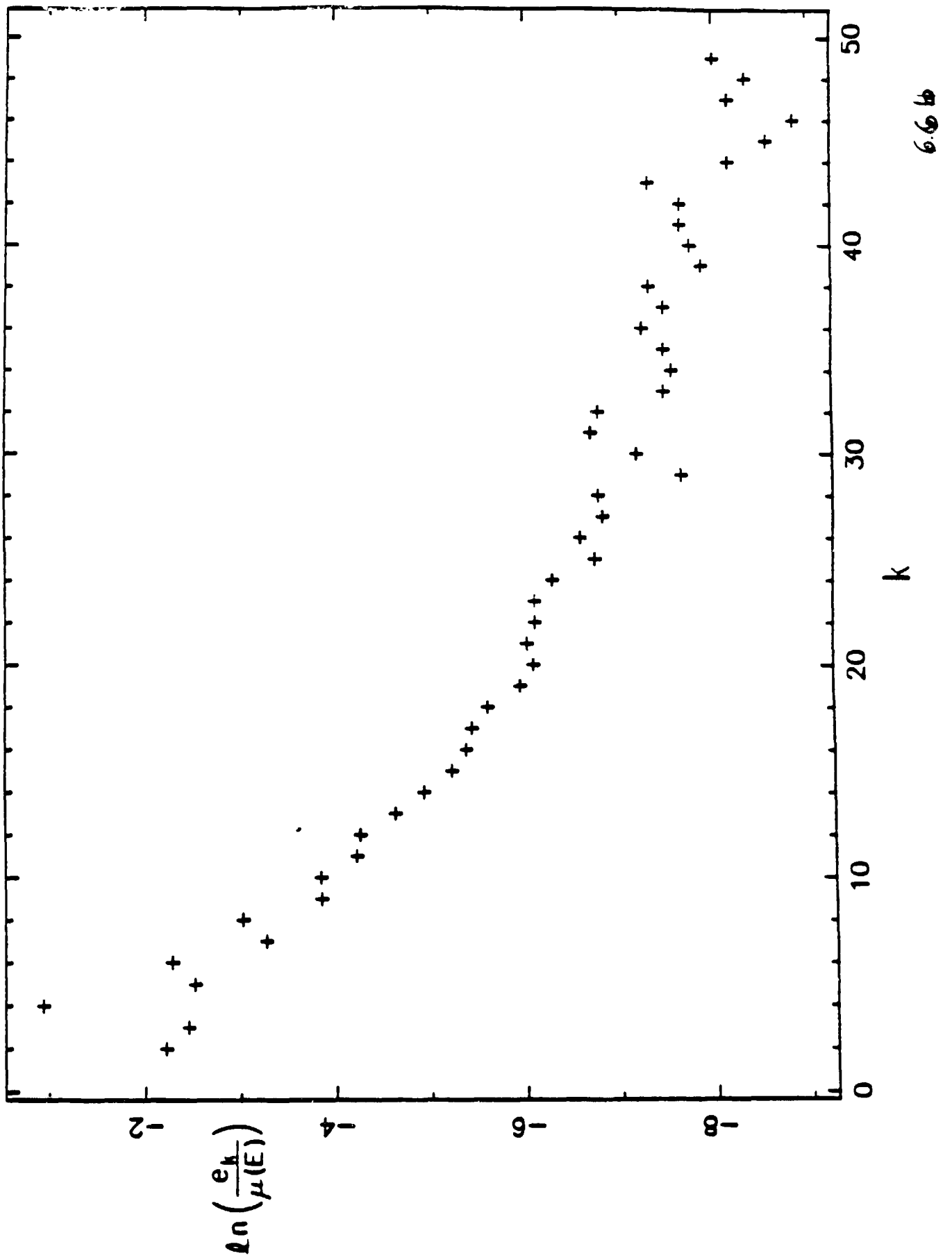
(b)

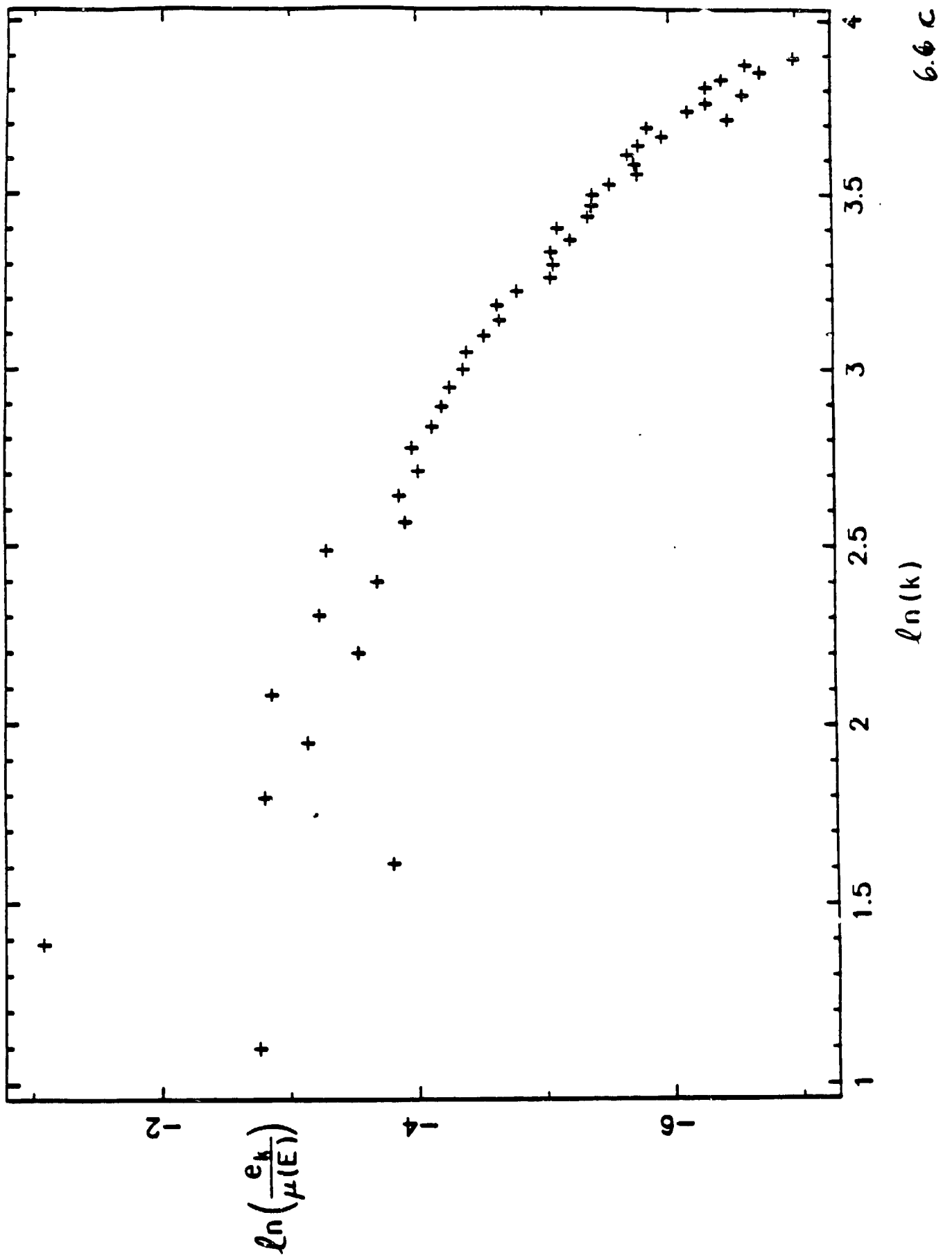


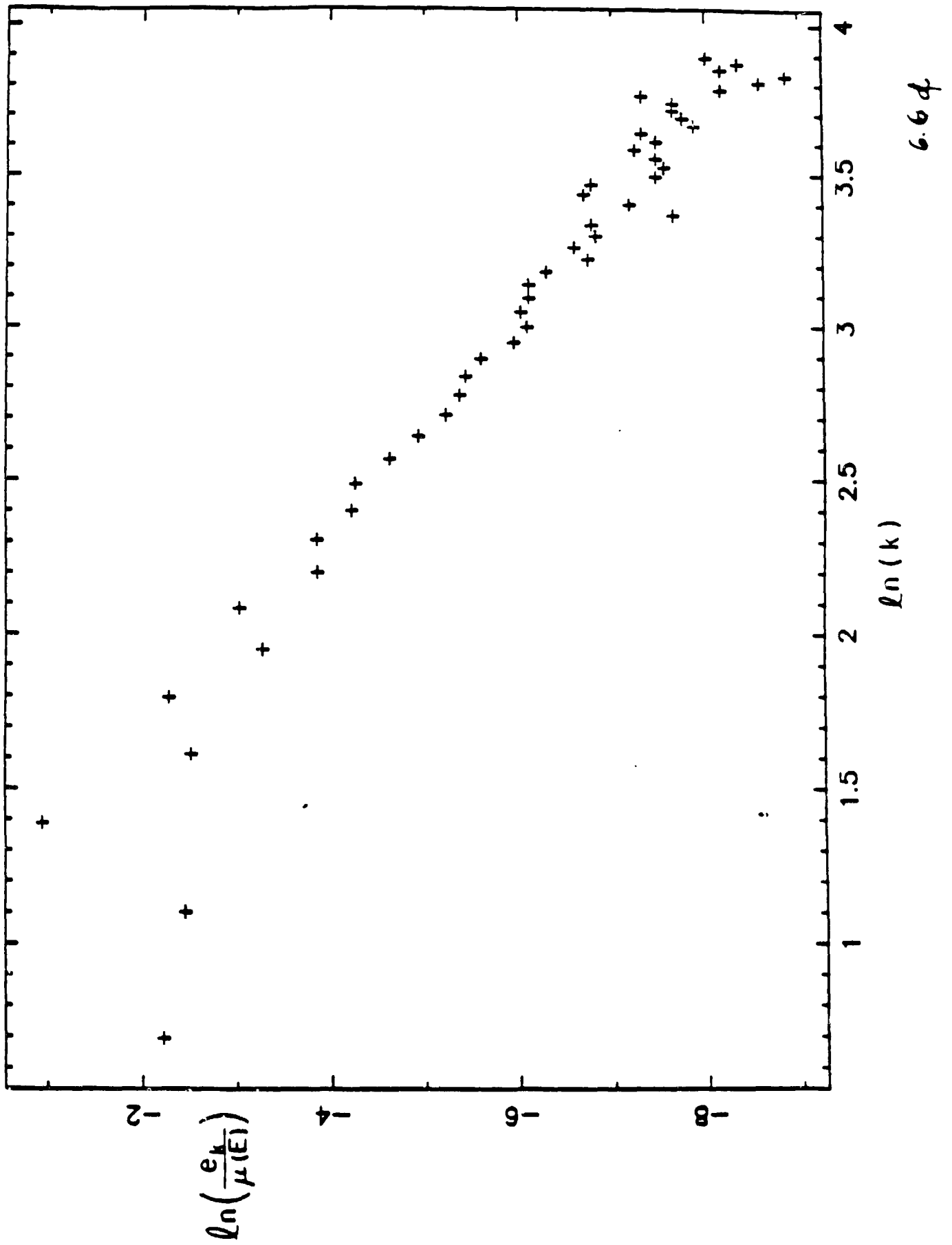
(c)

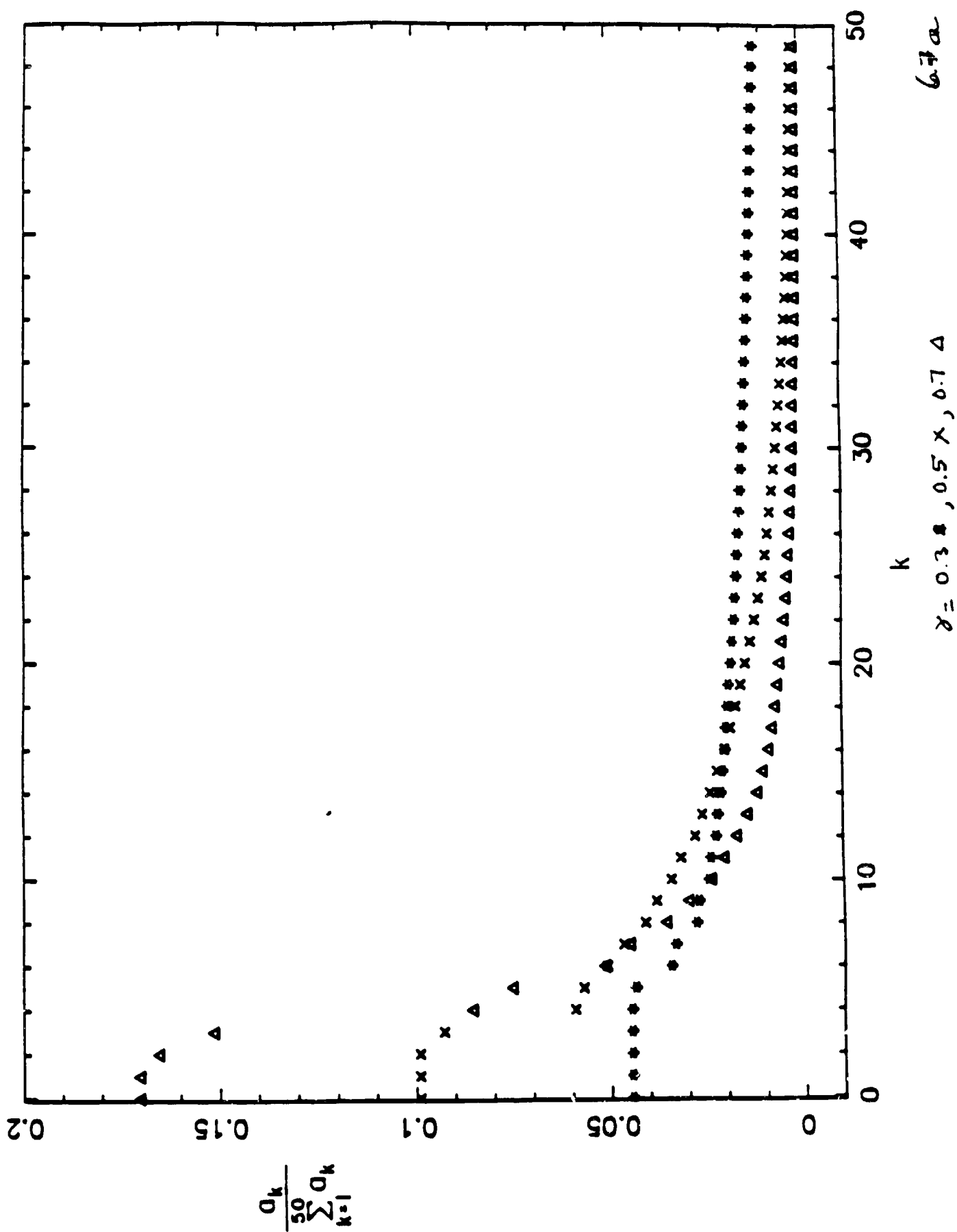


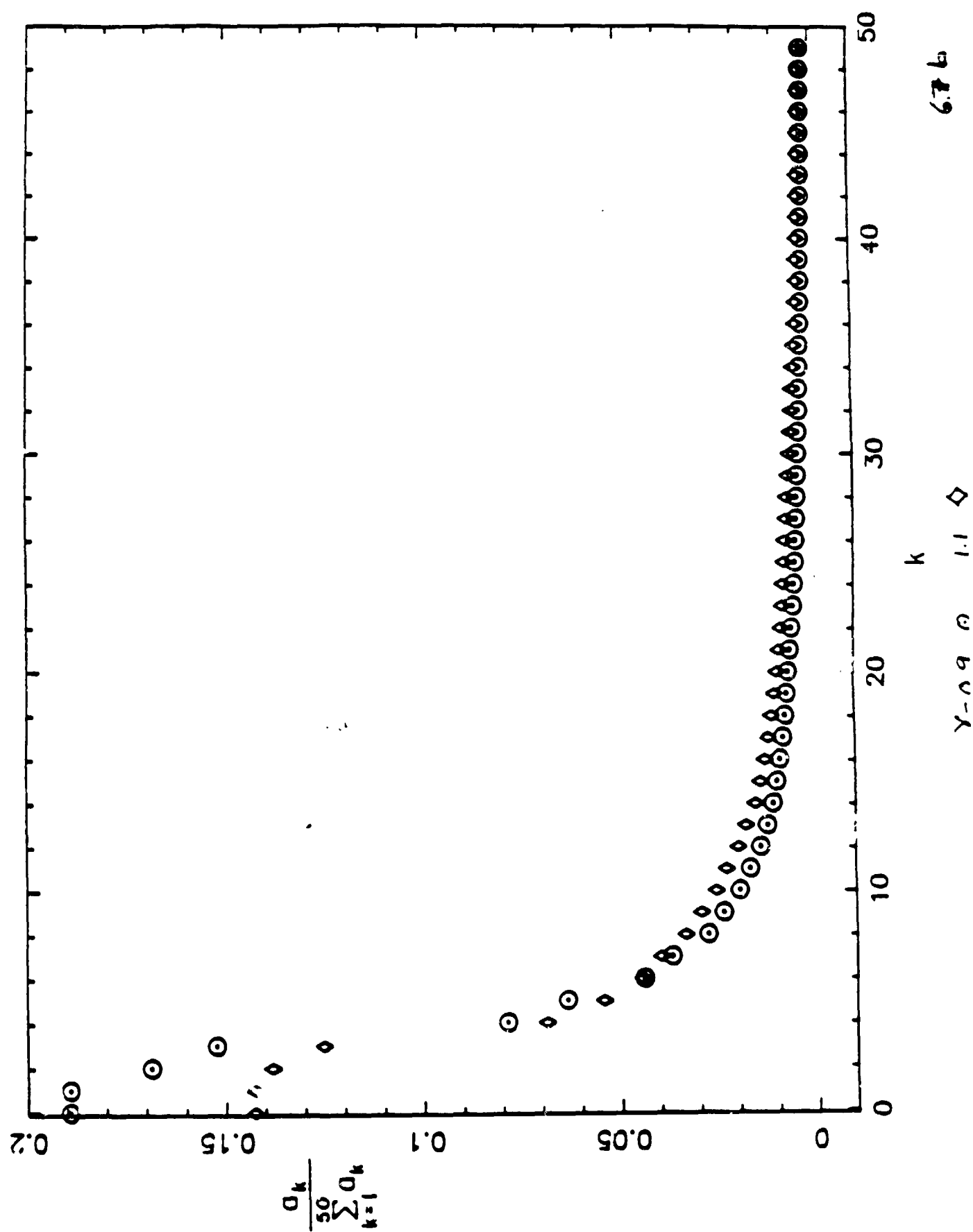


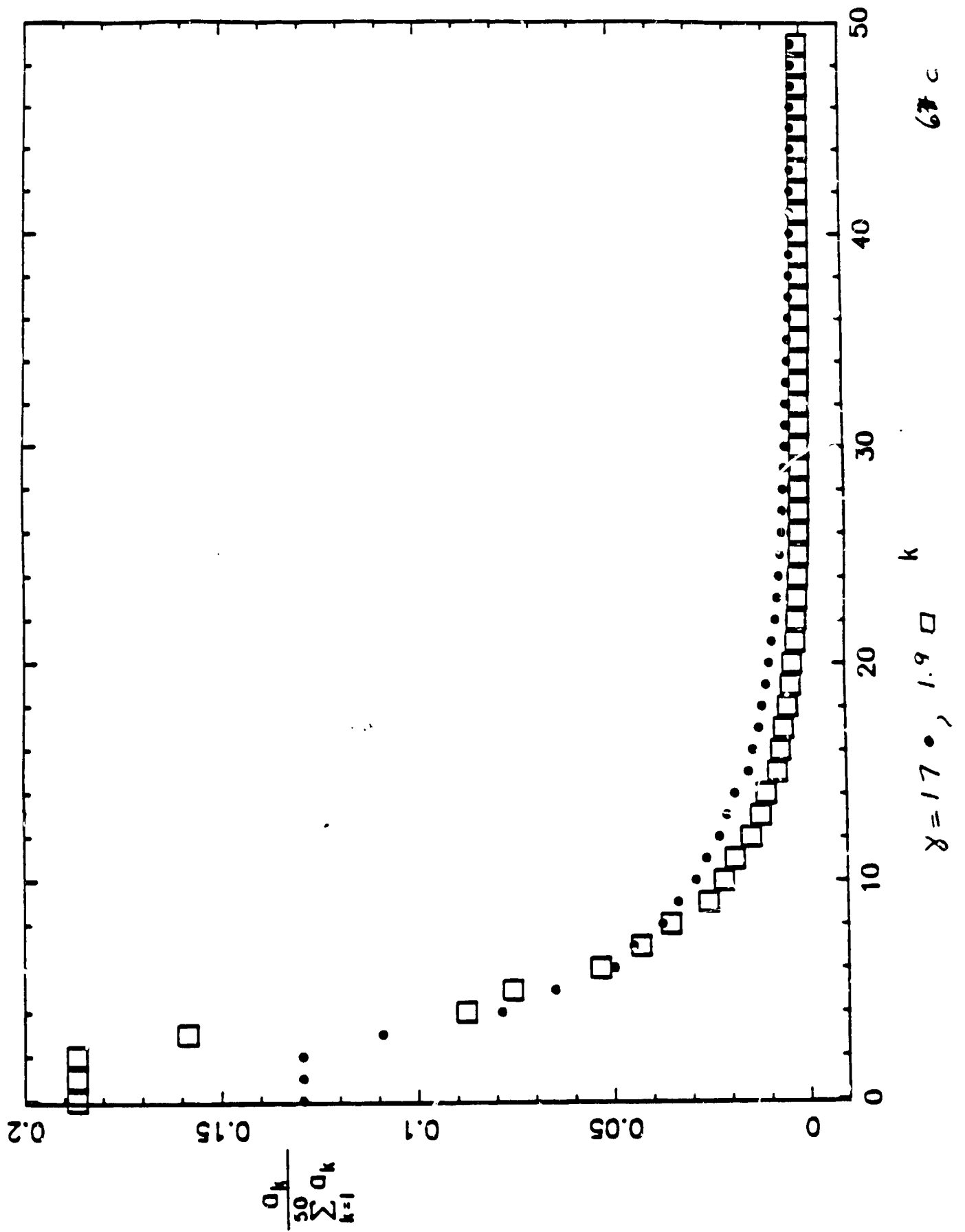


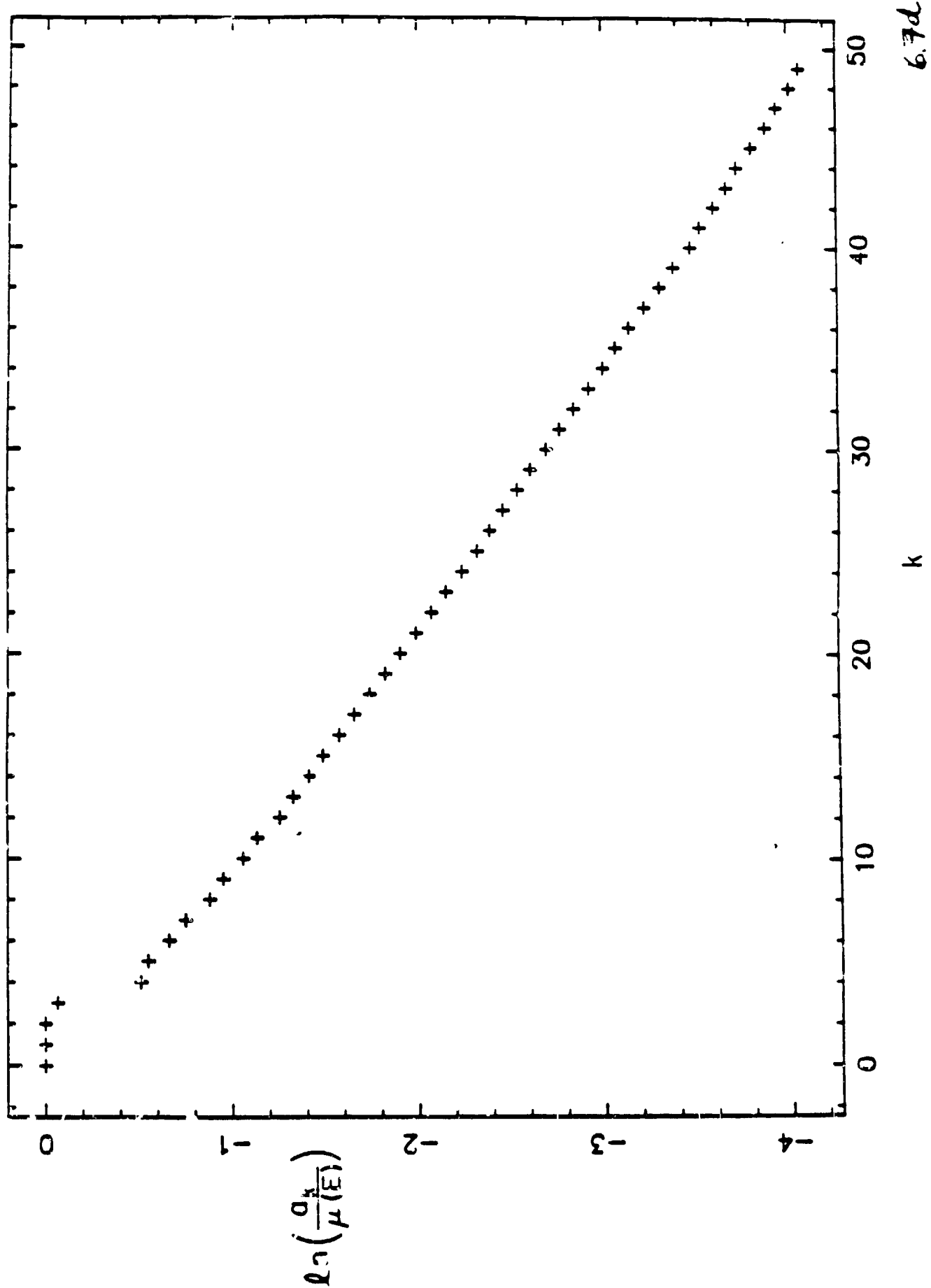


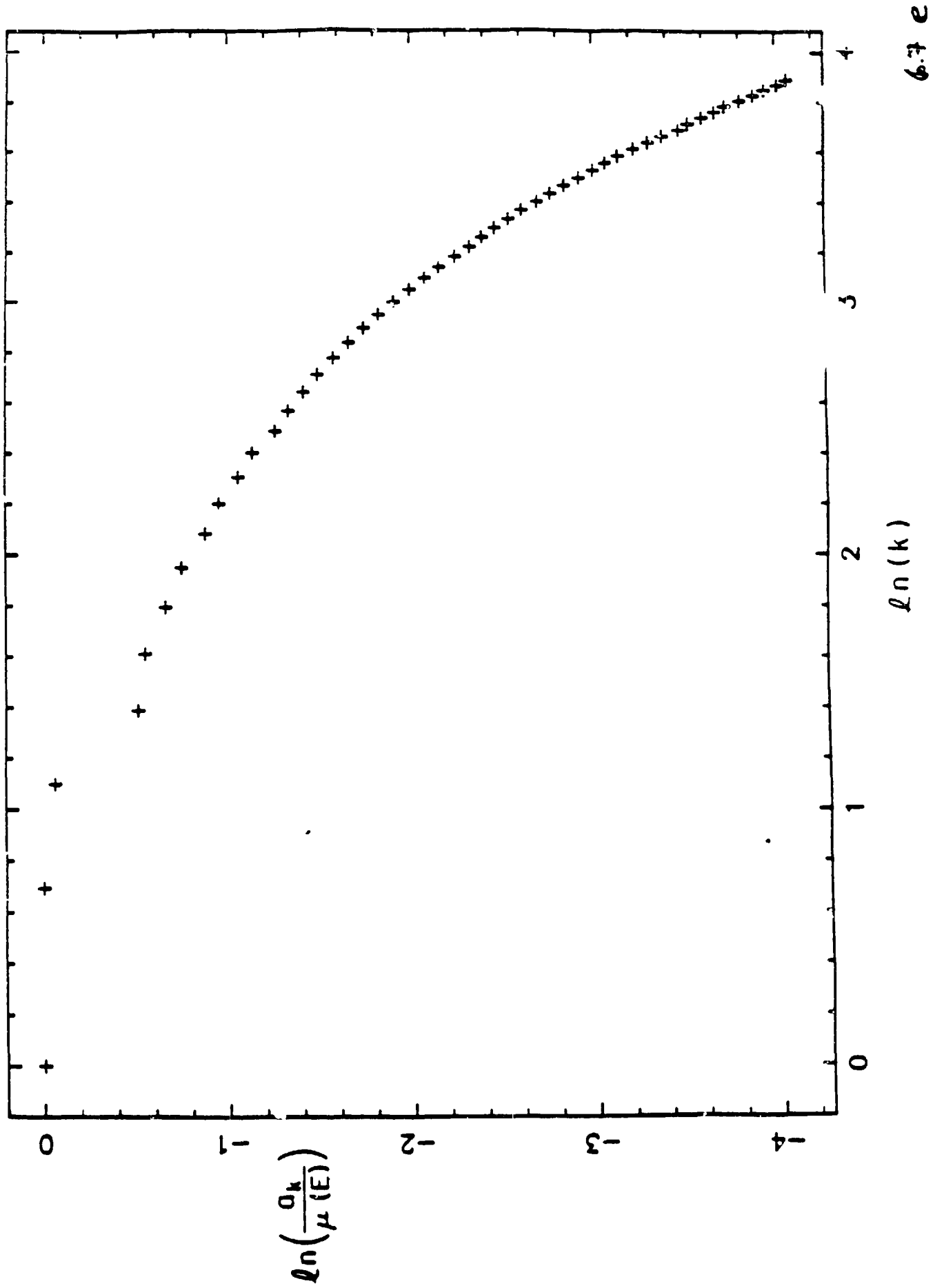


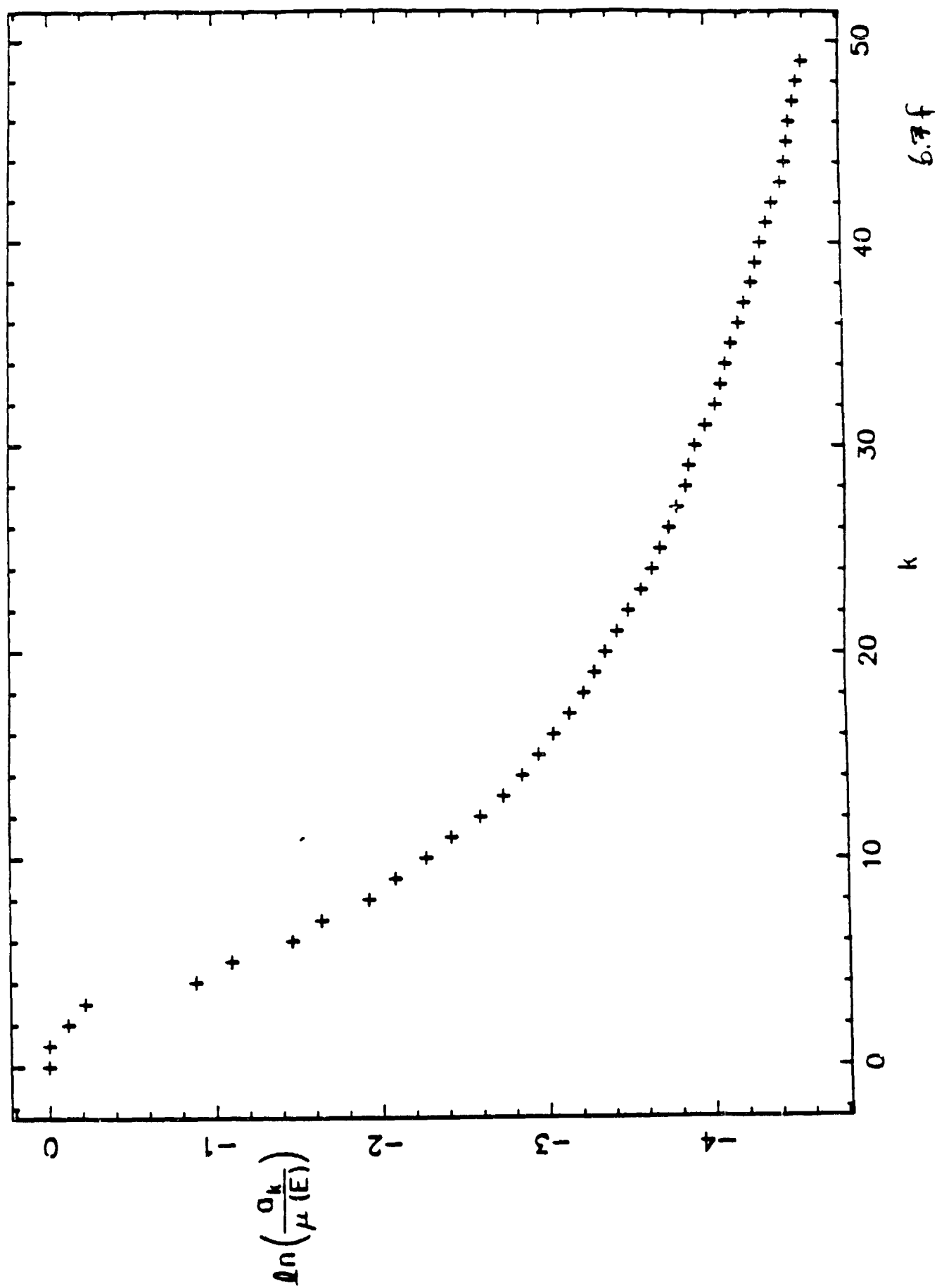


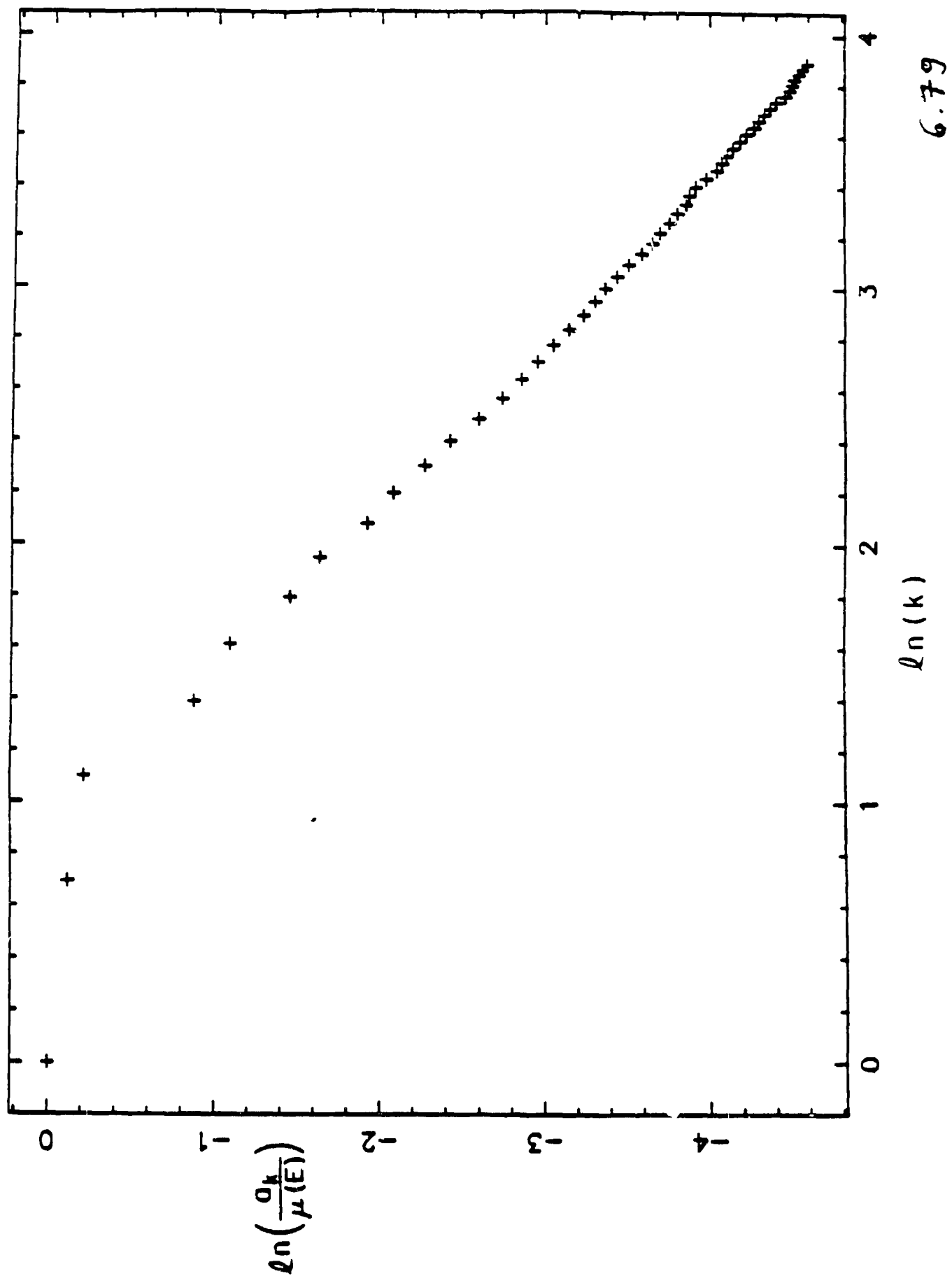


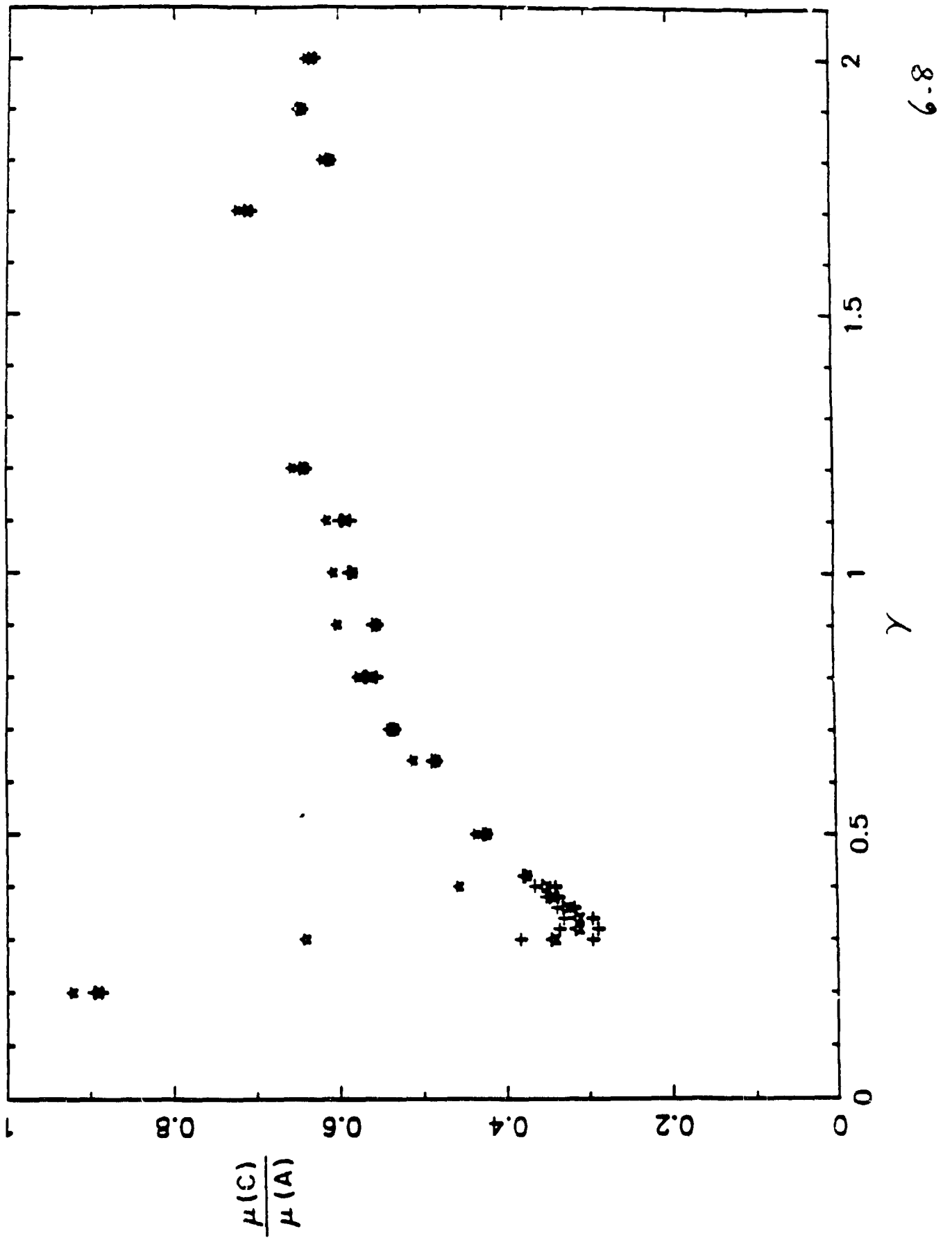


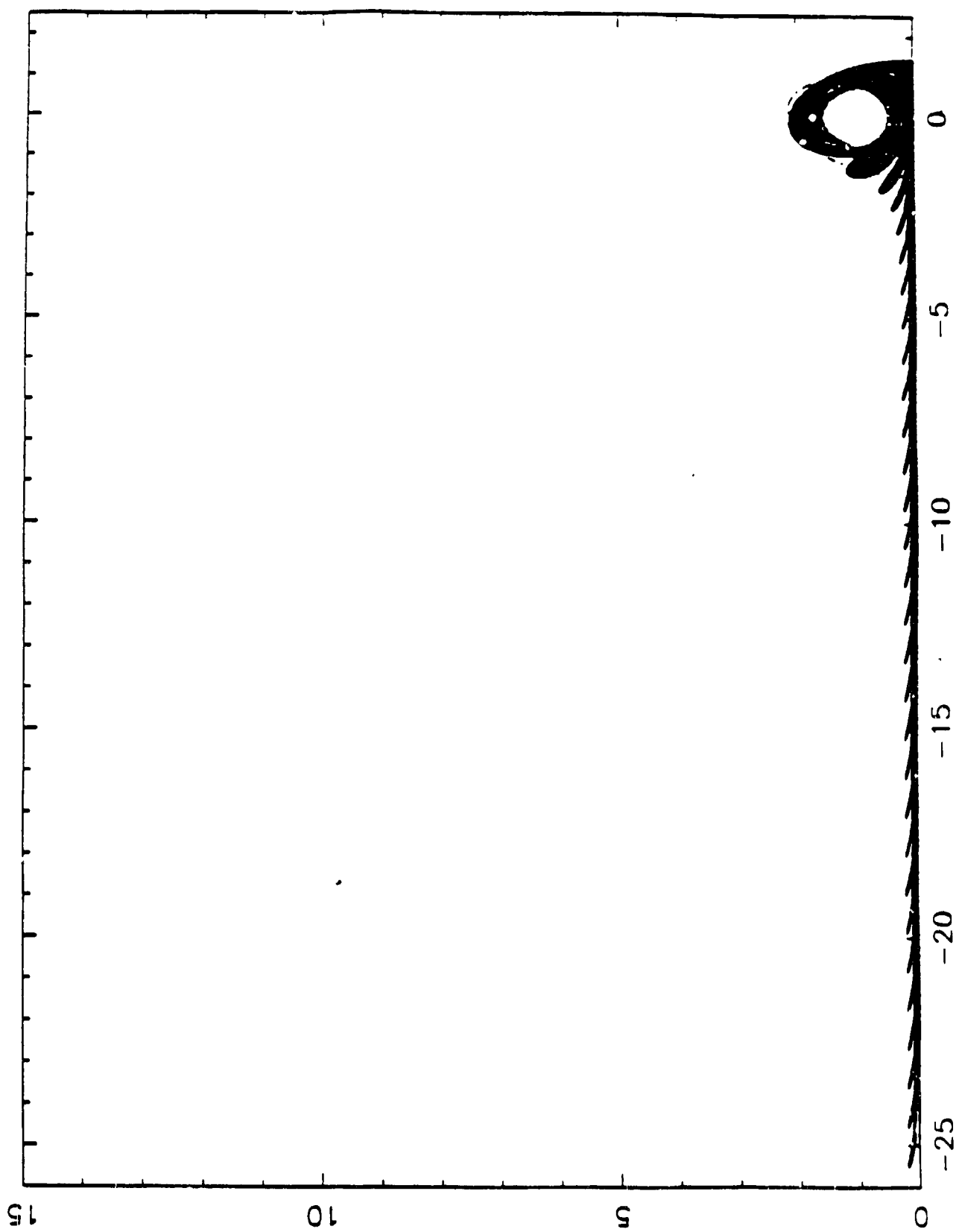


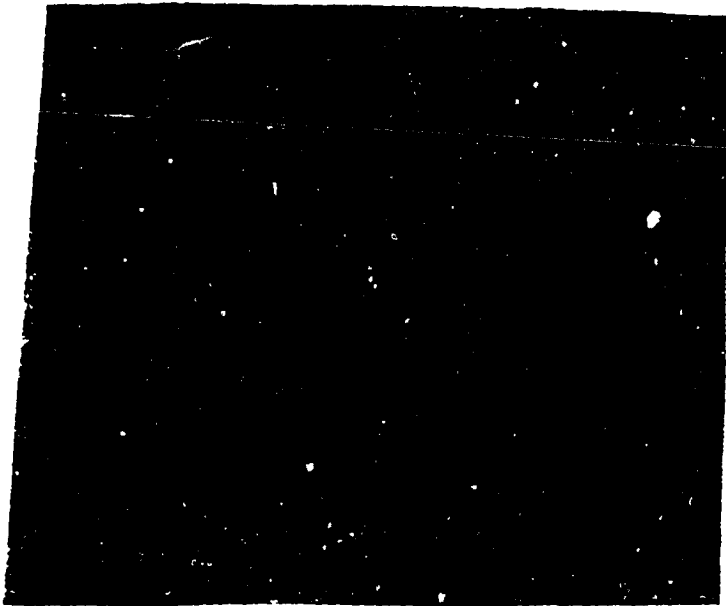












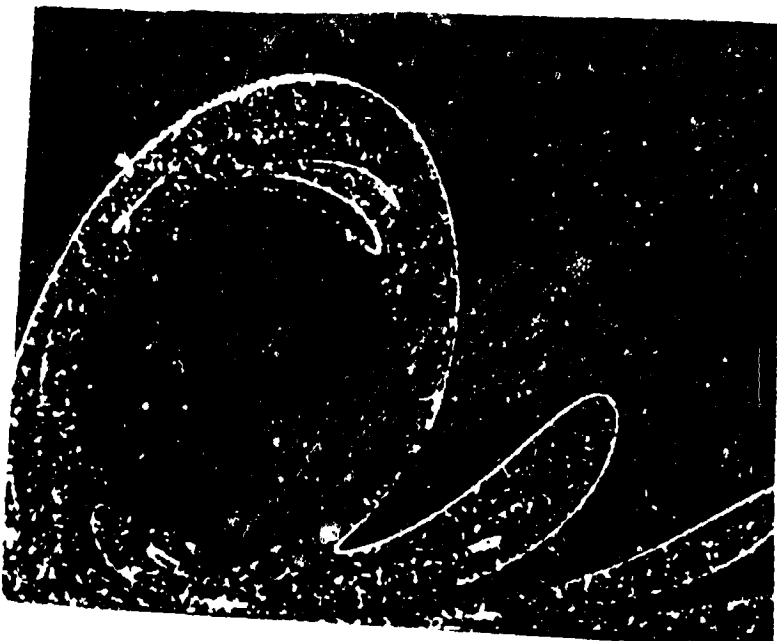
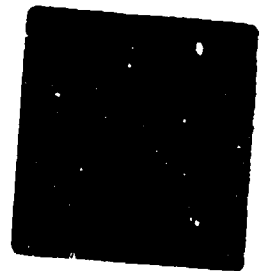
$$\epsilon = 0.1$$

$$\gamma = 0.5$$



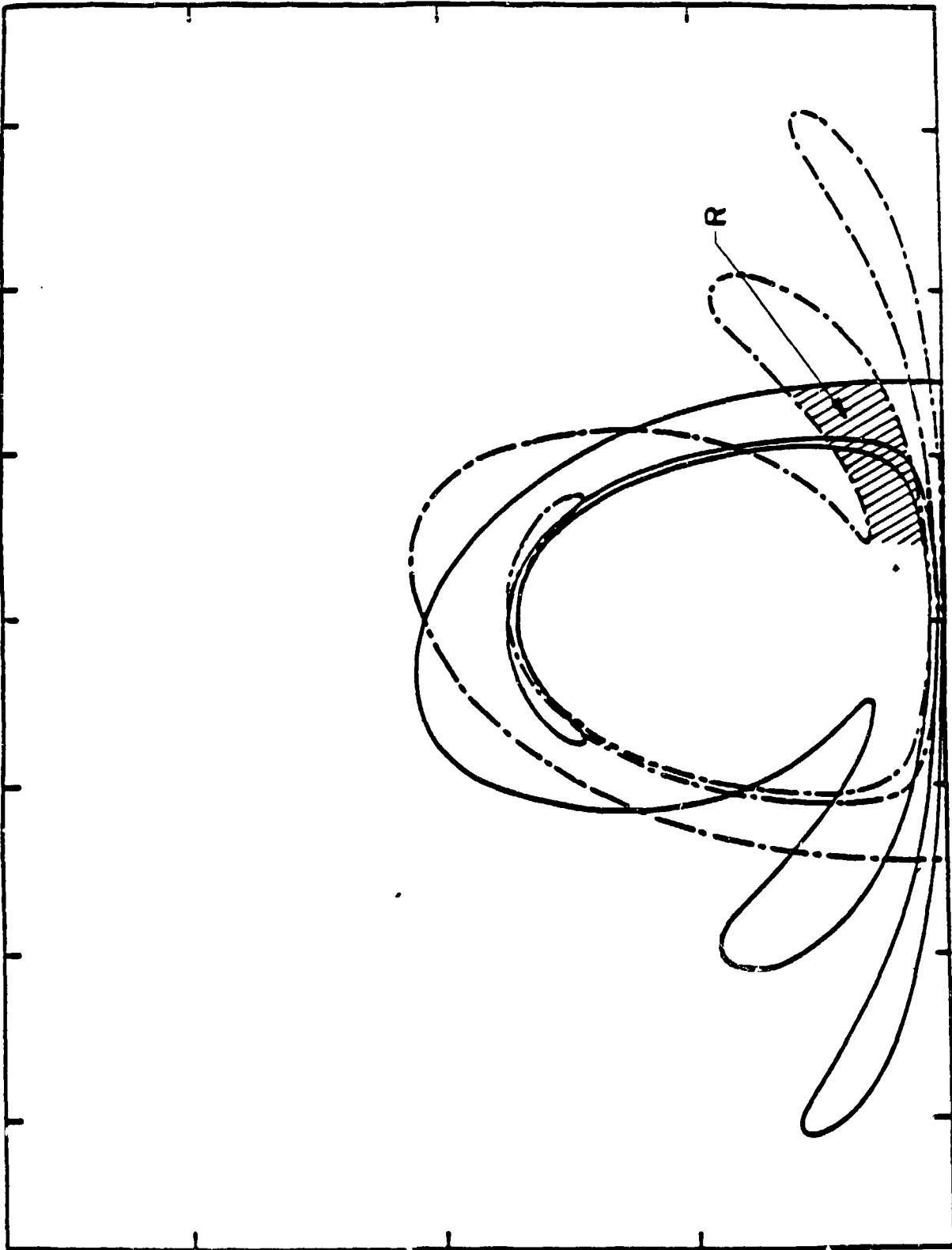
$$\epsilon = 0.1$$

$$\gamma = 1.38$$



$$\epsilon = 0.1$$

$$\gamma = 0.5$$

*Fig. 7/a*

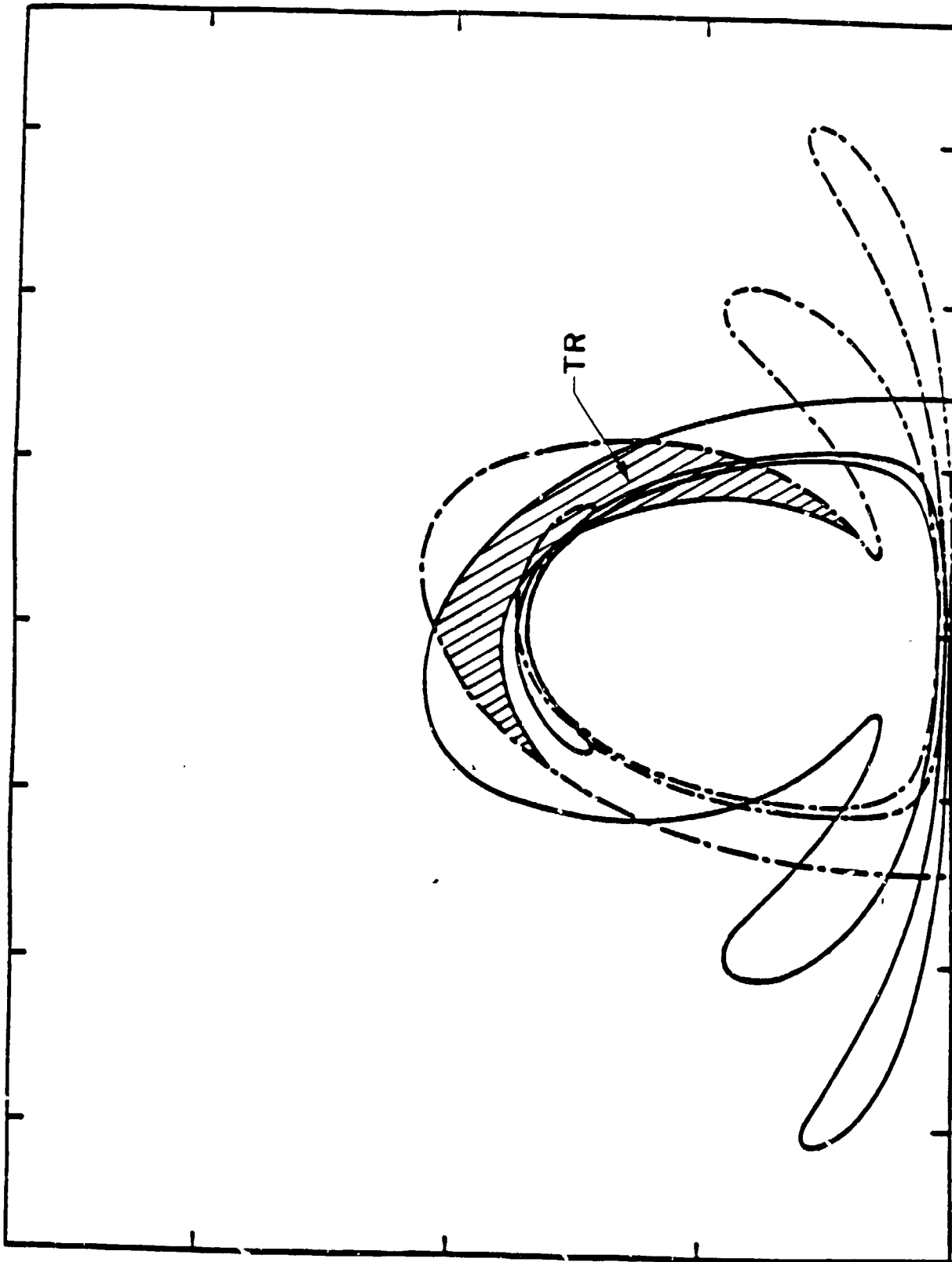


Fig 7.16

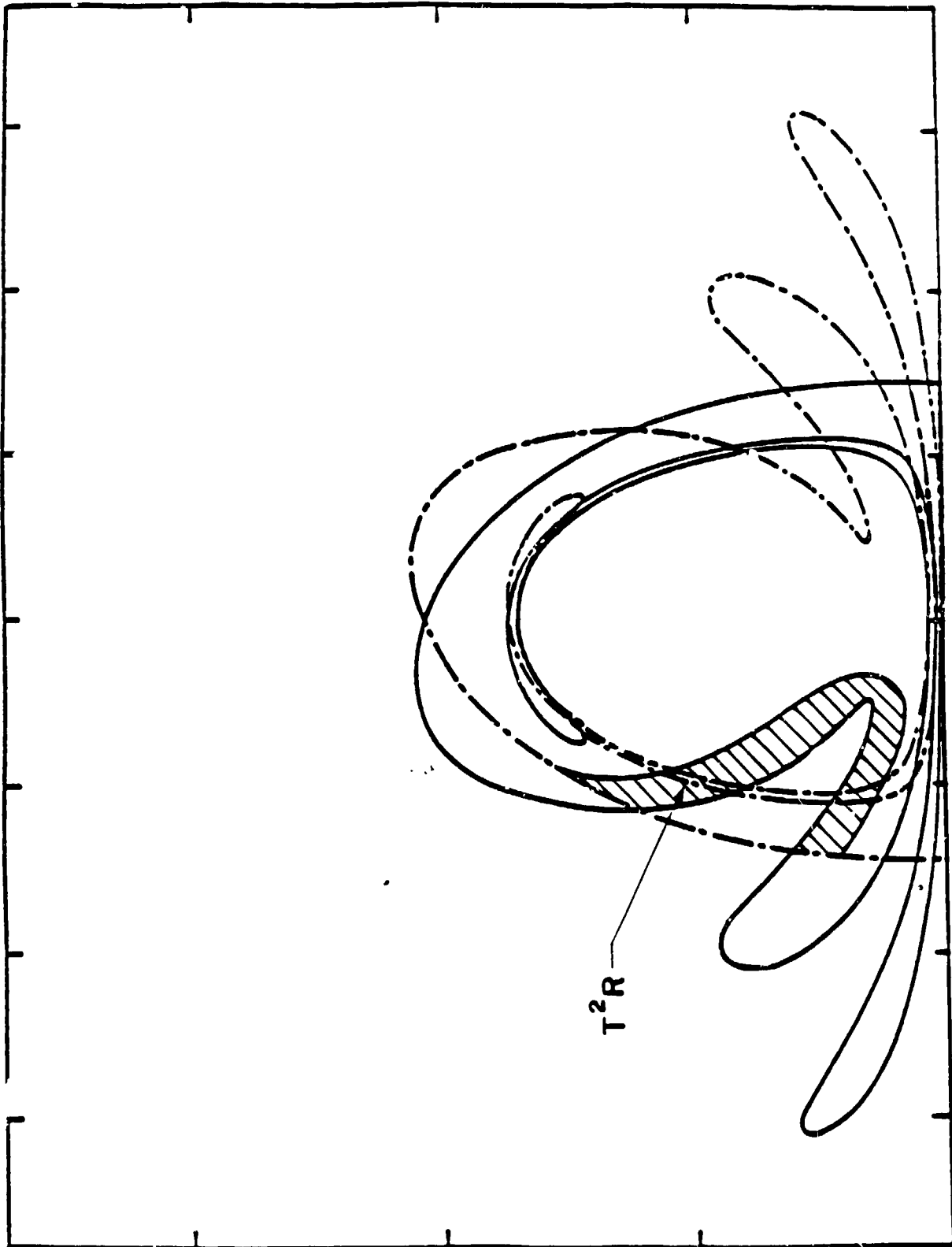


Fig 7.1c

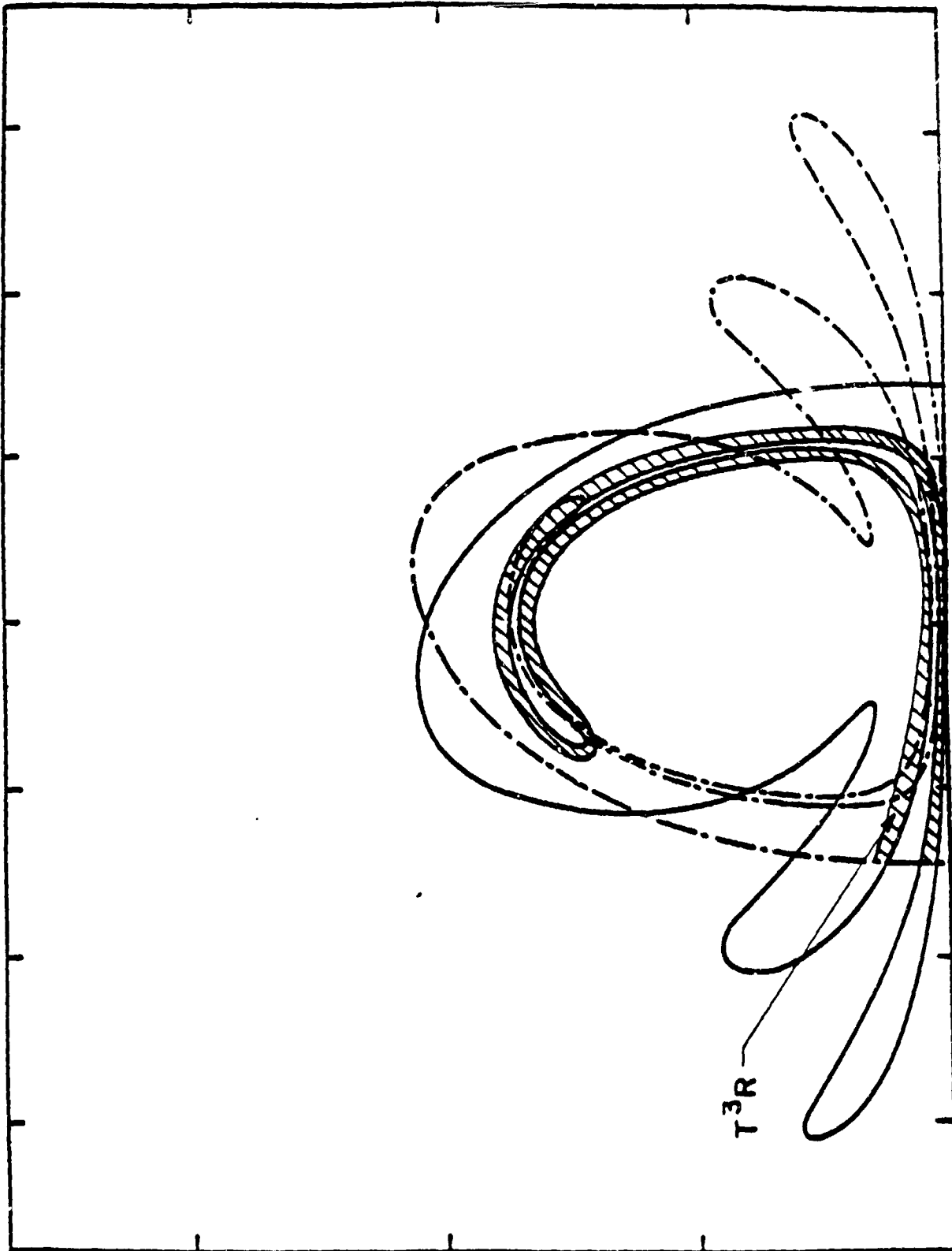


Fig 7.1d

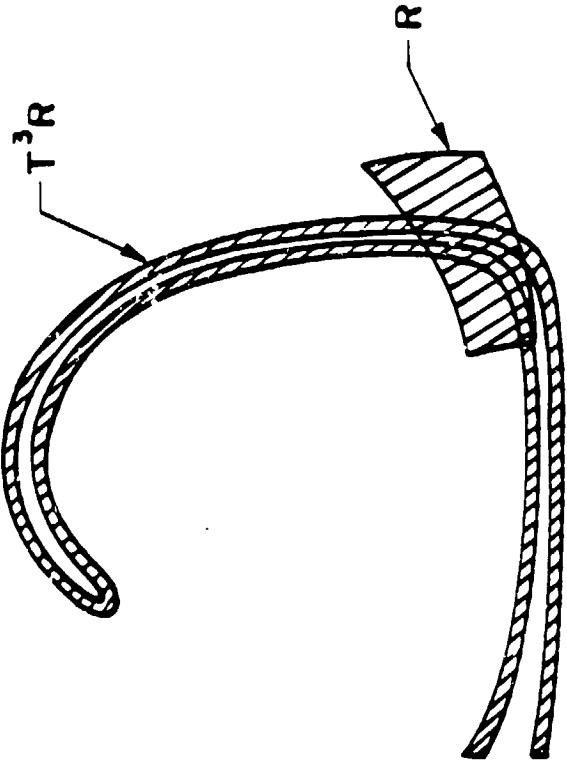
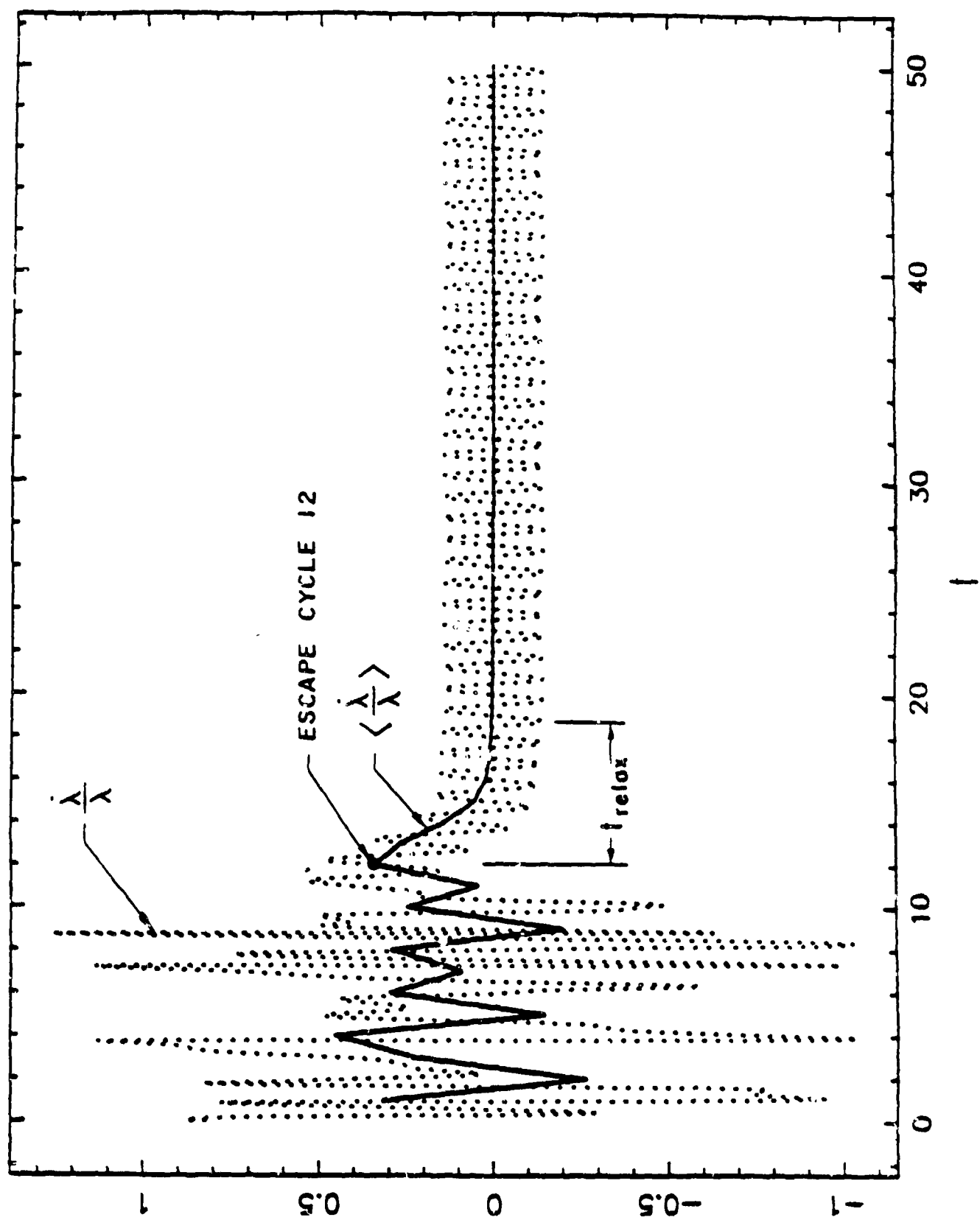
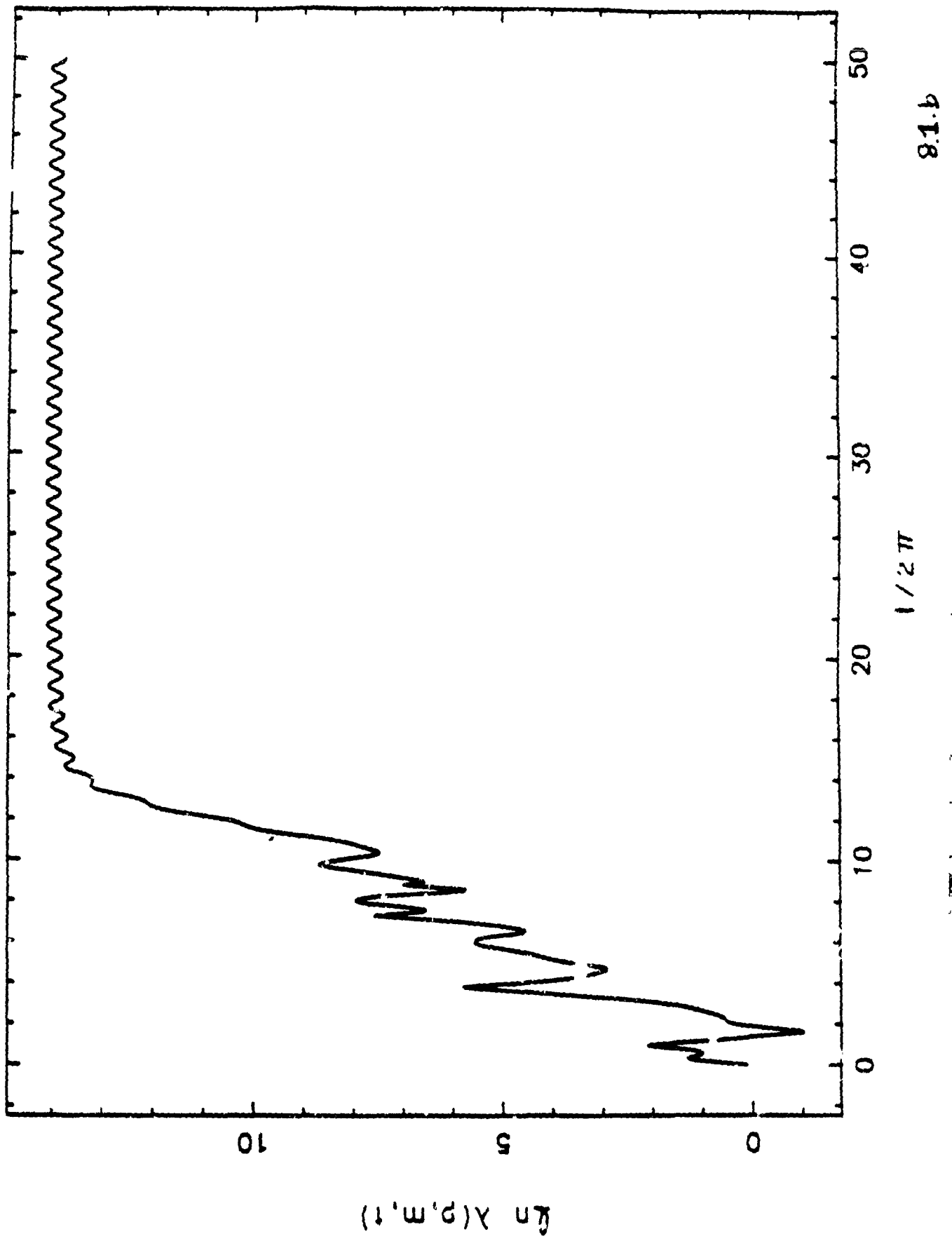
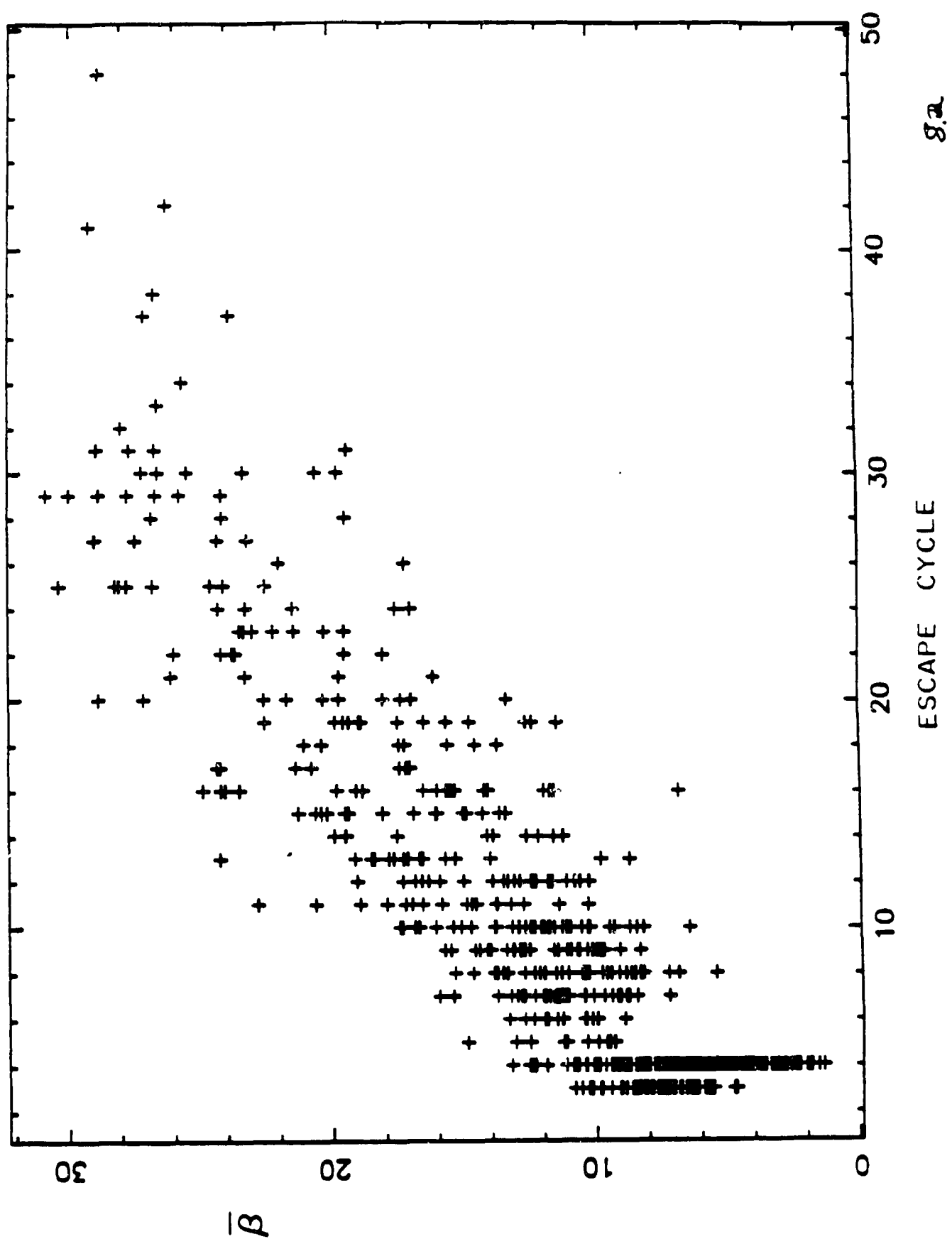
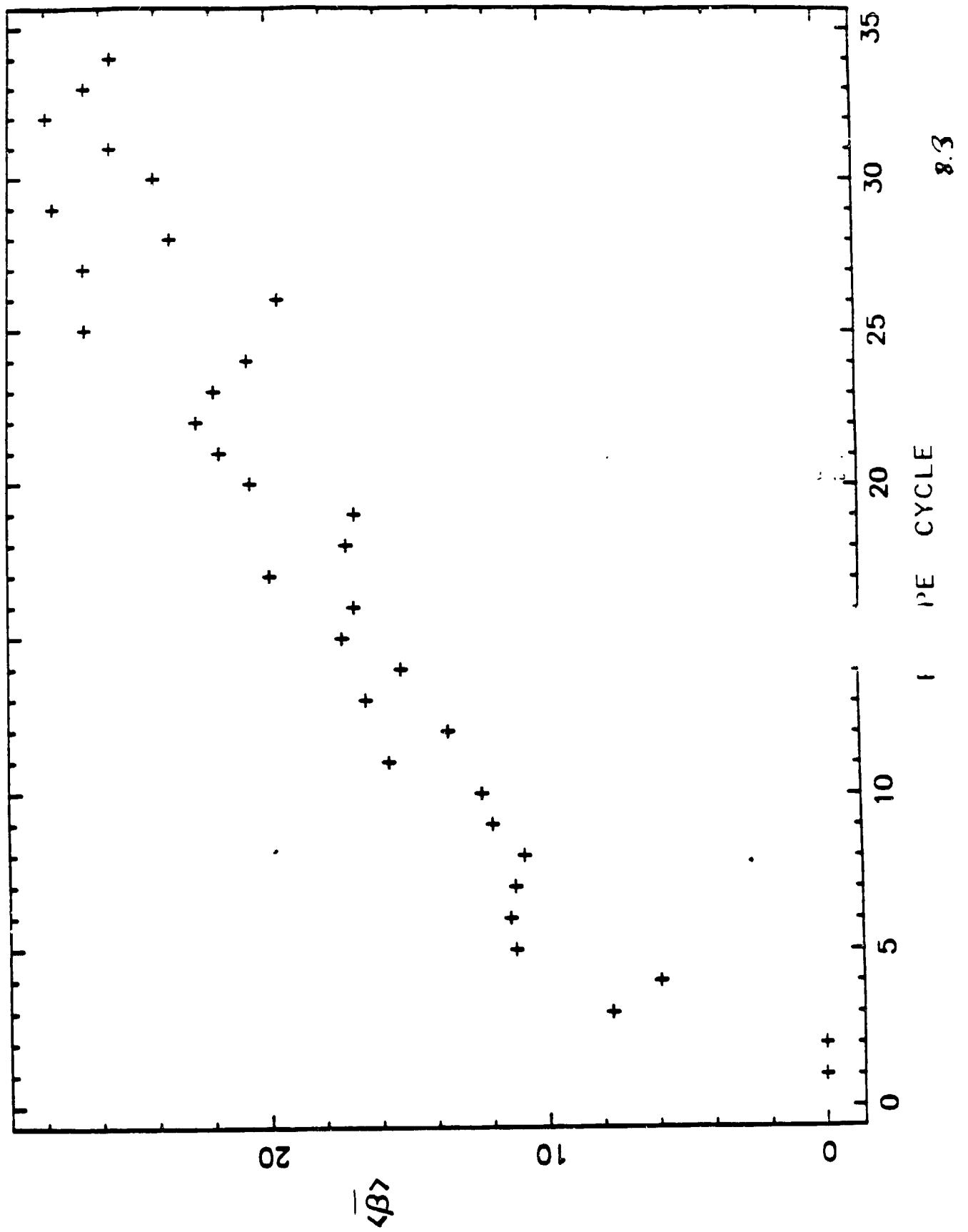


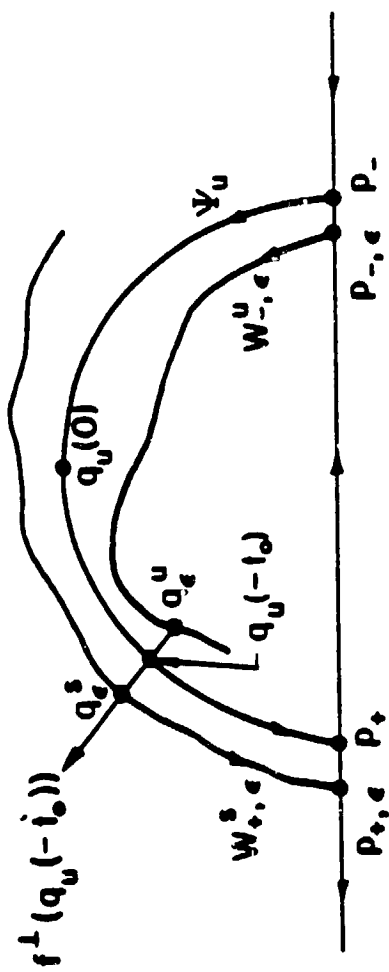
Fig. 7/c

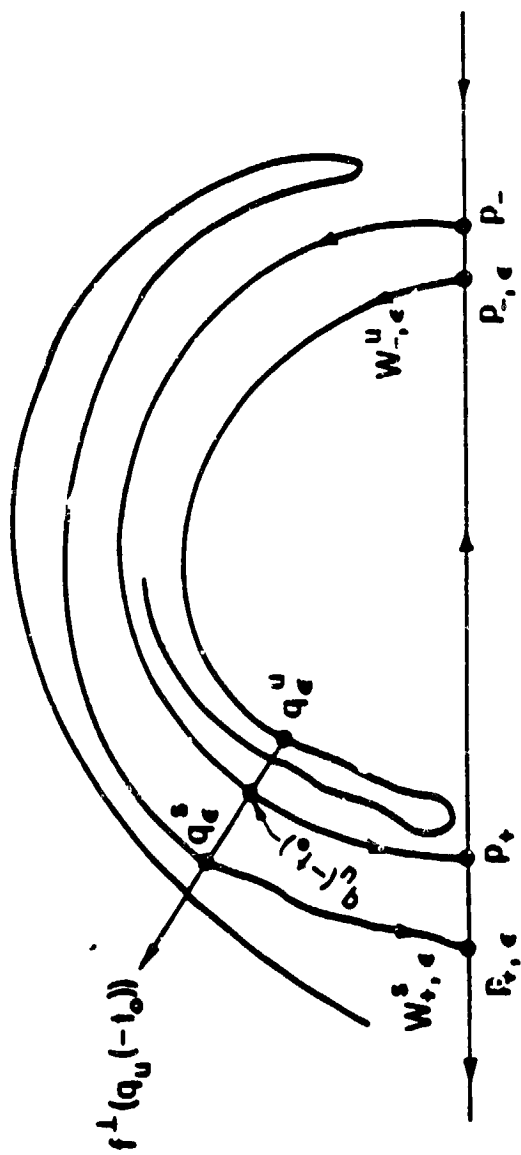


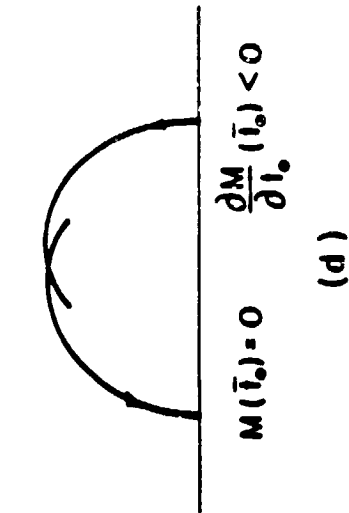
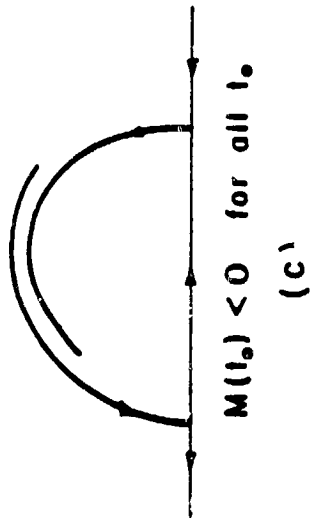
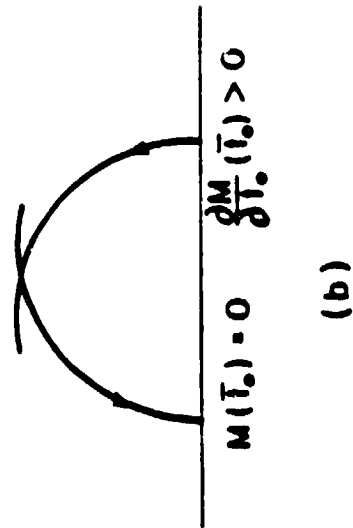
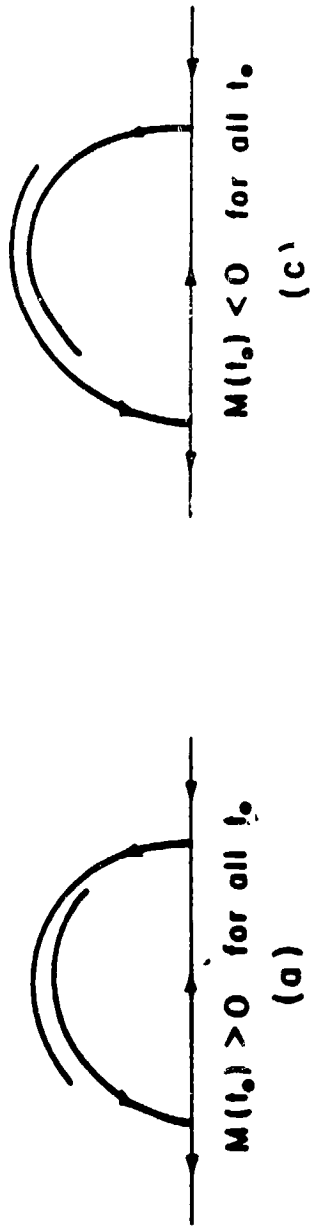


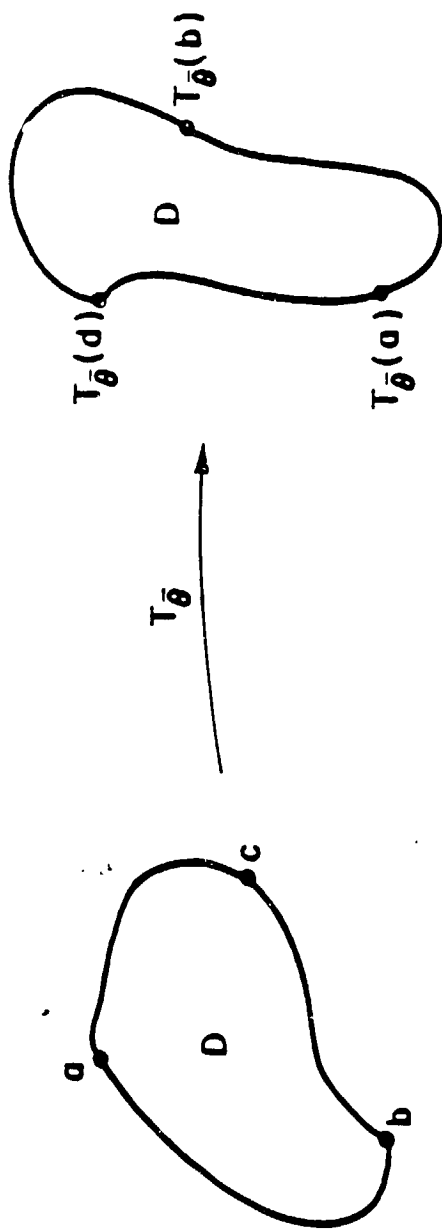












TRANSPORT, MIXING AND STRETCHING IN A CHAOTIC STOKES FLOW: THE TWO-ROLL MILL

Paper published in the Proceedings of the Third Joint ASCE/ASME Mechanics Conference in La Jolla, CA, July 9-12, 1989. Editor: K.Ghia.

Tasso J. Kaper and Stephen Wiggins
Applied Math and Applied Mechanics Departments
Caltech, Pasadena, CA 91125

Abstract *We present the outline and preliminary results of an analytical and numerical study of transport, mixing, and stretching in a chaotic Stokes' flow in a two-roll mill apparatus. We use the theory of dynamical systems to describe the rich behavior and structure exhibited by these flows. The main features are the homoclinic tangle which functions as the backbone of the chaotic mixing region, the Smale horseshoe, and the island chains. We then use our detailed knowledge of these structures to develop a theory of transport and stretching of fluid in the chaotic regime. In particular, we show how a specific set of tools for adiabatic chaos- the adiabatic Melnikov function [4,5,6,19], lobe area and flux computations [6], and the adiabatic switching method [7]- is ideally suited to develop this theory of transport, mixing, and stretching in time-dependent two-dimensional Stokes' flows.*

1.Introduction

Chaotic advection or lagrangian turbulence in two-dimensional time-periodic low Reynolds number fluid mechanics problems has been observed experimentally and numerically [1,2,3,8,9,16]. Under slow time modulation of a steady state configuration these flows simultaneously exhibit chaotic particle paths and large scale structures [1,2,3,8,9,16]. These features include homoclinic tangles [8], Smale horseshoes with their attendant chaotic dynamics [8,16], island chains [1,2,3,8,9,16], and whorls and tendrils [1,2,3].

The theory of dynamical systems has been used to explain some of these phenomena. This is because time-dependent two-dimensional fluid mechanics problems can, depending on the stirring protocol, be treated either as one degree of freedom Hamiltonian systems [3,8,9,16] or as nonintegrable area-preserving maps [1,2,16].

The field of time-dependent, two-dimensional Stokes' flows remains largely unexplored, however. In addition to developing the mathematical description of these flows within the framework of the quasisteady Stokes' approximation, there are many open questions about the transport and mixing of fluid particles, and about the stretching of line elements in these flows. For example, what is the size of the mixing zone? Given that one can define different regions within the mixing zone, what is the rate of transport of fluid into and out of these regions? What are the characteristics of the residence time distribution in each of these regions? At what rate must the flow field be modulated to achieve the most efficient mixing and the most efficient stretching of a line segment of tracer particles? We emphasize that this is just a partial list.

Furthermore the dynamical systems tools [4,5,6,7,19] specific to time-periodic, two-dimensional Stokes' flows have not been applied to any of these problems, except in a brief talk on the eccentric journal bearing problem by the first author [8]. These tools include the adiabatic Melnikov function [4,5,6,19], action integrals for flux and lobe area [6], as well as the adiabatic switching method [7].

The purpose of this paper is twofold. First we demonstrate why time-dependent, two-dimensional Stokes' flows constitute adiabatic dynamical systems. Second we show how detailed knowledge of both the structures in the fluid and the theory of adiabatic dynamical systems can be used to answer some of the questions asked above. The first part is valid for flows with general time dependence and is discussed in section 2. The second part focuses specifically on continuously modulated time-periodic Stokes' flows in the two-roll mill apparatus and occupies the remainder of the paper. Despite this narrow focus in the second part, however, our results are applicable to other two-dimensional Stokes' flows which are periodic or quasiperiodic in time.

This paper is split into six sections. As mentioned before, we present the discussion, comprising the first part of this paper, of why time-dependent, two-dimensional Stokes' flows are adiabatic dynamical systems in section 2. In section 3 we present the steady state flows in the corotating two-roll mill device. The stirring protocols for the time-periodic flows we study are detailed in section 4. In section 5 we use dynamical systems tools to describe the rich dynamics and structures present in the time-periodic flows. In section 6 we show how a detailed knowledge of this rich dynamics leads to specific formulas for computing some of the quantities enumerated above. We report on our preliminary results concerning the location and quantitative measurements of the size of the mixing zone for two different stirring protocols. Finally, in the conclusion we discuss the relation between the flow fields generated by continuous in time protocols and those generated by blinking protocols.

We remark that this extended abstract constitutes a brief report of our work to date. We are planning a more complete paper for later publication. We also remark that we are also in the preliminary stages of cooperating on a joint analytical and experimental effort to study this problem with Dr. L.G. Leal in the chemical engineering department at UC Santa Barbara.

2. Time-Dependent 2-D Stokes' Flows as Adiabatic Dynamical Systems

In this section we demonstrate why a time-dependent, two-dimensional Stokes' flow constitutes an adiabatic dynamical system. First we discuss what an adiabatic dynamical system is, and then we present the two main arguments justifying the above statement.

For the purposes of this paper an adiabatic dynamical system is a Hamiltonian system which depends continuously and periodically on a parameter which varies slowly in time. The Hamiltonian for these systems is $H = H(p, q; \lambda = \epsilon t)$, where p and q are canonically conjugate variables coordinatizing a two-dimensional symplectic manifold, λ is the time-dependent parameter, and $\epsilon \ll 1$. The equations of motion are

$$\begin{aligned}\dot{q} &= \frac{\partial H}{\partial p}(p, q; \lambda) \\ \dot{p} &= -\frac{\partial H}{\partial q}(p, q; \lambda) \\ \dot{\lambda} &= \epsilon.\end{aligned}\tag{1}$$

We remark at the outset that similar results exist for flows which are quasiperiodic and aperiodic in time [6] although we do not discuss these in this paper.

During the time evolution of (1) _{ϵ} through one period of the modulation $\mathcal{O}(1)$ changes can occur in the vector field. These $\mathcal{O}(1)$ changes include $\mathcal{O}(1)$ changes in the position

of a hyperbolic orbit, $\mathcal{O}(1)$ motions of the stable and unstable manifolds of a hyperbolic orbit, and $\mathcal{O}(1)$ changes in the areas in phase space of regions which are occupied by a given type of orbit.

Examples in which the position of the hyperbolic orbit of (1)_c varies over an $\mathcal{O}(1)$ distance as λ is changed slowly in time include: the corotating eccentric journal bearing problem when the ratio of the angular velocities of the shaft and casing is greater than a critical ratio which depends on the geometry, the pendulum with Hamiltonian, $H(p, q, \lambda) = \frac{p^2}{2} - \cos(q + \lambda)$, and as we shall shortly see the corotating two-roll mill, as well as many other examples from particle accelerators, celestial mechanics, and plasma-confinement systems.

The first reason that time-dependent two-dimensional Stokes' flows are adiabatic dynamical systems is that they are Hamiltonian systems which depend on a parameter which changes slowly and continuously in time. These flows are described by the Hamiltonian vector field

$$\begin{aligned}\dot{x} &= \frac{\partial H}{\partial y}(x, y; \lambda) \\ \dot{y} &= -\frac{\partial H}{\partial x}(x, y; \lambda) \\ \dot{\lambda} &= \epsilon,\end{aligned}\tag{2}$$

where λ is the parameter which varies slowly in time, H is the Hamiltonian (streamfunction), and the two spatial coordinates x and y are the canonically conjugate variables. Time dependent Stokes' flows must satisfy $\frac{Re}{St} = \frac{(UL)}{\nu} \ll 1$, where τ is the time-scale of the modulation and U and L are the characteristic velocity and length scale, respectively, of the flow. U and L depend on the geometry of the flow field at hand. Hence if the parameter λ , such as the ratio of the angular velocities of the rollers in the two-roll mill device or the ratio of the shaft and casing angular velocities in the eccentric journal bearing problem, is modulated in time, this modulation must be done continuously and slowly enough so that the system stays within the quasi-steady Stokes' approximation, $\tau \gg L^2/\nu$. Thus from a purely kinematical point of view once one accepts the validity of the quasisteady Stokes' approximation for describing these flows adiabatic dynamical system theory should be used to study them.

The second reason adiabatic dynamical systems theory should be used is that large scale changes can occur in the flow field during the time modulation. For example, the saddle point may move a distance as large as the characteristic length scale of the problem - an $\mathcal{O}(1)$ distance - during one period of the modulation. If this happens, as it will under the second of our two stirring protocols in the two-roll mill device, then the stable and unstable manifolds of this stagnation point which form the homoclinic tangle and the Smale horseshoe also move an order one distance during the modulation. As we discussed above, adiabatic dynamical systems theory is ideally suited to this type of slow, large amplitude modulation.

We conclude this section by making two remarks. First, although we do not pursue it in this paper, all of the above analysis applies to Stokes' flows with general time-dependence, not just to those flows which are periodic in time, as long as one stays in the quasisteady Stokes' regime. This is because many of the techniques which exist for adiabatic systems apply to systems with general time dependence [4,6,13,19].

Secondly, regular Melnikov function theory will not be of much use for Stokes' flows. This is because regular Melnikov theory applies only to autonomous Hamiltonian systems

with small amplitude, $\mathcal{O}(1)$ frequency forcing. Hence it can only be used for flows which undergo small amplitude changes during the modulation. Although some chaotic advection still occurs in this case it is not nearly as extensive as when the flow undergoes large amplitude changes. Furthermore the requirement that the forcing be of $\mathcal{O}(1)$ frequency in order for the theory to apply takes one out of the quasi-steady Stokes' approximation. Thus the use of regular Melnikov theory cannot be justified from a fluid mechanical standpoint.

3. Steady State Flow Geometry

In this section, we study the steady state Stokes' flow generated externally by two counter-rotating rollers of equal radii. The fluid has no velocity parallel to the axis of the rollers. As a result, the flow is two-dimensional and the problem can be studied as an integrable one degree of freedom Hamiltonian system treating the streamfunction as a Hamiltonian and the two Cartesian spatial coordinates as canonically conjugate coordinates. Fluid is constrained to move on streamlines, and the dynamics of the flow is completely determined by the streamfunction.

We formulate the steady state problem using the natural bipolar coordinate system with α and β as the orthogonal coordinates. See figure 1 for the geometry of this coordinate system.

Figure 1.
Bipolar Coordinate System
A & B are the points $\alpha = \pm\infty$

The equations of motion for the steady state are:

$$\begin{aligned}\dot{\alpha} &= h(\alpha, \beta) \frac{\partial \Psi}{\partial \beta}(\alpha, \beta; \frac{\Omega_L}{\Omega_R}) \\ \dot{\beta} &= -h(\alpha, \beta) \frac{\partial \Psi}{\partial \alpha}(\alpha, \beta; \frac{\Omega_L}{\Omega_R})\end{aligned}\tag{3}$$

with no slip boundary conditions on the rollers and zero velocity at infinity, where Ω_L and Ω_R are the constant angular velocities of the left and right rollers, respectively, and $h(\alpha, \beta)$ is the metric coefficient in the bipolar coordinate system. Figure 2 shows the streamline pattern. We remark that a position-dependent change of the time variable can make (3) Hamiltonian in bipolar coordinates.

Figure 2.
Steady State for $\Omega_L = \Omega_R$.

The flow field has one saddle stagnation point along the line of centers of the rollers and two stagnation streamlines, shown in figure 2, terminating on the saddle stagnation point. The saddle point is a hyperbolic fixed point of the autonomous Hamiltonian vector field (3), and the two stagnation streamlines are orbits homoclinic to the hyperbolic fixed point. These homoclinic orbits are also called separatrices. In fact, each homoclinic orbit is the coincidence of one branch of each of the stable and unstable manifolds of the hyperbolic fixed point. We observe that the saddle stagnation point is located at the midpoint of the line of centers of the rollers, when $\Omega_L = \Omega_R$, and that the areas enclosed by the stagnation streamlines depend on the value of $\frac{\Omega_L}{\Omega_R}$. See figure 3.

The streamfunction used in (3) will be derived in a forthcoming paper [17]. It is a solution of the biharmonic equation $\nabla^4 \Psi = 0$ expressed in bipolar coordinates satisfying the boundary conditions stated above. We give it for the special case in which $\Omega_L = \Omega_R$ and then discuss the general case.

When $\Omega_L = \Omega_R$, we find

$$\Psi(\alpha, \beta; \frac{\Omega_L}{\Omega_R}) = \frac{1}{h(\alpha, \beta)} \left(\sum_{n=1}^{\infty} \Phi_n(\alpha) \cos n\beta \right. \\ \left. + K(\cosh \alpha - \cos \beta) \log(\cosh \alpha - \cos \beta) + D \cosh \alpha \right), \quad (4)$$

where $\Phi_n(\alpha) = A_n \cosh((n+1)\alpha) + B_n \cosh((n-1)\alpha)$. Because the coefficients in $\Phi_n(\alpha)$ decay rapidly with n , one can truncate the series after a finite number of terms. Then the coefficients can be determined by imposing the following four conditions: symmetry conditions, the no slip boundary condition on the rollers, the condition of no normal velocity at the surface of the rollers, and the condition of zero velocity at infinity. The streamfunction for the steady flow when the corotating rollers have unequal angular velocities is obtained by adding a counterrotating flow of the appropriate strength to (4). We have obtained the solution for the purely counterrotating case using the method of matched asymptotic expansions and will discuss it in [17].

4. Stirring Protocols

In this section we focus on the time-periodic flows generated in the two-roll mill device by two stirring protocols. In the first, the angular velocities of the rollers are modulated continuously and periodically in time such that at every instant in time their magnitudes are equal, $\Omega_L(t) = \Omega_R(t)$. In the second, the angular velocities are again modulated continuously and periodically but now such that they are out of phase. See figure 3.

For both protocols we require that the saddle stagnation point be present at all times during the modulation in order to use the results of [4,5,6,7,19]. This is equivalent to requiring that the streamline pattern for every value of the parameter $\lambda = \frac{\Omega_L}{\Omega_R}$ taken on during the modulation must have a saddle stagnation point on the line of centers between the two rollers. It means that the angular velocities must maintain the same sign as they have initially. We also require of both protocols that the modulation is done slowly and continuously so that one stays in the Stokes' limit of $\frac{Ra}{St} = \frac{(\frac{\Omega R^2}{\eta D})}{(\frac{\eta R}{\rho D^2})} \ll 1$, where $\Omega = \frac{\Omega_L + \Omega_R}{2}$, the average of the angular velocities of the two rollers, $R = R_L = R_R$, the radii of the left and right rollers, and D is the distance between the centers of the rollers.

Figure 3.

First and Second Stirring Protocols

We will use (4) when studying the time-periodic flow generated by the first stirring protocol because $\Omega_L(t) = \Omega_R(t)$ for all t . The streamfunction valid for the general corotating case will be used in studying the flow generated by the second protocol.

For both protocols, Smale horseshoe chaos is present and the dynamics of the flow in the mixing zone is governed by the homoclinic tangles. In the next section we will discuss the rich dynamics of these time periodic flows. We emphasize here that one will not see a sequence of smooth stagnation streamlines, one corresponding to each value of $\frac{\Omega_L}{\Omega_R}$ taken

on during the modulation. Even if one did not know anything about dynamical systems theory one could predict this result from the incompressibility of the fluid.

5. Geometry of the Time-Periodic Flow

In this section we describe the wealth of new behavior found when the angular velocities of the rollers undergo large amplitude, slow and periodic in time modulations both of the stirring protocols discussed above. The main result is that a mixing created in which chaotic advection occurs, large scale structures arise, and stretching of line elements is exponential.

The application of either of our two stirring protocols causes the stagnation streamlines to break. The stable and unstable manifolds of the hyperbolic orbit intersect each other as shown in figure 4 and form homoclinic tangles and Smale horseshoes [4,5,19].

Periodicity allows us to simplify the transport analysis via the use of a Poincare map, T . The Poincare map associates points from D with their first return to D , where D is the two-dimensional fluid domain. That is $T : (x(t), y(t)) \rightarrow (x(t + \tau), y(t + \tau))$ for every $(x, y) \in D$. We remark that the period of the modulation, τ , is proportional to $\frac{1}{\epsilon}$ where ϵ is the frequency of the modulation. Thus as $\epsilon \rightarrow 0$ $\tau \rightarrow \infty$ and the simulation of these systems, both experimental and numerical, becomes more and more time consuming.

On the domain of the Poincare map the pieces of the broken stagnation streamlines form homoclinic tangles. These broken stagnation streamlines are the unstable manifolds of the saddle point in the fluid and from a fluid mechanical point of view are streaklines. The saddle point also has stable manifolds (these one can see by simply reversing the flow). Together the stable and unstable manifolds of the saddle point form the homoclinic tangles that are the backbone of the main mixing zone. We describe the mixing process in detail below in discussing figure 6.

On the Poincare section shown in figure 4, four distinct regions, defined by pieces of the stable and unstable manifolds of the hyperbolic fixed point present themselves.

Figure 4
Domain of Poincare Map for Second Protocol
Mixing Zone is Region III.

The two annular regions, I and II, adjacent to the rollers, correspond to the area bounded by Arnold tori [14,12] these are the tori which persist under the modulation just as the so-called KAM tori are the tori which persist under small-amplitude periodic perturbations

of autonomous Hamiltonians. The flow appears to be smooth in most of these regions except for in the resonance bands manifested experimentally by so-called island chains. Chaotic advection is also associated with these resonance bands. They are located near the broken separatrix because the periodic orbits whose period is at least as large as that of the modulation lie near the separatrix. Fluid in regions I and II cannot escape by advection but only by the much slower process of molecular diffusion. Since the time scale for diffusion is much longer than that of the chaotic advection, the fluid in these two regions is called trapped. Arnold tori also exist in region III adjacent to the container walls. Thus, region III is also a region in which fluid is trapped.

Finally, region IV, the region complementary to the other three, is the main mixing region. Its backbone is the homoclinic tangle. This is the region, besides the island chains, in which particle paths are chaotic, in which mixing occurs, and in which material lines stretch exponentially. We present results about its size and the rate of transport of fluid in this region in the last section of this paper. Region IV has been enlarged for clarity in figure 4. The region will be narrower than shown, and the lobes, defined shortly, shown will be narrower and longer than is shown [6]. The region can be split into three parts corresponding to the parts inside and outside of the solid black lines which are also called pseudo-separatrices.

We define a lobe as follows. Let X denote the saddle point in the flow and $W^U(X)$ and $W^S(X)$ one branch of each of its stable and unstable manifolds. For definiteness, we take the branches emanating to the right of the saddle point, though the concept applies equally well to the branches emanating to the left. Let P denote a point of intersection of $W^S(X)$ and $W^U(X)$ and W^SP and W^UP denote the segments of $W^S(X)$ and $W^U(X)$, respectively, connecting P and X . We say that P is a primary intersection point (pip) if W^SP and W^UP intersect only in P . Now take two pips, P and Q , such that there are no other pips on the segments of $W^S(X)$ and $W^U(X)$ connecting them. The region bounded by the pieces of $W^S(X)$ and $W^U(X)$ connecting P and Q is defined as a lobe. See figure 5.

Figure 5. A Lobe

Now we discuss the mixing in these flows and the mechanism underlying it. One will see fluid particles transported between distinct regions defined by pieces of these broken streamlines. In addition tracer line elements in the fluid will stretch exponentially.

The sequence of pictures in figure 6 shows how an initial distribution of tracer particles evolves after the first two periods of the modulation.

Figure 6.

Evolution of Tracer Particles Illustrating Transport of Lobes

A. Poincare map with initial distribution of tracer. B. Poincare map after one period. C. Poincare map after two periods.

In each period of the modulation a lobe of fluid leaves region III1 and enters region III2 and vice versa. The same is happening between regions III1 and III3, not shown in figure 6. (We remark that the system can be said to have a turnstile [18] and the two lobes of fluid which change regions in one period of the modulation are referred to as turnstile lobes). The picture gets more complicated after each subsequent period. Note that incompressibility guarantees that equal amounts of fluid enter and leave the regions bounded by pseudo-separatrices in each period. Thus the homoclinic tangle is the backbone of the mixing zone, and the lobe dynamics associated to the tangle governs the fluid motion there.

Quantitative measurements of transport and stretching in region IV can now be made given quantitative knowledge of the lobes, and we discuss this in detail in the next section. As we remarked before adiabatic dynamical system theory [4.5.6,19] is ideally suited to systems in which the flow field undergoes $O(1)$ amplitude changes. Finally we remark that the problem is nonintegrable [4.5.19] and, in the absence of molecular diffusion, reversible.

Before concluding this section, we discuss a second approach based on the adiabatic switching method that we are taking to arrive at these quantitative measurements. The adiabatic switching method represents a highly developed approximation scheme to determine whether or not a particle crosses the pseudo-separatrix during any given period of the modulation. This is akin to the role the whisker or separatrix map [15] plays for vector fields which are time-dependent small amplitude perturbations of autonomous Hamiltonians. The adiabatic switching method has not been applied in the context of low Reynolds number fluid mechanics and represents a potentially powerful tool to measure the transport quantities we seek. Furthermore, results from this method have not been compared with results obtained from an exact dynamics-based technique such as the one we are using in the principal part of our study.

6. Results from Applying Adiabatic Tools

In this final section we state our results for the areas of the mixing zone and of a lobe and also give the basic formulas to be used in studying the transport in the mixing region.

The size of the main mixing zone under the first protocol is given to a certain order of approximation by the area between the minimum and maximum frozen separatrix [12,13,6], A_s . See figure 7. In addition the area of a lobe in (2) is given to leading order by $A_s/6$.

Frozen separatrices can be understood as follows. For any instantaneous value of the angular velocities of the rollers one has a corresponding steady state flow pattern. This flow field has a stagnation streamline which is called a frozen separatrix. We emphasize that frozen separatrices are never realized by the flow of (2) because the periodic modulation of the roller angular velocities breaks the stagnation streamline. Instead frozen separatrices serve merely as a convenient fiction for aiding in determining the area of the mixing zone and that of a lobe. In particular, during the modulation, the sequence of areas enclosed by frozen separatrices, one area for each instantaneous steady state flow pattern, is an alternately expanding and contracting sequence. Thus the area enclosed by the frozen separatrix oscillates between a minimum and maximum area [12,13,6]. The difference between the minimum and maximum areas is exactly A_s . We remark that frozen separatrices are distinct from the pseudo-separatrices formed by pieces of the stable and unstable manifolds.

Figure 7. Frozen Separatrices for First Protocol

The shaded area shown in figure 7 is then the area between the minimum and maximum frozen separatrices and to leading order gives the area of the mixing zone [6]. This result is valid to $O(\epsilon)$ and thus gives a good approximation to the area of the mixing zone for slowly modulated flows.

Under the second protocol the area of the main mixing zone can also be determined to leading order from two frozen separatrices. The area can be obtained directly from the shaded region in figure 8. We refer the reader to [6].

Figure 8.

Frozen Separatrices for Second Protocol

To obtain quantitative information about the lobes for both protocols, we rely primarily on the adiabatic Melnikov function [4,5,6,10]. It is given by

$$M_A(\lambda) = \int_{-\infty}^{\infty} t \left[\frac{\partial \Psi}{\partial x} \frac{\partial^2 \Psi}{\partial y \partial \lambda} - \frac{\partial \Psi}{\partial y} \frac{\partial^2 \Psi}{\partial x \partial \lambda} \right] (q_0^\lambda(t)) dt, \quad (5)$$

where $q_0^\lambda(t)$ represents the separatrix for the system with the parameter λ fixed at $\lambda = \frac{\Omega}{\Omega_A}$. $M_A(\lambda)$ is, up to a normalization, the first term of the Taylor expansion of the distance between the stable and unstable manifolds of the hyperbolic orbit as a function of the time of flight along the separatrix of the steady state flow. Integrating it between two zeroes, which correspond to intersection points of those manifolds, gives the area of a lobe [6] and this quantity is equal to leading order to A , [6]. We remark here that this result cannot be proven directly from the Poincaré map of the flow but instead relies entirely on the connection between the theory of action in classical mechanics and the adiabatic Melnikov theory [6].

Now we mention only one of the transport formulas we need. Given an initially uniform distribution of tracer fluid in region 1, the amount of fluid which leaves this region after n periods is given by

$$a_n = \mu(D^{12}) - \sum_{k=0}^{n-1} \mu(D^{12} \cap T^k E^{12}), \quad (6)$$

where μ gives the area of the lobe [10,11]. The lobes E^{12}, D^{12}, \dots are marked in figure 6. This formula only requires knowledge of the intersections of all forward iterates of one of the two turnstile lobes with the second turnstile lobe. This simplifies the numerical work except that one must still integrate over long time intervals because the return time of the Poincaré map is proportional to $\frac{1}{\epsilon}$.

We have additional formulas, given the initial distribution of tracer particles in the fluid, to determine the amount of tracer fluid in each of the three regions after the first several periods [10,11]. Furthermore, we have extended these formulas so that we can compute the rates of multiple region changes. For example, if some of the tracer fluid initially in region 1 flows into region 2 during the k -th period, we can compute the amount of it which will reenter region 1 during the $(k+n)$ -th period for any n . These are based in part on the same simplifying idea used in the derivation of formulas such as (6) and a detailed understanding of Birkhoff signatures.

Finally, we remark that using the results from the above transport computations we can establish residence time distributions for each of the regions, or even of subregions, in the flow. This entails obtaining statistics from the above transport calculations and determining the amount of tracer fluid in a given region as a function of time.

7. Conclusion

We have presented the outline of our transport, mixing, and stretching study in chaotic Stokes' flows which is based on the structures found in these flows and on the ideas of adiabatic dynamical systems. We have given analytic formulas for the area of the mixing zone, for the area of a lobe, and for the evolution of a given distribution of tracer particles.

We now make a few comments about extension of our results. The technique behind our mixing zone size result is valid for continuous, periodic stirring protocols other than the ones we study [6].

In particular suppose one takes a sequence of protocols, for each of which Ω_L and Ω_R are 180 degrees out of phase, which limit on a square wave (here we are not concerned about maintaining the quasisteady approximation). For each continuous protocol in this sequence, our technique gives the size of the mixing zone in the flow. Thus, we have a sequence of mixing zone sizes.

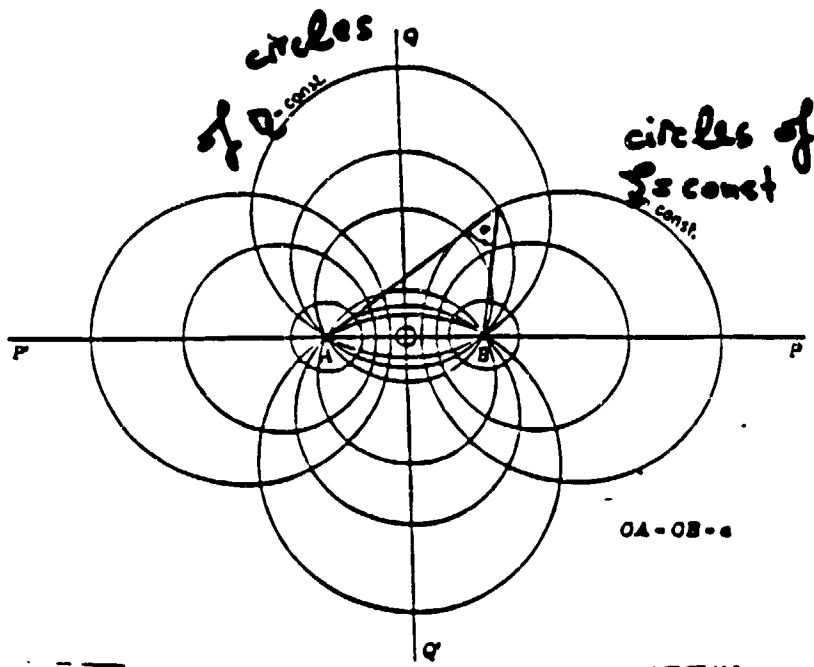
Now the limit of our protocol sequence is called the blinking or alternating protocol. Thus the question arises as to whether the limit obtained above is the area of the mixing zone in the blinking two-roll mill. Blinking protocols have been studied in several flows, however the area of mixed fluid has only been determined numerically. The present idea may yield an analytical result. In general the relationship between continuous protocols and discontinuous ones deserves further exploration, certainly since a blinking type protocol is easier to achieve experimentally.

Acknowledgement T.K. would like to thank Dr.L.G.Leal for his guidance and inspiration during the process of finding the streamfunctions for both the corotating and counterrotating two-roll mill. One of us, T.K., acknowledges partial financial support from the AFOSR.

References

1. Chaiken,J., et al, 1987, "Lagrangian Turbulence and Spatial Complexity in a Stokes Flow," *Physics of Fluids*, 30, no.3, pp.687-699.
2. Chaiken,J., et al, 1986, "Experimental Study of Lagrangian Turbulence in a Stokes Flow," *Proceedings of the Royal Society, Series A*, 408, pp.165-174.
3. Aref,H. and Balachandar,S., 1986, "Chaotic Advection in a Stokes Flow," *Physics of Fluids*, 29, no.11, pp.3515-3521.
4. Wiggins,S.,GLOBAL BIFURCATIONS & CHAOS: ANALYTICAL METHODS, 1st ed., Springer Verlag, 1988.
5. Wiggins,S., 1988, "Adiabatic Chaos," *Physics Letters A*, 128, no.6-7, pp.339-342.
6. Kaper,T.J., Kovacic,G., and Wiggins,S., "Melnikov Functions, Action, and Lobe Area in Hamiltonian Systems," Caltech Preprint.
7. Cary,J.R., Skodje,R.T., 1988, *Computer Physics Reports*, 8, pp.221-292.
8. Kaper,T.J., Nov., 1987, APS Fluid Dynamics Division Annual Meeting, Eugene, OR.
9. Ottino,J.M., 1988, "Chaos in Deterministic Systems: Strange Attractors, Turbulence, and Applications in Chemical Engineering," *Chem Eng Sci*, 43, No.2, 1988, pp.139-183.
10. Rom-Kedar,V., Leonard,A., and Wiggins,S., "An Analytical Study of the Transport, Mixing and Chaos in an Unsteady Vortical Flow," submitted to *Journal of Fluid Mechanics*.
11. Rom-Kedar,V., Wiggins, S., "Transport in Two-Dimensional Maps," to appear in *Archive for Rational Mechanics and Analysis*, 1989.
12. Escande,D., "Hamiltonian Chaos and Adiabaticity," Proc. Intl.Workshop, Kiev, April 13-25, 1987.
13. Cary,J.R.,Escande,D.F., Tennyson,J., 1986, "Adiabatic Invariant Change Due to Separatrix Crossing," *Physical Review A*, 34, no.5, pp.4256-4275.

14. Arnol'd, V.I., 1963, "Small Denominators II." *Russian Math Surveys*, 18, no.5, pp.9-35.
15. Lichtenberg and Liebermann, REGULAR and STOCHASTIC MOTION, 1st ed., Springer, 1983.
16. Chien, W.-L., Rising, H., Ottino, J.M., 1986, "Laminar Mixing and Chaotic Mixing in Several Cavity Flows," *JFM*, 170, pp.355-377.
17. Kaper, T.J., Leal, L.G., "Steady Stokes' Flow External to Two Rotating Cylinders," in preparation.
18. Meiss, J.D., MacKay, R.S., Percival, I.C., 1984, "Transport in Hamiltonian Systems," *Physica D*, 13D, pp.55-81.
19. Wiggins, S., 1988, "On the Detection and Dynamical Consequences of Orbits Homoclinic to Hyperbolic Periodic Orbits and Normally Hyperbolic Invariant Tori in a Class of Ordinary Differential Equations," *SIAM Journal of Applied Math*, 48, no. 2, pp.262-285.



A, B are poles of coord. sys.

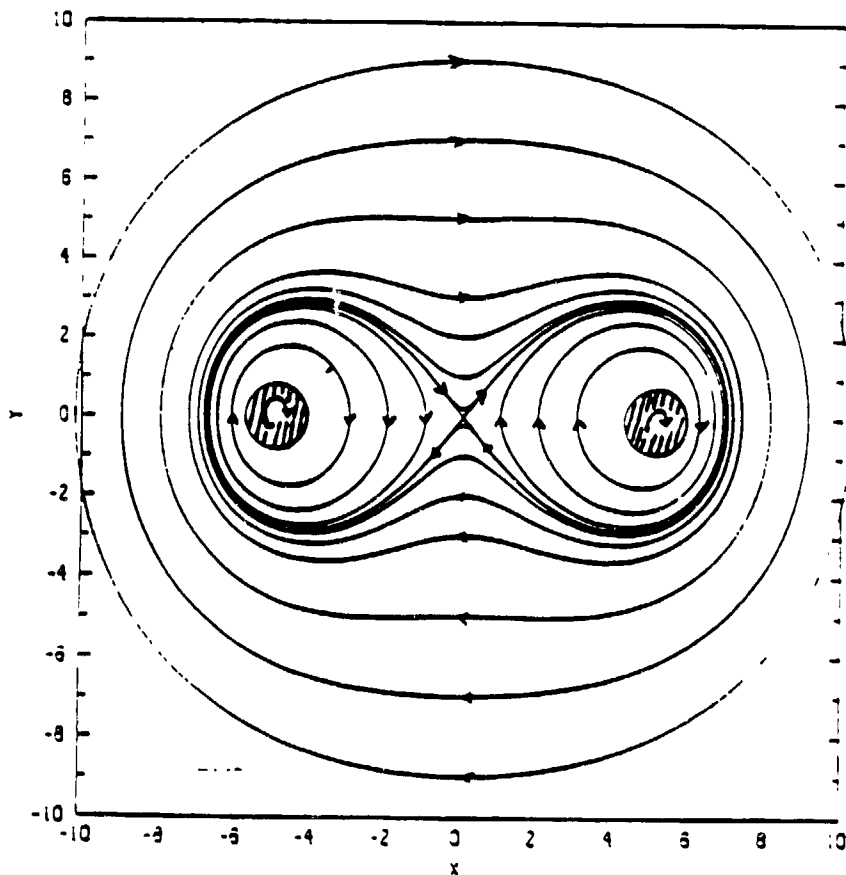


FIG. 2

Steady state streamlines in the case of equal angular velocities.

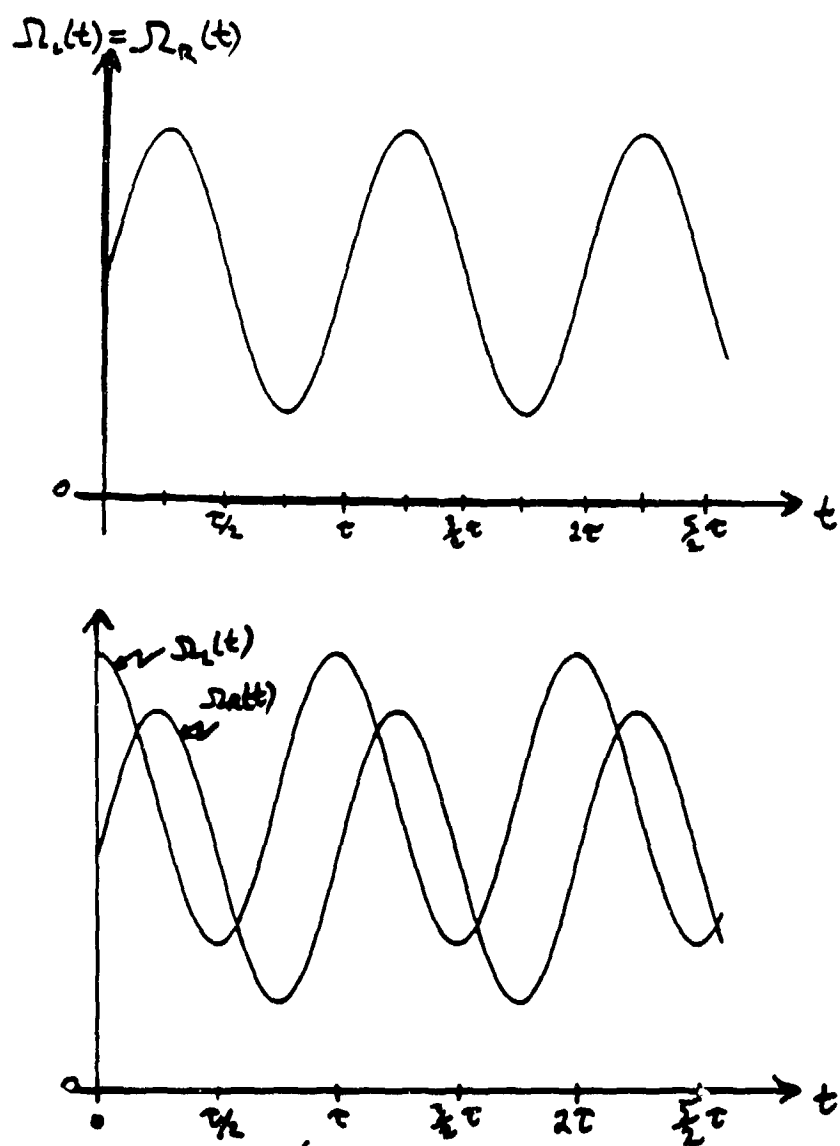


Figure 3. Stirring protocols 1 and 2.

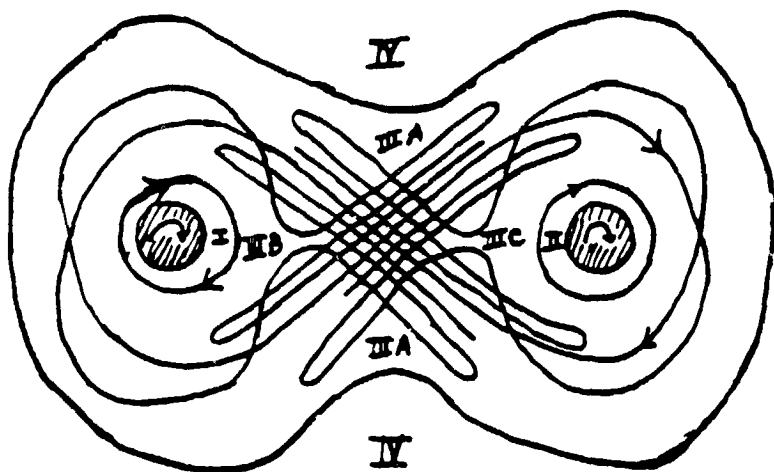


Figure 4. Four regions of time-periodic flow.
Region III is the mixing zone.

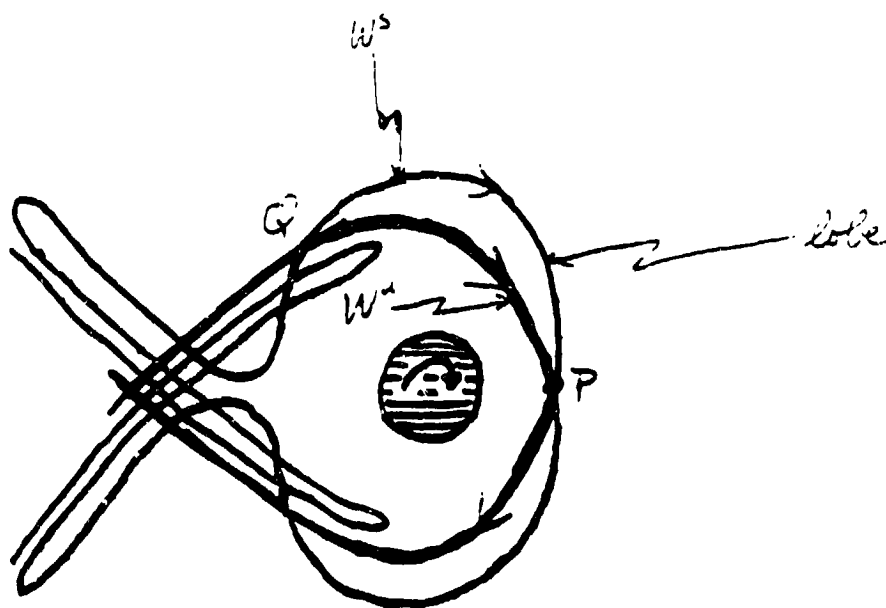


FIG. 5
ALCBE

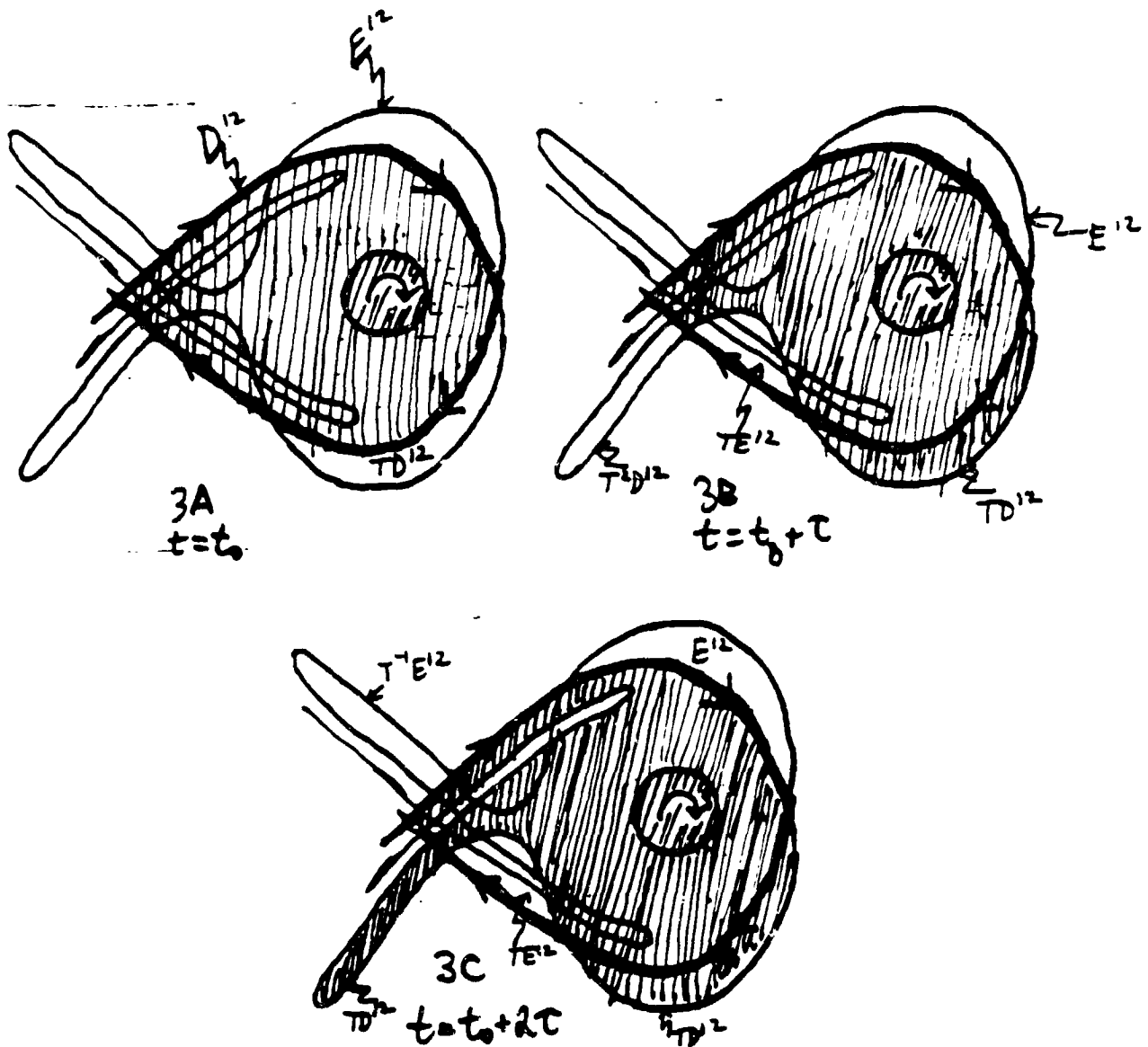


Figure 6 Evolution of an initial distribution of tracer particles. The mechanism for transport is the lobe dynamics of the homoclinic tangle.
 A shows the initial distribution.
 B shows the Poincare map one period of the flow later
 C shows the Poincare map after two periods of the evolution.
 After each period one sees that a lobe of fluid leaves region IIIA and enters region IIIC and vice versa.
 The same is happening between regions IIIA and IIIB.

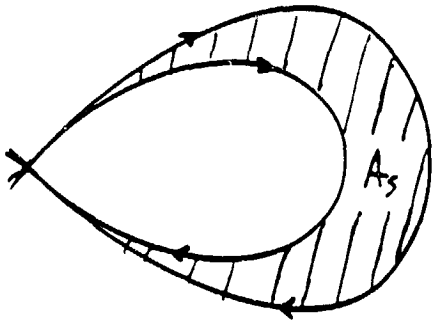


FIG. 7

Area between the minimum and maximum frozen separatrices.

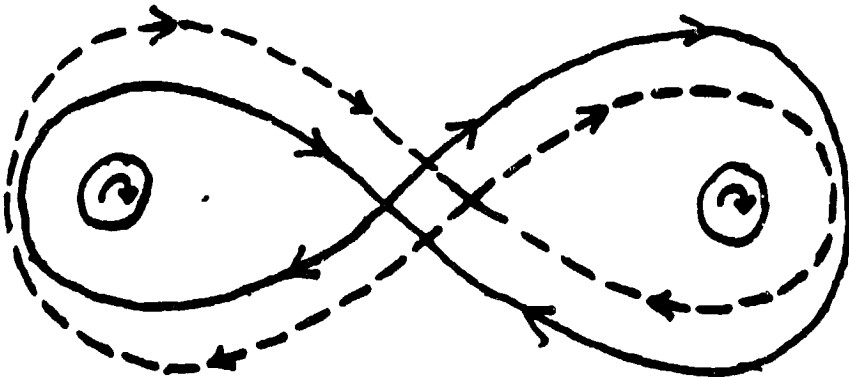


FIG. 8

FROZEN SEPARATRICES FOR SECOND
STIRRING PROTOCOL

Turbulence effects during evaporation of drops in clusters

J. BELLAN and K. HARSTAD

Jet Propulsion Laboratory, California Institute of Technology, 4800 Oak Grove Drive,
Pasadena, CA 91109, U.S.A.

(Received 9 June 1987 and in final form 22 January 1988)

Abstract—A model of droplet evaporation in clusters and the exchange processes between the cluster and the gas phase surrounding it are presented. This model is developed for use as a subgrid model in calculations of spray evaporation and combustion and thus describes only global features of cluster behavior. The gas pressure in the cluster remains constant during evaporation and as a result the volume of the cluster and the drop number density inside the cluster vary. Two turbulence models are considered. The first one describes cluster evaporation in surroundings initially devoid of turbulence and turbulence is allowed to build up with time. The second model describes cluster evaporation in surroundings where turbulence is present initially. The results obtained with these models show that turbulence enhances evaporation and is a controlling factor in the evaporation of very dense clusters. Examples are shown where with the first turbulence model saturation was obtained before complete evaporation whereas the opposite was obtained with the second turbulence model. As the initial air/fuel mass ratio increases, both turbulence history and the initial relative velocity between drops and gases can control evaporation. It is shown that the evaporation time decreases with an initial increase in turbulence levels or relative velocity. When the initial air/fuel mass ratio increases further and the initial drop number density falls within the dilute regime, neither of the above parameters can control evaporation. Moreover, the evaporation time decreases with the decreasing size of the cluster for dense clusters of drops, whereas for dilute clusters of drops the size is not a controlling factor. The practical implications of these results are discussed.

1. INTRODUCTION

THE MATHEMATICAL formulation of spray combustion is extremely complicated due not only to the great number of phenomena to be described but also due to the fact that the space scales involved in these phenomena are vastly different. For example, a few of the most obvious scales are: the scale of the combustor itself, the many turbulent scales associated with turbulence build up and decay, the scale of droplet interactions and the scale of the drops themselves. These scales vary by many orders of magnitude from the largest one to the smallest one and thus it is obvious that an accurate mathematical description at all scales is impractical. Instead, a sound approach is to describe in detail the macroscale where many of the phenomena of interest to engineers involved in the design of combustors occur, and to associate and couple to this description that of phenomena occurring at scales much smaller than those of immediate interest. This second part of the formulation is called a subgrid or subgrid model because the phenomena to be described occur at a scale much smaller than that of the grid size used to computationally solve the macroscale problem. By the very nature of this two-level formulation, the subgrid models are more approximate than the macroscale models and lack the detail that the latter one must have in order to be useful.

The work described here pertains to a subgrid model to be used for the description of spray evaporation in a combustor. Within the frame of this approximation it is intended that the gas phase in the combustor be described by the solution of the

macroscale equations at certain grid points; this is an Eulerian approach. In contrast, the spray is partitioned into clusters of drops that have a size smaller than that of the grid, and each cluster is followed in its trajectory; this is a Lagrangian approach. The coupling between the two formulations is achieved through the transfer of mass, species and heat to and from the cluster. The partition of the spray into clusters as explained above is not an artifact because it is corroborated by experimental evidence [1].

What is described below is only the subgrid model uncoupled from the macroscale formulation. This means that the properties of the gas phase surrounding the cluster of drops are assumed known, and what is of interest to describe, solve for and analyze is the behavior of a cluster of drops in this given environment.

2. MODEL FORMULATION

Figure 1 shows the situation under consideration. A monodisperse collection of uniformly distributed droplets of a single-component volatile compound is immersed into gases at a higher temperature and exposed to a convective flow. As a result, heating of the drops and evaporation occurs. At each instant of time the envelope of the cluster of particles is called the surface of the cluster. The volume enclosed by the surface is called the cluster volume; it contains both drops and gas. Since the pressure is maintained constant during this process, the volume of the cluster will change with time.

The point of departure of the present model is the

NOMENCLATURE

A_c	transverse area of the cluster [cm ²]	t	time [s]
A_d	cross-sectional area of a drop [cm ²]	r	radial coordinate centered at a drop's center [cm]
a	radius of the sphere of influence [cm]	\tilde{r}	radial coordinate centered at the cluster's center [cm]
C	$-m [4\pi(\rho_g D)^2 R^0]$	R_2	a/R^0
C_p	specific heat at constant pressure [cal g ⁻¹ K ⁻¹]	Sh	Sherwood number
ΔC_p	fitted $C_{p1} - C_{p2}$ for the saturation pressure curve [cal g ⁻¹ K ⁻¹]	u	velocity [cm s ⁻¹]
C_T	constant	V	volume of the cluster [cm ³]
D	diffusivity [cm ² s ⁻¹]	v	radial gas velocity inside the sphere of influence [cm s ⁻¹]
E_i	rate of enthalpy transfer, equation (19)	W	'trapping factor', equation (13)
E_t	rates of enthalpy transfer for turbulence models 1 and 2 ($j = 1$ and 2), equations (22) and (25)	w_i	molecular weight [g mol ⁻¹]
H	enthalpy [cal]	y	r/R^0
H_{ref}	$4R^0 \rho_g^* L_{bn}$	z	r/R
\tilde{H}	H/H_{ref}	Greek symbols	
h	specific enthalpy [cal g ⁻¹]	α	constant for the Langmuir-Knudsen evaporation law, 4π
h^G	enthalpy of the gases at T_{ref} [cal g ⁻¹]	γ	w_F/w_{sg}
h^L	enthalpy of the liquid at T_{ref} [cal g ⁻¹]	Γ	generic function representing θ or Y
L	latent heat of evaporation [cal g ⁻¹]	ϵ	evaporation efficiency, equation (29)
Le	Lewis number	θ	$C_{pg} T' L_{bn}$
l_T	turbulent length scale [cm]	λ	conductivity [cal cm ⁻¹ s ⁻¹ K ⁻¹]
\dot{M}	rate of mass transfer, equation (21)	μ	viscosity [g cm ⁻¹ s ⁻¹]
\dot{M}_i	rate of species i transfer, equation (20)	ν	kinematic viscosity, μ/ρ [cm ² s ⁻¹]
$\dot{M}_{i,t}$	rate of species i transfer for turbulent models 1 and 2 ($j = 1$ and 2), equations (23) and (26)	ρ	density [g cm ⁻³]
m	evaporation rate, $-(1/V) dm_d/dt$ [g s ⁻¹]	$\hat{\rho}$	ρ/ρ_{ref}
m_d	mass of all drops in the cluster [g]	ρ_{ref}	$\rho^* w_F C_{pg} (R_g^0 L_{bn})$
m_{Fv}	mass of fuel vapor [g]	σ	$1 - \gamma$
m_g	mass of gases inside the cluster [g]	τ	t/t_{ref}
m_{ref}	$4\pi \rho_g^* R^0$	Subscripts	
\tilde{m}	m/m_{ref}	a	at the edge of the sphere of influence
N	total number of drops	ag	ambient gas
n	drop number density [cm ⁻³]	bn	normal boiling point
Nu	Nusselt number	c	cluster
p	pressure [atm]	ch	characteristic value
Pr	Prandtl number	d	drop
Re	$2Ru_g/v_g^2$	Fv	fuel vapor
Re_c	$2[A_c(u_g/u_d)/\pi]^{0.5} u_d/v_g^2$	g	gas
R_g^0	universal gas constant [atm cm ³ mol ⁻¹ K ⁻¹]	l	liquid
R_u	universal gas constant [cal mol ⁻¹ K ⁻¹]	r	relative
\tilde{R}	radius of the cluster [cm]	s	drop surface.
$\tilde{\tilde{R}}$	\tilde{R}/R^0	Superscripts	
R_i	R/R^0	∞	in the far field of the external gas phase
R	drop radius [cm]	0	initial value
T	temperature [K]	f	final: either when $R_i = 0.04$ or when evaporation stopped.
T_{ref}	R^0/D^2		
T_{ref}	L_{bn}/C_{pg}		

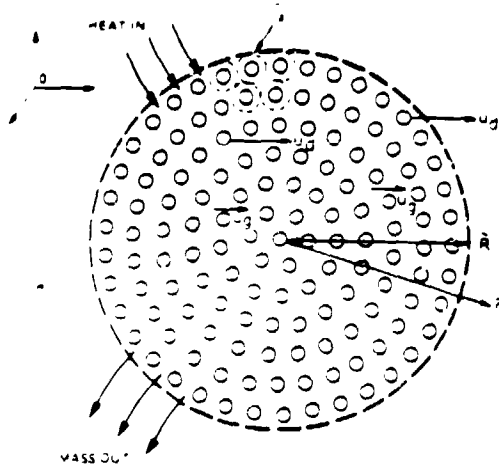


FIG. 1 Sketch of the physical situation modeled

model of convective drop evaporation given by ref. [2]. In that model the cluster of drops was adiabatically insulated from the surroundings and the drops were moving together as a rigid entity through the flow. As a result, the gas pressure inside the cluster varied during evaporation. In contrast, in the present model there is mass and energy exchange across the surface of the cluster and drops move with respect to each other. If they move away from each other, then expansion occurs; if they move towards each other than contraction occurs. Thus, in this new configuration the drop number density becomes a dependent variable whereas the pressure becomes a constant.

The main assumptions regarding the liquid and gas phases have been described in detail elsewhere [3] and thus will not be discussed here. Similar to the study of ref. [3], in the present study each drop is considered surrounded by a sphere of influence the radius, a , of which is the half distance between the centers of two adjacent drops. The ensemble of these spheres of influence and the space between them constitutes the cluster volume. However, whereas in ref. [2] the value of the radius of the sphere of influence was a constant, here it is a variable with time. Moreover, following a previous study [2], the present formulation has three components: (a) the description of mass, species and enthalpy conservation inside the sphere of influence of each droplet; (b) the description of mass, species and enthalpy conservation in the cluster volume; and (c) the description of convective effects using differential equations expressing momentum conservation for the gases and the drops. The present description of convective effects is unchanged from ref. [2]. However, since the assumption of constant gas density inside each sphere of influence [3] is no longer valid, the solution of the convective diffusive equations inside each sphere of influence changes from its simple expression [4] to

$$\Gamma(v) = C_1 + C_2 \exp \left[C(\rho_g D)^{-1} \int_0^R \frac{dv}{(\rho_g D)^{1/2}} \right] \quad (1)$$

where C_1 and C_2 are integration constants. Now since $Le_g = 1$, $\rho_g D = \mu / Pr$ and using the classical expression

$$\mu = \mu_{\infty} \theta_g^{0.67} \quad (2)$$

with the assumption $Pr = 0.8$ one obtains the following solution for θ_g

$$\theta_g(v) = C_{1g} + C_{2g} \exp \left[C(\theta_g^{1/2})^{-1} \int_0^R \frac{dv}{v^{1/2}} \right] \quad (3)$$

where C_{1g} and C_{2g} are functions of θ_{g0} and $\theta_{g\infty}$. Since following the Schvab-Zeldovich approach Y is a linear function of θ once θ is known so are the various Y 's in terms of v , Y_1 and Y_2 .

The derivation of equations (1)–(3) is the only novelty here in the treatment of the conservation laws inside the sphere of influence when compared with the formulation of ref. [2]. Both boundary conditions and evaporation law at the surface of the drops are the same as in ref. [2]. Moreover, the energy conservation for the liquid drops is also the same as in ref. [2] in that it considers the liquid temperature as being transient and a function of the radial position.

Note that the right-hand side of equation (3) is not analytically integrable and $\theta(v)$ can no longer be simply expressed as a function of v as in ref. [4]. This is due to the relaxation of the assumption that $\rho_g D$ is a constant. With this new formulation the equations must be solved numerically, unless some approximation is made in order to evaluate

$$Z(v) = (\theta_g^{1/2})^{-1} \int_0^R \frac{dv}{v^{1/2}} \quad (4)$$

A convenient way to evaluate $Z(v)$ is to use the weak evaporation, constant viscosity limit solution

$$\theta_g = \theta_1 + \theta_2 R_1^{-1} \quad (5)$$

and to perform the integration analytically. This approximation preserves both the concavity of the actual temperature and its boundary values at $r = R_1$ and R_2 and therefore is expected to fit well within the present model which takes a qualitative approach to modeling rather than a quantitative approach. This approximation is also used elsewhere [5]. The qualitative approach used here is specifically concerned with global effects and does not attempt to describe accurately spacial dependence of the dependent variables. Moreover, the present formulation is qualitatively accurate only when the total number of drops, N , is much larger than unity.

To complete the description of this formulation, the following is discussed below: (1) transfer of mass, species and enthalpy from the cluster to the external gas phase; (2) the behavior of the external gas phase and transport of mass, species and enthalpy to the cluster; and (3) the conservation equations for the entire cluster.

(1) *Transfer from the cluster to the external gas phase*

The challenge here is to describe in a simple way the mass, species and energy transfer from a cluster with a moving boundary using a model that does not discriminate between the various drops and their associated surrounding gas phase in the \bar{r} -direction (although nonuniformities in r are taken into account).

The global unsteady continuity equation inside the sphere of influence yields

$$\frac{d}{dt} \left[4\pi \int_R^{\infty} \rho_g r^2 dr \right] = 4\pi R^2 (\rho_g v)_s - 4\pi R^2 \frac{dR}{dt} \rho_g - 4\pi a^2 (\rho_g v)_a - 4\pi a^2 \frac{da}{dt} \rho_g \quad (6)$$

Since $(dR/dt) \ll (v)_s$

$$\frac{d}{dt} \left[4\pi \int_R^{\infty} \rho_g r^2 dr \right] = m - \dot{m}_{\text{loss}} \quad (7)$$

where

$$\dot{m}_{\text{loss}} = 4\pi a^2 \left[(\rho_g v)_s - \rho_g \frac{da}{dt} \right] \quad (8)$$

Two physical limits can occur

(a) The strictly steady situation where

$$4\pi R^2 (\rho_g v)_s = 4\pi a^2 (\rho_g v)_a \quad (9)$$

and according to equation (8) one obtains

$$\dot{m}_{\text{loss}} = m - 4\pi a^2 \frac{da}{dt} \rho_g \quad (10)$$

In this limit maximum new vapor passes through the sphere of influence and escapes to ambient. Then

$$(v)_a = \frac{m}{4\pi a^2 \rho_g}$$

(b) The limit where all new vapor is trapped into the sphere of influence as its surface moves. Then

$$\dot{m}_{\text{loss}} = 0 \quad (11)$$

and

$$(v)_a = \frac{da}{dt} \quad (12)$$

The physical reality is somewhat in between these two limits. We thus define a 'trapping factor'

$$W = m_s / (m_s + m_d) \quad (13)$$

and model

$$(v)_a = (1 - W) \frac{m}{4\pi a^2 \rho_g} + W \frac{da}{dt} \quad (14)$$

Thus this expression gives the velocity of the gases at the edge of the sphere of influence in the general case and also satisfies the above two limits because: (i) in the dilute limit $m_d \ll m_s$ and $W \rightarrow 1$, (ii) in the strong

evaporation, strictly steady, limit $W \rightarrow 0$ because $m_s \ll m_d$.

Since in this model there is no distinction between the surface of the cluster and surface of the spheres of influence the mass and enthalpy loss from the cluster are respectively \dot{m}_{loss} and $\dot{m}_{\text{loss}} h_{g,s}$. The effect of the convective flow on drop evaporation is contained in m which is the solution of the purely diffusive evaporation case multiplied by a corrective factor as described in ref. [2].

(2) *The behavior of the gas phase external to the cluster and transport to the cluster*

In order to be consistent with the treatment of convective drop evaporation of ref. [2], which is still preserved here, where convective effects are considered as a correction to diffusive evaporation, the external gas phase is first considered to have a purely diffusive behavior and Y and θ satisfy

$$\frac{1}{\bar{r}^2} \frac{d}{d\bar{r}} \left(\bar{r}^2 \frac{d\Gamma}{d\bar{r}} \right) = 0 \quad (15)$$

The solution of this equation is

$$\Gamma(\bar{r}) = (\Gamma_s - \Gamma_a) \frac{\bar{R}}{\bar{r}} + \Gamma_a \quad (16)$$

assuming continuity for Γ at $\bar{r} = \bar{R}$. Thus

$$-\rho_g \left. \frac{d\theta}{d\bar{r}} \right|_R = \rho_g (v_s - v_a) \frac{1}{\bar{R}} \quad (17)$$

$$-\rho_g D \left. \frac{dY_i}{d\bar{r}} \right|_R = \rho_g D (Y_i^s - Y_i^a) \frac{1}{\bar{R}} \quad (18)$$

Similarly to the description of convective effects of ref. [2], these are seen as a contribution both from the individual droplet and the entire cluster.

The contribution to heat transfer from the individual drops is due to the cluster 'porosity'. Consistent with the present homogeneous description for the cluster in the \bar{r} -direction this contribution for heat, species and mass is modeled as

$$E_s = (\rho_g^s h_g^s - \rho_{g,s} h_{g,s}) u_s A_s \quad (19)$$

$$\dot{M}_{i,s} = (\rho_g^s Y_i^s - \rho_{g,s} Y_{i,s}) u_s A_s \quad (20)$$

$$\dot{M} = (\rho_g^s - \rho_{g,s}) u_s A_s \quad (21)$$

The heat transfer to the entire cluster is highly dependent upon turbulent transfer between the surroundings and the cluster. Because of this, it is very important to understand how the history of turbulence with respect to that of evaporation influences the behavior of the cluster. For this reason, two turbulence models are considered and compared here. Since in our calculations the coordinate system is fixed with the state of the gases at $t = 0$, $u_g^s = 0$ and thus in the first model the drops do not act initially as an entity, but rather as individuals and turbulence builds up with time if the cluster 'porosity' diminishes significantly. In this model the rate of heat and species

transfer integrated over the entire surface of the cluster is

$$E_{1,1} = 4\pi \frac{u_g}{C_{\tau}} L_{bn} Nu_c \frac{u_g}{u_d} \bar{R}(\theta_g^* - \theta_{gs}) \quad (22)$$

$$M_{1,1} = 4\pi(\rho_g D)^2 Sh_c \frac{u_g}{u_d} \bar{R}(Y^* - Y_{gs}) \quad (23)$$

Under the assumption of similarity between heat and mass transfer $Sh_c = Nu_c$. In the computations further presented here the value of Nu_c was taken to be that for flows around a sphere up through the turbulent range [6]

$$Nu_c = 1 + 0.19 Pr^{1/4} Re_c^{1/2} \quad (24)$$

where Re_c is based upon the length scale $\{4\pi(u_g u_d)/\pi\}^{1/2}$ and velocity u_d [2]. The quantity $A_c(u_g u_d)$ is an effective cluster area which was found to be important in determining the drag due to the surface force on the cluster as a result of its motion through the gas [2]. The ratio $u_g u_d$ is in fact equal to the non-slip displacement gas flow divided by the total gas flux

The second turbulence model used here is different from the first one in that the turbulent part of the Nusselt number is changed in such a manner as to be consistent with the cluster surroundings being initially turbulent. This is done by making the turbulent contribution of Nu_c proportional to u_d rather than u_g . In this second formulation

$$E_{1,1} = 4\pi \frac{u_g}{C_{\tau}} L_{bn} \left(\frac{u_g}{u_d} + \frac{C_{\tau}}{2} Pr Re_{\tau} \right) \bar{R}(\theta_g^* - \theta_{gs}) \quad (25)$$

$$M_{1,1} = 4\pi(\rho_g D)^2 \left(\frac{u_g}{u_d} + \frac{C_{\tau}}{2} Pr Re_{\tau} \right) \bar{R}(Y^* - Y_{gs}) \quad (26)$$

where

$$Re_{\tau} = 2\rho_{gs} \bar{R} u_d / \mu_g^* \quad (27)$$

$$C_{\tau} \equiv l_{\tau} / \bar{R} \quad (28)$$

and C_{τ} is a constant

(3) The conservation equations for the entire cluster

Under the quasi-steady assumption these equations are as follows.

(a) *Conservation of total mass of liquid fuel.* This states that the mass of liquid fuel at time t is equal to the initial fuel mass minus the mass evaporated from the drops. Once nondimensionalized the equation becomes

$$\varepsilon = 1 - R_1^3 \quad (29)$$

(b) *Conservation of total gaseous mass inside the cluster.* The gaseous mass at time t is the sum of the initial gas mass, the mass evaporated from the fuel, and the mass entering the cluster of drops minus the

mass loss from the cluster to the surroundings. This is expressed as

$$\frac{dm_g}{dt} = Nm - Nm_{out} + (\rho_g - \rho_{gs}) u_c A_c \quad (30)$$

where

$$m_g = V \int_0^1 4\pi r^2 \rho_g(r) dr + \left(V - \frac{4\pi a^3}{3} \right) \rho_{gs} \quad (31)$$

and m_{out} is given by equations (8) and (14). To calculate the density integral, the equation of state is invoked to obtain

$$\int_0^1 \rho_g(r) r^2 dr = \frac{\rho_g^* R_1^3 C_{\tau}}{R_1^3 L_{bn}} R_1^3 \int_0^1 \frac{v^2 dv}{\theta_g(\sigma Y_{F,v} + \gamma)} \quad (32)$$

where

$$Y_{F,v} + Y_{F,g} = 1 \quad (33)$$

was used. The form of equation (31) becomes integrable when θ_g is given by the approximation of equation (5) and $Y_{F,v}$ is obtained in a similar way. In this manner m_g can be approximated by an analytic, non-linear function G

$$m_g = G(R_1, R_1, n, \theta_{gs}, \theta_{gs}, Y_{F,v}, Y_{F,g}) \quad (34)$$

(c) *Conservation of fuel vapor mass inside the cluster.* The time change of fuel vapor mass inside the cluster is due to mass addition from the evaporated drops, mass addition from fuel transported from the external gas phase to the cluster and mass depletion due to fuel escaping from the cluster to the external gas phase. This is expressed by

$$\frac{dm_{F,v}}{dt} = Nm + M_{F1} + M_{F2} - Nm_{out} Y_{F,v} \quad (35)$$

where

$$m_{F,v} = V \int_0^1 \rho_g Y_{F,v} 4\pi r^2 dr + \left(V - \frac{4\pi a^3}{3} \right) \rho_{gs} Y_{F,v} \quad (36)$$

and m_{out} , M_{F1} and M_{F2} are given, respectively, by equations (8), (14), (20), and (23) or (26). Now

$$\int_0^1 \rho_g Y_{F,v} r^2 dr = \frac{\rho_g^* R_1^3 C_{\tau}}{R_1^3 L_{bn}} \int_0^1 \frac{v^2 Y_{F,v} dv}{\theta_g(\sigma Y_{F,v} + \gamma)} \quad (37)$$

and using again the approximation of equation (5) we can approximate $m_{F,v}$ by an analytic, non-linear function F

$$m_{F,v} = F(R_1, R_1, n, \theta_{gs}, \theta_{gs}, Y_{F,v}, Y_{F,g}) \quad (38)$$

(d) *Conservation of total enthalpy inside the cluster.* The change of total enthalpy inside the cluster is due to enthalpy being transferred from the external gas phase to the cluster and enthalpy escaping with the gaseous outflow from the cluster. In all the calculations made here it was assumed that initially the

temperature of the external gas phase is much higher than that of the gases inside the cluster, so that heat conduction from the gases inside the cluster to the external gas phase is excluded. Thus the enthalpy equation is

$$\frac{dH}{dt} = E - E_{\text{ev}} - \lambda m_{\text{ev}} n_{\text{gs}} \quad (39)$$

where $n = E$ and E_{ev} are respectively given by equations (30) and (22) or (25) and

$$H = \lambda \int_0^{r_0} 4\pi r^2 \rho_g dr + \lambda \int_0^{r_0} 4\pi r^2 n_{\text{gs}} dr \\ = \left(1 - \frac{4\pi a}{3} \lambda\right) \rho_{\text{gs}} \rho_{\text{gs}} \quad (40)$$

with

$$n_{\text{gs}} = n_{\text{gs}}^0 + C_{\text{gs}}(T_{\text{gs}} - T_{\text{ev}}) \quad (41)$$

$$n = n_{\text{gs}} - C_{\text{gs}}(T - T_{\text{ev}}) \quad (42)$$

$$L \equiv h_{\text{gs}} - n_{\text{gs}} \quad (43)$$

With the above definitions H becomes

$$H = \lambda \rho_g 4\pi \left[\frac{R}{3} n^0 + C_{\text{gs}} \int_0^{r_0} (T - T_{\text{ev}}) r^2 dr \right] \\ - 4\pi \lambda \left[(h^0 - C_{\text{gs}} T_{\text{ev}}) \int_0^{r_0} \rho_g r^2 dr + C_{\text{gs}} \int_0^{r_0} r^2 T_{\text{gs}} dr \right] \\ = \left(1 - \frac{4\pi a}{3} \lambda\right) [h^0 + C_{\text{gs}}(T_{\text{gs}} - T_{\text{ev}})] \rho_{\text{gs}} \quad (44)$$

The first integral in equation (44) can be easily performed since, as it will be explained in the next section, $T(r)$ is solved as a series solution from the energy conservation equation inside each drop, and the two last integrals in equation (44) are calculated using the approximation previously described to calculate θ_{gs} from equation (3). Thus, one approximates H by an analytic, non-linear function

$$H = \mathcal{H}(R_1, R_2, n, \theta_{\text{gs}}, \theta_{\text{gs}}, Y_{\text{F},1}, Y_{\text{F},2}) \quad (45)$$

One can eliminate n as a dependent variable from the above equation by noting that for tightly packed spheres [7]

$$n = 0.74 \frac{3}{4\pi a^3} \quad (46)$$

Thus the dependent variables which are the unknowns in this problem are ε , R_1 , R_2 , θ_{gs} , θ_{gs} , $Y_{\text{F},1}$, $Y_{\text{F},2}$, C , u_1 , u_2 . The equations which are solved to find the solution for these ten variables are given in non-dimensional form in the Appendix

3 NUMERICAL PROCEDURES

The integrated drop energy equation is

$$\frac{d}{dt} \left(4\pi \rho_g \int_0^{r_0} n r^2 dr \right) = 4\pi R^2 \left(\frac{dT}{dr} \right)_{r=r_0} - m h_{\text{ev}} \quad (47)$$

The temperature distribution $T(r)$ in the drop is obtained by solution of the drop heat conduction equation by means of expansion in a small parameter inversely proportional to r_0 [3]. This results in the formation of two differential equations in time for functional parameters, which in conjunction with the surface gradient expression (A7) in the Appendix, determine the temperature distribution. The particulars are given in ref. [3]. The above equation is combined with the global energy equation, equation (39), to obtain an enthalpy equation for the gas phase

$$\frac{d}{dt} \left[(4\pi R^2 \rho_{\text{gs}}) \lambda h - \left(1 - \frac{4\pi a}{3} \lambda\right) \rho_{\text{gs}} L \right] \\ = \lambda m \left[\frac{n_{\text{gs}} - n_{\text{gs}}^0 \exp(CZ(R))}{1 - \exp(CZ(R))} \right] \frac{E}{L_{\text{ev}}} \\ + (\rho_{\text{gs}} n_{\text{gs}}^0 - \rho_{\text{gs}} n_{\text{gs}}) m_{\text{ev}} = \lambda m_{\text{ev}} n_{\text{gs}} \quad (48)$$

where the function h is given by equation (A3).

Since there is a linear relationship between the Y 's and temperature, equations (30), (35) and (39) are not independent. The following holds

$$Y_{\text{F},1}(\theta_{\text{gs}} - \theta_{\text{gs}}^0) = Y_{\text{F},1} \theta_{\text{gs}} - Y_{\text{F},1} \theta_{\text{gs}}^0 = (Y_{\text{F},1} - Y_{\text{F},1}^0) \theta_{\text{gs}}^0 \quad (49)$$

Variables and determining equations are as follows. θ_{gs} (or θ_{gs}) is obtained from the drop heat conduction equation, m_{ev} from equation (30), h from equation (48), $Y_{\text{F},1}$ and $Y_{\text{F},2}$ from equations (49) and (A8), C from equation (A5), R_1 from equation (A6), u_1 from equation (A9), and u_2 from equation (A10). Both m_{ev} and h are known functions of the dependent variables. m_{ev} (or function q) is considered as determining n_{gs} and h determines R_2 . (These functions vary most strongly with this particular variable selection.) The variables C , $Y_{\text{F},1}$, $Y_{\text{F},2}$, R_1 and θ_{gs} are governed by a non-linear set of algebraic equations, the other variables are determined directly from differential equations.

Eliminating $Y_{\text{F},2}$ from equations (49) and (A8) results in an equation relating $Y_{\text{F},1}$ to C . The evaporation equation, equation (A5), also relates these two variables. These two equations are iterated in an inner loop for the variables, considering all other variables fixed. In an outer loop, functions q and h are iterated for R_2 and θ_{gs} . This nested loop procedure allows for a relatively efficient solution of the algebraic equations at each time step of the differential equation integration. The differential equations are integrated using a standard ODE integrator, GEAR, with a local error tolerance of 10^{-4} .

The model equations depend on terms proportional

to dR_1/dt . Since R_1 is formed algebraically, this derivative needs to be estimated. The procedure for calculating this derivative is as follows. Define

$$\pi \equiv \bar{n} + \frac{1-0.74}{3 \times 0.74} \rho_{\text{gas}} \theta_{\text{gas}},$$

this is the unknown in equation (48). On the other hand $\pi \equiv R_1/J$, where J is a relatively weak varying function. Thus

$$\frac{dR_1}{dt} \approx \frac{d\pi}{dt} = \frac{dJ}{dt} \left(\frac{\pi}{J} \right),$$

where $d\pi/dt$ is known and dJ/dt is approximated by a first-order backward finite difference

4 RESULTS AND DISCUSSION

The results presented below were obtained from calculations performed for liquid *n*-decane drops evaporating in initially unstirred air. The thermophysical constants for *n*-decane that were used here are the same as those of ref. [3]. The interest here is on how turbulence can affect evaporation of drops in clusters and the behavior of the cluster as an entity.

Figure 2 shows a non-dimensional evaporation time vs the initial air-fuel mass ratio for three situations. The baseline case is that of the first turbulence model and $u_0 = 500 \text{ cm s}^{-1}$. The two cases are chosen such as to study the influence upon evaporation of both the initial relative velocity and the turbulence history. The plots show that in the very dense spray regime the initial relative velocity is not a good control parameter. However, by changing the history of turbulence with respect to that of evaporation, one can obtain now complete evaporation in situations where the gases in the cluster saturated before complete evaporation when the other turbulence model was used. The reason for this is that as the drops heat up, the gases cool off, if the exchange of mass and heat between the cluster and the surroundings is poor, the gases in the cluster will saturate and the drops will eventually be at the same temperature as the gases thereby stopping evaporation. On the other hand if fresh gases and energy can be brought inside the cluster from the surroundings, evaporation will proceed. These processes are most important during the initial part of evaporation, when the rate of mass loss from the drop is high. If turbulence is not present at that time, evaporation will eventually stop as shown by the baseline case, an increase in the initial relative velocity does not affect the outcome. Since turbulence model 2 portrays a case where turbulence is present initially, the exchange of mass and heat between the gases inside and outside the cluster occurs at the appropriate time, and evaporation can be completed.

For smaller ϕ^0 , there is a regime where both the turbulence history and u_0^0 can control evaporation. By increasing u_0^0 one can now obtain complete evaporation before saturation with the same turbulence history by keeping u_0^0 constant and changing the

turbulence history one obtains the same outcome, however, the evaporation time is now considerably shorter.

When ϕ^0 increases even further, and the regime of the slightly rich and further that of the lean mixtures is encountered, neither turbulence nor the initial relative velocity are good control parameters. In fact as π^0 decreases to a few drops/cm³ any one of the three models gives exactly the same result and all three models reach the same asymptote. The reason for this is that as the initial density of drops in the cluster decreases, the interstitial gas between the drops cools less during evaporation, and mass and heat transfer from the surroundings plays a decreasingly important role. In the same manner, as the initial density of drops in the cluster decreases, the drops reach the asymptote corresponding to the limit of the convective evaporation of 1 drop/cm³ [2].

These conclusions are substantiated by the results plotted in Figs. 3–5. Depicted in Fig. 3 are both the gas temperature drop and the gas density rise as a function of ϕ^0 . For very lean mixtures and dilute clusters there is no temperature drop since the heat going to the drops to support evaporation is minimal compared to the total heat available in the gases of the cluster. As ϕ^0 decreases and the regime of rich mixtures is reached, a temperature drop and a corresponding density rise are encountered. With a further decrease in ϕ^0 one can observe the influence of turbulent heat transfer from the surroundings in keeping the temperature at a level where it can support evaporation. In contrast, when turbulence is not present initially and instead develops with time the temperature drop is more substantial and eventually reaches the point where it can no longer support evaporation.

The reason that the initial history of turbulence is so important in controlling evaporation is illustrated in Fig. 4. Not only is m largest when the drops are larger [2], but also the loss fraction is largest initially. By the time $R_1 = 0.5$, the loss fraction is negligible. The oscillations in m_{loss}/m observed in the figure inset may be due to the inaccurate numerical evaluation of du/dt using a two step backward scheme. Since these oscillations occur in a region where $|m_{\text{loss}}/m| \ll 1$, no further effort has been made to improve the accuracy.

The loss fraction accounts only for the mass lost from the system as a result of the motion of the cluster surface, but does not account for the gain that occurs when mass is brought into the cluster by turbulent transfer from the surroundings. As a result, its value as a diagnostic is limited to indicating the relative importance of gaseous mass lost from the cluster to gaseous mass gained inside the cluster through evaporation. In contrast, the global mass conservation equation for the cluster does account appropriately for mass addition due to turbulent transport.

The variation of the final position of the cluster surface with respect to its initial position is shown vs ϕ^0 in Fig. 5. As expected, for lean mixtures and dilute

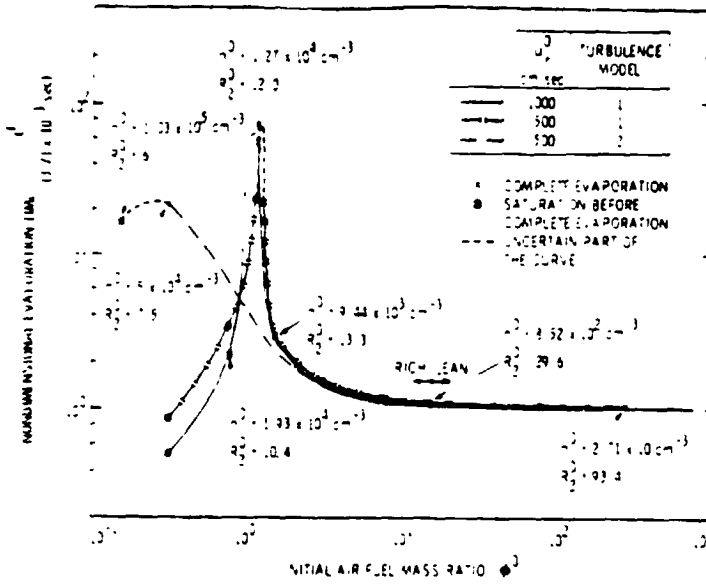


FIG. 2. Variation of τ , non-dimensional evaporation time with the initial air fuel mass ratio $T_{\infty}^0 = 1000$ K, $T_p^0 = 350$ K, $Y_{p,\infty}^0 = 0$, $R^0 = 10$ cm, $R^0 = 2 \times 10^{-1}$ cm.

sprays, when there is not much gaseous mass added through evaporation, the cluster maintains its original size. As ϕ^0 decreases the cluster shrinks in size due to internal cooling. However, this shrinkage is smaller for turbulence model 2, as the final temperature was also observed to be higher. This contraction is consistent with the observed decrease in pressure inside the cluster when evaporation occurred in a cluster that was adiabatically insulated from the surroundings [2]. This pressure drop was larger with decreasing ϕ^0 , which means that despite the very large increase in density in the very rich cases, the cooling effect was dominant.

If the mass lost from the cluster is integrated in time, converted into a volume by dividing by ρ_g^* , and finally nondimensionalized by the initial volume of

the cluster one finds that at fixed R , this value is larger for smaller ϕ^0 and at fixed ϕ^0 it is larger for turbulence model 1. When this value is added, at fixed R , to the non-dimensionalized cluster volume, one finds that for a given ϕ^0 the sum is larger for turbulent model 2. In all cases this sum is consistently smaller than unity and increases with the value of ϕ^0 approaching unity for large values of ϕ^0 . These results confirm the fact that even when one accounts for the mass escaping from the cluster, contraction due to cooling of the gases occurs. With turbulence model 1 more of the gas escapes to the surroundings and with turbulence model 2 less of a contraction occurs.

It is worth mentioning that the differences observed between the behavior of the clusters when the two turbulence models are considered is not due to the

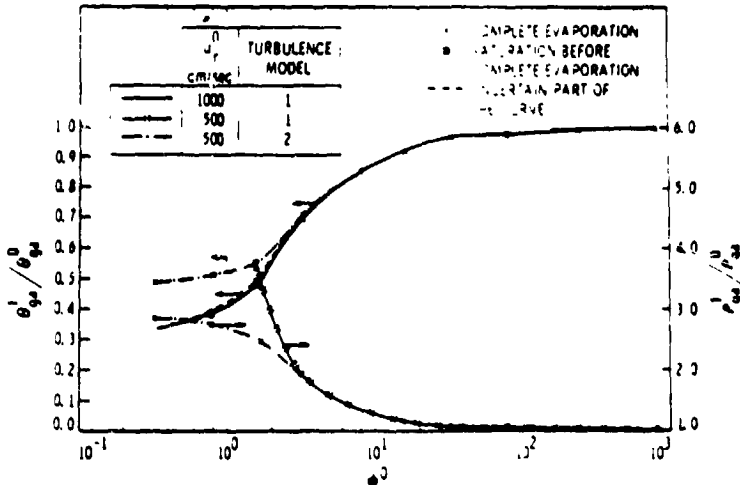


FIG. 3. Variation of θ_p^0 , θ_g^0 and ρ_p^0/ρ_g^0 with the initial air fuel mass ratio $T_{\infty}^0 = 1000$ K, $T_p^0 = 350$ K, $Y_{p,\infty}^0 = 0$, $R^0 = 10$ cm, $R^0 = 2 \times 10^{-1}$ cm.

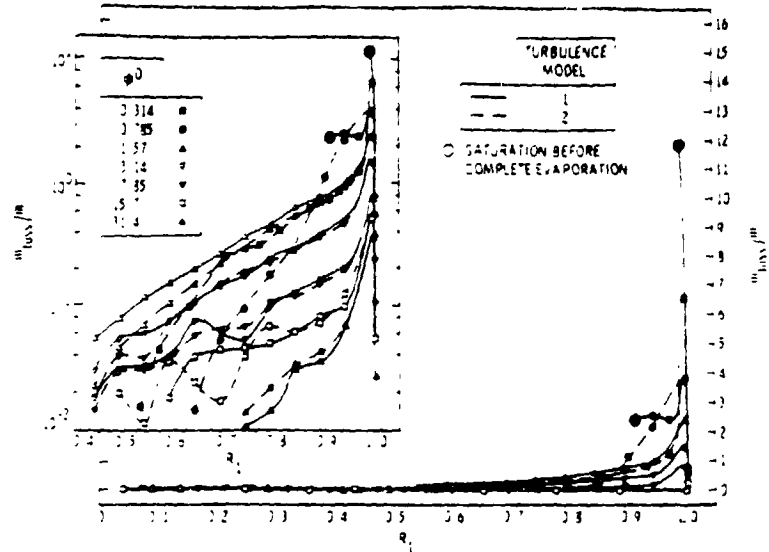


FIG. 4 Loss fraction vs R_i for various initial air/fuel mass ratios. $T_p^0 = 1000$ K, $T_\infty^0 = 350$ K, $Y_{F,\infty}^0 = 0$, $\bar{R}^0 = 10$ cm, $R^0 = 2 \times 10^{-1}$ cm, $u^0 = 500$ cm s $^{-1}$

fact that the drops evaporate in different regimes [2] (diffusive, convective-diffusive or convective) but rather due to the different exchange processes between the clusters and their surroundings. Figure 5 illustrates the fact that the initial penetration distance, which indicates the evaporation regime [2], varies only with u^0 and ϕ^0 and not with the turbulence model. At fixed ϕ^0 , as R_i decreases the penetration ratios continue to be extremely close for the two turbulence models.

The effect of varying the cluster size can be seen in Fig. 6 where a non-dimensional evaporation time is plotted vs the initial size of the cluster for both turbulence models. For a stoichiometric mixture neither the initial size of the cluster nor the turbulence model influence very much the evaporation time; however, there is a slight tendency to a larger evaporation time

with increased initial size. This effect is very substantial for rich mixtures and is observed for both turbulence models. There are several reasons for this. First, since u^0 is fixed, as the cluster becomes smaller, the initial penetration ratio is larger and the drops evaporate in a regime which changes from diffusive to predominantly convective thus reducing the evaporation time. This is illustrated in Fig. 7 where $(L_p/\bar{R})^0$ is plotted vs \bar{R}^0 . In contrast, for stoichiometric mixtures the evaporation regime is convective-diffusive to convective and as it has been pointed out previously [2], convective effects always dominate diffusive effects thus determining the evaporation time. Second, although at fixed ϕ^0 , n^0 is the same for all sizes of clusters, N decreases with \bar{R}^0 . This leads to a more pronounced interaction with the surroundings and thus faster evaporation.

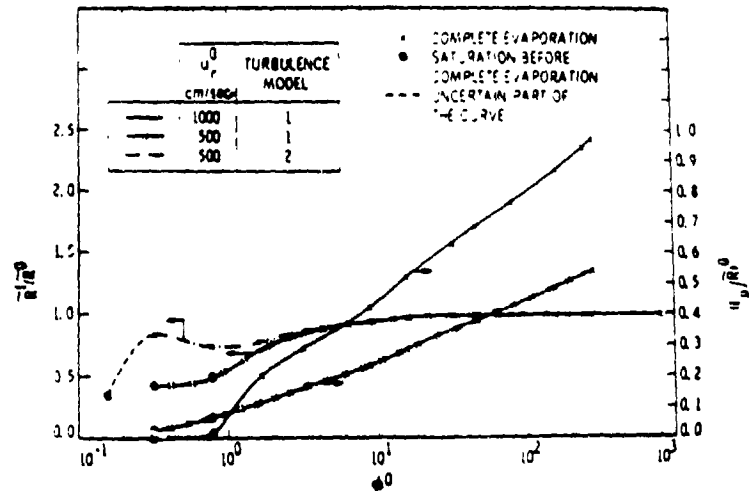


FIG. 5 Initial penetration ratio and final position of the cluster surface vs the initial air/fuel mass ratio. $T_p^0 = 1000$ K, $T_\infty^0 = 350$ K, $Y_{F,\infty}^0 = 0$, $\bar{R}^0 = 10$ cm, $R^0 = 2 \times 10^{-1}$ cm.

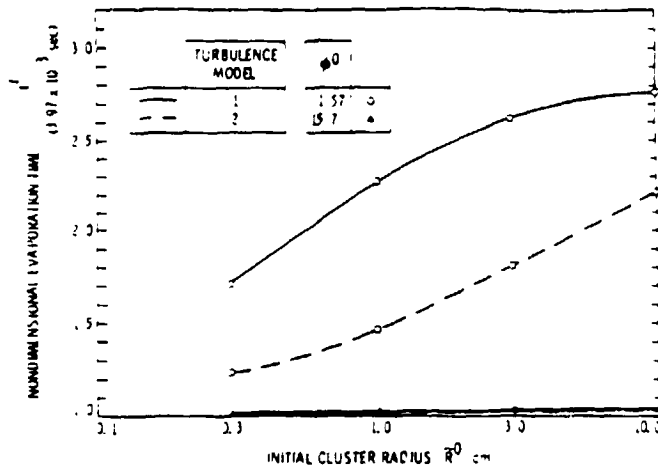


FIG. 6. Variation of a non-dimensional evaporation time with the initial radius of the cluster. $T_g = 1000$ K, $T_w = 350$ K, $Y_{F,w}^0 = 0$, $R^0 = 2 \times 10^{-3}$ cm, $u_g = 500$ cm s $^{-1}$.

The total effect upon the final cluster size is presented in Fig. 7. In all cases larger clusters contract more, relative to their initial size, than do smaller clusters due again to the cooling effect discussed above. A smaller number of drops in a cluster results in less cooling of the gas phase and complete evaporation and faster evaporation.

Similarly to the discussion pertinent to Fig. 2, turbulence model 2 predicts shorter evaporation times for dense clusters and the same evaporation time for dilute clusters as does turbulence model 1. The trends regarding \bar{R}/\bar{R}^0 are also similar.

In order to gain a better understanding about the behavior of the cluster we display in Figs. 8 and 9 the history of \bar{R}/\bar{R}^0 . Since there is a certain uncertainty about the time taken to evaporate, and since it depends strongly upon the evaporation model, in order to partially eliminate this uncertainty, the plots are made vs R . Figure 8 represents the situation for a rich mixture, whereas Fig. 9 represents the situation for a stoichiometric mixture. The striking feature in Fig. 8 is the initial drop in \bar{R}/\bar{R}^0 which, as discussed above, is due to the cooling of the gas phase and the continual heating of the drops. Following this decrease in \bar{R}/\bar{R}^0 , a minimum in this value is reached, after which there ensues a recovery. This recovery is due to the unvitiated (by fuel) hot gas brought in through turbulent transport from the gas phase surrounding the cluster. As expected, turbulence model 2 offers more possibilities for recovery. As the cluster is smaller and the number of drops decreases, there is less of a drop in \bar{R}/\bar{R}^0 , the minimum \bar{R}/\bar{R}^0 occurs earlier with respect to R , and the final value of \bar{R}/\bar{R}^0 is closer to unity. Figure 9 shows that in contrast to the rich mixtures, for stoichiometric mixtures there is no minimum in \bar{R}/\bar{R}^0 ; the size of the cluster continuously decreases with R . However, there is less of a cluster shrinkage due to the fact that there is less mass in the cluster, less cooling and less mass loss.

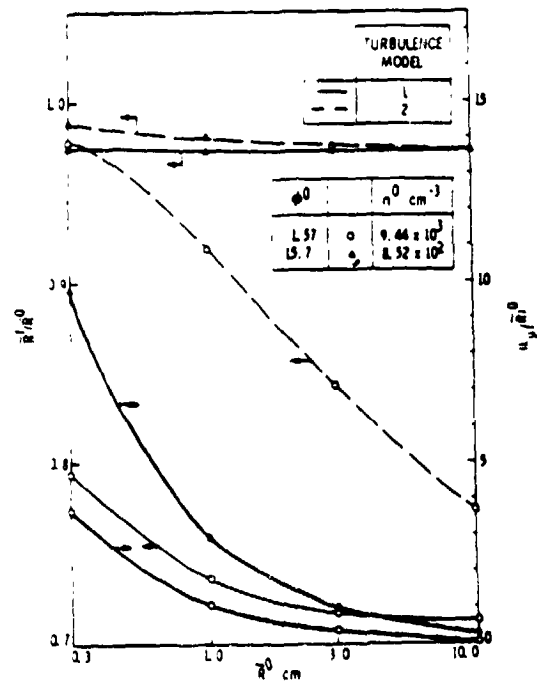


FIG. 7. Initial penetration ratio and final position of the cluster surface vs the initial radius of the cluster: $T_g^0 = 1000$ K, $T_w^0 = 350$ K, $Y_{F,w}^0 = 0$, $R^0 = 2 \times 10^{-3}$ cm, $u_g^0 = 500$ cm s $^{-1}$.

The practical implications of these results with regard to optimization of evaporation is straightforward. Turbulence should be induced in the gas in which the spray is injected prior to or at the same time as injection. Turbulence can help to evaporate the drops of the spray through two processes. First it can break the spray into clusters and the smaller the cluster, the shorter the evaporation time. Second, it brings in unvitiated (by fuel) hot gas from the surrounding of the clusters thereby enhancing and supporting evaporation. Moreover, the results show that evaporation of drops in dense clusters can be con-

mining the outcome of evaporation. Between these regimes of very dense and dilute clusters there exists a regime where both the history of turbulence and the initial relative velocity between drops and gases can be important control parameters.

Furthermore, the results show that the evaporation time of a dilute cluster cannot be decreased by reducing its initial size while keeping the initial air fuel mass ratio constant. In contrast, for dense clusters, the evaporation time decreases with the initial size of the cluster at the same initial air fuel mass ratio. Moreover, by having turbulence present initially, rather than letting it build up, the evaporation time of the cluster can be further decreased.

Thus gas phase turbulence can be important in reducing the evaporation time in two ways. First, turbulence breaks up the spray in small size clusters right at the exit of the atomizer, where the spray is dense. Second, turbulence acts as a vehicle for transporting mass, species and heat to the cluster, thus supporting evaporation. The above results have shown that turbulence is a strong control parameter for dense clusters but it is not a control parameter for dilute clusters. This means that in order to influence evaporation in sprays one should install turbulence enhancement devices right at the exit of the atomizer where the spray is dense and not further down the length of the combustor where the spray has become dilute. Indeed it is well known empirically that this is true and the present results provide a theoretical justification for a well-known fact. However, it would be very desirable to have a set of experiments to compare with the predictions of the present theory. The present conclusions show that most of the sensitivity of our model and thus most of the control in an experiment can be expected in the dense-cluster regime. This makes a comparison so much more difficult because it is precisely in this regime that experiments are most difficult to perform because of the lack of resolution.

Acknowledgements—The research described in this paper was performed by the Jet Propulsion Laboratory, California Institute of Technology, and was supported by the Air Force Office of Scientific Research, Directorate of Aerospace Sciences, the Army Research Office, Engineering Sciences Division, and the U.S. Department of Energy, Office of Energy Utilization Research, Energy Conversion and Utilization Technologies Program, through interagency agreements with the National Aeronautics and Space Administration.

REFERENCES

1. N. A. Chigier, C. P. Mao and V. Oechel: Structure of air-assist atomizer spray, Paper 7-6A, CSS/WSS/Combustion Institute Spring Meeting, April (1985); also private communication.
2. J. Bellan and K. Harstad, The details of the convective evaporation of dense and dilute clusters of drops, *Int. J. Heat Mass Transfer* 30, 1083-1093 (1987).
3. J. Bellan and K. Harstad, Analysis of the convective evaporation of non dilute clusters of drops, *Int. J. Heat Mass Transfer* 30, 125-136 (1987).
4. J. Bellan and R. Cuffel, A theory of non dilute spray evaporation based upon multiple drop interactions, *Combustion Flame* 51, 55-67 (1983).
5. G. M. Hidy and J. R. Brock, *The Dynamics of Aero-colloidal Systems*, pp. 99-101 Pergamon Press, Oxford (1970).
6. E. R. C. Eckert and R. M. Drake, Jr., *Heat and Mass Transfer*, McGraw-Hill, New York (1959).
7. C. Kittel, *Introduction to Solid State Physics*, 3rd Edn Wiley, New York (1966).

APPENDIX

As explained in Section 3 θ is obtained as a function of r from the conduction equation. The ten equations that are solved for the ten dependent variables identified at the end of Section 2 are as shown below. Define

$$g(\theta_m, \theta_m, Y_{F,0}, Y_{F,\infty}, R_1, P_1) = \int_{R_1}^{R_0} \frac{1}{\eta_g(\sigma Y_{F,\infty} - 1)} dr \quad (A1)$$

$$f(\theta_m, \theta_m, Y_{F,0}, Y_{F,\infty}, R_1, R) = \int_{R_1}^{R_0} \frac{1}{\eta_g(\sigma Y_{F,\infty} - 1)} dr \quad (A2)$$

$$h(Y_{F,0}, Y_{F,\infty}, R_1, R) = \int_{R_1}^{R_0} \frac{1}{\sigma Y_{F,\infty}} dr \quad (A3)$$

where the integrations are performed using η_g and $Y_{F,\infty}$ as given by the approximation of equation (5).

The equations solved are as follows

$$(1) \quad \epsilon = 1 - R_1^3 \quad (A4)$$

$$(2) \quad C = -ZR_1^3 \frac{R_0^3}{4\pi(\rho_g D)^2} \left\{ (1/\text{atm}) \exp \left[\frac{C_g w_F}{R_g} \left(\frac{1}{\eta_m} - \frac{1}{\eta_{m,0}} \right) - \frac{\Delta C_g w_F}{R_g} \left(1 - \frac{\theta_m}{\theta_{m,0}} - \ln \frac{\theta_m}{\theta_{m,0}} \right) - Y_{F,\infty} \frac{P_1}{\sigma Y_{F,\infty}} \right] - Y_{F,\infty} \frac{P_1}{\sigma Y_{F,\infty}} \right\} \times \left(\frac{w_F C_g}{2\pi R_g L_m \theta_{m,0}} \right)^{-1} \quad (A5)$$

$$(3) \quad R_1 = \left[1 + 3 \frac{(\rho_g D)^2}{\rho_l R_0^3} \int_0^1 C dr \right]^{1/3} \quad (A6)$$

$$(4) \quad C = \frac{1}{-Z(R_1)} \ln \left\{ 1 + \frac{\theta_m - \theta_{m,0}}{\frac{L}{L_m} - \frac{R_1}{C} \frac{\lambda_1}{C_g(\rho_g D)^2} \left(\frac{\theta_m}{\theta_{m,0}} \right)} \right\} \quad (A7)$$

$$(5) \quad Y_{F,\infty} = 1 + (Y_{F,0} - 1) \exp(CZ(R_1)) \quad (A8)$$

$$(6) \quad m_d \frac{du_d}{dt} = -\frac{1}{2} \left[\sqrt{\rho_g A_d C_D} u_d^2 + \frac{3 \times 0.74}{4\pi R_1^3} \frac{m_d}{R_0^3} W u_d A_d C_{De} N \right] \quad (A9)$$

$$(7) \quad \frac{du_r}{dt} = -\frac{3 \times 0.74}{4\pi R_1^3} \frac{1}{R_0^3} \times \left\{ m u_r \rho_g + \frac{1}{2} \left[1 + \frac{4\pi R_1^3}{3 \times 0.74} \frac{R_0^3 \rho_g N}{m_d} \right] A_d C_D u_r^2 \right\} \quad (A10)$$

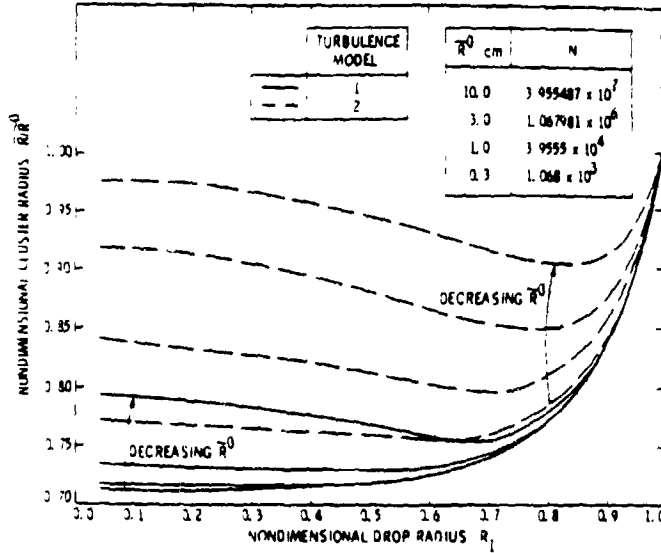


FIG. 8 Variation of the residual cluster radius with R_1 for different initial cluster radii for a dense cluster of drops: $T_{\infty}^0 = 1000$ K, $T_p^0 = 350$ K, $Y_{F,\infty}^0 = 0$, $R^0 = 2 \times 10^{-3}$ cm, $u^0 = 500$ cm s $^{-1}$, $\phi^0 = 1.57$ ($n^0 = 9.44 \times 10^3$ cm $^{-3}$, $R_1^0 = 13.3$).

trolled whereas when they are in a dilute configuration it cannot. This means that evaporation control should be envisaged near the injector in order to be truly effective, rather than further along the combustor.

5. SUMMARY AND CONCLUSIONS

The model presented above is one example of subgrid models that are needed to describe spray evaporation and combustion. As such, the predictions of the model pertain to the global behavior of clusters of drops rather than the detail of the behavior of each drop in the cluster and the difference in behavior between the drops belonging to the same cluster.

Despite the simplicity of the turbulence models used herein there are many important aspects that have been elucidated by the results obtained with the two models. First, in contrast to dilute clusters of drops, the evaporation of very dense clusters of drops is greatly affected by the initial level of turbulence in the surrounding gas. Not only is the evaporation time affected but also it is shown that by having turbulence initially present rather than letting it build with time, one can obtain complete evaporation before saturation in situations where otherwise saturation was obtained before complete evaporation. Thus, for dense sprays the transfer processes between the gases in the cluster and the surroundings are crucial in deter-

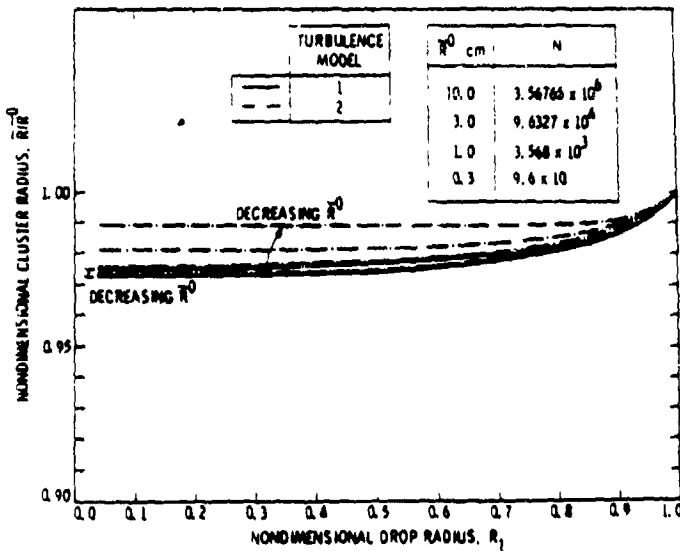


FIG. 9 Variation of the residual cluster radius with R_1 for different initial cluster radii for a dilute cluster of drops: $T_{\infty}^0 = 1000$ K, $T_p^0 = 350$ K, $Y_{F,\infty}^0 = 0$, $R^0 = 2 \times 10^{-3}$ cm, $u^0 = 500$ cm s $^{-1}$, $\phi^0 = 1.57$ ($n^0 = 8.52 \times 10^2$ cm $^{-3}$, $R_1^0 = 29.6$).

$$(8) \quad \frac{dm_1}{dt} = -VC \frac{m_1}{m_1 + m_2} - V \frac{m_2}{m_1 + m_2} \frac{1}{\rho_g^*} \frac{1}{\theta_{gs}(\sigma T_{F,2} + 1)} \quad \dot{m}_{F,1} = \frac{V}{\rho_g^*} \left[f(\theta_{gs}, \theta_{gs}, Y_{F,2}, Y_{F,1}, R_2, R_1) \right. \\ \left. + \frac{1-0.74}{0.74} \frac{R_2^3}{3} \frac{Y_{F,2}}{\theta_{gs}(\sigma Y_{F,2} + 1)} \right] \quad (A11)$$

where

$$m_1 = \frac{V}{\rho_g^*} \left[g(\theta_{gs}, \theta_{gs}, Y_{F,2}, Y_{F,1}, R_2, R_1) \right. \\ \left. + \frac{1-0.74}{0.74} \frac{R_2^3}{3} \frac{Y_{F,2}}{\theta_{gs}(\sigma Y_{F,2} + 1)} \right] \quad (A12)$$

$$(9) \quad \frac{dm_{F,1}}{dt} = -VC \left(1 - Y_{F,2} \frac{m_2}{m_1 + m_2} \right) \\ - \frac{V_{F,1}}{4\pi(\rho_g D)^2 R^2} - \frac{u_{F,1}}{4\pi D^2 R^2} \left[Y_{F,1} - \frac{1}{\rho_g^*} \frac{Y_{F,2}}{\theta_{gs}(\sigma Y_{F,2} + 1)} \right] \\ - \frac{V}{\rho_g^*} \frac{Y_{F,2}}{\theta_{gs}(\sigma Y_{F,2} + 1)} \frac{m_1}{m_1 + m_2} R_2 \frac{dR_2}{dt} \quad (A13)$$

where

$$(10) \quad \frac{d\bar{H}}{dt} = \frac{u_{F,1}}{4\pi R^2 D^2} \left[\frac{h^G}{L_{nn}} + \theta_{gs} - 1 + \frac{h^G}{\rho_g^* \theta_{gs}(\sigma Y_{F,2} + 1)} \right] \\ - \frac{E_1}{4\pi R^2 L_{nn}(\rho_g D)^2} - V \frac{m_2}{m_1 + m_2} \left(\frac{h^G}{L_{nn}} + \theta_{gs} - 1 \right) \\ + \left[C + \frac{1}{\theta_{gs}(\sigma Y_{F,2} + 1) \rho_g^*} R_2 \frac{dR_2}{dt} \right] \quad (A14)$$

where

$$\frac{R_2^3}{\rho_g^* C_{F,2} 4\pi R^2} V H = \rho_g \left[\frac{R_2^3}{3} \frac{h^G}{L_{nn}} + \frac{C_{F,1}}{C_{F,2}} \right] (11 - 1) \frac{dR_2}{dt} \\ + \left(\frac{h^G}{L_{nn}} - 1 \right) g(\theta_{gs}, \theta_{gs}, Y_{F,2}, Y_{F,1}, R_2, R_1) \\ - h(Y_{F,2}, Y_{F,1}, R_2, R_1) + \frac{1-0.74}{0.74} \frac{R_2^3}{3} \frac{h^G}{\rho_g^* \theta_{gs}(\sigma Y_{F,2} + 1)} \quad (A15)$$

EFFETS DE LA TURBULENCE PENDANT L'EVAPORATION DE GOUTTES DANS DES GRAPPES

Résumé—On présente un modèle d'évaporation de gouttelette dans des grappes et les mécanismes d'échange entre la grappe et la phase gazeuse environnante. Ce modèle est développé pour utiliser un modèle de sous-échelle dans les calculs d'évaporation et de combustion d'aérosols et pour décrire le comportement global de la grappe, la pression du gaz demeure constante pendant l'évaporation et par suite le volume de la grappe et la densité du nombre de gouttes varient. On considère deux modèles de turbulence, le premier décrit l'évaporation dans l'environnement initialement sans turbulence laquelle se constitue au cours du temps, le second modèle décrit l'évaporation dans l'environnement lorsque la turbulence existe initialement. Les résultats obtenus montrent que la turbulence augmente l'évaporation et qu'elle est un facteur de commande de l'évaporation des grappes très denses. Lorsque le rapport initial des masses air combustible augmente, à la fois l'histoire de la turbulence et la vitesse relative initiale entre gouttes et gaz peuvent contrôler l'évaporation. On montre que le temps d'évaporation diminue avec un accroissement initial des niveaux de turbulence ou de la vitesse relative. Lorsque le rapport initial des masses air combustible augmente encore plus et que la densité initiale du nombre de gouttes entre le régime de dilution, aucun des deux paramètres ne peut contrôler l'évaporation. Le temps d'évaporation décroît avec la diminution de la taille de la grappe pour des grappes de gouttes denses, tandis que la taille de la grappe n'est pas un facteur limitant pour les grappes diluées. On discute des implications pratiques de ces résultats.

EINFLUSS DER TURBULENZ AUF DIE VERDAMPFUNG VON TROPFEN IN SCHWARMEN

Zusammenfassung—Ein Modell für die Tropfenverdampfung in Schwärmen und für die Austauschprozesse zwischen dem Schwarm und der umgebenden Gasphase wird vorgestellt. Dieses Modell wurde zur Berechnung der Sprühverdampfung und der Verbrennung entwickelt und beschreibt nur globale Verhaltensmerkmale von Tropfenschwärmen. Der Gasdruck im Tropfenschwarm bleibt während der Verdampfung konstant, als Folge davon variiert das Volumen des Tropfenschwarms und die Tropfenanzahl pro Volumeneinheit. Zwei Turbulenzmodelle werden herangezogen. Das erste Modell beschreibt die Verdampfung von Tropfenschwärmen in einer Umgebung, die anfänglich turbulenzfrei ist; die Turbulenz baut sich erst mit der Zeit auf. Das zweite Modell beschreibt die Verdampfung von Tropfenschwärmen in einer Umgebung, in der von Anfang an Turbulenz vorliegt. Die mit diesen Modellen erhaltenen Ergebnisse zeigen, daß Turbulenz die Verdampfung begünstigt und ein kontrollierender Parameter bei der Verdampfung von sehr dichten Tropfenschwärmen ist. Beispiele werden gezeigt, in denen mit dem ersten Turbulenzmodell Sättigung vor der vollständigen Verdampfung erhalten wurde, wogegen sich mit dem zweiten Turbulenzmodell das Gegenteil ergab. Steigt das Anfangs-Massenverhältnis Luft/Brennstoff, so kann sowohl die Vorgeschichte der Turbulenz als auch die Anfangs-Relativgeschwindigkeit zwischen Tropfen und Gas die Verdampfung beeinflussen. Es wird gezeigt, daß die Verdampfungszeit mit einer Erhöhung des Turbulenzgrades oder der Anfangs-Relativgeschwindigkeit abnimmt. Steigt das Anfangs-Massenverhältnis Luft/Brennstoff weiter und fällt die Tropfenanzahl pro Volumeneinheit zu Beginn in den Bereich für lockere Schwärme, so beeinflusst keiner der beiden obengenannten Parameter die Verdampfung. Bei dichten Tropfenschwärmen verkürzt sich die Verdampfungszeit mit abnehmender Größe des Schwarms, bei lockeren Schwärmen hat die Größe keinen Einfluß. Die praktischen Folgerungen aus den Ergebnissen werden diskutiert.

ЭФФЕКТЫ ТУРБУЛЕНТНОСТИ ПРИ ИСПАРЕНИИ КЛАСТЕРОВ КАПЕЛЬ

Аннотация—Представлена модель испарения кластеров капель и описаны процессы обмена между кластерами и несущей газовой средой. Разработанная модель, являясь подсчетной, используется для расчета испарения и горения распылов капель, а поэтому учитывает только глобальные особенности поведения испаряющихся кластеров. Предполагается, что в процессе испарения давление газа в кластере остается постоянным, так что переменными являются объем кластера и плотность числа капель в нем. Рассмотрены две модели турбулентности. Первая описывает испарение кластера в среде, в которой изначально турбулентность отсутствует, но "подключается" со временем по мере испарения кластеров. Вторая модель описывает испарение кластера в среде с начальной турбулентностью. Согласно обеим моделям турбулентность ускоряет испарение, являясь определяющим фактором при испарении очень плотных кластеров. Приведены примеры, в которых показано, что с использованием первой модели насыщение наступает до полного испарения капель, а с использованием второй наблюдается противоположный эффект. При увеличении начального массового отношения воздух/горючее испарение зависит как от предистории турбулентности, так и от начальной относительной скорости движения капель и газа. Показано, что время испарения уменьшается, если начальный уровень турбулентности или относительная скорость возрастают. При существенном увеличении начального массового отношения воздух/топливо и уменьшении начальной плотности числа капель до разреженного режима ни один из вышеуказанных параметров не оказывает решающего влияния на испарение. Кроме того показано, что время испарения уменьшается с уменьшением размера кластера при большой плотности числа капель, а при малой плотности размер кластера не является определяющим фактором.

Обсуждаются практические аспекты полученных результатов.

Transport-Related Phenomena For Clusters Of Drops

J. Bellan and K. Harstad

Jet Propulsion Laboratory

California Institute of Technology

4800 Oak Grove Drive

Pasadena, CA 91109

ABSTRACT

Two global models of droplet cluster evaporation which take into account drop interactions are compared. Comparisons between the results obtained with the two cluster models show that although the qualitative trends are the same, quantitative discrepancies exist. To evaluate and improve the models it is suggested that experimentalists measure evaporation times and cluster decay/growth rates in the dense cluster regime, and for small clusters, where the sensitivity of the results is highest.

INTRODUCTION

Measurements performed in sprays characteristic of power systems show that sprays are composed of several regions [1]. Near the atomizer the drops might not be entirely formed and liquid sheets and filaments might still exist. There follows a region where the drops are already formed but have not yet been dispersed, so that they cluster together with a typical distance between the drops that is of the order of magnitude as that of the average radius of the drops themselves. of the spray is called the dense spray region. Finally, further from this dense spray region there exists a region where the drops might still cluster, but in these clusters the distance between drops is much larger than the average radius of the drops. This region is called the dilute spray region.

In the dilute spray region drops are far apart from each other and thus when the spray is exposed to a convective flow, these drops practically behave like isolated drops in a convective flow. In contrast, in the dense spray regime, the drops are close to each other and thus their history is controlled by how much of the surrounding gas can enter in contact with them. This is to say that, unlike for drops belonging to dilute clusters of drops, transport phenomena are crucial in determining the behavior of drops belonging to dense clusters of drops because transport imposes limits on heat and mass transfer between the two phases. These phenomena pertain to indirect interactions and they can control the drops motion, their heat-up time, evaporation, ignition and combustion.

Previous work of Bellan and Cuffel[2] and Bellan and Harstad [3,4,5] pointed out some important consequences of these indirect interactions. Two models of turbulent transport were used in Ref. 5 in order to investigate the importance of turbulent transport from the surroundings to the cluster. Because of the global aspect of the model in which all the drops were assumed to behave identically, the transport from the cluster to surroundings was modeled using a "trapping factor." Basically, the "trapping factor" is a weighing factor which allows the modeling of intermediary situations between those of dilute clusters where evaporated mass was assumed to be trapped in the cluster and that of dense clusters where evaporated mass was assumed to escape to ambient. It was found[5] that whereas in the dilute regime turbulence is not a controlling parameter, in the dense regime it becomes the crucial control parameter. This is a fact well known by experimentalists and design engineers who locate turbulent enhancement devices near the injector where the spray is dense, rather than further down the combustor where the spray is dilute.

Since the transport processes between the cluster and its surroundings were found to be so important in the case of dense clusters, it was thought very important to improve the description of the transport of heat, mass and species from the cluster and its surroundings. This new model is described in detail in Ref. 6 for electrostatically charged drops, and is used to calculate the results presented below for the special case of null charge. Due to the brief nature of the Technical Note, the nomenclature is the same as in Refs. 5 and 6.

The model developed in Ref. 6 is similar to that of Ref. 5 in that the drops and gas have two velocity components: a uniform axial component along the trajectory direction and a radial component. The difference between the two models is in the description of the radial velocity component. Whereas in Ref. 5 a "trapping factor" was used as discussed above, the new formulation uses the assumption of self-similarity in the radial direction as explained in detail in Ref. 6.

RESULTS AND DISCUSSION

Calculations were performed using the models of Refs. 5 and 6 for n-decane drops evaporating in a spherical cluster surrounded by unvitiated ambient air at atmospheric pressure. The thermophysical constants used in the calculation have been listed in Ref. 3.

Figure 1 shows a comparison of the results obtained with the two turbulence models for each one of the "trapping factor" and similarity models. The evaporation time which is plotted versus the initial air/fuel mass ratio represents either the time when $R_1 = 0.05$ or the time at which saturation was obtained. As can be seen in Fig 1 the discrepancy between the four sets of results is small in the lean mixture and dilute spray regime. This is because in this regime transport processes are not important in determining the evaporation time due to the fact that the drops are far apart and enough heat is available for their evaporation. As the initial mixture becomes rich the discrepancy between the "trapping factor" and similarity models becomes larger. In contrast to the results obtained with "trapping factor" model, the similarity model predicts that turbulent transport is important even in the rather dilute cluster regime ($n^0 = 5 \times 10^3 \text{ cm}^{-3}$).

When ϕ^0 decreases further, the initial mixture becomes richer and the drop number density falls into the dense regime ($n^0 > 10^4 \text{ cm}^{-3}$). As the initial drop number density is larger, turbulence becomes crucial in determining the evaporation time as it is clearly shown by both cluster models. However, the results become extremely sensitive to the cluster model itself because for example for $n^0 = 5 \times 10^4 \text{ cm}^{-3}$ the "trapping factor" model predicts saturation before complete evaporation whereas the similarity model predicts the opposite. It is expected that the regime of saturation before complete evaporation will be encountered with the similarity model at higher n^0 . What this comparison shows is that global models such as one of Refs. 2-5 can be expected to offer only a qualitative understanding. The quantitative predictions can be obtained only when the results of these global models can be compared with experimental observations. On the other hand experimentalists need information on

what to measure, and where to make measurements. The present results show that in order to validate global models, measurements of evaporation times should be made in the dense cluster regime where the sensitivity is highest.

In Fig. 2 the evaporation time is displayed versus the initial radius of the cluster for an air/fuel mass ratio corresponding to a drop number density which is the dividing value for dense/nondense sprays under the initial conditions shown in the legend. Both cluster models predict that turbulent transport effects are more important for smaller clusters. This is due to the smaller volume to surface ratio and thus to the greater need to transport hot unvitiated gas to the drops in order to promote evaporation. Although the qualitative predictions of the two cluster models are the same, quantitatively the smilarity model predicts a smaller effect. Once again, experimental observations are needed to show the quantitative effect of turbulence, and these experiments should be performed in the small cluster regime where the sensitivity is highest.

The importance of the cluster model used is again illustrated in Fig. 3 where the final size of the cluster is compared with the initial size of the cluster for several initial cluster sizes. In all cases larger clusters contract more, relatively to their initial size, than do small clusters. This is due to the heating of the drops and the consequent cooling of the gas phase. A smaller number of drops in a cluster results in less cooling of the gas phase at complete evaporation and shorter evaporation time; this is the case of the smaller clusters. A higher turbulence level will enhance transport of heat to the cluster and thus there will be less cooling and consequently less cluster contraction; this is the case of turbulence model 2. For small clusters and high turbulence levels the similarity model predicts that the cluster actually expands. This is another trend that needs experimental verification. In this case observations should be performed again in the small cluster regime.

Finally, plotted in Fig. 4 and 5 are respectively the relative fuel mass loss and the relative total mass loss from the cluster at the end of evaporation. These results were obtained with the similarity model, which is believed to be the more

accurate of the two cluster models. In the case of dense clusters, the relative fuel mass loss from the cluster is important because ignition outside of the cluster is expected[7] with only the ejected fuel participating in ignition. The fuel loss ratio depends strongly on the cluster size and the turbulence model. In contrast, the total mass ratio is nearly insensitive to the turbulence model for large clusters, with a larger sensitivity shown for smaller clusters. However, similar to the fuel mass ratio, the total mass loss ratio increases substantially as the cluster size decreases. The larger fuel loss and greater entrainment for smaller clusters may be attributed to their larger surface to volume ratio. It is important to notice that the present model does not account for vortical motion of the drops inside the cluster and thus the results predict a minimum amount of mass escaping from the cluster due to the lack of centrifugal force effects. In order to validate experimentally models such as those described above, rates of growth or decay of clusters are needed for comparison.

Acknowledgement

This work was supported by Air Force Office of Scientific Research, Army Research Office and Department of Energy-Energy Conservation and Utilization Technologies Programs through interagency agreements with National Aeronautics and Space Administration.

REFERENCES

1. Chigier, N. A., Mao, C. P., and Oechsle, V., Paper 7-6A presented at the CSS/WSS/CI Spring Meeting, April, 1985; also private communication.
2. Bellan, J. and Cuffel, R., "A Theory of Nondilute Spray Evaporation Based Upon Multiple Drop Interactions," Combust. and Flame, 51, 1, pp. 55-67, 1983.
3. Bellan, J. and Harstad, K., "Analysis of the Convective Evaporation of Dense and Dilute Clusters of Drops," Int. J. Heat Mass Transfer, 30, 1, pp. 125-136, 1987.
4. Bellan, J. and Harstad, K., "The Details of the Convective Evaporation of Dense and Dilute Clusters of Drops," Int. J. Heat Mass Transfer, 30, 6, pp. 1083-1093, 1987.

- 5 Bellan, J. and Harstad, K., "Turbulence Effects During Evaporation of Drops in Clusters," Int. J. Heat Mass Transfer, 31, 8, pp. 1655-1668, 1988.
6. K. Harstad and J. Bellan, "Electrostatic Dispersion of Drops in Clusters," Combust. Sci. and Techn., in press.
7. Bellan, J. and Harstad, K., "Ignition of Non Dilute Cluster of Drops in Convective Flows," Combust. Sci. and Techn., 53, pp. 75-87, 1987.

FIGURE CAPTIONS

Fig. 1 Evaporation Time versus Initial Air/Fuel Mass Ratio.

$$T_{ga}^0 = 1000^\circ\text{K}, T_{gs}^0 = 350^\circ\text{K}, Y_{Fva}^0 = 0, u_r^0 = 500 \text{ cm/sec},$$

$$R^0 = 2 \times 10^{-3} \text{ cm}, \bar{R}^0 = 10 \text{ cm}.$$

Fig. 2 Evaporation Time versus Initial Cluster Radius.

$$\phi^0 = 1.57 (n^0 = 9.44 \times 10^3 \text{ cm}^{-3}, R_{O_2}^0 = 13.3), T_{ga}^0 = 1000^\circ\text{K}, T_{gs}^0 =$$

$$350^\circ\text{K}, Y_{Fva}^0 = 0, u_r^0 = 500 \text{ cm/sec}, R^0 = 2 \times 10^{-3} \text{ cm}.$$

Fig. 3 Nondimensional Final Cluster Radius versus Initial Cluster Radius.

$$\phi^0 = 1.57 (n^0 = 9.44 \times 10^3 \text{ cm}^{-3}, R_{O_2}^0 = 13.3), T_{ga}^0 = 1000^\circ\text{K}, T_{gs}^0 =$$

$$350^\circ\text{K}, Y_{Fva}^0 = 0, u_r^0 = 500 \text{ cm/sec}, R^0 = 2 \times 10^{-3} \text{ cm}.$$

Fig. 4 Fuel Loss Ratio versus Initial Cluster Radius Obtained with the Similarity Model.

$$\phi^0 = 1.57 (n^0 = 9.44 \times 10^3 \text{ cm}^{-3}, R_{O_2}^0 = 13.3), T_{ga}^0 = 1000^\circ\text{K}, T_{gs}^0 =$$

$$350^\circ\text{K}, Y_{Fva}^0 = 0, u_r^0 = 500 \text{ cm/sec}, R^0 = 2 \times 10^{-3} \text{ cm}.$$

Fig. 5 Total Mass Loss Ratio versus Initial Cluster Radius Obtained with the Similarity Model.

$$\phi^0 = 1.57 (n^0 = 9.44 \times 10^3 \text{ cm}^{-3}, R_{O_2}^0 = 13.3), T_{ga}^0 = 1000^\circ\text{K}, T_{gs}^0 =$$

$$350^\circ\text{K}, Y_{Fva}^0 = 0, u_r^0 = 500 \text{ cm/sec}, R^0 = 2 \times 10^{-3} \text{ cm}.$$

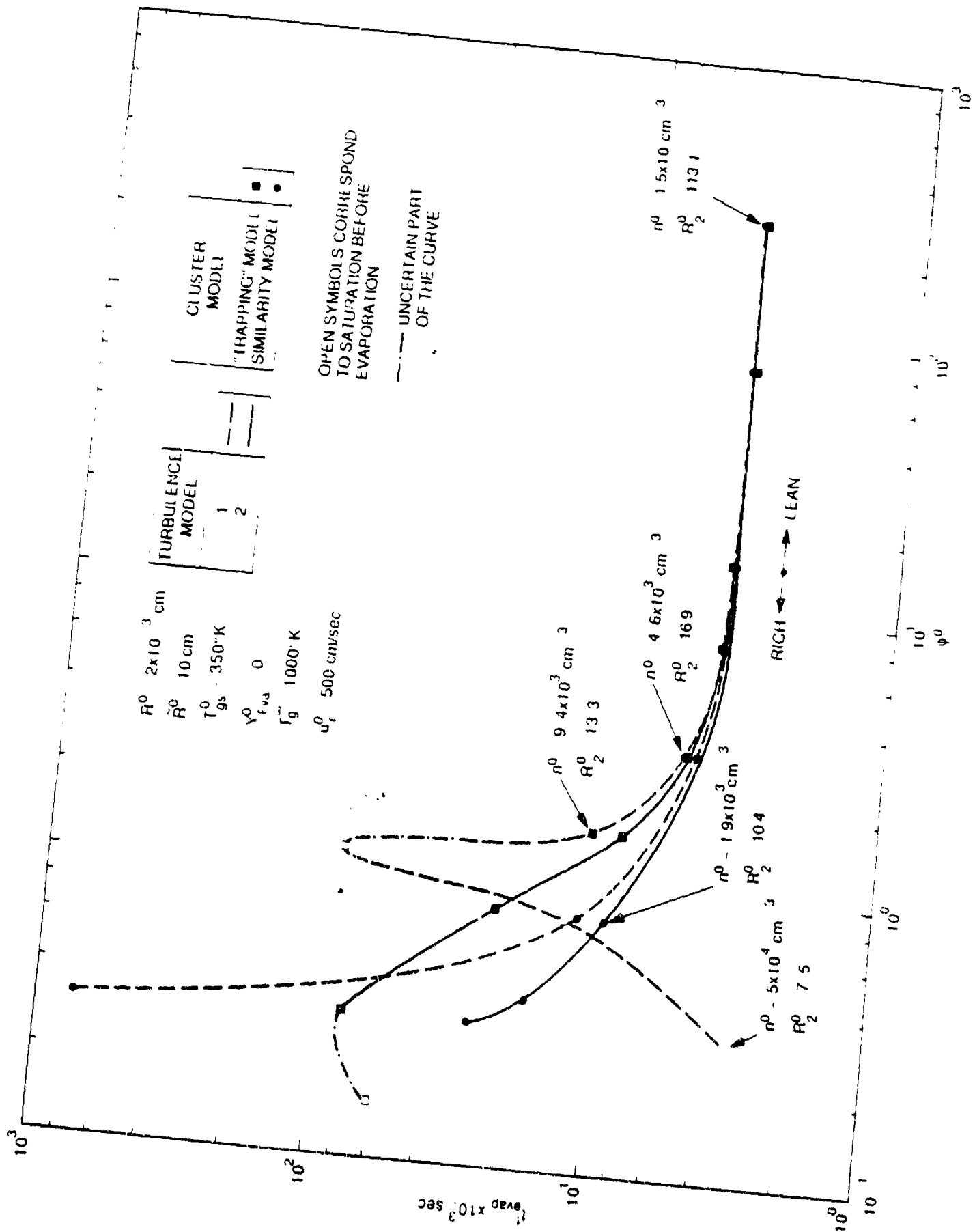


Figure 1

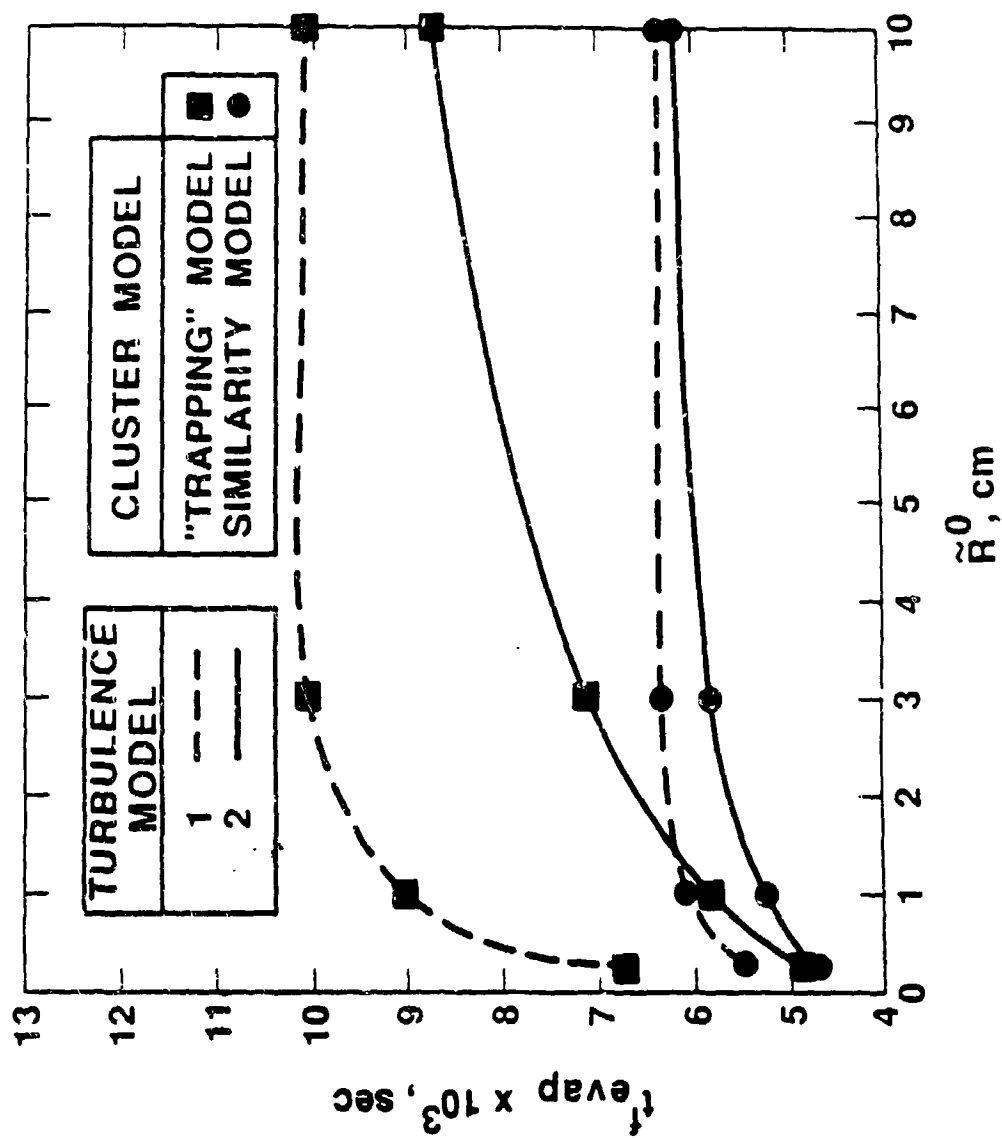


Figure 2

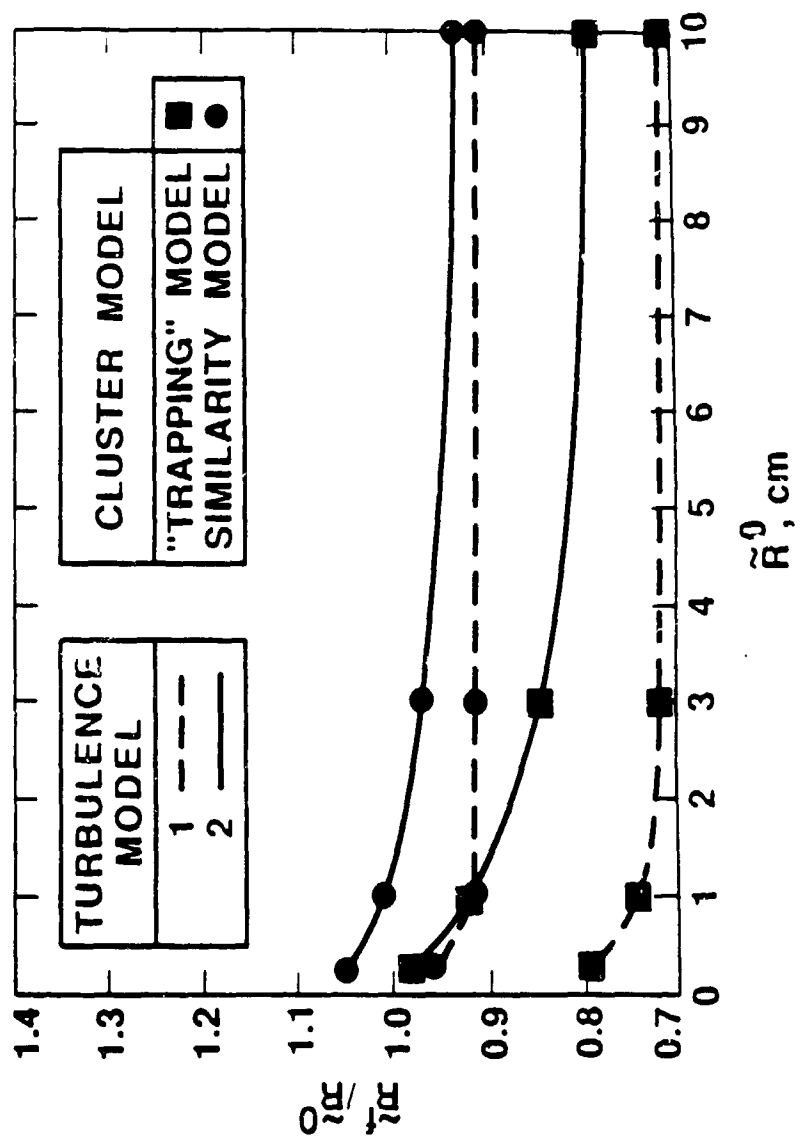
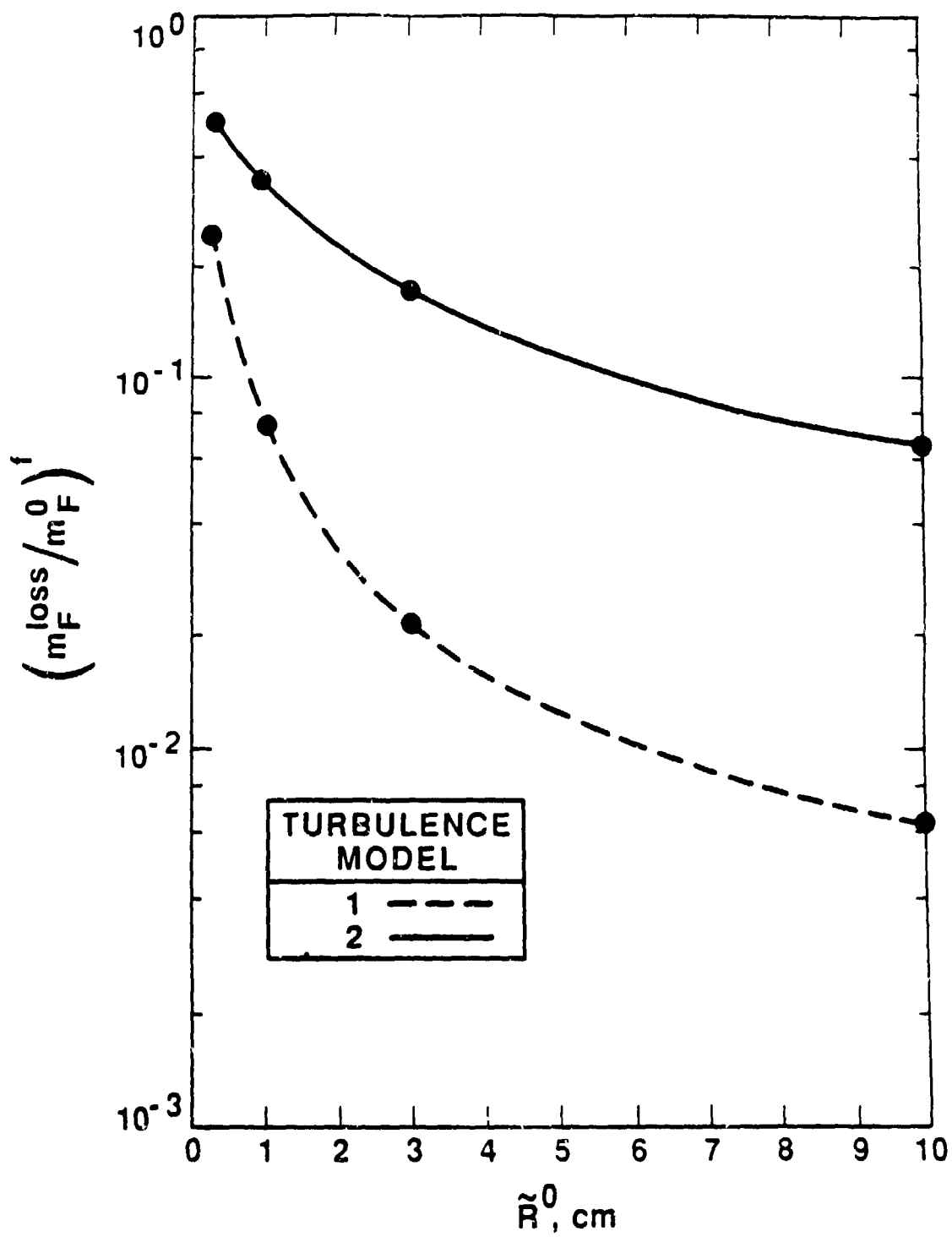
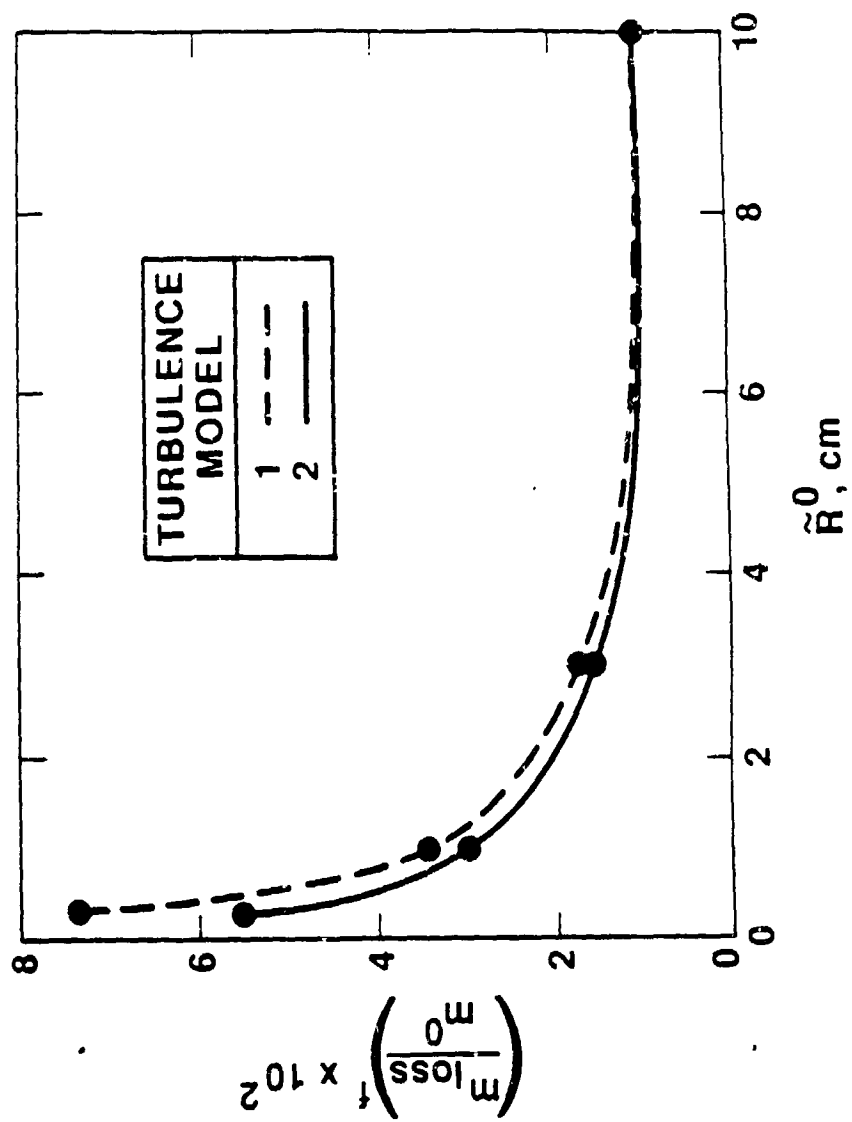


Figure 2





LIQUID DROP BEHAVIOR IN
DENSE AND DILUTE CLUSTERS

BY

JOSETTE BELLAN
JET PROPULSION LABORATORY
CALIFORNIA INSTITUTE OF TECHNOLOGY
4800 OAK GROVE DRIVE
PASADENA, CA 91109

I. INTRODUCTION

Sprays, created by atomizing liquid fuels, have been considered for a long time as one of the most efficient ways of burning liquids. This is because in a spray the surface-to-volume ratio is greatly increased compared to a blob of liquid. The extra surface increases the efficiency of transport of heat to the liquid, thereby promoting evaporation, ignition and combustion of the fuel. Liquid sprays are also used in agriculture to spray crops, in the food industry, in coating, and in printing.

In order to improve all these processes, one needs first to understand them. Such understanding can be achieved in a variety of ways. For many years now, the only universally accepted way of improving a process was to physically experiment with it. This involves building a prototype operating under a variety of conditions. The results of these experiments are recorded and compared. The prototype system can then be "tuned" to operate under the optimal conditions achieved during the experiment. The simplistic "cut and try" method described above is making room for a growing use of analytical methods and computational techniques based on the availability of large computers. Experimental techniques, which have become themselves increasingly sophisticated, are usually very expensive and are limited not only by the sensitivity of the diagnostic but also by the range of conditions that can be studied. In many cases, it is cheaper to vary the parameters in an existing computer code to simulate a different physical situation than it is to build or alter an experimental set-up to obtain new experimental results. The flexibility of computer codes in terms of input conditions and output results make them a very powerful tool both for engineering calculations and understanding the fundamentals of physical phenomena.

Below I shall describe how the computational approach has helped the understanding the fundamentals of spray evaporation, the interactions between the drops in a spray, the interactions between the drops and the gas surrounding them, and subsequent ignition and combustion. This understanding in turn provides the basis for controlling these phenomena.

A typical liquid spray is composed of three main regions, although the boundary between these regions is not always very distinct. Near the atomizer there is a region of liquid filaments that are the precursors of drops. Adjacent to this region is a region of very closely spaced drops such that the spacing between the drops is of the same order of magnitude as their size; this is called the dense spray region. Further downstream one encounters a region where the drops are no longer closely spaced; this is called the dilute spray region.

Recent observations of liquid-fuel sprays have revealed that although the fuel flow to the injector is constant, drops appear to cluster in the spray and remain clustered during combustion (1,2,3,4). Thus, there is not one continuous flame surface in a burning spray, but instead there are many flame surfaces, each one enclosing groups of drops (3,4).

A characteristic feature of sprays is the wide range of space scales involved in their description. For example, a few of the most obvious scales are: the scale of the enclosure, if any, where the liquid is sprayed; the many turbulent scales associated with turbulence build up and decay; the scale of droplet interactions; the average distance between drops; and the scale of drops themselves. These scales vary by orders of magnitude from the largest to the smallest, and this implies that an accurate mathematical description at all scales is impractical. To circumvent this difficulty it has been proposed (5)

that the macroscale, which is the scale where phenomena occur that are of interest to engineers, be described in detail and that the microscale, which encompasses the scales much smaller than the macroscale, be described in an approximate and global manner. The coupling between the two scales must be achieved through the boundary conditions at the microscale level. The microscale formulation is also sometimes called a subscale or subgrid model because the phenomena that are involved occur at a scale much smaller than that of the grid size used to computationally resolve the macroscale problem. Inherent to this two-level description is the understanding that the subscale models are more approximate than the macroscale models and lack of detail that the latter are required to have in order to be useful. This concept is similar but not identical to the proposed particle-source-in cell model by Crowe et.al. (6).

The observation of clusters of drops in sprays points to the natural choice of the cluster size as one of the important microscales. Within this frame it is envisaged that each cluster should be followed on its trajectory in a Lagrangian way and that the coupling between the cluster and its surroundings should be achieved through proper boundary conditions at the cluster surface. One example of the implementation of this concept can be found in Tambour (7). He partitions the spray into section of drops of known characteristics and follows each group of vaporizing drops along a streamline in a Lagrangian manner while calculating one integral characteristic quantity for each section. In his model this integral quantity can be either the number of drops, surface area of the drops, or volume of the drops. A missing input of this model is a calculation of drop evaporation rate in each section; instead, the author cleverly estimates this rate from the experimental data of Yule et. al. (8)

using the d^2 - law approximation. As expected, the characteristics of each group of drops change during a calculation. Thus, it is important to calculate these changes as they occur rather than to fit them in an approximate way *a priori* using experimental data. This example indicates that models of droplet clusters must be able to handle the many areas where drops exist in a spray, going from the dense region to the dilute region as discussed above.

Experimental observations show that dense and dilute collections of drops behave very differently. In the dilute regime the drops are so far away from each other that they behave as if isolated for all practical purposes. The behavior of individual, isolated drops under a variety of assumptions is described by classical theory (9). In contrast, when drops are closely spaced, their behavior changes due to limitations on heat and mass transfer which result from drop interactions with the background gas. These interactions are called indirect or long range interactions. Direct or short range interactions, such as drop collisions, coalescence or breakup, will not be discussed here. Béer and Chigier (10) show that the quantity obtained by dividing the difference between the initial droplet diameter squared and the actual diameter squared by the time elapsed from the initial condition, varies non-monotonically with the average inter-droplet separation distance. In contrast this quantity is a constant for an isolated drop and is called "the burning constant." As the inter-droplet separation distance is reduced from large values for which drop interactions are negligible, the burning constant increases to a maximum, and then decreases. This behavior arises because heat losses are reduced when the drops are brought slightly closer together, thereby increasing the burning constant. However, when the separation is greatly reduced, the amount of oxygen available for combustion diminishes and thus decreases the burning constant.

This latter situation, which typically prevails in spray, was investigated experimentally by Koshland (11,12) and Koshland and Bowman (13). Their results show that, in agreement with Chigier and McCreath (14) and Rao and Lefebvre (15), both evaporation and combustion of groups of interactive drops depend on drop number density as well as the oxygen concentration in the ambient gas. Oxygen competition was identified (11, 12, 13) as one of the processes that can change the combustion mode of groups of drops from individual flames around drops (in an oxygen-rich environment) to a group combustion mode where the flame surrounds the droplet cloud (in an oxygen-lean environment). Thus, the prediction of the global gas phase characteristics inside the drop cloud is of paramount importance for the calculation of both evaporation and burning rates.

Moreover, many of the pollutant forming reactions also depend indirectly on the drop number density and the oxygen concentration. Sangiovanni and Liscinsky (16) showed experimentally that soot production is a strong function of the interspacing between drops. Their results are actually conservative with respect to the situation in a spray, because in their droplet-stream experiment there was no way to account for the influence of lateral spacing between drops in the direction perpendicular to the stream. In a real spray, the average drop is surrounded in all three dimensions by other drops. For a variety of fuels and ambient oxygen concentrations, it was shown that by increasing the droplet spacing, a substantial decrease can be obtained in the soot emission (16). Reductions in spray flame temperature and NO_x levels were also associated with droplet interactions as shown by Chernansky and Sarv (17) who interpreted their results in terms of oxygen depletion during burning. Additionally, the question of whether the drops disappear well before the entire amount of fuel-vapor is burnt has direct bearing to the formation of carbonaceous, porous particles

called cenospheres. These particles form from each individual drop during combustion of heavy-oil sprays once the more volatile hydrocarbons have evaporated and the tar-like material is left behind. It appears that contrary to the classical d^2 -law assumption of equal vaporization and burning rates, even for mildly dilute groups of drops (initial drop number densities of 18-80 drops/cm³), the vaporization rate is higher than the fuel vapor oxidation rate (11). Thus, the drops disappear well before the vapor fuel is burnt, and homogenous burning prevails during the latter time of drop cluster combustion.

The above discussion indicates that models of droplet clusters must be flexible enough to accommodate both dilute and dense configurations and that the cluster drop number density influences many of the crucial aspects of combustion. The remainder of this article is organized as follows: In Section II, I describe some current models of drop interactions and show that they have limitations important enough to preclude them from being used as subgrid models. In the third section I present the approach that we propose for modeling drop interactions. I show that our model has the potential of being used as a subgrid model. In addition, I discuss specific situations that were modeled and the results obtained using this formulation. Finally, the Conclusion, Section IV, contains a discussion of the needs for further research.

II. SURVEY OF DROP INTERACTION MODELS

In the present context, models of droplet interactions describe the interactions among a large number of drops. This precludes models of detailed interactions between small numbers such as two or three drops. While the few-drop models have helped to understand departures from single, isolated-drop behavior, they themselves are not candidates for subgrid models of dense sprays.

Moreover, these few-drop models involve large computational expense as well, and thus are not economically suitable as subgrid models.

One of the earliest contributions to the modeling of multiple drop interactions was made by Zung (18) for the evaporation of drops in atmospheric clouds. The cloud is approximated by a series of cubes having sides equal to the distance between the centers of two adjacent drops. Thus, each cube contains an identical drop in its center, and these cubes are further approximated by spheres of equivalent volume. Zung assumes that no mass transfer occurs between cells, and uses this assumption to predict the rate of drop disappearance in terms of an average concentration inside the cell. The results of this model show that the evaporation rate of a cloud is strongly dependent upon both the drop radius and the distance between drops. In particular, saturation of the vapor in the ambient gas can occur before complete evaporation in some cases.

The drop-in-a-cell idea is also used by Fishkoff (19) who simulated the interactions among evaporating drops by using an isolated drop in a "bubble" of finite and constant radius. Because boundary conditions at the "bubble" surface are specified as a function of time, the actual interactions between drops during evaporation are given and not calculated. However, by cleverly changing the size of the bubble, Fishkoff shows that the initial spacing between drops strongly influences the outcome of evaporation. When the bubble is large compared to the drop, the drop evaporates completely; whereas when it is small, vapor phase saturation may occur before complete evaporation.

Chiu and his co-workers (20, 21, 22, 23) took a very different approach. In their initial analysis, a parameter G , which is the ratio of total heat transfer between the two phases to the heat needed to evaporate the drops, is

identified as a crucial number indicating the combustion mode for the drops in the spray. If G exceeds a critical value, a single flame surrounds the entire spray and the drops burn in what is called an "external group" mode. In contrast, below this critical value of G , isolated droplet burning occurs. This analysis was later (22) refined to include other combustion modes between these two extremes. The weakest aspect of this model is the difficulty in obtaining information necessary to calculate G . Finding G involves the use of empirical formulas characterizing the exchange of mass, momentum and energy between the phases. These formulas are based upon those of the classical single-drop evaporation in infinite surroundings. Realizing this, an attempt was made recently (24) to improve this model through the use of a modified drop-in-a-bubble model. The "test" drop is surrounded here by a "first coordination" shell which corresponds to the radial position of the largest number of drops close to the test drop. Thus, statistically there can be other drops inside the cell, but the model will not take this into account. Using the same idea, a series of second, third, etc. coordination shells are developed. The farthest shell from the drop is a transition shell, the outer edge of which has a continuum of drops; and at this outer edge the gas properties are prescribed for the determination of the drop evaporation rate. The droplet arrangement inside these shells must be provided either experimentally or theoretically through a pair-distribution function that represents the joint probability of finding a drop located at a given distance from the test drop. Since this information must be provided at every instant of time, and it is very difficult to obtain, except for the simplest of situations which can be treated using simple formalisms, this latest model of Chiu et.al. does not seem practical.

The idea of group combustion was also examined by Correa and Sichel (25). Their model assumed that the temperature of the gas in a spherical, uniform, monodisperse cloud of fuel drops immersed in a quiescent atmosphere was initially in saturated equilibrium and that it stayed so during combustion. This assumption precludes the calculation of the influence of drop proximity upon the gas temperature inside the cloud and this has a bearing upon the calculation of the drop evaporation rate. Additionally, they also assumed the ratio of the inter-drop distance to the drop diameter to be of order 10, so that the conclusions based upon results obtained with this model apply only to this regime and not to much denser collections of drops. The largest drop number density for which results were presented was $3 \times 10^3 \text{ cm}^{-3}$. The results predicted the existence of a thin inwardly propagating vaporization wave at the edge of the cloud, a decrease in cloud radius following the classical d^2 -law with a modified "evaporation constant", and a flame-radius to cloud-radius ratio and flame temperature independent of the cloud parameters. The flame temperature was found to be independent of the cloud parameters because the gas temperature inside the cloud was assumed fixed at the saturated equilibrium condition during evaporation and combustion.

Group combustion of drops was modeled in a totally different manner by Labowsky and Rosner (26), and Labowsky (27, 28, 29). Under the quasi-steady gas phase assumption, two different approaches are used to model interacting droplet burning (26). In the first approach, the cloud is treated as a continuum with the droplets acting as distributed sources of fuel and sinks of oxygen. In the second approach, the flame location is calculated for cubical arrays of up to 729 particles. The flame location is found by solving the Schvab-Zeldovich equations. These equations are further transformed to Laplace equations which

in principle can be solved by the method of images. However, since the computational costs of the second approach become prohibitive when the number of particles reaches about 20, the authors solve the equations using a superposition method which is an approximation of the method of images. In this approximation, higher-order terms on the image series are neglected with the result that particles are again treated as point sources and their fields are simply superimposed. Thus, again, interactions due to particle proximity are neglected as these interactions would have been contained in the higher-order terms. The continuum method yields reliable solutions only when the number of particles is large (in a dilute cloud), and the second method yields reliable solutions only when the number of particles is small. The results show that in virtually all practical situations of interest, clouds burn as a total group. This condition is defined as that occurring when the cloud as an entity provides sufficient vapor so that fuel and oxygen meet in stoichiometric proportion precisely at the cloud boundary where they will burn.

Although drop interactions are not accounted for by Labowsky et.al (26), one important contribution of this work is to have identified the ratio of the fuel-cloud radius divided by the fuel-particle radius as the important characteristic which determines the mode of combustion of the drop in the cloud. If this ratio is less than a critical value, the particles burn individually. On the other hand, if this ratio is larger than another critical value, the flame surrounds the entire cloud. Presumably, if the characteristic ratio falls between these two critical values, there will be several separate flames surrounding groups of drops inside the cloud. Although the superposition approximation is not made by Labowsky in (27), the actual calculations are limited to a three-droplet array which limits the generality of the results.

Additionally, the analysis uses the assumption that the particle temperature is not affected by the drop interactions, an assumption which is certainly not valid for closely spaced drops, as it will be shown later. In fact, all the comparisons between this theory using the method of images and experimental observations (28, 29, 30), are made with experiments containing two, three, or a stream of drops. This is because, the method of images leads to financially prohibitive calculations for arrays of more than about 20 drops (26). The largest number of drops considered in a calculation performed with this method was 25, and the comparison was made with a stream of interacting drops (30). For the two, three or 25 linear-drop array, the comparisons with experiments showed reasonable agreement for the drop lifetime when compared with experiments involving two, three, or a stream of drops, respectively.

Samson et al. (31) developed a simple model to describe spray combustion by combining the classical isolated drop theory devoid of hydrodynamic effects, and various statistical concepts. In this model, the burning rate of the drops is identified with their evaporation rate, a fact that is contradictory to experimental evidence (11). Some favorable comparisons with experimental data are presented, but, in order to obtain these results, the unknown radius of the spherical fuel cloud had to be assigned. The values chosen for this radius were selected to obtain best comparisons between experiments and theory. However, the authors point out (31), that the experiments used are not really appropriate to compare with the theory because they involve well defined droplet arrays for which statistical models are not applicable.

Umemura (32) identifies a function, f , intrinsic to the geometrical configuration of the cloud and independent of the combustion characteristics, as the characteristic indicator of droplet interactions. In Umemura's (32) quasi-

steady quiescent-atmosphere theory, the drop-evaporation rate is again identified somewhat incorrectly with the burning rate just as in the isolated drop theory. Results are presented for a system of two droplets.

The effect of particle interactions, first on drop evaporations and then on drop burning, was also modeled by Ray and Davis (33) and Marberry et al. (34). The isothermal droplet evaporation model of Ray and Davis (33) further assumes that, despite evaporating, the particles do not change size (rate of change of size much smaller than the diffusive velocity of the transferred species) and thus there is no convective transport. By assuming that the particles can be treated as point sources or sinks, the authors preclude the treatment of dense collections of particles where the concentration or temperature field around each drop interacts with that of the neighboring drops. Further, the results show that the model becomes invalid if the number of particles exceeds the ratio of the distance between particles divided by the particle radius. This represents a serious restriction to the model. The same assumptions of quiescent atmosphere and constant particle size are kept in Marberry et al. (34). The burning rate of each drop is given by material and energy balance at the drop surface and these are the equations that now determine the source strength at each droplet location. The results indicate significant deviations from the isolated droplet burning rate if the distance between the drops is smaller than 20 times the droplet radius. These results were obtained for systems of 2, 3 and 4 drops, tetrahedral and cubical arrays so that none of the drops was entirely surrounded by other drops. In that respect the estimate of the above ratio of 20 should be understood as a lower limit.

Annamalai (35) modeled the evaporation, ignition and combustion of a droplet cloud as well. However, the results cannot be expected to be reliable

because his formulation did not contain a genuine description of droplet interactions.

The 3-dimensional numerical study of Shuen (36) was meant to investigate the effect of droplet interactions on transport phenomena for droplet Reynolds numbers of 5-100, droplet spacings of 2-24 diameters, and oxygen concentrations of 0.1 to 0.2. The physical situation studied is that of a monosize, planar, semi-infinite droplet array oriented perpendicular to the direction of the flow. Shuen also assumed a quasi-steady gas phase with respect to the liquid phase and no drop heating. The geometry studied suggests immediately that droplet interactions will be underpredicted since there is no drop that is surrounded on all sides by other drops in a 3-dimensional sense. Furthermore, since the array is semi-infinite, the amount of heat available to the drops is not a limiting factor as it is in real sprays. Moreover, the neglect of droplet heating immediately suppresses one of the most important modes of droplet interaction; that is, competition among drops for the available heat. It is not surprising that the author finds that interactions between drops become negligible for spacings greater than six droplet diameters and Reynolds numbers greater than ten. He also finds that drop interactions result in an insignificant change in drag per drop.

All above-discussed models of drop interaction are deficient in some important way which precludes both the prediction of the behavior of dense clusters of drops and their inclusion as subgrid models as discussed in the Introduction. In the following, I discuss models that have promise in both these respects. In contrast to the models discussed so far, they include explicitly the effects of drops interactions. In addition, they are formulated

in such a way that boundary conditions with the surrounding gas can be changed in order to describe a variety of situations.

III. MODELS OF DROP EVAPORATION, IGNITION AND COMBUSTION BASED UPON MULTIPLE DROP INTERACTIONS

The models described below pertain to a variety of situations and a description of their assumptions can be found in Table I.

1. Constant-Volume (Variable-Pressure) Cluster Models

In the approach taken by Bellan and Cuffel (37), a cluster of spherical monodisperse, uniformly distributed drops is considered, and the cluster volume, V_c , can have an arbitrary shape and contain an arbitrary number of drops, N . Figure 1 shows each drop of the cluster surrounded by a fictitious sphere of influence whose radius is half the distance between the centers of two adjacent drops. Thus, the volume of the cluster is in fact the volume of these spheres of influence added to the volume of the space between the spheres of influence. From simple geometrical considerations usual in solid-state theory (38), it is known that the radius of the sphere of influence thus defined is

$$a = \left(\frac{0.74 V_c}{N \frac{4\pi}{3}} \right)^{1/3} \quad (1)$$

where V_c is the cluster volume, N is the total number of drops and "a" is the radius of the sphere of influence. In reference (37), the volume V_c was adiabatically insulated, but this restriction is removed in later studies which will be discussed below. On the length scale of many drops, the cluster is considered spatially homogeneous in the thermodynamic quantities. This means that each drop behaves like all other drops in the cluster. Moreover, all

dependent variables are assumed to be uniform in the interstitial space between the spheres of influence. Thus, the conservation equations for this cluster of drops consist of: (1) the differential conservation equations for each drop and gas phase inside a sphere of influence, (2) the global conservation equations for all drops inside the cluster volume, and (3) the perfect gas law. In reference (37), the classical quasi-steady assumption for the gas phase is made and thus the differential equations for the gas-phase inside the sphere of influence can be solved exactly. The quasi-steady assumption is well-justified at atmospheric pressure since $\rho_g/\rho_l \approx 10^{-3}$ where ρ_g and ρ_l are the gas and liquid densities respectively. For simplicity it is assumed that thermodynamic equilibrium prevails in the gas phase at the drop surface, and that the drop temperature is uniform but transient. (These assumptions are also relaxed in the later studies which are discussed below.) The solution of these equations contain as parameters the unknown values of species and temperature at the edge of the sphere of influence. Since these quantities also appear in the global conservation equations and the perfect gas law, the system of equations is closed. At every time step, the solution consists of the evaporation rate, the radius of the drop, the value of the fuel mass fraction and temperature at the drop surface and at the edge of the spheres of influence, the density and the pressure (both assumed uniform in V_c).

Comparing this model to some of the previously described models one notices that this model is different both from Tishkoff's (19) bubble model and Zung's (18) cell model, even though it also isolates each drop in a sphere of influence. It is different from Tishkoff's model because the conditions at the edge of the sphere of influence are not imposed, but instead are calculated as a consequence of the droplet interactions. It is different from Zung's model in

quite a few aspects, but mainly because it does not impose zero mass transfer between the spheres of influence and it relates the evaporation rate to an exact mass fraction inside the sphere of influence instead of an averaged value. When the volume of the cluster is constant and the cluster is insulated from the surroundings, the quasi-steady and spacial homogeneity assumptions imply that there is no transport between the spheres of influence because there is no transport out of the cluster and because of symmetry. In contrast to Zung's model, however, we can evaluate how well the quasi-steady assumption holds by calculating the gradient at the edge of the sphere of influence. The results show that because the quasi-steady assumption deteriorates as the radial coordinate, r , increases, the model improves as " a " in Eq. (1) is smaller, that is for dense collections of drops.

All the calculations presented below are for n-decane. Symbols in the figures and text are defined in the Nomenclature. Figure 2, produced from Ref. (37) shows plots of both the cluster evaporation time, τ_{nd1}^e , obtained with the model described above and the ratio of this time to that of the evaporation time obtained with a model of dilute spray evaporation (39), τ_{nd1}^e/τ_{d1}^e . For dilute collections of drops, the predictions of the two models agree. However, as soon as the non-dimensional radius of the sphere of influence, R_2 , is smaller than or of order 10, (see Figure 3), departures from the dilute theory occur. In fact, when comparing with the dilute theory, four universal regimes are identified as the equivalence ratio, ϕ , varies from very large values (fuel-lean) to very small values (fuel-rich). In the first very lean regime, the results of the two theories agree. In the second regime, evaporation is completed before saturation but the ratio of the two evaporation times, τ_{nd1}^e/τ_{d1}^e , is a function of ϕ . In the third regime, non-dilute spray theory

predicts saturation before complete evaporation, whereas the dilute spray theory predicts the opposite. Finally, in a fourth regime, both theories predict saturation before complete evaporation but at different times and values of the residual drop radius, R_1 . In the first and the second regime, t_{nd1}^e is a decreasing function of ψ , whereas in the third and fourth regime it becomes an increasing function of ψ .

Although these regimes are believed to be universal, the values of ψ separating them change as a function of the fuel and the initial conditions. Thus, non-dilute effects can occur even at larger values than $R_2 = 10$. For example, non-dilute effects can be found even for very dilute sprays when the total mixture is rich. This is illustrated in Figure 4. When ψ is constant and the initial interstitial mass fraction of fuel vapor, Y_{FVa}^0 , increases, the cluster becomes more dilute and the liquid fuel mass decreases. Because of this, the interstitial gas temperature, T_{ga} , stays higher than at lower values of Y_{FVa}^0 since less heat is transferred to the evaporating drops. Thus, as Y_{FVa}^0 increases, two competing effects determine the rate of evaporation and therefore the value of t_{nd1}^e : Y_{FVa}^0 is larger which tends to decrease the evaporation rate, but T_{ga} is larger as well which tends to increase the evaporation rate. The interplay between these two effects is such that as Y_{FVa}^0 increases from zero, the vapor-pressure effect dominates and therefore t_{nd1}^e increases with increasing Y_{FVa}^0 . In contrast, the dilute spray theory predicts that t_{d1}^e decreases monotonically with increasing Y_{FVa}^0 .

The results of Figure 4 are not directly comparable with those of Koshland (11) because in those experiments, the oxidizer mass fraction and droplet spacing were decreased independently. Here, as Y_{FVa}^0 increases (and thus the mass fraction of oxidizer decreases), the droplet spacing increases because the

equivalence ratio is kept constant. However, since Figure 4 shows that τ_{nd1}^e is a very weak function of Y_{FVa}^0 and since a decrease in droplet spacing results in increasing τ_{nd1}^e (see Figures 2 and 3) for complete evaporation before saturation, it is expected that τ_{nd1}^e increases when the oxidizer mass fraction decreases while the droplet spacing is constant. This yields the same result as that of Koshland (11) who found the burning rate decreasing with decreased ambient oxidizer mass fraction. The results of the theory of Bellan and Cuffel (37) also showed that the square of the normalized radius does not decrease linearly with time, and thus the d^2 -law does not hold for interacting droplets.

To improve the predictive abilities of this model some simplifying assumptions of the above formulation were relaxed in Bellan and Harstad (40). In particular the more realistic Langmuir-Knudsen kinetic evaporation law replaced the Clausius-Clapeyron relationship, and the drop temperature was considered not only transient but a function of radial position.

The general idea of the model is to account for global effects. Thus, even though there is a net flow of gas and heat through the surface of the cluster, these effects are not modeled in detail, but only globally. In this particular case mass and heat inflow or outflow through the boundary are assumed negligible with respect to the mass and heat content of the cluster. The results show that in fact this is a very good approximation for nondilute clusters where penetration of the clusters by surrounding gas is confined to a very thin shell. On the other hand for dilute clusters where penetration is substantial, convective flow effects are appropriately taken into account by correlations relating the evaporation rate in convective flows to those in quiescent flow and to the Reynolds number. For intermediate regimes of drop number density the model is still expected to be a good global approximation. Consistent with the

assumption of small pressure gradients, the exchange of momentum between drops and gas is treated on a local basis and is considered to be due to: (i) transfer due to evaporation, (ii) transfer by fluid flow interaction in the form of a drag coefficient, and (iii) transfer due to small pressure gradients. The ensuing momentum equations are

$$\frac{du_r}{dt} = -n \left\{ \dot{m} u_r / \rho_g + \frac{1}{2} \left[1 + \rho_g / (n m_d) \right] A_d C_D u_r^2 \right\} \quad (2)$$

$$m_d \frac{du_d}{dt} = - \frac{1}{2} \left[\rho_g A_d C_D u_r^2 + \frac{n m_d}{(\rho_g + n m_d)} \rho_g u_g u_d C_{Dc} A_c / N \right] \quad (3)$$

where $u_r = u_d - u_g$ is the relative velocity between drops and gas inside the cluster, \dot{m} is the evaporation rate, n is the drop number density, ρ_g is the gas density, m_d is the mass of one drop, N is the total number of drops, A_c is the transverse area of the cluster, A_d is the transverse area of a drop, and C_D and C_{Dc} are respectively the drag coefficient for one drop and the drag coefficient for the cluster as an entity. These momentum equations are coupled to the other equations. Here C_{Dc} is based upon a length scale $[A_c(u_g/u_d)/\pi]^{0.5}$ and is a function of the resultant Reynolds number only. In contrast, C_D depends both upon Re and m . The dependence of C_D upon R_2/R_1 , and thus the "blockage" effect due to drops shielding other drops from the flow, is here neglected. The Reynolds number is based upon u_d . It is important to notice that these two equations yield the correct limits in the cases of no evaporation ($\dot{m} \rightarrow 0$), no slip ($u_r \rightarrow 0$), and quiescent ambient gas ($u_g \rightarrow 0$).

Since the kinetic evaporation law and the equation of state form a non-linear implicit set of equations for the pressure and evaporation rate, a

predictor-corrector scheme is used to solve the entire set of equations. The drop temperature is solved as a four-term truncated series in powers of the nondimensional radial coordinate, z , and a GEAR integrator package is used to solve the set of ODE's. For each integrator step, the iteration starts with the prediction of the drop temperature. Then the equation of state and kinetic evaporation law are solved using a Newton-Raphson iteration for the pressure and evaporation rate. Next, the convective correction is applied to the evaporation rate and finally the drop temperature is corrected. The iteration is repeated, starting with the Newton-Raphson procedure, until convergence is obtained. Thus, each time step requires a nested double-loop iteration to calculate the drop temperature, evaporation rate and pressure. The calculations can be performed on a personal computer or on a faster computer if more speed is desired.

An interesting quantity to calculate is the penetration distance of the surrounding flow into the cluster. This is done by following the cluster on its trajectory and identifying this distance with the relaxation distance, which is the distance travelled to the location where $u_r=0$. Thus, Eq. (2) is rewritten in Lagrangian variables and integrated. The solution is

$$L_p = \frac{2 \ln [1 + u_r^0 \rho_g (\rho_g / m_d + n) A_d C_D / (2mn)]}{(\rho_g / m_d + n) A_d C_D} \quad (4)$$

If the ratio L_p / \tilde{R} , where \tilde{R} is the cluster radius, is larger than unity, penetration is important and thus evaporation is controlled by convection. In contrast if L_p / \tilde{R} is much smaller than unity, evaporation is controlled by diffusion. Between these two regimes there is an intermediate regime where both convection and diffusion are important. In this intermediate regime, the evaporation rate is very close to that in the convective evaporation regime

since convective effects dominate diffusive effects during evaporation. This is illustrated in Figure 5 reproduced from Ref. 40. Calculations (40) of L_p/\bar{R} with $\bar{R}=10$ cm show that the diffusive regime correspond to the very dense ($n \geq 10^5 \text{cm}^{-3}$) and dense ($10^5 \text{cm}^{-3} > n \geq 10^4 \text{cm}^{-3}$) clusters, whereas the convective regime corresponds to dilute clusters ($n < 10^3 \text{cm}^{-3}$; $\phi > \phi_s = 15.7$ for n-decane where ϕ and ϕ_s are the air/fuel and stoichiometric air/fuel mass ratio respectively). Figure 5 shows that the evaporation time reaches an asymptote fast as ϕ increases from the dense to the dilute regime. Additionally, this figure shows that the model is not very sensitive to the drag model used, providing the drag model accounts appropriately for the "blowing" effect due to evaporation. This blowing effect tends to decrease the drag coefficient by comparison to the non evaporation case.) The conclusion regarding drag modeling is valid for the small to moderate range of relative velocities used in the calculation. Furthermore, the plots of Figure 5 show that u_r^0 is a relatively weak parameter for controlling evaporation in both the dense and dilute regime.

The variation of the relative velocity of drops evaporating in clusters of various initial equivalence ratios is shown in Figure 6. Figures 7 and 8 show respectively the variation of the drop velocity and Reynolds number with residual drop radius. Figure 6 shows that the relative velocity of a dense cluster of drops decreases faster than does the relative velocity of a dilute cluster. The opposite is true for the drop velocity, as shown in Figure 7. This is due to the fact that when a dense cluster of drops moves through the gas it exposes a greater surface area to the flow because at fixed \bar{R} , the number of drops in the cluster is larger. For this reason there is a stronger interaction between drops and gas, and thus faster relaxation of u_r to zero. In contrast, u_d depends on the inertial effect of the cloud. Since a dense cloud has a

larger mass, it slows down less than a more dilute cloud. Finally, we find that the Reynolds number decreases very fast during the drop lifetime, in agreement with the isolated drop results of Dwyer and Sanders (44). These results also show that in convective flows, the concept of cluster density is strongly related to the value of the relative velocity between drops and gas. Dense clusters quickly become "non-porous," that is, impenetrable to the outer flow. In this case only the outer shell of drops is exposed to the flow. In contrast, dilute clusters are "porous" and the ambient flow substantially penetrates into the cluster.

The results of Bellan and Harstad (40) show that the drop temperature becomes uniform very fast in dense clusters of drops (about 1% of the drop lifetime). Additionally, as depicted in Figure 9 it is found that the drop temperature also becomes quickly uniform even for dilute collections of drops, although the heat-up time is now about 20% of the drop lifetime, and thus cannot be ignored. This is to be contrasted with computational results for single drops which showed that the temperature was staying nonuniform during most of the drops lifetime (45). In agreement with the results of Ref. (45) Figure 9 shows that the drop temperature continues to increase during the entire drop lifetime for dense and dilute clusters of drops. It must be pointed out that the results of Ref. (40) were obtained using a transient conduction equation to describe droplet heating. This is justified because the ratio of the characteristic time for circulation to the characteristic time for heat-up, $[\lambda_l/(\rho_l C_{pl})]/(\mu_l/\rho_l)$, is of the order of 3×10^{-2} . Here λ , C_p and μ are heat conductivity, heat capacity at constant pressure and viscosity, respectively, and the subscript "l" refers to liquid. Thus, the heating time is indeed independent of the circulation time, justifying the use of the spherically-

symmetric heat-conduction equation. Based upon these results, it seems appropriate to ignore drop-temperature nonuniformities when one considers the evaporation of dense clusters of drops for single - component fuels. Thus it is appropriate to use a one dimensional spherically symmetric model to describe the evolution of the drop temperature, instead of the more sophisticated model of Ref. (45). Since subgrid models should be computationally economical, because they are to be incorporated into large and expensive macroscale codes, the use of a simpler model could yield substantial computational savings.

2. Constant Pressure (Variable-Volume) Cluster Models.

2.A. Evaporation

While the models described above contribute to understanding the difference between the evaporation of dense and dilute clusters of drops, such models are not appropriate as subgrid models. The reason for this is the lack of appropriate boundary conditions at the macroscale level in order to describe the interactions with the surroundings appropriately and self consistently. These boundary conditions provide the coupling between the microscale and the macroscale and thus are crucial to a subgrid model.

The models described next apply to clusters of drops that are as large as, or larger than the Taylor macroscale in a flow; that is, they are at least as large as the largest dynamically significant eddies in the flow. This means that, unless the scale of the computational grid is larger than the Taylor macroscale, the following models cannot be used as subgrid models. Unfortunately, this means that if such models are incorporated as submodels, the grid may have to be rather coarse and thus the calculations will lack detail.

The development of submodels for a finer grid scale is an important area of future research.

In Bellan and Harstad (5) a model accounting for mass, species and energy transfer across the surface of the cluster is formulated. In this model the drops move with respect to each other and thus expansion and contraction of the cluster may occur. Thus, in contrast to the models of References (37) and (40), the drop number density becomes a time-dependent variable, whereas pressure is taken as constant. A pictorial representation of the situation studied is shown in Figure 10a. In this formulation the gas density inside each sphere of influence is no longer uniform, but becomes a function of the radial position in the sphere. The model still keeps the previous basic features with conservation equations for the drop and gas inside the sphere of influence, global conservation equations for the entire cluster and the perfect gas law, but there are two new elements here: (a) a model for transport from the surrounding gas to the cluster, and (b) a model for the drop motion inside the cluster that pertains to transport from the cluster to the surrounding gas.

2.A a. Transfer from the surrounding gas to the cluster.

Consistent with the assumption that the cluster size is much larger than the size of the smallest dynamically important eddies, turbulent heat transfer may be described using a Nusselt number approach. Further, similarity between heat and mass transfer is assumed and thus $Sh_c = Nu_c$. Because it is very important to understand how the history of turbulence affects cluster behavior, two turbulence models are considered and compared.

In the first turbulence transfer model the drops do not act initially as an entity, but rather as individuals and turbulence builds up with time if the

cluster porosity, that is if u_r , diminishes significantly. In the second turbulence model, the cluster surroundings are assumed to be initially turbulent.

2.A.b. Transfer from the cluster to the surrounding gas.

Similar to the above, two models are considered here as well. In the first model transport is represented using a "trapping factor" model for the gas velocity at the edge of the sphere of influence (45) to calculate the mass loss. The trapping factor is an interpolation coefficient between a strictly steady gas phase limit where there is strong evaporation and maximum new vapor passes through the sphere of influence (representing the dense case, $m_g \ll m_d$), and the limit of null loss where all new vapor is trapped inside the sphere of influence (representing the dilute case, $m_d \ll m_g$).

The second model for the drop motion inside the cluster (46) introduces a similarity parameter, $\xi = \tilde{r}/\tilde{R}$. For a given drop, ξ is a constant which varies in the cluster between zero and unity. Whereas in the previous model drops and gas were moving respectively with velocities u_d and u_g in the axial direction, now there is an additional radial velocity component, respectively $\xi \, d\tilde{R}/dt$ and $\xi \, u_{ge}$ where u_{ge} is the gas velocity at the edge of the cluster. Thus the radial slip velocity at the edge of the cluster is $u_{re} = d\tilde{R}/dt - u_{ge}$. Note that on a large length scale the evaporating drops form a uniform mass source density and this is consistent with the similarity assumption. In this model, global momentum equations for radial and axial velocities are formulated in a manner similar to Bellan and Harstad (40); unlike in Reference (40), ξ now appears in the momentum equations. In general, the momentum equations are consistent with similarity with the exception of nonlinear drag and convective derivative terms. To be consistent with the other global equations where the radial dependence

does not appear, average equations are formed by integrating over ξ . This eliminates some coupling between axial and radial velocities due to convective derivative terms, and also means that the tendency of nonlinear drag to destroy the self similar radial motion is neglected.

Figure 11 reproduced from Bellan and Harstad (47) shows a comparison between the prediction of the four models. These models are listed in Table II. In the dilute cluster regime there is excellent agreement between the predictions of all four models because evaporation of drops in this regime is not controlled by transport processes. In contrast, in the dense cluster regime transport processes control evaporation, resulting in substantial quantitative disagreement among the results of the four models. Qualitatively, the predictions should be similar: τ_{evap} reaches a maximum in the dense regime and decreases as ϕ decreases. The cluster is initially denser, and eventually saturation is obtained before complete evaporation. Thus, validation of dense cluster or dense spray models requires experimental results precisely in this large drop number density regime.

The models of References (5) and (47) also predict that in absence of internal vortical motion inside the cluster, dense clusters will first contract due to internal gas cooling and then expand due to turbulent transport of hot external gas inside the cluster. The stronger is the turbulent transport and the smaller is the cluster, the smaller the contraction and the larger the recovery towards the original size. In general, it seems that clusters do not recover their original size by the time the drops have evaporated. Total fuel-mass loss from clusters turns out to be very small for large clusters of drops, but increases substantially for small clusters of drops (47). The accurate prediction of this quantity is crucial for dense clusters of drops because

ignition is expected to occur outside of the cluster (48) and it is precisely this ejected fuel vapor which ignites to establish a flame surrounding the cluster.

2.B. Ignition and Combustion

The prediction of droplet ignition in clusters is very challenging from many points of view. In power generation systems, clusters of drops are exposed to convective flows that sweep fuel vapor ejected from the cluster into the wake regime behind the cluster. Thus, ignition will be a result of the interplay between transport processes from the cluster to the surroundings which bring the fuel vapor from the interior to the exterior of the cluster, convective effects outside of the clusters which sweep the fuel vapor into the wake regime, and chemical kinetics. This interpretation is in agreement with the experimental results of Sato et al. (50). The authors (50) infer from their experiments that ignition occurs at the stagnation point of the tip of the fuel spray. The ignition delay is due to the interplay between two effects described by two characteristic times. The first effect is convection, and thus the characteristic time is that spent for reducing the velocity gradient at the spray tip below a critical velocity gradient at which ignition occurs. The second effect is chemical kinetics, and thus the characteristic time is that for ignition (that is chemical run-away) to occur at a given velocity gradient. Sato's conclusion is that in their particular experiment the latter time is much smaller than the former, and thus chemistry dominates ignition delay times. In other experiments convection effects might dominate chemical effects. This picture is very different from that of the ignition of a single, isolated drop in quiescent surroundings or even that of single-droplet ignition in a convective flow (49).

It is important to notice that in cluster ignition, convective effects are important. If the cluster is dilute, the effect of convection around each drop will be important. If the cluster is dense, the convective effects around the drops located on a shell at the boundary of the cluster will be important because outer flow penetration is confined to this shell. The denser the cluster is, the thinner will be the shell.

The experimental observation of thin flames surrounding clusters of drops (2, 3) suggests that it may be reasonable to describe ignition and combustion using the classical flame-sheath concept (8). This means that instead of using a chemical kinetic approach to ignition and combustion, an ignition criterion combined with a flame-sheath approach might be used instead.

Such an ignition criterion was developed by Bellan and Harstad (48). To predict the ignition location, a two dimensional map is built to compare convective and diffusive effects. The convective effects are measured by the extent of flow penetration into the cluster, quantified as the ratio of the penetration distance to the radius of the cluster. If this ratio is much smaller than unity, evaporation and thus ignition is diffusion controlled. Therefore the ignition location can be identified using the criteria developed by Labowsky and Rosner (26) for quasi-steady combustion to determine whether particles burn individually or collectively. Moreover, in this diffusion-controlled regime, the ignition timing is predicted using a Damköhler number criterion which compares characteristic diffusion and reaction times. This Damköhler number criterion is valid only for diffusion-controlled situations, and thus the corresponding ignition criterion is valid only for nondilute clusters of drops exposed to a moderate to weak convective flow. When the ratio of the penetration distance to the cluster radius is of the order of, or much

larger than unity, evaporation is respectively convection-diffusion and convection controlled. Since convection effects are always stronger than diffusion effects, the role of convection must be important during ignition. It is this author's opinion that a field computation, taking into account both convection and chemical kinetics is necessary to determine the ignition time in these situations. Ignition criteria similar to that of the Domköhler number, but also involving the Reynolds number for a single, isolated drop, would be irrelevant to cluster ignition, except for very dilute clusters. Such criteria cannot take into account the very important transport processes between the cluster and the surroundings. Bellan and Harstad (48) show that ignition of nondilute clusters of drops invariably occurs external to the cluster, and that the boundaries between the diffusive, convective-diffusive, and convective regimes defined above are functions of the fuel and the initial conditions.

Using the above model of cluster ignition, Bellan and Harstad (51) have formulated a model of nondilute cluster combustion. In this model, fuel evaporated from the drops is ejected out of the cluster at a rate determined by the balance of transport processes across the boundary of the cluster. After ignition there is a very short-lived, weak, premixed flame depleting all oxygen inside the cluster which is followed by a thin, counterflow diffusion flame. One crucial aspect of this combustion model is that the burning rate is not equal to the evaporation rate, in agreement with the experimental results of Koshland (11). Also, the flame temperature depends upon the cluster parameters unlike in the work of Correa and Sichel (25).

Figure 12 reproduced from Reference (51) shows the fraction of fuel burnt, f_B , at ignition and at the moment of drop disappearance for the weak and strong turbulence models described above versus the initial air/fuel mass ratio. As

experimentally observed by Koshland (11), there is still a substantial amount of fuel vapor left to burn when the drops disappear. Figure 13 shows the ratio between the fraction of fuel burnt and the fraction of fuel lost, f_B/f_{F2} , when $R=0$ versus ϕ^0 for the same conditions as those of Figure 12. When the cluster is initially denser (smaller ϕ^0 's), this ratio is smaller because more fuel is ejected from the cluster, making the flame stand further from the cluster.

More vigorous fuel evaporation and fuel loss, and shorter evaporation time, explains why the ratio between the flame radius and the cluster radius, \tilde{R}_F/\tilde{R} , is larger for turbulence model 2 than for turbulence model 1. This results in smaller values for f_B/f_{F2} when turbulence is strong (turbulence model 2) than when turbulence is weak (turbulence model 1).

In all calculations carried out with this model, varying parametrically the initial cluster size, the ambient gas temperature and the initial drop temperatures, the flame establishes itself very close to the cluster boundary and \tilde{R}_F/\tilde{R} is at most 1.01. During burning \tilde{R}_F/\tilde{R} varies but never exceeds 1.01. This is in complete agreement with the experimental observations of Allen and Hanson (2, 3) and Nakabe et al. (4) for "pockets" of drops.

The restricted range of initial air/fuel mass ratios investigated with this model corresponds to the range of moderately-dense clusters. For larger values of ϕ^0 , the gas phase inside the cluster becomes lean at ignition. The present model is limited to describing combustion after ignition when the gas phase inside the cluster is rich. For smaller values of ϕ^0 , the cluster becomes very dense and ignition does not occur before the drops disappear. This means that burning will occur in presence of the gas phase only, a situation that the present model does not treat properly. In this latter situation turbulence

effects and flame wrinkling become dominant, and these phenomena are not modeled here.

Figure 14, reproduced from Reference (51) shows that smaller clusters of drops are more efficient at burning fuel, a fact which agrees with intuition.

2.C. Evaporation and Dispersion of Electrostatically Charged Drops

It was mentioned in the Introduction that soot production is a strong function of drop proximity, increasing as the drops get closer and trap the fuel rich gas between them where soot formation reactions occur. Calculations based upon a simple model of electrostatic drop dispersion carried out by Bellan (52) indicated that electrostatic drop dispersion might be a viable concept for rendering clusters more dilute and thus controlling soot production. Recently, a more realistic model of evaporation of electrostatically charged drops has been formulated by Harstad and Bellan (46), and some of the results obtained with this model are presented below in order to illustrate another aspect where there is a difference of behavior between dense and dilute clusters of drops.

The model describing electrostatic dispersion and evaporation is the same as that of Bellan and Harstad (47) with the further addition of the charge effects. The radial electric field and electrostatic force are taken proportional to the similarity parameter ξ defined earlier. Both momentum and energy equations take into account these effects which are averaged by integrating over ξ . Figures 15, 16 and 17, reproduced from Reference 46, show respectively the evaporation time and the volume ratio (final volume/initial volume) versus the initial air/fuel mass ratio for various charge ratios, as well as the evaporation time versus the charge ratio for a dense cluster of drops. The charge ratio is the charge divided by the maximum charge feasible for a given drop size (53). As seen in Figure 15, only dense clusters are

affected by drop charge. The charge acts to expand the cluster into the hot ambient air, as seen in Figure 16, thus promoting evaporation. For dilute clusters the electrostatic forces are too weak to produce any significant expansion.

Some of the results discussed above, together with the results illustrated in Figure 17, show that the predicted evaporation time does not depend upon turbulence models for nondense clusters of drops, independently of whether the drops are charged or uncharged. In contrast, the turbulence models can greatly affect the predictions for uncharged dense clusters of drops (5, 47). This is due to the restricted available thermal energy for evaporation in the relatively small interstitial region of dense clusters, along with comparative isolation from the hot ambient gas. For uncharged drops, only turbulence can break this isolation, whereas for highly charged drops, charge-induced expansion dominates. As seen in Figure 17, for drop charges greater than half the value proposed by Kelly (53), the evaporation time is independent of the turbulent model. In Figures 15-17 the evaporation time is that obtained at $R_1 = 0.3$ which is the value close to that at which Rayleigh instability occurs. The calculations are stopped at this point thus avoiding the modeling of the ensuing drop breakup.

IV. CONCLUSIONS

The models and results presented in Sections II and III underscore the difficulty of formulating appropriate subgrid models for use in computationally intensive codes that could describe a variety of combustors. The difficulty is associated with the many phenomena involved, some of which are important only in limited regimes. However, since subgrid models must be reliable over a wide

range of physical situations, it is important to account for all these phenomena.

The computational and experimental results obtained so far show that dense and dilute collections of drops behave very differently. For dense clusters of drops, the numerical results show that the initial turbulence level of the surrounding flow is crucial in determining the evaporation time and the dynamics of the cluster size. This is due to several interaction factors. In the absence of vortical motion inside the cluster, any initial relative velocity between drops and gas inside the cluster decays very fast to zero and thus relative convection effects primarily enhance evaporation initially. The internal temperature of the drops increases rapidly, becomes uniform very fast compared to the drops lifetime, and continues to increase during the entire evaporation time. The energy thus transferred from the gas phase to a relatively large quantity of liquid, particularly in the absence of turbulent mixing with large volumes of hot gas, cools the gas very rapidly during this initial period and the cluster size decreases as a result. The turbulent transfer of heat and mass from the ambient to the cluster can significantly influence evaporation. If this transfer is vigorous, evaporation continues and the cluster size increases rather than decreases. In the absence of turbulent mixing, saturation may occur before complete evaporation.

In contrast, the evaporation of dilute clusters of drops is not controlled by turbulence. In dilute clusters the energy transferred from the gas to the drops has a negligible impact upon the total energy content of the gas. Thus, in the absence of internal vortical motion the cluster size stays nearly equal to its initial value. Both the relaxation time of the relative velocity between

drops and gas inside the cluster, and the time taken for internal drop temperature to become uniform are comparable to the drop lifetime.

The above results have direct bearing upon the validation of such subgrid models using comparison with experimental observations. They show that results obtained only from dilute portions of a spray are inappropriate to use for comparison because they cannot take into account the importance of the transport phenomena which are crucial in the dense regions of the spray. This is especially important for the subgrid models since, as pointed out here, appropriate boundary conditions for the microscale of the computation are critical in order to couple to the macroscale. It should be noticed that the models presented here are not truly appropriate as subgrid models, except for calculations where the macroscale of the system is larger than or comparable to the Taylor macroscale. Modified approaches must be used to mathematically describe situations where the Taylor microscale and the cluster size are of the same order of magnitude.

The above considerations of spray and cluster ignition have shown that there is still a considerable uncertainty regarding the description of this phenomenon, even qualitatively, at the microscale level. The difficulty arises because in practical systems ignition is always controlled by convection. For dense clusters of drops ignition occurs outside the cluster where convective effects are important. For dilute clusters of drops ignition might occur inside the cluster. Since the relative velocity between drops and gas has a characteristic relaxation time comparable to the lifetime of the drop in this case, convection effects are important again. Thus, it appears that it would be necessary to solve differential equations taking into account both convection and chemical kinetics at the microscale level. Clearly, a simpler

method is desirable, making this an area where new strategies definitely are needed to deal with the situation. It should be pointed out that this discussion is relevant not only to the mathematical description of ignition, but also to flame stability.

Cluster flames cannot be either quasi-steady or thin just after ignition. However, the flame sheath approximation still seems to be a useful concept which qualitatively describes flames around clusters, providing one accounts properly for transport processes to and from the cluster and does not make the assumption that the burning rate equals the evaporation rate. When the flame sheath concept is properly incorporated into a model, this model yields two important results: 1) that the flame sits just at the periphery of the cluster, and 2) that the drops disappear well before the entire fuel vapor is burnt. Both these results are in complete agreement with experimental observations.

Finally, although numerical methods have not been discussed here in detail, they are a very important component of these two-level (macroscale-microscale) models and are expected to become even more important once these subgrid models have to be incorporated into the macroscale calculations.

Most present large scale codes are based upon the assumption that the volume element does not change in size and that the pressure is variable within the volume (54). Lagrangian calculations, where the volume does change, are also occasionally performed, but their implementation in multidimensions requires much more effort (54). Typically, all large scale codes solve nonlinear, coupled mass, species, momentum and energy equations using a variety of techniques. In unsteady codes, the solution is obtained by iterating several times at each time step until convergence of the nonlinear and of the coupled terms is obtained.

Since clusters of evaporating drops change their volume during the drops lifetime, even in the absence of internal vortical motion, it seems that the Lagrangian codes are physically much more appropriate to describe the macroscale in this two-level (macroscale - microscale) description. The Lagrangian description also offers the advantage of the simplest boundary conditions at the surface of the cluster. These boundary conditions couple the microscale to the macroscale and they describe transfer of mass, species, momentum and energy across the surface of the cluster. The density, composition, temperature and velocity field of the gas surroundings the cluster must be provided at each time step iteration by the solution of the macroscale equations. The motion of the cluster surface is given by the solution of the global conservation equations for the cluster. In the Lagrangian description the cluster has an identity because it contains the same drops throughout the calculation and the volume of the cluster is defined as the volume contained inside the envelope of these drops.

In contrast, in an Eulerian calculation a fixed volume element cannot represent the same drops throughout the calculation, and thus the cluster representation is no longer meaningful. In the Eulerian representation drops move between volume elements and thus conservation equations for the number of drops in each volume element are additionally needed. Moreover, the boundary conditions at the fixed surface of the volume element have to include now terms representing transport of drops, gaseous mass, species, momentum and energy required to keep the volume constant. Similar to the microscale-macroscale coupling at each time step iteration in a Lagrangian code, the macroscale Eulerian code must also provide the density, composition, temperature and

velocity field of the gas surrounding the cluster for coupling with the microscale calculations.

The present calculations (5) of cluster evaporation, ignition and combustion are rather inexpensive. In average, less than 10 sec. of CPU time is spent on a UNIVAC 1100 to calculate the entire history of the cluster for a given set of initial conditions and fixed values of the density, composition, temperature and velocity field in the gas surrounding the cluster. The model and code are flexible enough to allow the use of more realistic boundary conditions and to be coupled to a macroscale code. The final cost of a code based upon the two-level description will be determined by the macroscale code and by the efficiency with which the microscale code is coupled to the macroscale code.

ACKNOWLEDGEMENTS

The author wrote this manuscript while supported by the U.S. Department of Energy Utilization Research, Energy Conversion and Utilization Technologies Program, Mr. Marvin Gunn, Jr., Program Manager, and by the Air Force Office of Scientific Research, Directorate of Aerospace Sciences, Airbreathing Combustion, Dr. Julian Tishkoff, Program Manager, both through interagency agreements with the National Aeronautics and Space Administration.

The author would also like to acknowledge numerous enlightening discussions with Dr. Kenneth G. Harstad of the Jet Propulsion Laboratory.

REFERENCES

1. Chigier, N. A., Mao, C. P. and Oechsle, V., "Structure of Air-Assist Atomizer Spray," paper 7-6A, CSS/WSS/Combustion Institute Spring Meeting, April, 1985; also private communication.
2. Allen, M. G. and Hanson, R. K., "Planar Laser-Induced-Fluorescence Monitoring of OH in a Spray Flame," Optical Engineering, **25**, 12, pp. 1309-1311, (1986).
3. Allen, M. G. and Hanson, R. K., "Digital Imaging of Species Concentration Fields in Spray Flames," 21st Symp.-(International) on Combustion, pp. 1755-1762, (1986).
4. Nakabe, K., Mizutani, Y., Tanimura, S., and Hirao, T., "Burning Characteristics of Premixed Sprays in Gas-Liquid Combusting Mixtures," Proceedings of the Joint Conference WSS/JS/The Combustion Institute Honolulu, Hawaii, pp. 227-229, (1987); also Combust and Flame, **74**, pp. 39-51, (1988).
5. Bellan, J., and Harstad, K., "Turbulence Effects During Evaporation of Drops in Clusters," Int. J. Heat Mass Transfer, **31**, 8, pp. 1655-1668, (1988).
6. Crowe, C. T., Sharma, M.P., and Stock, D.E., "The Particle-Source-In Cell (PSI-CELL) Model for Gas-Droplet Flows", Journal of Fluids Engineering, pp. 325-332, 1977.
7. Tambour, Y., "A Lagrangian Sectional Approach for Simulating Droplet Size Distribution of Vaporizing Fuel Sprays in a Turbulent Jet," Combust. and Flame, **60**, pp. 15-28, (1985).
8. Yule, A. J., Ah Seng, G., Felton, P. G., Ungut, A., and Chigier, N. A., "A Laser Tomographic Investigation of Liquid Fuel Sprays", 18th Symposium (International) on Combustion, pp. 1501-1509, (1981).
9. Williams, F. A., "Combustion Theory," Addison-Wesley, pp. 37-56, (1965).
10. Beer, J. M., and Chigier, N. A., "Combustion Aerodynamics," Applied Science Publisher Limited, London 1972.
11. Koshland, C. P., "Combustion of Monodisperse Hydrocarbon Fuel Droplet Clouds," Topical Report T-248, High Temperature Gasdynamics Laboratory, Stanford University, 1985.
12. Koshland, C. P., "Combustion of Interacting Droplets in a Droplet Cloud Flame," paper 85-10 presented at the Western States Section/The Combustion Institute Fall Meeting, Davis, CA, 1985.

13. Koshland, C. P., and Bowman, C. T., "Combustion of Monodisperse Droplet Clouds in a Reactive Environment," presented at the Western States Section/The Combustion Institute Fall Meeting, Oct. 17-18, Los Angeles, CA.
14. Chigier, N. A., and McCreath, C. G., "Combustion of Droplets in Sprays," Acta Astronautica, 1, pp. 667-710, (1976).
15. Rao, K. V. and Lefebvre, A. M., "Evaporation Characteristics of Kerosene Sprays Injected Into a Flowing Air Stream," Combust. and Flame, 26, pp. 303-309, 1976.
16. Sangiovanni, J. J., and Liscinsky, D. S., "Soot Formation Characteristics of Well-Defined Spray Flames," Proc. of the 20th Symp. (Int.) on Combustion, pp. 1063-1073, 1984.
17. Chernansky, N. P., and Sarv, H., "Pollutant Formation in Monodisperse Fuel Spray Combustion," NASA Conference Publication 2268, pp. 39-47, 1982.
18. Zung, J. T., "Evaporation Rate and Lifetimes of Clouds and Sprays in Air-The Cellular Model," J. of Chem. Phys., 46, 6, pp. 2064-2070, 1967.
19. Tishkoff, J. M., "A Model for the Effect of Droplet Interactions on Vaporization," Int. J. Heat Mass Transfer, 22, pp. 1407-1415, 1979.
20. Suzuki, T. and Chiu, H. H., "Multi-droplet Combustion of Liquid Propellants," Proceedings of the 9th Int. Symp. and Space Technology and Science, pp. 145-154, 1971.
21. Chiu, H. H. and Liu, T. M., "Group Combustion of Liquid Droplets," Combust. Sci. and Techn., 17, pp. 127-142, 1977.
22. Zhou, X-Q., and Chiu, H. H., "Spray Group Combustion Processes in Air Breathing Propulsion Combustors", paper AIAA-83-1323, presented at the AIAA/SAE/ASME 19th Joint Propulsion Conference, Seattle, June, 1983.
23. Kim, H. Y., and Chiu, H. H., "Group Combustion of Liquid Fuel Sprays," paper AIAA-83-0150, presented at the AIAA 21st Aerospace Sciences Meeting, Reno, January, 1983.
24. Jang, S. D., and Chiu, H. H., "Theory of Renormalized Droplet: II Non-Steady Vaporization of Droplet in Non-Dilute Sprays," paper AIAA-88-0639 presented at the 26th Aerospace Sciences Meeting, Reno, January, 1988.
25. Correa, S. M., and Sichel, M., "The Group Combustion of a Spherical Cloud of Monodisperse Fuel Droplets," Proc. of the 19th Symp. (Int.) on Combustion, pp. 981-991, 1982.
26. Labowsky, M., and Rosner, D. E., "Group Combustion of Droplets in Fuel Clouds., I. Quasi-steady Predictions," Proc of the ACS Meeting, pp. 63-79, San Francisco, Aug. 31 - Sept. 1, 1976.

27. Labowsky, M., "A Formalism for Calculating the Evaporation Rates of Rapidly Evaporating Interacting Particles," Combust. Sci. and Techn., 18, pp. 145-151, 1978.
28. Labowsky, M., "Burning Rates of Linear Fuel Droplet Arrays," paper 80-WA/HT-34 presented at the ASME/WAM, Chicago, 1980.
29. Labowsky, M., "Calculation of the Burning Rates of Interacting Fuel Droplets," Combust. Sci. and Techn., 22, pp. 217-226, 1980.
30. Sangiovanni, J. J. and Labowsky, M., "Burning Times of Linear Fuel Droplet Arrays: A Comparison of Experiment and Theory," Combust. and Flame, 47, pp. 15-30, 1982.
31. Samson, R., Bedeaux, D., Saxton, M. J., and Deutch, J. M., "A Simple Model of Fuel Spray Burning I: Random Sprays," Combust. and Flame, 31, pp. 215-221, 1978.
32. Umemura, A., "A Unified Theory of Quasi-Steady Droplet Combustion," Proc. 18th Symp. (Int.) on Combustion, pp. 1355-1363, 1980.
33. Ray, A. K., and Davis, E. J., "Heat and Mass Transfer with Multiple Particle Interactions. Part I. Droplet Evaporation," Chem. Eng. Commun., 6, pp. 61-79, 1980.
34. Marberry, M., Ray, A. K., and Leung, K., "Effect of Multiple Particle Interactions on Burning Droplets," Combust. and Flame, 57, pp. 237-245, 1984.
35. Annamalai, D., "Evaporation, Ignition and Combustion of a Cloud of Droplets," Paper 3-6B-85 presented at the Joint Western States Section/Central States Section Spring Meeting of the Combustion Institute, San Antonio, 1985.
36. Shuen, J-S., "Effects of Droplet Interactions on Droplet Transport at Intermediate Reynolds Numbers," Paper AIAA-87-0137, presented at the 25th Aerospace Sciences Meeting, Reno, January, 1987.
37. Bellan, J. and Cuffel, R. "A Theory of Non-Dilute Spray Evaporation Based Upon Multiple Drop Interaction", Combust. and Flame, 51, pp. JJ-67, 1983
38. Kittel, C., "Introduction to Solid State Physics", 3rd Edition, John Wiley and Sons, Dec., 1966
39. Law, C. K., "Adiabatic Spray Vaporization with Droplet Temperature Transient", Combust. Sci. and Techn., 15, pp. 65-76, 1977
40. Bellan, J., and Harstad, K., "The Details of the Convective Evaporation of Dense and Dilute Clusters of Drops", Int. J. Heat Mass Transfer, 30, 6, pp. 1083-1093, 1987

41. Cliffe, K. A., and Lever, D. A., "Isothermal Flow Past a Blowing Sphere", Int. J. Numer. Meth. Fluids, 5, pp. 709-725, 1985
42. Yuen, M. C., and Chen, L. W., "On Drag of Evaporating Liquid Droplets", Combust. Sci. Tech., 14, pp. 147-154, 1976
43. Eisenkham, P., Arunchalam, S. A., and Weston, J. A., "Evaporation Rates and Resistance of Burning Drops", Proc. 11th Symp. (Int.) on Combustion, pp. 715-728, 1966
44. Dwyer, H. A., and Sanders, B. R., "Detailed Computation of Unsteady Droplet Dynamics", Proc. 20th Symp. (Int.) on Combustion, pp. 1743-1749, 1984
45. Prakash, S., and Sirignano, W.A., "Theory of Convective Droplet Vaporization with Unsteady Heat Transfer in the Circulating Liquid Phase", Int. J. Heat Mass Transfer, 23, pp. 253-268, 1980
46. Harstad, K., Bellan, J., "Electrostatic Dispersion of Drops in Clusters", Combust. Sci. and Tech., 63, 4-6, pp. 169-172.
47. Bellan, J., and Harstad, K., "Transport-Related Phenomena for Clusters of Drops:", Int. J. Heat Mass Transfer, in press
48. Bellan, J., and Harstad, K., "Ignition of Nondilute Clusters of Drops in Convective Flows", Combust. Sci. and Tech., 53, pp. 75-87, 1987
49. Dwyer, H. A. and Sanders, B. R., "A Detailed Study of Burning Fuel Droplets", Proc. 21st Symp. (Int.) on Combustion, pp. 633-639, 1986
50. Sato, J., Konishi, K., Okada, H., and Niioka, T., "Ignition Process of Fuel Spray Injected in the High Pressure High Temperature Atmosphere," Proc. 21st Symp. (Int.) on Combustion, pp. 695-702, 1986
51. Bellan, J. and Harstad, K., "Evaporation, Ignition and Combustion of Nondilute Clusters of Drops", presented at ASME/WAM, November 20 - December 2, 1988, Chicago, ILL; Combust. and Flame, in press
52. bellan, J., "A New Approach to Soot Control in Diesel Engines by Fuel-Drop Charging, Combust. Flame, 51, pp. 117-119, 1983
53. Kelly, A. J., "The Electrostatic Atomization of Hydrocarbons", J. of the Inst. of Energy, pp. 312-320, 1984
54. Oran, E. S., private communication.

NOMENCLATURE

A	area, cm^2
a	radius of the sphere of influence, cm
A_c	cluster transverse area, cm^2
C_D	drag coefficient for one drop
C_{Dc}	drag coefficient for the cluster of drops
C_p	heat capacity at constant pressure, $\text{cal/g}^\circ\text{K}$
f_B	mass of fuel burnt between ignition and drop disappearance/total fuel mass
f_{Fl}	mass of fuel lost from cluster from $t=0$ to drop disappearance/total fuel mass
L_{bn}	effective heat of evaporation at normal boiling point, cal/g
L_p	penetration distance, cm, Eq. (4)
\dot{m}	evaporation rate for one drop, $\text{g}/(\text{cm}^2 \text{ sec})$
m	mass, g
n	drop number density, cm^{-3}
N	number of drops
Nu_c	Nusselt number for the cluster
\tilde{R}	cluster characteristic length (radius, if cluster is spherical), cm
\tilde{r}	radial coordinate centered at the drop cluster, cm
r	radial coordinate centered at the cluster center, cm
R	radius of drop, cm
Pe	$2Ru_T/\nu$
\tilde{R}_f	radial location of the flame measured on the r coordinate, cm
R_1	R/R^0
R_2	a/R^0
Sh_c	Sherwood number for the cluster

T	temperature, °K
t	time, sec
u	velocity, cm/sec
V_c	cluster volume, cm ³
Y_i	mass fraction of species i
z	r/R

SUBSCRIPTS

0.3	instant when $R_1 = 0.3$
a	at the edge of the sphere of influence; interstitial
d	drop
d1	dilute
evap	evaporation
F	fuel
g	gas
nd1	nondilute
r	relative
v	vapor

SUPERSCRIPTS

o	initial
∞	in the far field

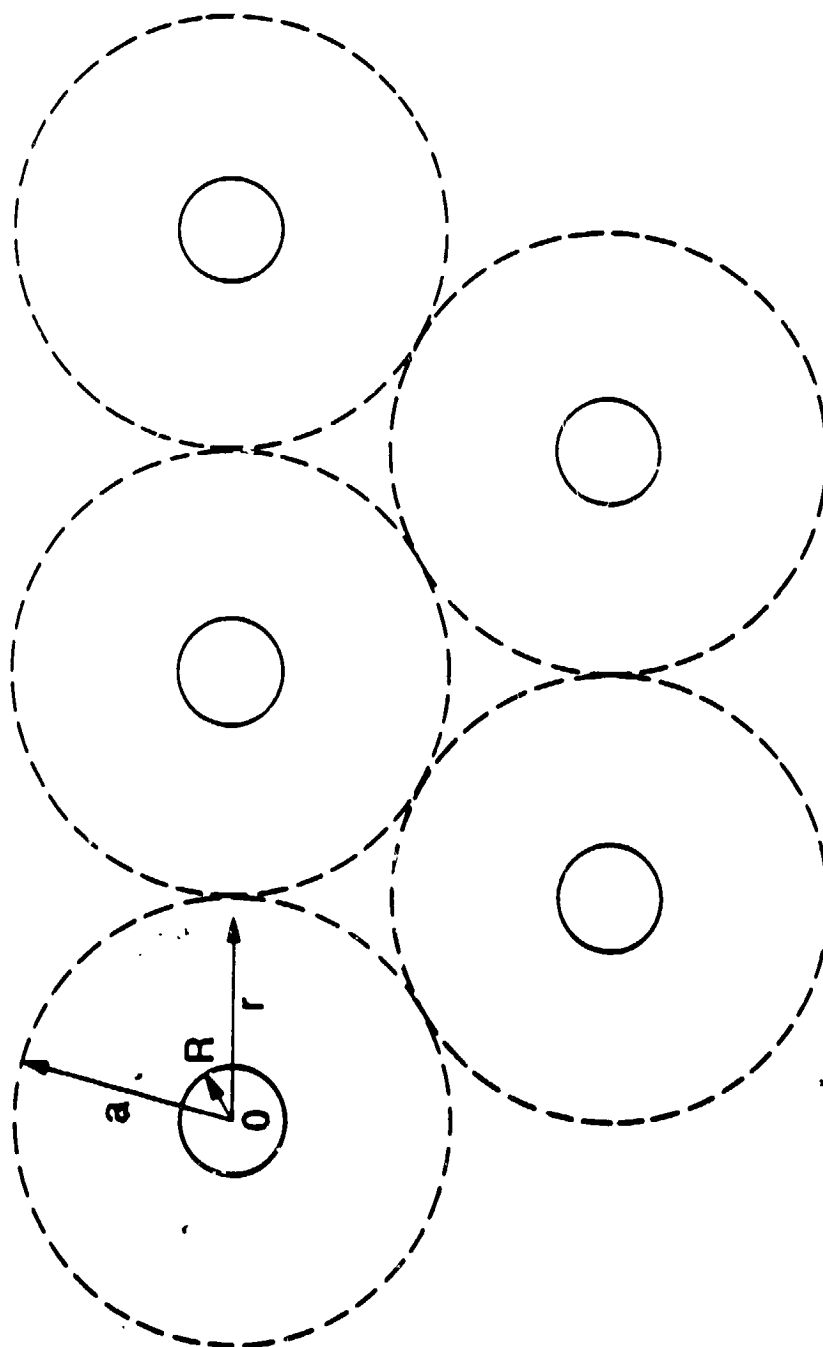
GREEK SYMBOLS

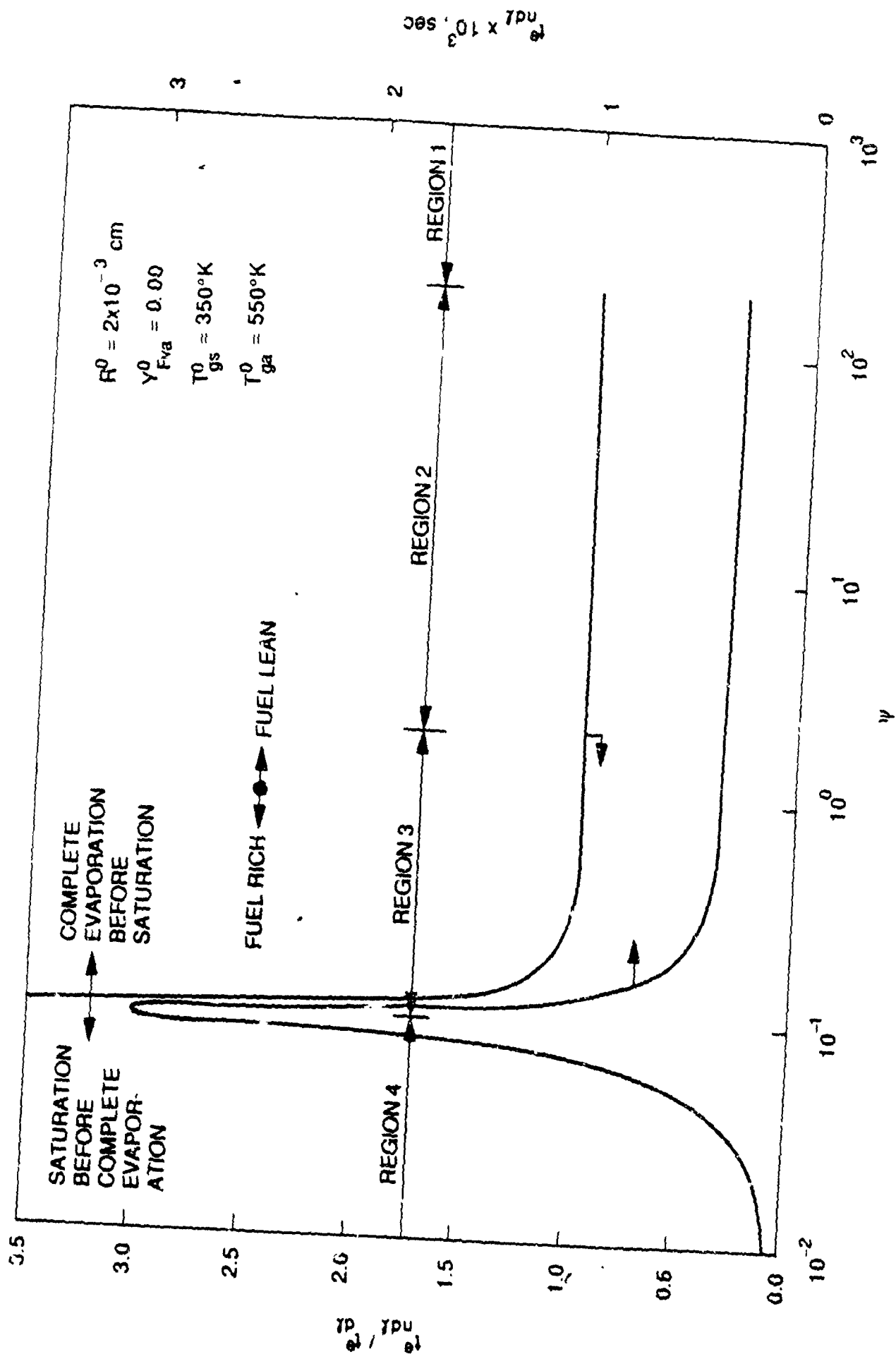
ν	kinematic viscosity, μ/ρ , cm^2/sec
ϕ	air-to-fuel mass ratio
ϕ_s	stoichiometric value of ϕ
ψ	equivalence ratio ϕ/ϕ_s
ρ	density, g/cm^3
θ	nondimensional temperature $C_p T/T_{bn}$
ξ	similarity parameter

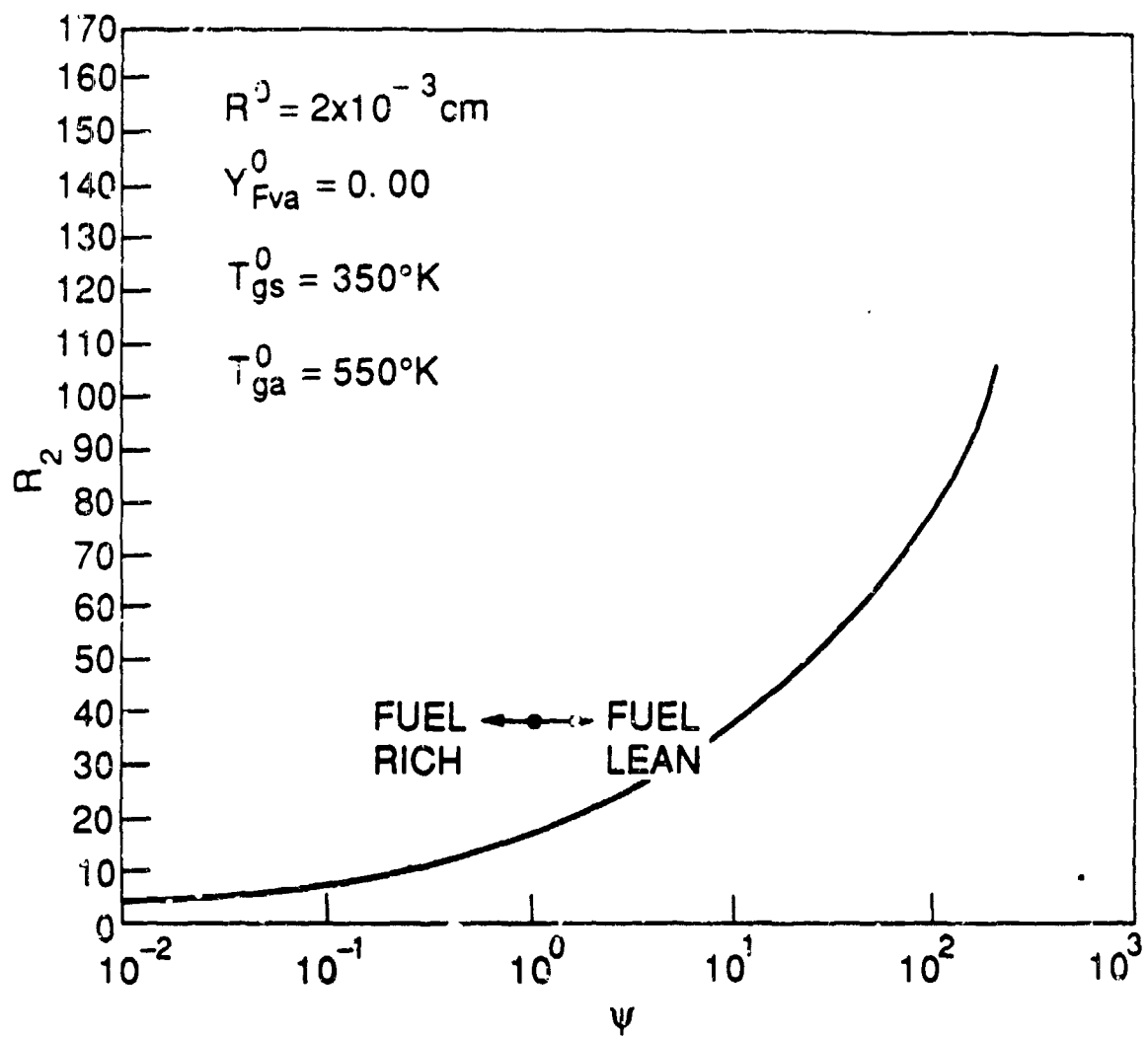
FIGURE CAPTIONS

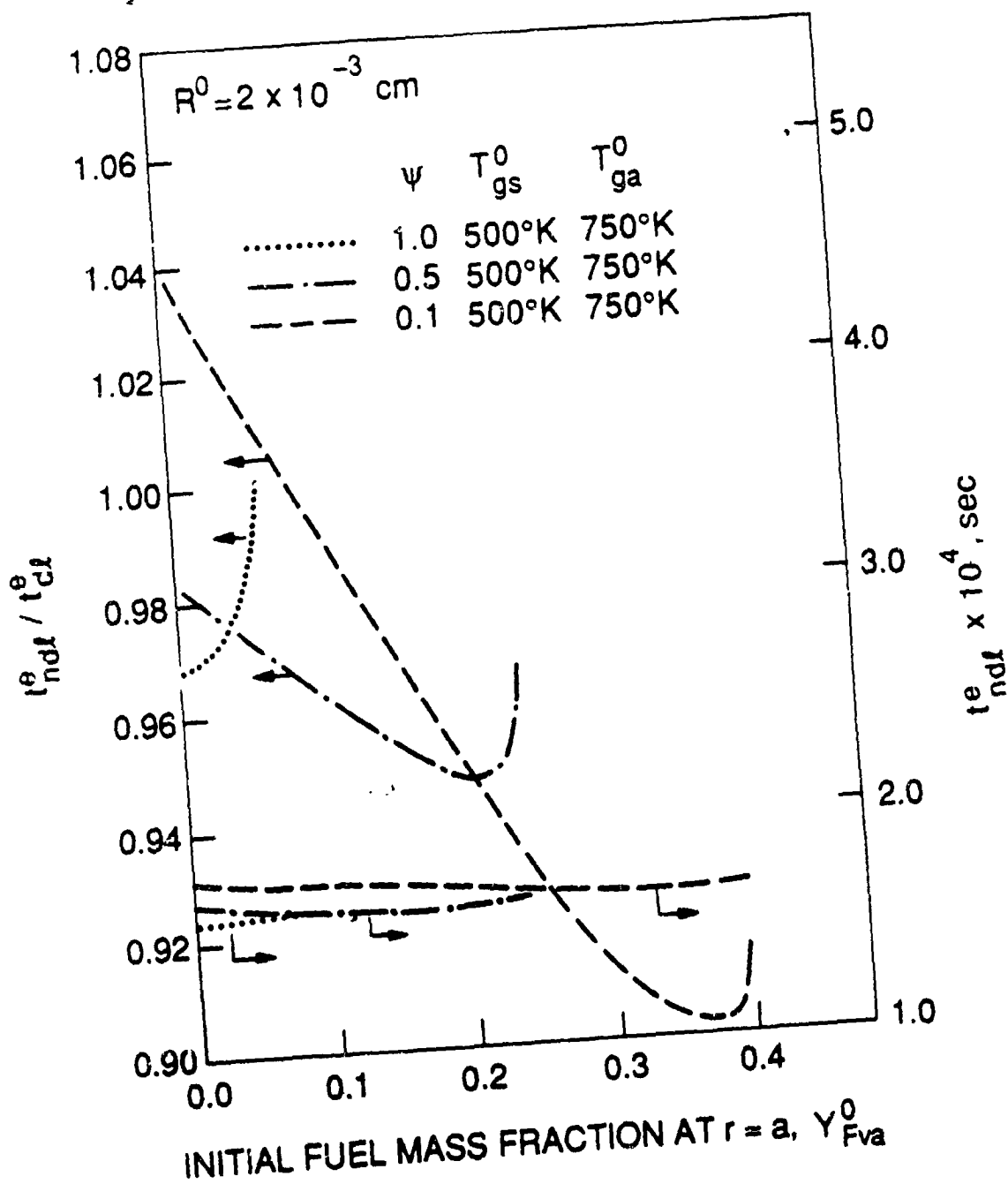
- Figure 1 Pictorial of drops in a cluster surrounded by fictitious spheres of influence.
- Figure 2 Variation of τ_{nd1}/τ_{dl}^e with ψ for a constant volume, adiabatically insulated cluster of drops.
- Figure 3 Nondimensional radius of the sphere of influence versus ψ .
- Figure 4 Variation of τ_{nd1}^e/τ_{dl}^e and τ_{nd1}^e with Y_{Fva}^0 for a constant volume, adiabatically insulated cluster of drops.
- Figure 5 The evaporation time versus ψ for several initial relative velocities and several drag models. $\tilde{R}=10\text{cm}$.
- Figure 6 Variation of the relative velocity with residual drop size for several ϕ 's. $\tilde{R}=10\text{cm}$.
- Figure 7 Variation of the drop velocity with residual drop size for several ϕ 's. $\tilde{R}=10\text{cm}$.
- Figure 8 Variation of the Reynolds number with residual drop size for several ϕ 's. $\tilde{R}=10\text{cm}$.
- Figure 9 Nondimensional drop temperature versus nondimensional radial coordinate in a drop for a dense and dilute cluster of drops at several residual drop sizes. $\tilde{R}=10\text{cm}$.
- Figure 10 Pictorial of the two different models for describing the drop motion inside the cluster.
- Figure 11 The drop evaporation time versus ψ for four different models describing transport from and to the cluster of drops.
- Figure 12 The burned fuel fraction versus ϕ^0 .
- 0 - at ignition
● - at drop disappearance, turbulence model 1
Δ - at drop disappearance, turbulence model 2
- Figure 13 Ratio of the burned fraction to the fraction of fuel that escaped the cluster, evaluated at drop disappearance versus ϕ^0 for two models of turbulent transport to the cluster. The similarity model was used to describe the drop motion inside the cluster.
- Figure 14 The burned fuel fraction versus \tilde{R}^0 .
- 0 - at ignition
● - at drop disappearance, turbulence model 1
Δ - at drop disappearance, turbulence model 2

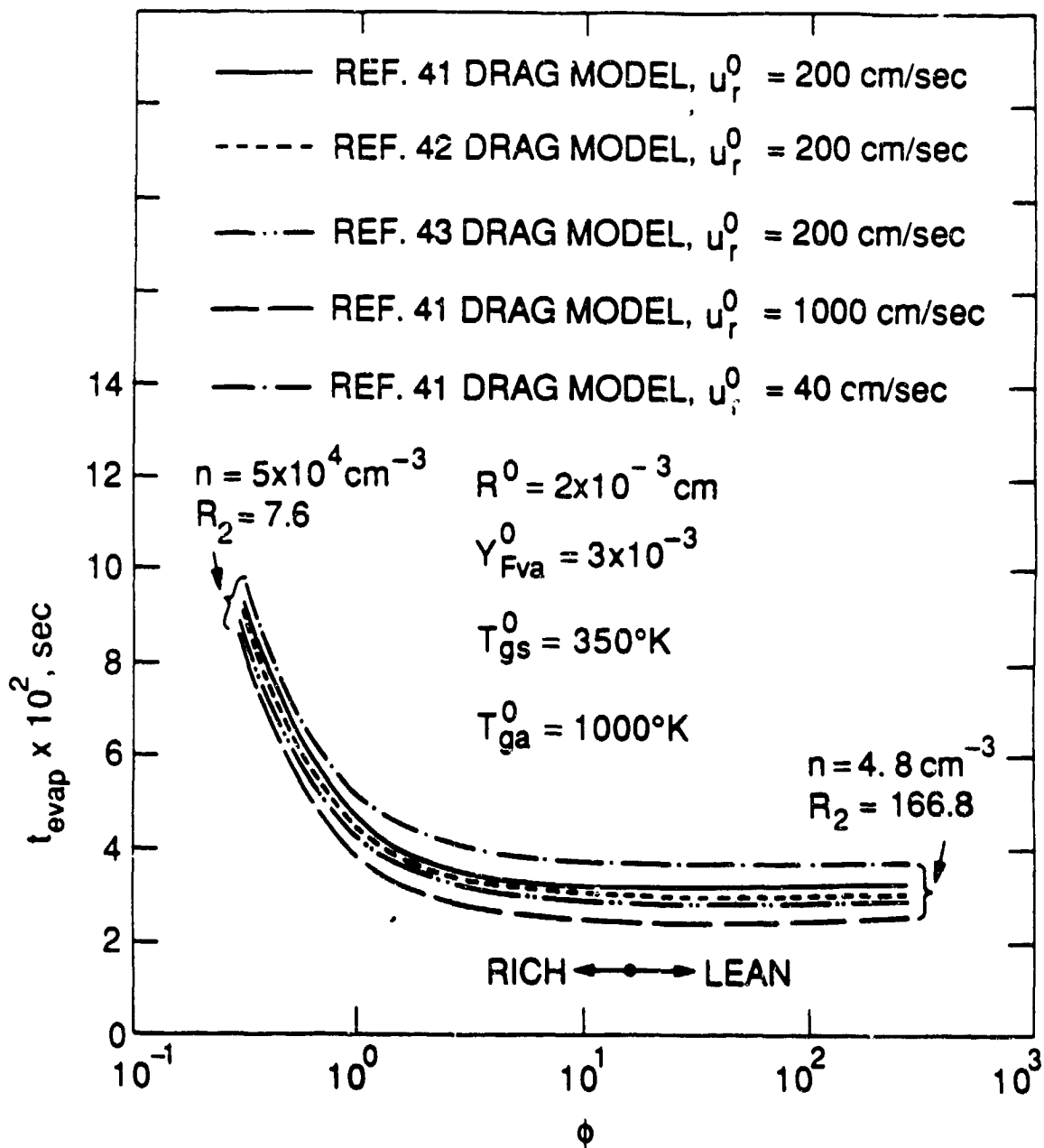
- Figure 15 Time for drops to evaporate to 30% of their initial radius versus ϕ^0 for null and various finite charge ratios.
- Figure 16 Volume ratio at $t_{0.3}$ versus ϕ^0 for null and various finite charge ratios.
- Figure 17 Time for drops to evaporate to 30% of their initial radius versus the charge ratio for two turbulence models.

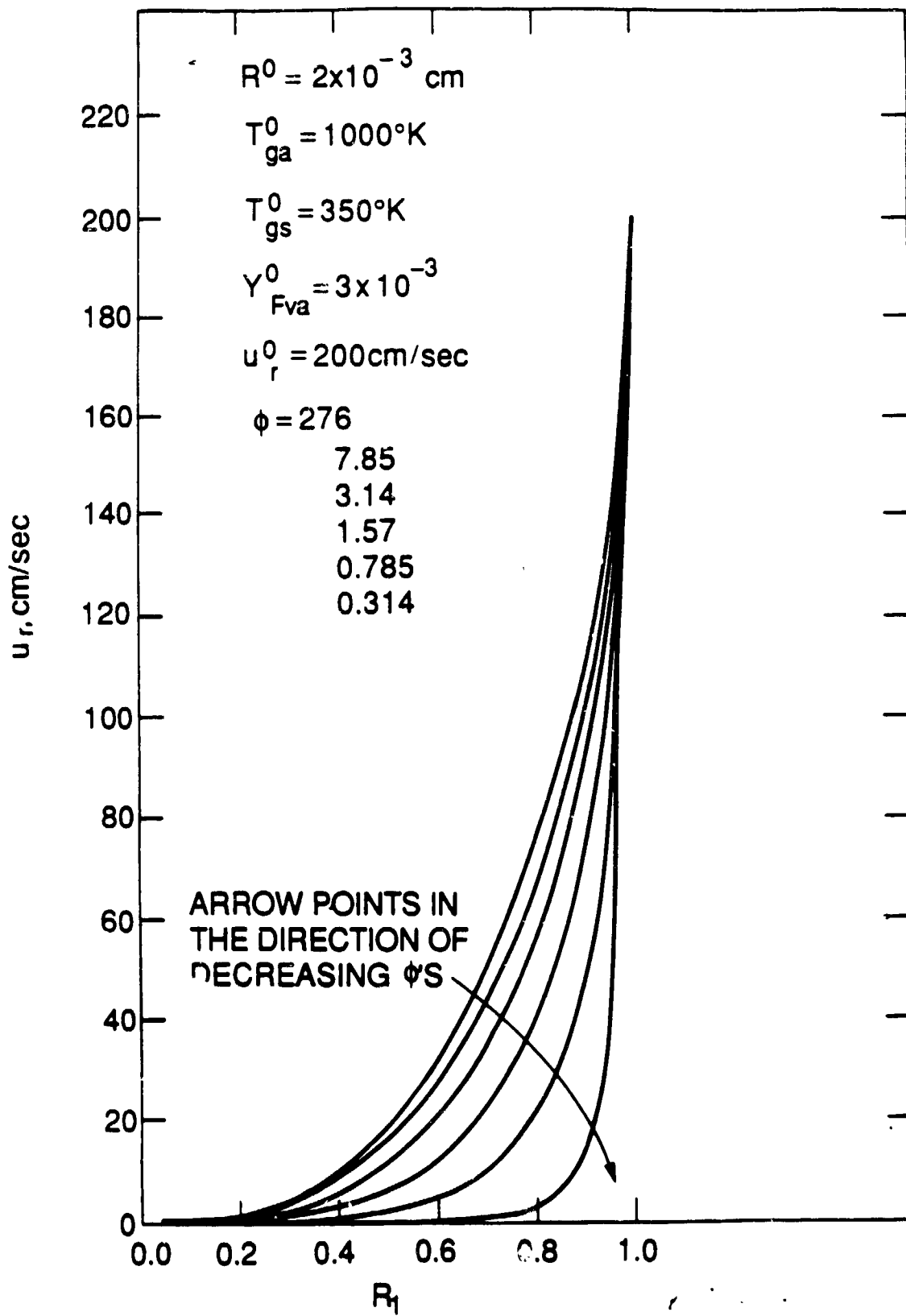


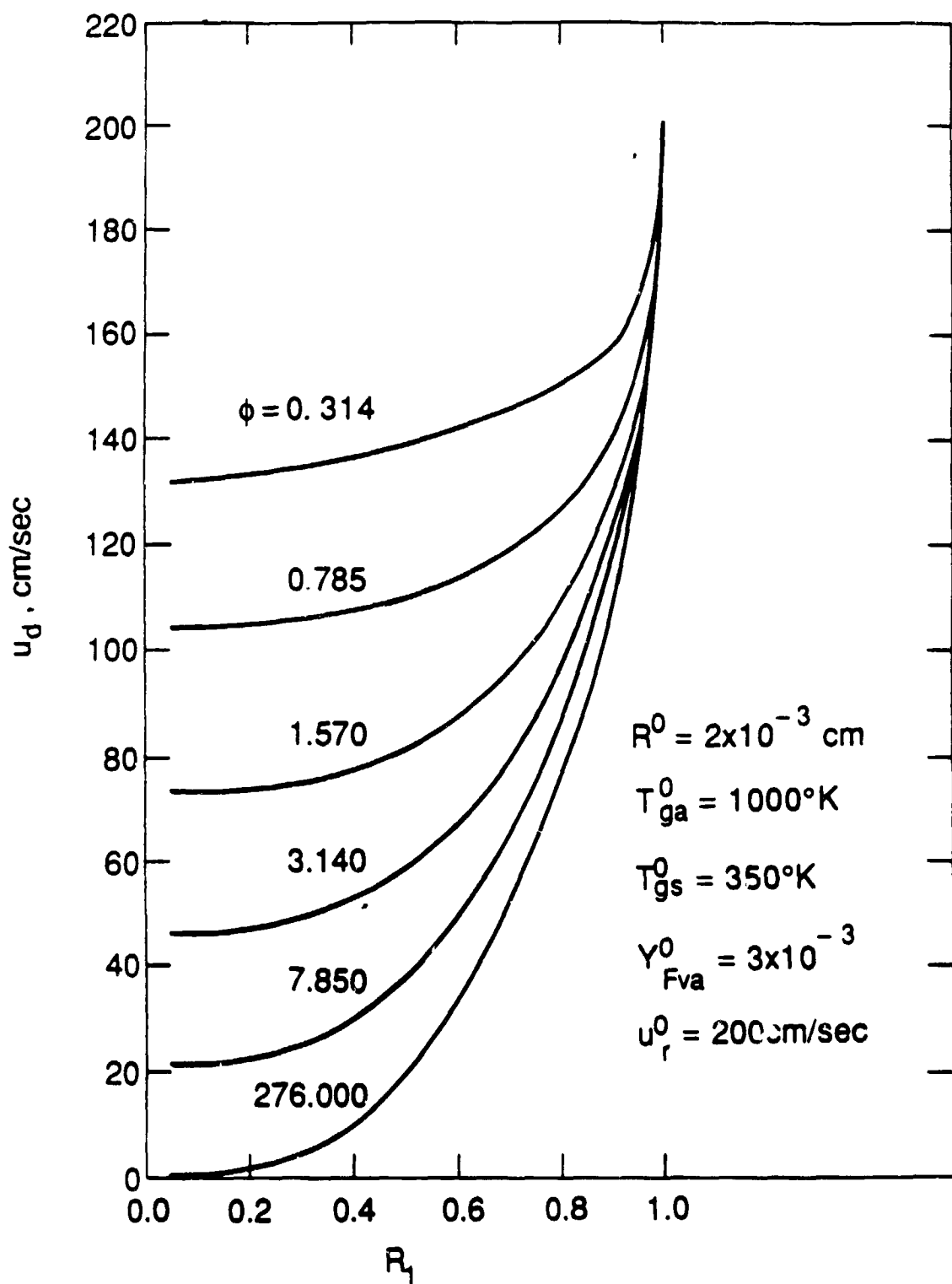


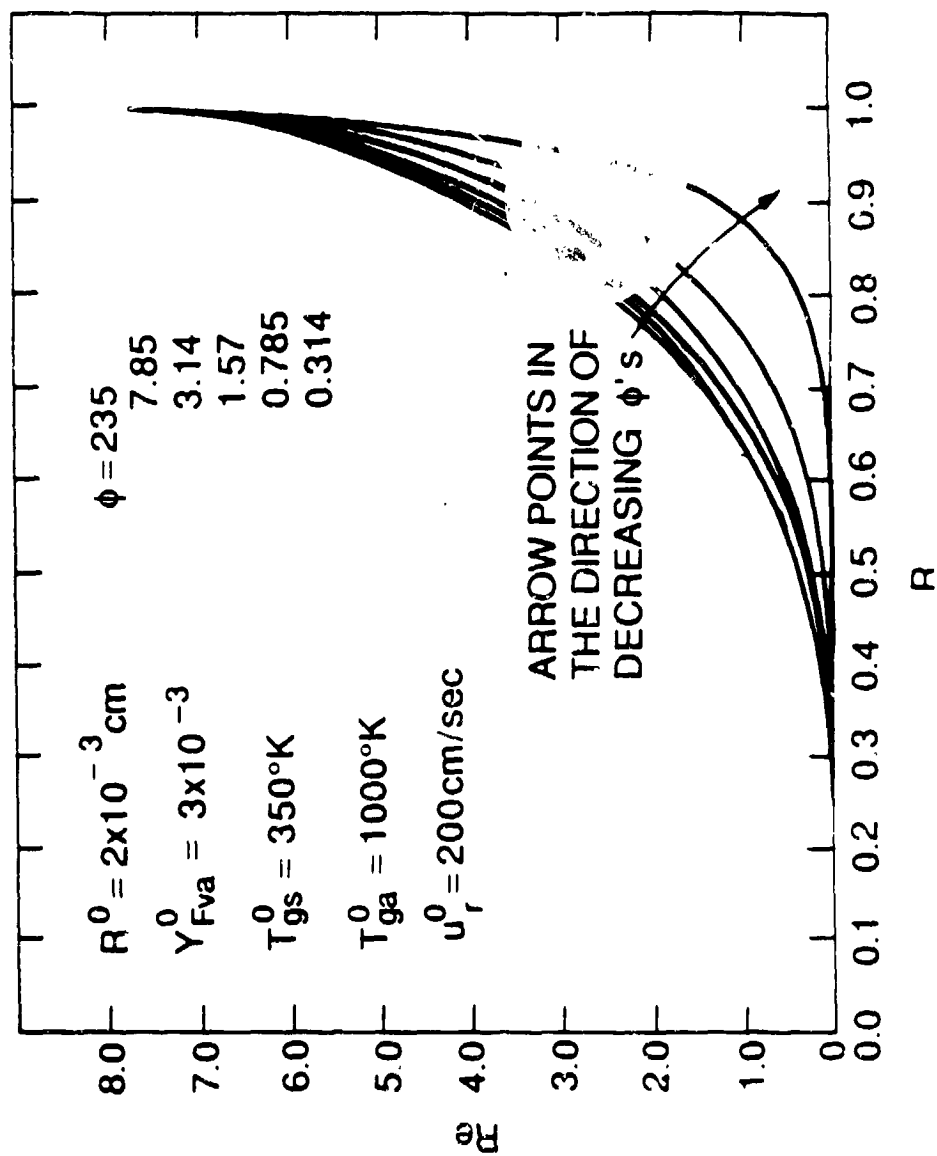


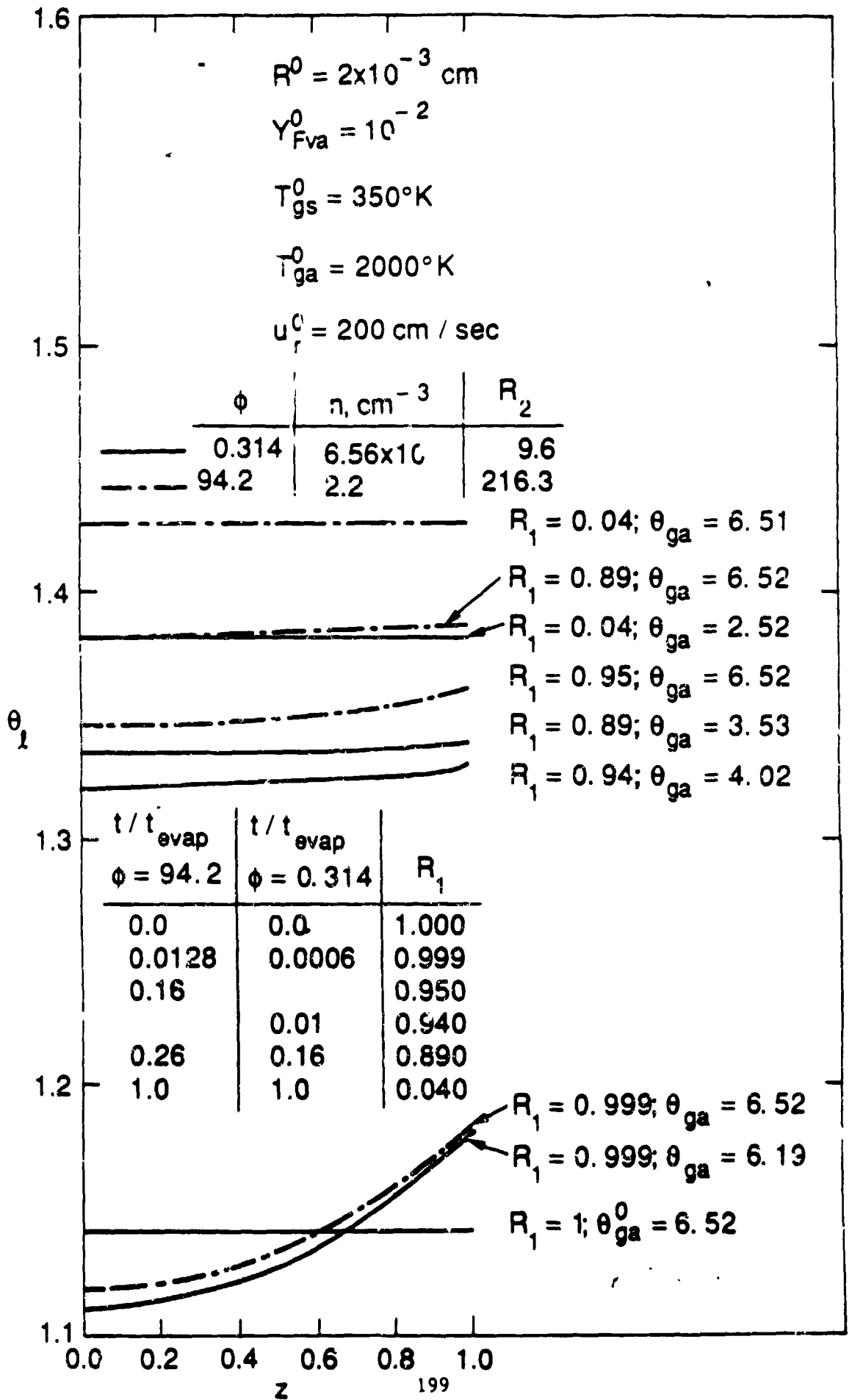


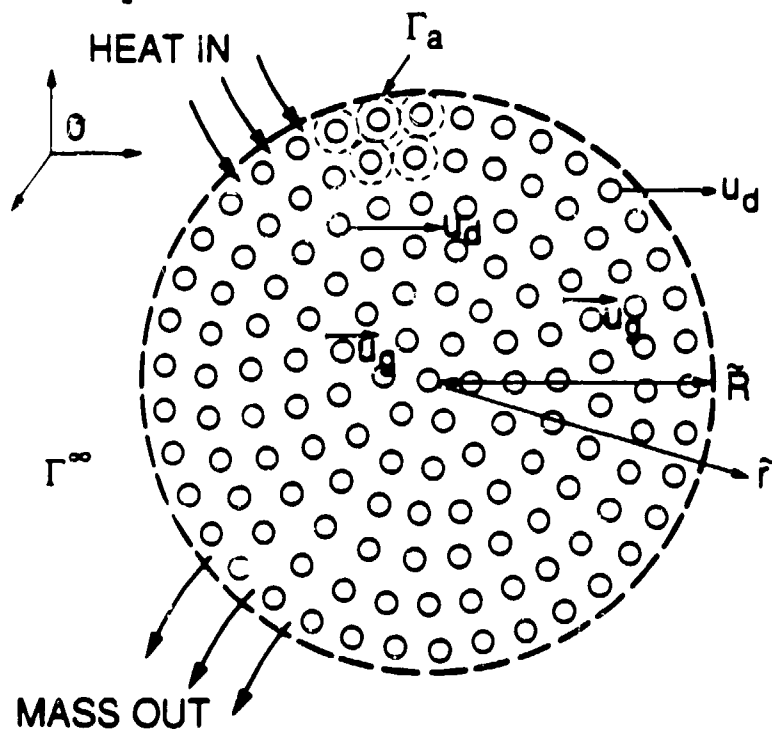




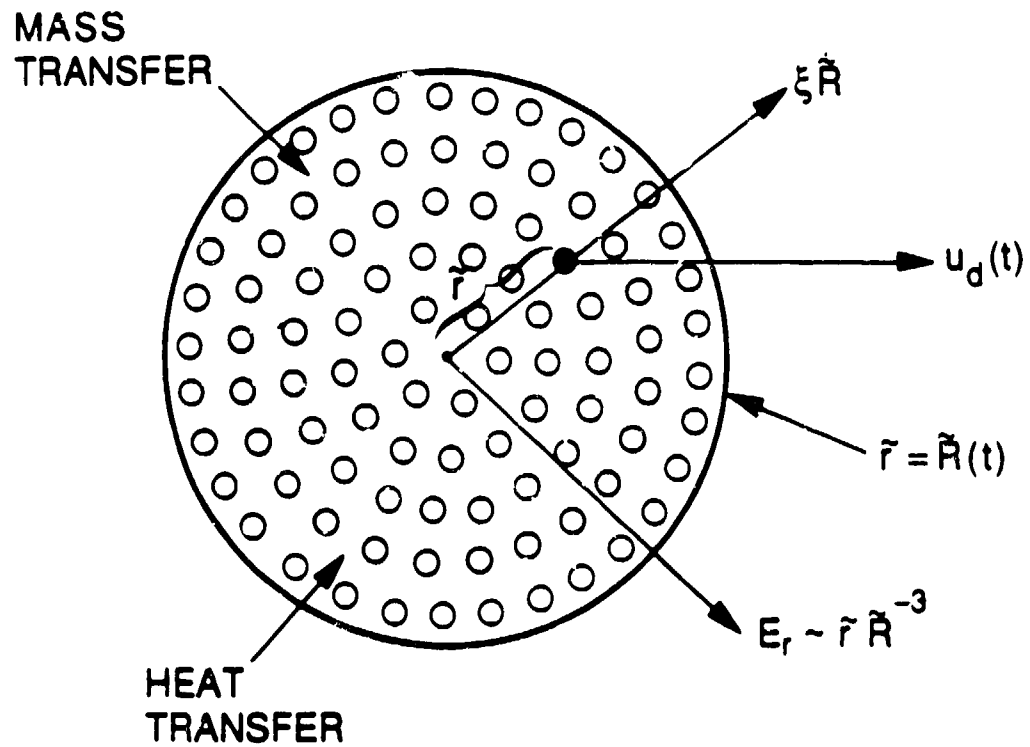




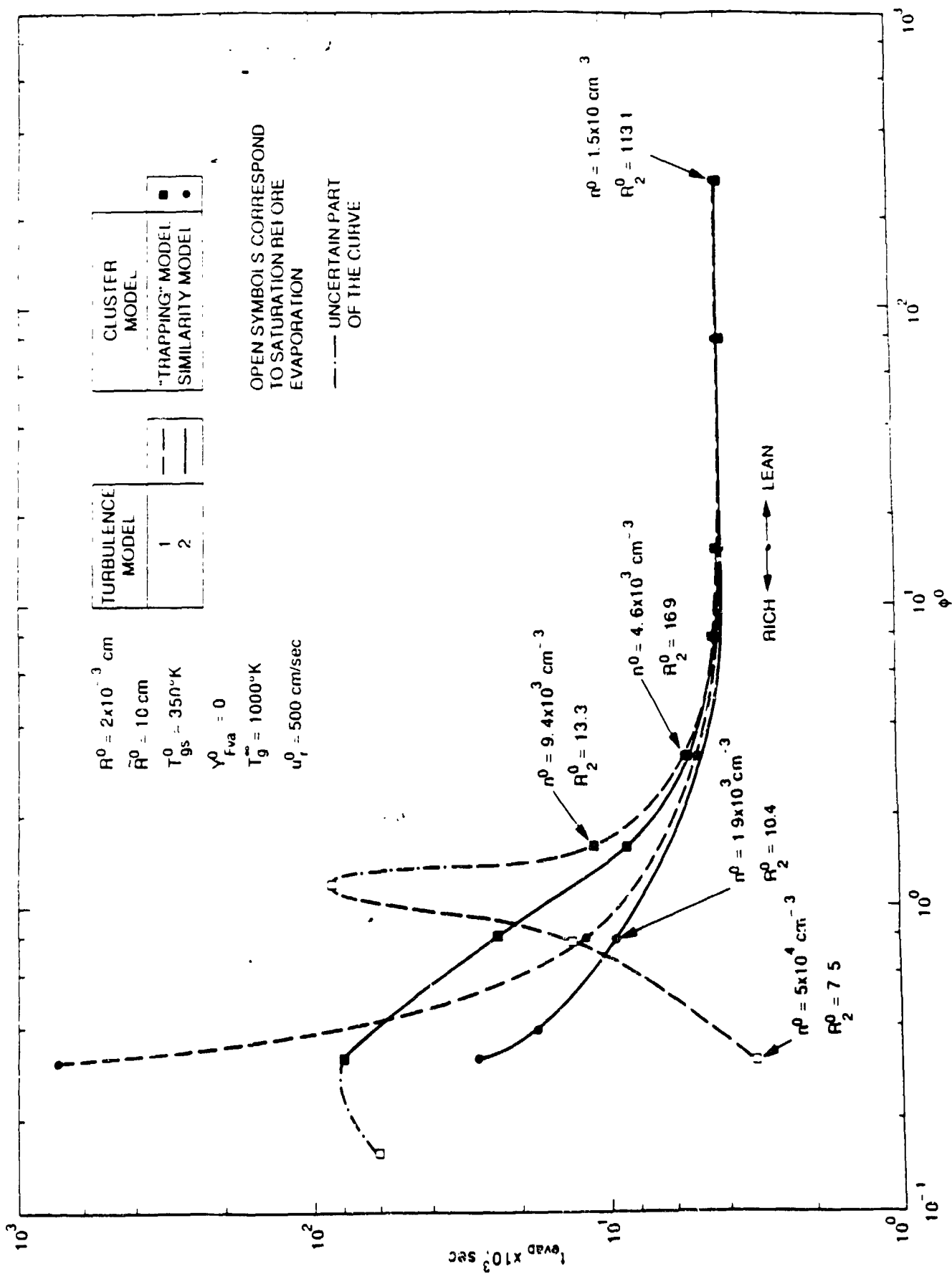


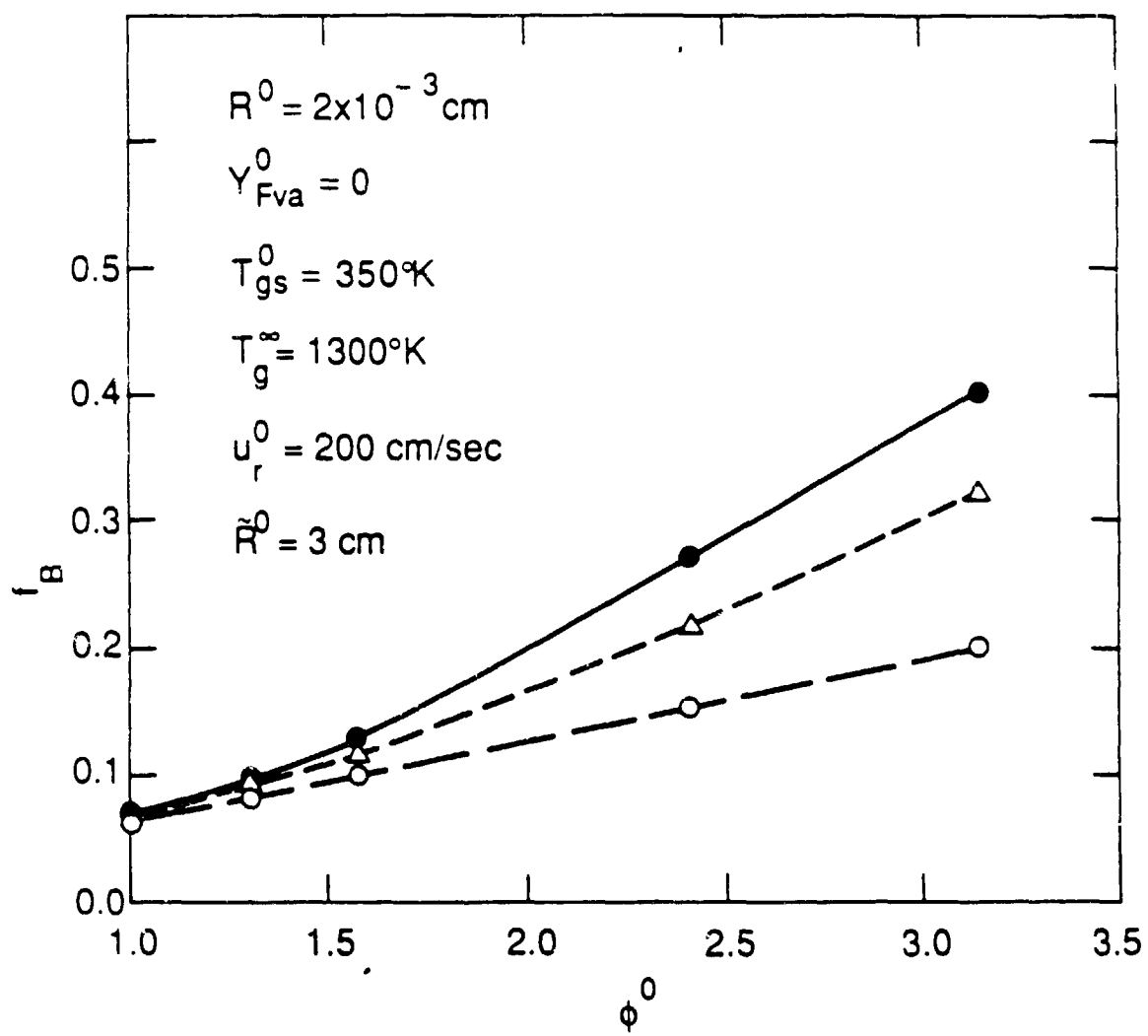


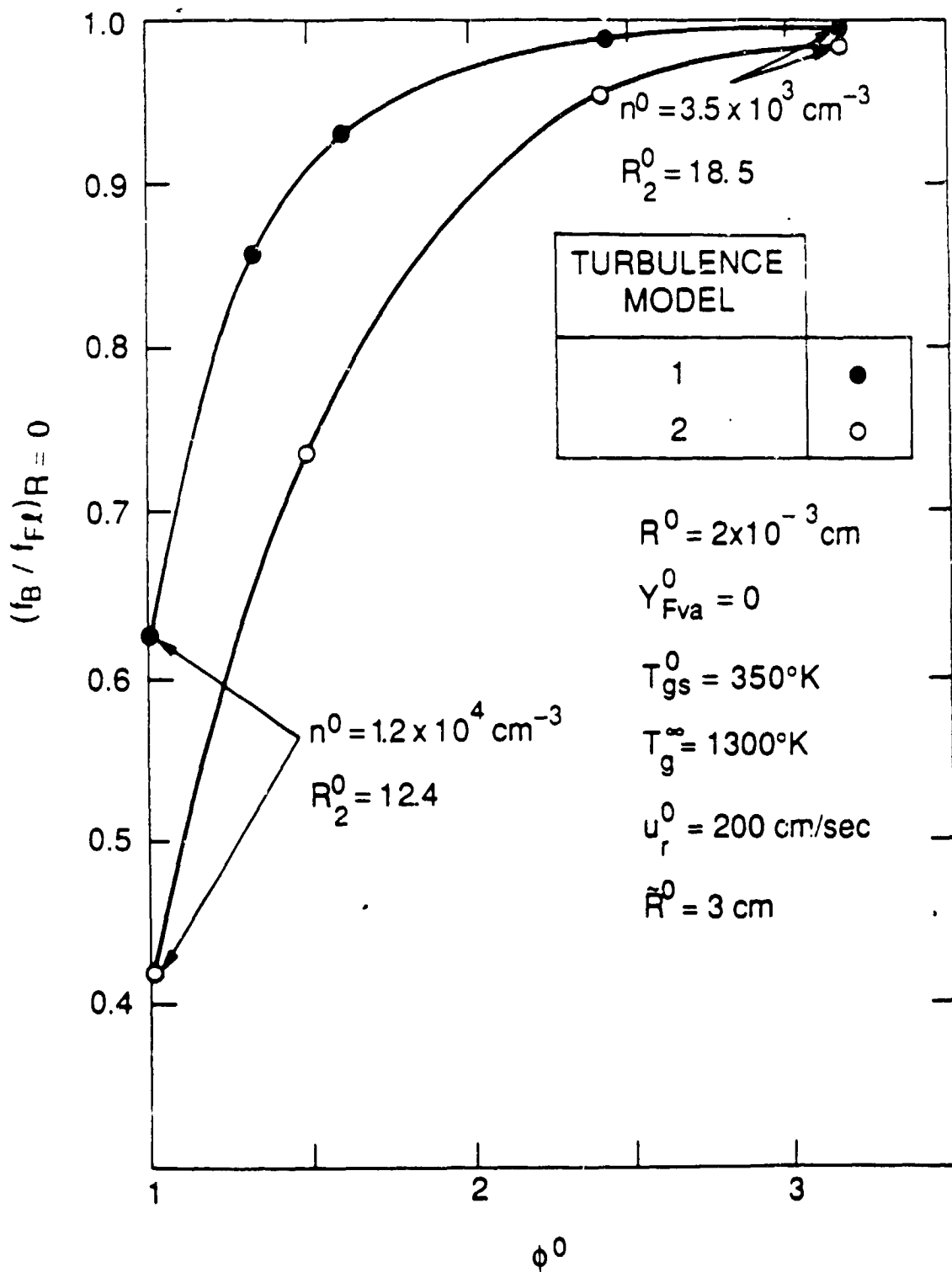
(a) THE "TRAPPING FACTOR" MODEL

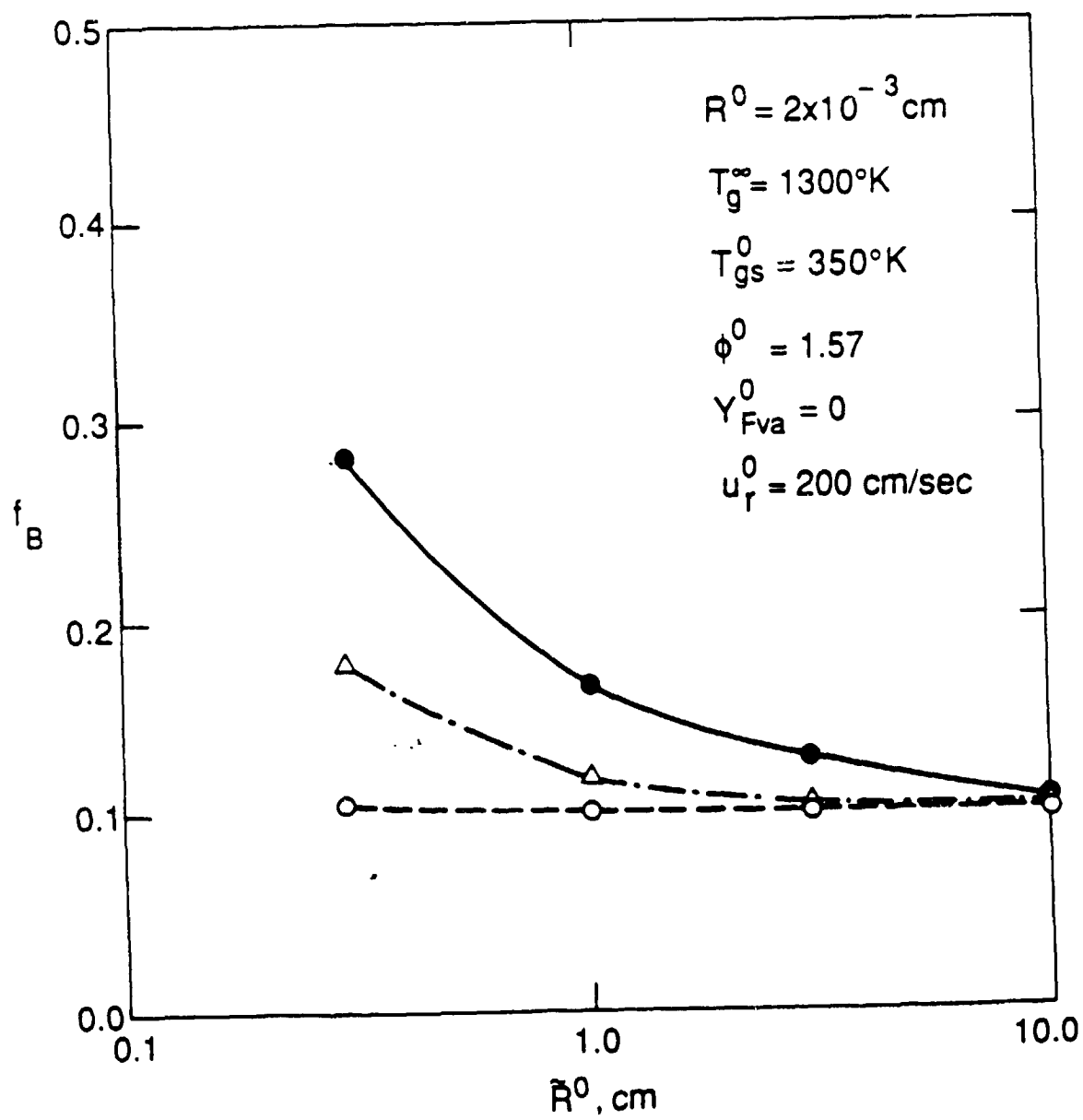


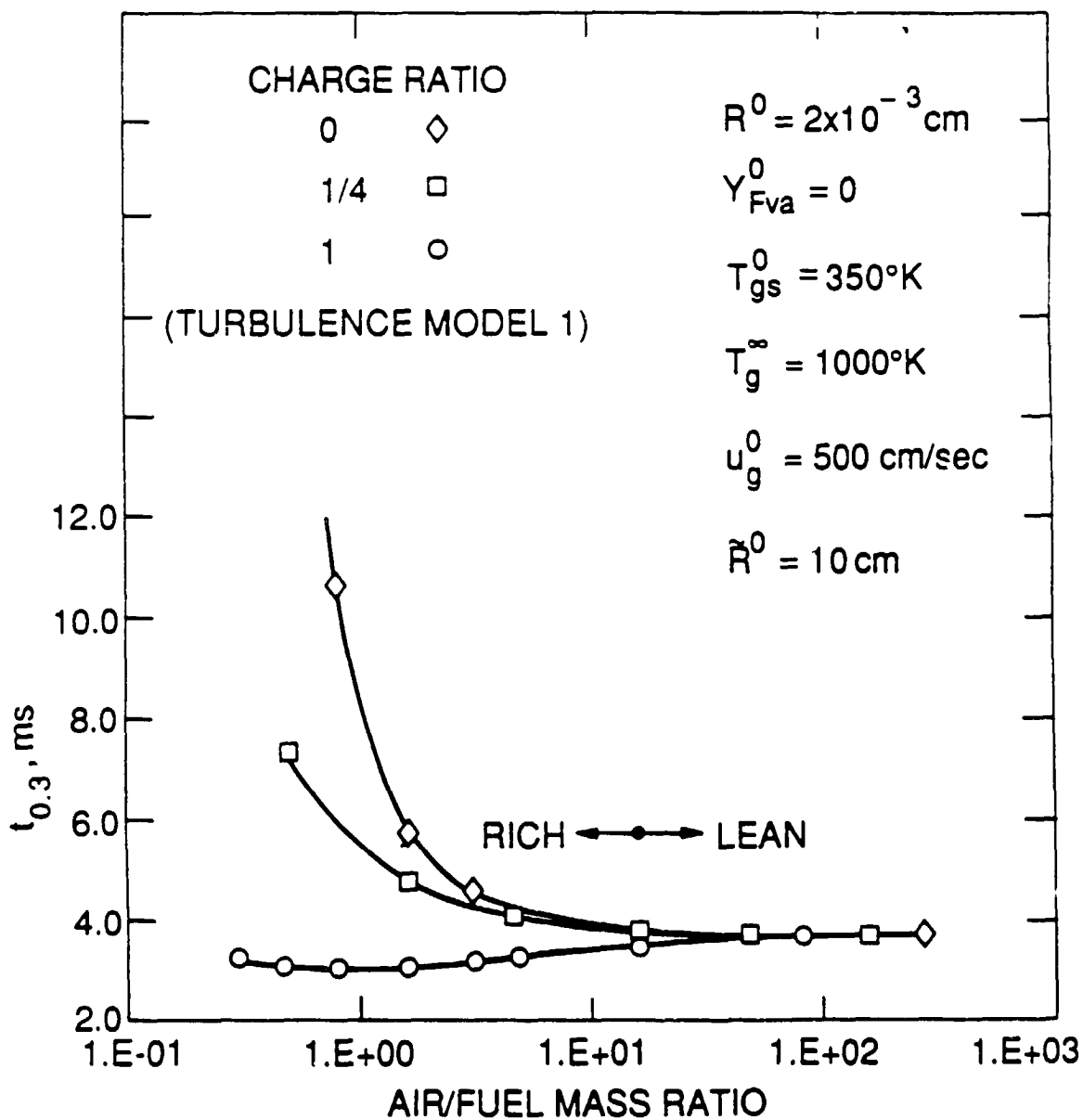
(b) THE SIMILARITY MODEL. E_r IS ASSOCIATED WITH THE ELECTROSTATIC FORCE IF THE DROPS ARE CHARGED

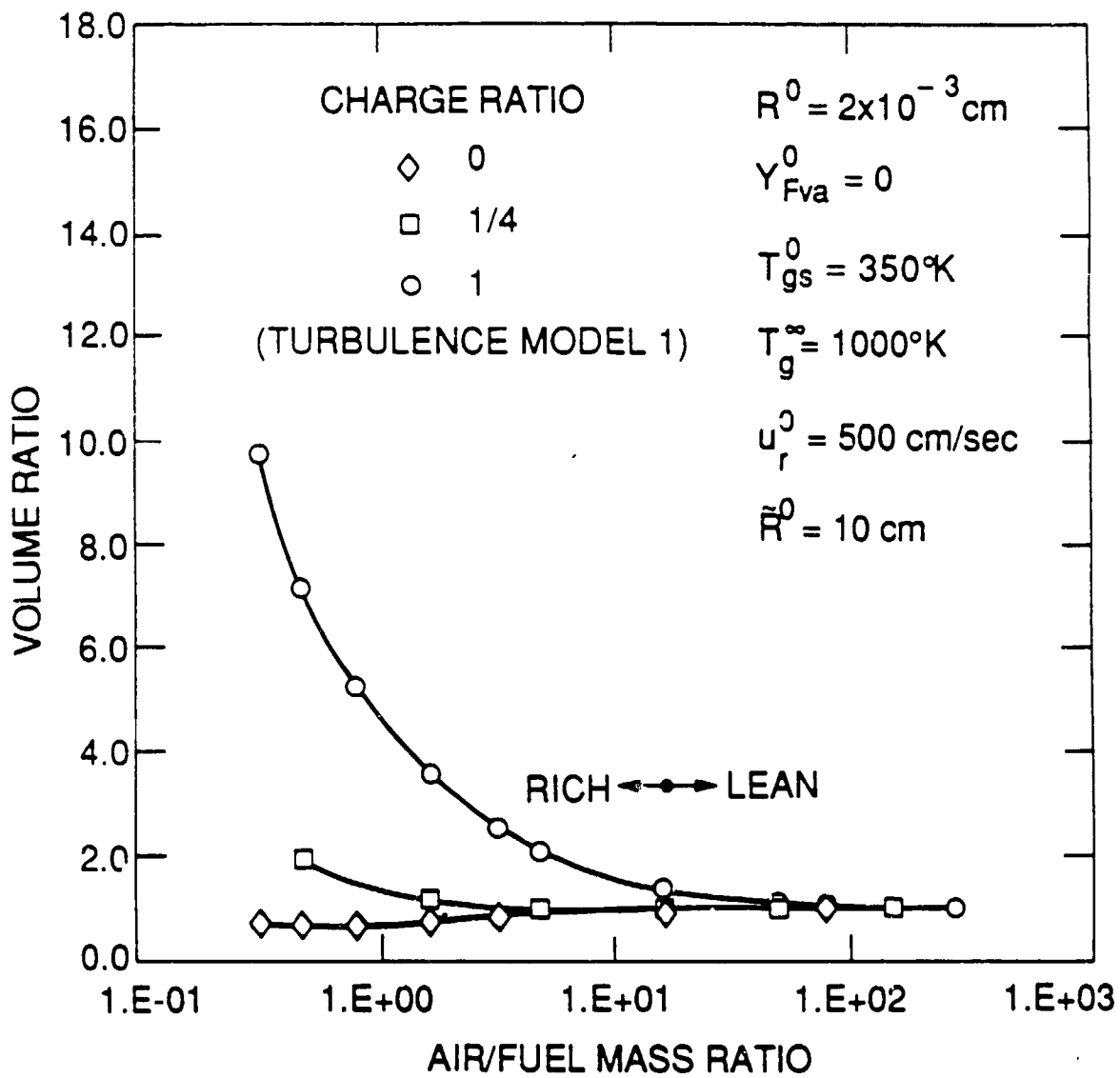












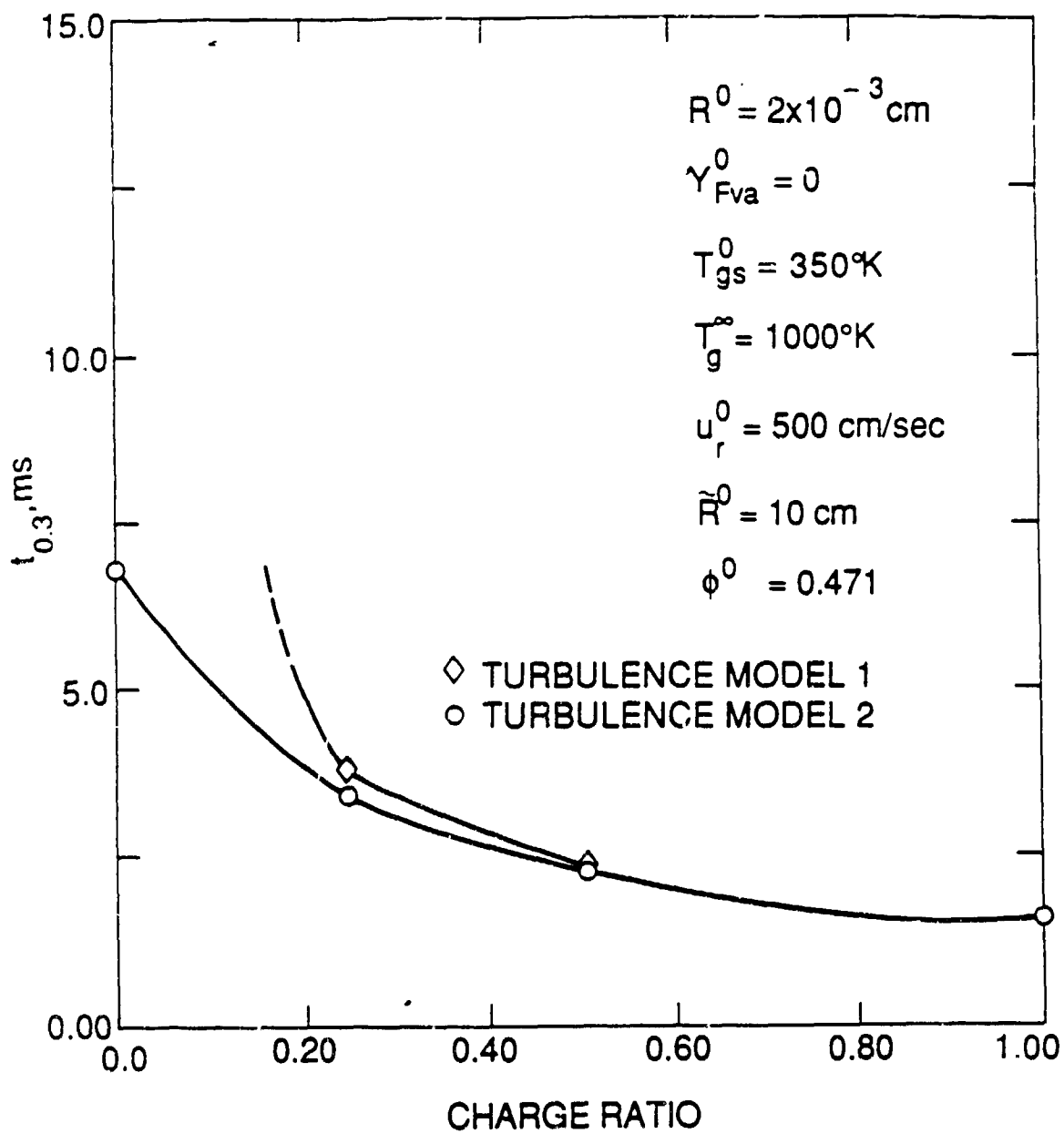


TABLE I

SUMMARY OF SUBGRID MODELS

NO.	SITUATION DESCRIBED BY THE MODEL	MODEL ASSUMPTIONS	REFERENCES
1.	Constant-volume, variable pressure cluster • evaporation	a. Unsteady liquid phase b. Uniform drop temperature c. Gas phase quasi-steady with respect to liquid phase d. Equilibrium evaporation e. No convective effects f. Cluster volume is adiabatically insulated from surrounding gas	27
	• evaporation	a and c g. Heat conduction in drops in the radial direction h. Kinetic evaporation i. Convective flow in the gas surrounding the cluster j. Mass, species, momentum and energy transfer across the cluster boundary is negligible with respect to the mass, species and energy content of the cluster	40
2.	Constant-pressure, variable volume cluster • evaporation	a,c,g, and h. k. Turbulent flow exists around the cluster. It can be of two types: 1. Turbulence model 1---turbulence is not present initially, but develops with time 2. Turbulence model 2---turbulence is present initially. 1. The drops inside the cluster move radially with respect to each other. The cluster boundary is found by assuming that all of the evaporated fuel exits the cluster in the dense case. In the dilute case all of the evaporated fuel is trapped inside the cluster. An interpolating factor, called "trapping factor" is used for intermediate situations.	5

TABLE I
SUMMARY OF SUBGRID MODELS
(CONTINUATION)

NO.	SITUATION DESCRIBED BY THE MODEL	MODEL ASSUMPTIONS	REFERENCES
		m. Transport of mass, species, momentum and energy across the surface of the cluster is important	
	• evaporation	a, c, g, h, k, and m. n. The drops inside the cluster move radially with respect to each other in a self-similar manner. The similarity parameter is the ratio of the radial coordinate inside the cluster divided by the radius of the cluster	46, 47
	• evaporation and ignition	a, c, g, h, k, m, and n. o. The drops are electrostatically charged with the same charge p. Ignition is dominated by diffusion	46
	• evaporation, ignition and combustion	a, c, g, h, k, m, n, and p. q. The burning rate is not necessarily equal to the evaporation rate. r. Burning occurs according to the following scenario: a very shortly-lived premixed flame depletes all the oxygen inside the cluster and is followed by a thin, sheath-like, counterflow diffusive flame.	51

TABLE 11

MODELS WHOSE RESULTS ARE COMPARED IN FIGURE 11

SYMBOL IN FIG. 11	MODEL DESCRIPTION
MODEL A -----■-----	<ul style="list-style-type: none"> ● Turbulence Model 1 - Assumption (k.1.) in Table I ● Drop motion described by the trapping factor model - assumption 1. in Table I
MODEL B -----●-----	<ul style="list-style-type: none"> ● Turbulence Model 1 - Assumption (k.1.) in Table I ● Drop motion described by the similarity model - assumption n. in Table I
MODEL C -----■-----	<ul style="list-style-type: none"> ● Turbulence Model 2 - Assumption (k.2.) in Table I ● Drop motion described by the trapping factor model - assumption 1. in Table I
MODEL D -----●-----	<ul style="list-style-type: none"> ● Turbulence Model 2 - Assumption (k.2.) in Table I ● Drop motion described by the similarity model - assumption n in Table I

THE DYNAMICS OF DENSE AND DILUTE
CLUSTERS OF DROPS EVAPORATING IN
LARGE, COHERENT VORTICES

by

J. Bellan and K. Harstad
Jet Propulsion Laboratory
California Institute of Technology
Pasadena, CA 91109

Subject Areas

Drop and Spray Combustion
Heterogenous Combustion
Modeling

ABSTRACT

The behavior of evaporating clusters of drops embedded into large, coherent vortices is described using a formulation which is valid for both dense and dilute clusters. Drops and gas interact both dynamically and thermodynamically. Dynamic coupling occurs through a force on the drops due to drag resulting from a slip velocity between the two phases. The net interaction force on the gas with drops is due to a source thrust from evaporation plus drag on each drop. The drag coefficient accounts for blowing from the drop surface. Thermodynamic coupling is a result of drop heating and evaporation. Limitations due to drop proximity on heating and evaporation are taken into account.

The vortical motion of the drops in the cluster results in the formation of a core region devoid of drops at the center of the vortex, and a shell region containing the drops and surrounding the inner core. Results are presented showing the dependence of the evaporation time, the final to initial volume ratio and the final to initial shell thickness ratio upon the initial air/fuel mass ratio and as a function of the initial tangential velocities, upon the initial Stokes number, initial drop radius and initial outer cluster radius. Differences in behavior between and control parameters of dense and dilute clusters are pointed out. It is found that for dense clusters the final to initial volume ratio and final to initial shell thickness scale with the initial Stokes number.

I. INTRODUCTION

Liquid fuel sprays are composed of many regions which are distinguished by the important phenomena influencing the fate of both gas and drops. As the drops exit the atomizer, the drops which are in the spray core penetrate the gas phase and interact with small scale turbulent eddies before they vaporize and burn. In contrast, the drops which are at the edge of the spray get entrained into the larger scale vortical structures produced by the shear layer between the spray and the surrounding gas, and their fate is closely related to that of these larger eddies. This physical picture emerges from the recent experiments of Lazaro and Lasheras^(1,2) who observed a plane, two-dimensional, turbulent mixing layer formed between a one-dimensional, uniform liquid spray and a stagnant air flow. These experimental observations showed that the larger coherent vortices at the edge of the spray play a critical role because not only do they control the entrainment of air into the spray, but also they determine the drop number density and size distribution throughout the mixing region. As the particles are entrained into these eddies, they are centrifuged to the outer part of the eddy leaving behind a core devoid of particles. Similar observations of particle dispersion in plane mixing layers have previously been made by Kamalu et. al.⁽³⁾

The mathematical modeling of evaporating particles dispersing in large, coherent vortices is a challenging task due to the many coupled phenomena involved. The drops motion is coupled to the gas motion, although to which extent it is still not known⁽⁴⁾. Crowe et al.⁽⁴⁾ point out that the coupling between particles and gas is a function of the Stokes number, St , which is a ratio of the aerodynamic time and the fluid time. If $St > 1$, the particles exit the vortex and do not interact with it. If $St \ll 1$, the particles follow entirely the gas motion. If $St \sim O(1)$, the particles have enough time to interact with the gas and eventual relaxation of the slip velocity between phases occurs. Clearly, there are other factors, such as particle number density and evaporation effects, which also influence the particle-fluid interaction.

Most existing models have so far addressed the situation of dilute and/or non-evaporating particle dispersion in large vortices. Such models can be found in Chung and Troutt⁽⁵⁾, Lazaro and Lasheras⁽²⁾, Yang⁽⁶⁾ and Yang and Sichel⁽⁷⁾. However, recent experimental results have revealed that particles cluster in a spray and that these clusters can be both dilute and dense^(8,9). In fact, flames have been observed in sprays around clusters of drops^(10,11) rather than individual drops suggesting that the dense clusters of drops injected by the atomizer persist in their dense configuration during burning.

In contrast to the existing models⁽⁵⁻⁷⁾, the present model of particle dispersion in large coherent vortices describes evaporating drop clusters that can be either dilute or dense. Thus, one can identify the different behavior of initially dense and initially dilute clusters of drops, and determine the controlling factors for evaporation and dispersion in the two different cases.

II. PHYSICAL PICTURE AND MODEL

Figure 1 depicts the configuration which is modeled here. A cylindrical cluster of single-component fuel, uniformly distributed, monosize drops of radius R is embedded into a cylindrical, infinite, vortical structure. Uniformity is assumed in the axial direction, z , so that an axial, two-dimensional section is representative of the configuration. Uniformity is also assumed in the azimuthal direction, θ . There are no body forces, the pressure, p , is atmospheric and the far field conditions (subscript " ∞ ") are given.

Both drops and gas have radial and azimuthal velocities, respectively u_{dr} , u_{gr} , $u_{d\theta}$ and $u_{g\theta}$, which are functions of time, t , and the radius, r , from the vortex center. The boundary of the cluster is the envelope of the drops which becomes in the two dimensional representation of Fig. 1 an inner, $\tilde{R}_{in}(t)$, and an outer, $\tilde{R}(t)$, boundary. The inner surface develops with time as a result of the centrifugal force created by vortical motion. Inside the cluster each drop is imagined surrounded by a fictitious sphere of influence whose radius, a , is the half distance between the centers of two adjacent drops⁽¹²⁾ Thus, the volume of

the cluster, V , is that of the spheres of influence and the space between the spheres of influence. The liquid in each drop has a temperature T_d which is a function of t and the radius from the drop center, r_d . The gas inside each sphere of influence has a density ρ_g and temperature T_g which are both functions of t and r_d . The composition of the gas inside the sphere of influence is given by the mass fraction of the "j" various compounds, $Y_j(t, r_d)$. At the edge of the sphere of influence the gas temperature, density and mass fractions are respectively $T_{ga}(t)$, $\rho_{ga}(t)$ and $Y_{ja}(t)$ which are also the uniform values in the spaces between the spheres of influence. Thus, whereas the velocities of drops and gas are functions of (t, r) , on a large length scale equivalent to many drop radii the cluster is assumed spatially homogenous in thermodynamic quantities. This assumption is consistent with the goal of describing the cluster behavior globally. Consistent with the monodisperse assumption, the drop number density, n , is independent of r .

The equations for the drops, the gas and the global cluster equations are:

A. Drops. In Eulerian coordinates the conservation equations are:

(i) Continuity.

$$\frac{\partial n}{\partial t} + \frac{1}{r} \frac{\partial}{\partial r} (r n u_{dr}) = 0 \quad (1)$$

(ii) Momentum.

$$m_d \left[\frac{\partial u_{dr}}{\partial t} + u_{dr} \frac{\partial u_{dr}}{\partial r} - \frac{1}{r} u_{d\theta}^2 \right] = F_{dr} \quad (2)$$

$$m_d \left[\frac{\partial u_{d\theta}}{\partial t} + u_{dr} \frac{\partial u_{d\theta}}{\partial r} + \frac{1}{r} u_{dr} u_{d\theta} \right] = F_{d\theta} \quad (3)$$

where $\overline{F_d} = -0.5 \rho_g A_d C_D |\overline{u_s}| \overline{u_s}$ is the force on the drops, F_{dr} and $F_{d\theta}$ are its components, A_d is the drop cross-sectional area, C_D is the drag coefficient, m_d is the drop mass, and $\overline{u_s} = \overline{u_d} - \overline{u_g}$ is the slip velocity where $\overline{u_d}$ and $\overline{u_g}$ are drop and gas velocities respectively. As a result of the previous assumptions, m_d is independent of r . C_D accounts for surface blowing from the drops(13,14).

(iii) T_d is found by solving the liquid conduction equation coupled through

the boundary conditions with the equations for the gas inside the sphere of influence(14,15). The gas inside the sphere of influence obeys the ideal gas law(14,15).

(iv) The Langmuir-Knudsen law is used to describe evaporation(14).

B. Gas In Eulerian coordinates the conservation equations are:

(i) Continuity

$$\rho_g \frac{\partial}{\partial t} + \frac{1}{r} \frac{\partial}{\partial r} (r \rho_g u_{gr}) = \dot{m} \quad (4)$$

where $\dot{m} = - dm_d/dt$ is the drop evaporation rate.

(ii) Momentum. The flow is considered inviscid, consistent with the high keynolds number situations treated here.

$$\rho_g \left[\frac{\partial u_{gr}}{\partial t} + u_{gr} \frac{\partial u_{gr}}{\partial r} - \frac{1}{r} u_{g\theta}^2 \right] + \frac{\partial p}{\partial r} = F_{gr} \quad (5)$$

$$\rho_g \left[\frac{\partial u_{g\theta}}{\partial t} + u_{gr} \frac{\partial u_{g\theta}}{\partial r} + \frac{1}{r} u_{gr} u_{g\theta} \right] = F_{g\theta} \quad (6)$$

where $\vec{F}_g = n(\dot{m} + 0.5 \rho_g A_d C_D |\vec{u}_s|) \vec{u}_s$ is the force exerted on the gas; F_{gr} and $F_{g\theta}$ are its components. Eq. (5) determines the dynamic pressure which is the very small deviation from the constant thermodynamic pressure. Since it is assumed that the p is constant Eq. (5) is not used.

(iii) The ideal gas law is used.

C. Global. The global conservation equations for the cluster are transient and account for phase change and contributions due to transport across the cluster surface(s). There are two types of boundary conditions which occur at the cluster outer boundary (subscript "o") according to the sign of $F(r) = 2\pi r(u_{dr} - u_{gr})$: (a) if $F_o = F(\tilde{R}) \geq 0$, then $T_{go} = T_{g\infty}$ and $Y_{jo} = Y_{j\infty}$, and (b) if $F_o = F(\tilde{R}) < 0$, then $T_{go} = T_{ga}$ and $Y_{jo} = Y_{ja}$. At the inner boundary, (subscript "in"), $T_{gin} = T_{ga}$, and mass and fuel exchange across that boundary are due to fluxes $\rho_g F_{in}$ and $\rho_g Y_{fv} F_{in}$ respectively, where $F_{in} = F(\tilde{R}_{in})$, subscript "Fv" denoting fuel vapor. Thus for the core the global continuity equation is

$$\frac{d}{dt} (\pi \tilde{R}_{in}^2 \rho_g) = \rho_g F_{in} \quad (7)$$

and the fuel vapor conservation equation is

$$\frac{d}{dt} (\pi \tilde{R}_{in}^2 \rho_g Y_{FVC}) = \rho_g \bar{Y}_{FV} F_{in} \quad (8)$$

where Y_{FVC} is fuel vapor mass fraction (assumed uniform) in the core and \bar{Y}_{FV} is an average value of Y_{FV} in a sphere of influence. The cluster gas mass, air mass, and enthalpy are defined respectively as

$$Nm_g = 2\pi N \int_R^a \rho_g r dr + (S - \pi a^2 N) \rho_{ga} \quad (9)$$

$$Nm_{air} = 2\pi N \int_R^a \rho_g (1 - Y_{FV}) r dr + (S - \pi a^2 N) \rho_{ga} (1 - Y_{FVa}) \quad (10)$$

$$NH_g = 2\pi N \int_R^a \rho_g C_p T_g r dr + (S - \pi a^2 N) \rho_{ga} C_p T_{ga} \quad (11)$$

where N is the number of drops per unit vortex length, C_p is the gas heat capacity at constant pressure, the reference temperature is zero and $S = \pi(\tilde{R}^2 - \tilde{R}_{in}^2)$. Under the assumption of a very small Mach number the global conservation equations are

$$\frac{dm_g}{dt} = \dot{m} + \frac{1}{N} [\rho_{ga} (F_0 - F_{in})] \quad (12)$$

$$\frac{dm_{air}}{dt} = \frac{\rho_{ga}}{N} [(1 - Y_{FVo}) F_0 - (1 - Y_{FVa}) F_{in}] + \frac{2\pi\mu_{g\infty}}{N Sc} (Y_{FVa} - Y_{FV\infty}) \quad (13)$$

$$\begin{aligned} \frac{d}{dt} \left[H_g + \frac{m_d}{2} \langle u_d^2 \rangle_r \right] = \dot{m} \left\{ C_{pFV} T_{gs} - \frac{C_p (T_{ga} - T_{gs})}{\exp \{C[Z(R_1) - Z(R_2)]\} - 1} \right\} + \\ \frac{C_p \rho_{ga}}{N} (T_{go} F_0 - T_{ga} F_{in}) + \frac{2\pi\mu_{g\infty}}{N Pr} C_p (T_{g\infty} - T_{ga}) \end{aligned} \quad (14)$$

where $C = \dot{m} / [4\pi(\rho_g D)_\infty R^0]$, μ_g is the gas viscosity, Sc is the Schmidt number, Pr is the Prandtl number, D is the diffusivity, T_{gs} is the gas temperature at the drop surface, $\langle \rangle_r$ denotes a radial average, $R_1 = R/R^0$ (superscript "0" denotes initial conditions), $R_2 = a/R^0$ and

$$Z(y) = (\theta_g^\infty)^{0.65} \int_y^{R_2} \frac{dy}{y^2 \theta_g^{0.65}} \quad (15)$$

with $y=r_d/R^0$ and $\theta=C_p T_g/L_{bn}$, L_{bn} being the latent heat of evaporation at the normal boiling point. The details of the solution for $T_g(t, r_d)$ involving the function $Z(y)$ are explained elsewhere(15). In all the calculations $Sc=Pr=0.8$ was taken. Vortex stretching is not considered, hence N is constant. By definition $St=2\rho_d R^2 \langle u_{d\theta} \rangle_r / (9\mu_g \tilde{R})$.

III. SOLUTION PROCEDURE

A slip relaxation frequency is defined $\nu_s = \rho_g A_d C_D |\vec{u}_s| / (2m_d)$ which is independent of r when $Re_d \ll 1$ (Stokes regime). For larger Re_d , consistent with the present global approximation, ν_s is averaged over r .

The velocities are taken to have the following functional form:

$$u_{ik}(t, r) = \frac{A_{ik}(t)}{r} + r B_{ik}(t) + r^3 C_{ik}(t) \quad (16)$$

where $i=d, g$; $k=r, \theta$; $q=0$ for $k=r$; and $q=1$ for $k=\theta$. In Eq. (16), A_{ik} 's are the irrotational part of the solution resulting from a line vortex, B_{ik} 's represent the solid body rotation or spin and C_{ik} 's represent a distortion. A solution is sought for which there exists a self-similar radial drop motion with the similarity parameter $\xi = (r^2 - \tilde{R}_{in}^2) / (\tilde{R}^2 - \tilde{R}_{in}^2)$ which is fixed for a given drop. Additionally, the radial drop momentum equation is averaged by taking its first two moments with respect to ξ . Thus, whereas the tangential velocities are solved for exactly, the radial drop velocity distribution is solved for approximately. To solve for the velocities, their functional forms are replaced into the azimuthal equations which are now transformed into polynomials in r whose coefficients are then null. This gives nonlinear, coupled, ODE's for A_{ik} 's, B_{ik} 's and C_{ik} 's. It turns out that if $C_{ik}'s=0$ then $C_{ik}(t)=0$ which is the choice here. A_{gr} and B_{gr} are determined algebraically from boundary conditions and consistency considerations.

The given initial conditions are: ϕ^0 , the initial air/fuel mass ratio, R^0 , \tilde{R}^0 , \tilde{R}_{in}^0 , T_{gs}^0 , Y_{js}^0 , $T_{ga}^0 = T_{g\infty}$, $Y_{ja}^0 = Y_{j\infty}$, A_{ik}^0 's and B_{ik}^0 's. Due to lack of experimental data regarding velocities of gas and drops in large vortical structures the choice was made to take $A_{ir}^0 = B_{ir}^0 = 0$ so that the drops have initially only tangen-

tial velocities. The dependent variables for which solutions are found are: $n(t)$, $m(t)$, $u_{dr}(t,r)$, $u_{gr}(t,r)$, $u_{d\theta}(t,r)$, $u_{g\theta}(t,r)$, $\tilde{R}(t)$, $\tilde{R}_{in}(t)$, $\rho_g(t)$, $T_{ga}(t)$, $\rho_{ga}(t)$, $Y_{js}(t)$, $Y_{ja}(t)$ and $R(t)$. Solutions obtained on a UNIVAC 1100 require in average 4 sec of CPU time per solution, the computation ending when $R_1 = 0.04$.

IV. RESULTS

All calculations for which results are presented here were performed for n-decane. The values of the physical constants used in the calculations are given elsewhere⁽¹⁴⁾. The specified far field conditions are $p=1\text{atm}$, $T_{g\infty}$ and $Y_{j\infty}$.

A substantial number of calculations were performed. General observations show that the short time behavior of the solution is dominated by relaxation of the initial conditions. This implies that quantitative agreement with experimental observations requires correct initial conditions since it is during this initial period that most mass is evaporated. The long time behavior shows generally weakly varying Y_j 's, ρ_g , T_g , n , and sometimes A_{gk} and B_{gk} , and also a self similar variation of both the liquid/gas mass ratio and with R_1 . This implies that perhaps some correlations could be extracted from these calculations for usage in large codes.

According to the discussion of Crowe et al.⁽⁴⁾ St^0 was chosen 0(1) or less to insure that the particles stay confined to the vortex. Figure 2 shows the evaporation time, t_{evap} , versus ϕ^0 for four choices of initial velocities made to purposely delineate the separate effects of vortex and spin motion. The range of ϕ^0 's goes from an initially dilute cluster corresponding to stoichiometric conditions for n-decane ($\phi=15.7$) to a dense cluster of drops at an equivalence ratio $\psi^0=\phi^0/\phi_s=0.01$. For two choices of initial velocities ($B^0_{g\theta}=B^0_{d\theta}=0$; $B^0_{g\theta}=2B^0_{d\theta}=10^3 \text{ sec}^{-1}$) the calculations could not be performed for $\psi^0=0.01$ because saturation occurred before complete evaporation. This emphasizes the importance of the initial spin motion in the dense cluster regime. $B^0_{d\theta}$ turns out to be more important in this regime than $B^0_{g\theta}$. In the dilute cluster regime the reverse is true. A comparison between the results of Fig. 2 also shows that $A^0_{d\theta}$ and $B^0_{g\theta}$ affect evaporation in both dense and dilute regime. As ϕ^0 decreases, two regimes appear to exist. When

$\phi^0 \gg 1$, t_{evap} is not a strong function of ϕ^0 , but as ϕ^0 decreases, the gas temperature decreases, the total vapor fuel loss from the cluster decreases and Y_{FVC} increases while the cluster expansion also increases. If $B_{d\theta}^0 \neq 0$ and $B_{g\theta}^0 \neq 0$, the mass loss from the cluster decreases as ϕ^0 increases, whereas when $B_{d\theta}^0 = B_{g\theta}^0 = 0$ increasing mass gain occurs. When $\phi^0 \lesssim 1$, t_{evap} increases substantially and is a strong function of the initial velocities. For the first 1-2ms ($R_1 \leq 0.8$), n decreases sharply as the drop velocity angle from the tangent increases from zero to its maximum; this maximum increases as ϕ^0 decreases. The largest maximum angle, 52° , is obtained for the run where numerically $A_{g\theta}^0 = B_{d\theta}^0 = 2A_{d\theta}^0 = 2B_{g\theta}^0 = 10^3$. During this initial period, n relaxes to $O(10^4 \text{ cm}^{-3})$ which means physically that for this size of drops and velocities, a vortex cannot support a cluster of larger n without disintegrating. The ratio of the final to initial volume ratio, V^f/V^0 , also depicted in Fig. 2, increases with decreasing ϕ^0 because as there is more liquid mass in the cluster, the centrifugal force is larger, and thus there is more expansion. The illustration also shows the importance of $B_{d\theta}^0$ and $B_{g\theta}^0$. For $B_{d\theta}^0 = B_{g\theta}^0 = 0$, there is no volume expansion in the dilute regime and the volume expansion in the dense regime is entirely due to the irrotational motion since $B_{d\theta}(t) = B_{g\theta}(t) = 0$. As irrotational motion tends to pack or compact the particles (because the part of the centrifugal force proportional to A_{ik} 's has a r^{-3} dependance) as \tilde{R} increases, the ratio of final to initial shell thickness, $\mathcal{R} = (\tilde{R}^f - \tilde{R}_{in}^f) / (\tilde{R}^0 - \tilde{R}_{in}^0)$ (superscript "f" denotes "final", occurring at $R_1 = 0.04$), stays below unity for all ϕ^0 's. In contrast, solid body rotation tends to pull apart the cluster (because the part of the centrifugal force proportional to B_{ik} 's has a r dependance) as \tilde{R} increases, and thus the largest V^f/V^0 and \mathcal{R} are obtained with the largest $B_{d\theta}^0$. The decrease in \mathcal{R} , with increasing ϕ^0 can be explained by the fact that in all cases $A_{g\theta}^0 > A_{d\theta}^0$. For $t > 0$, irrotational motion is transferred from gas to the drops, however for a leaner mixture (and more dilute cluster) the same momentum is transferred to less mass resulting in a larger increase in $A_{d\theta}$ versus

R_1 . Thus the drops will be centrifuged out with more packing than for the dense clusters, and thus the shell will stay thinner.

Figure 3 shows the dependence of t_{evap} , V^f/V^0 and \mathcal{R} upon St^0 for initially dense clusters of drops ($n^0 > 10^4 \text{ cm}^{-3}$). As expected, t_{evap} does not correlate with St^0 ; t_{evap} increases with R^0 and decreases with increasing initial velocities. Here R^0 was varied between 10^{-3} cm and $5 \times 10^{-3} \text{ cm}$ and numerically $A_{g\theta}^0 = B_{d\theta}^0$ were varied between 50 and 10^3 . When St^0 is constant, the smallest t_{evap} corresponds to the smallest R^0 and largest velocity. One of the most important findings of this study is that V^f/V^0 and \mathcal{R} correlate very well with St^0 and that there is a very small dependence upon ϕ^0 when St^0 is small. V^f/V^0 increases with St^0 because if the initial drop velocity is larger, a larger expansion is obtained as explained above, or if R^0 is larger, t_{evap} is larger and thus there is more time for expansion. V^f/V^0 also increases with decreasing ϕ^0 because denser clusters have more momentum resulting in a larger expansion. When St^0 is small the drops follow more closely the gas motion. In the case of dense clusters, if $B_{d\theta}^0$ is small, no new gas is entrained into the cluster and thus cooling and contraction occur, evidenced by $V^f/V^0 < 1$. These results are consistent with previous findings⁽¹⁵⁾ with $St^0 = 0$, showing contraction for dense clusters of drops. Now if R^0 is small, evaporation is fast and no new gas penetrates the cluster before complete evaporation. During this time cooling and contraction occur again. \mathcal{R} is a decreasing function of ϕ^0 because denser clusters have more mass and as the drops move out radially they lose solid body rotation and acquire irrotational motion. For smaller ϕ^0 the same momentum is transferred through vortex motion to more mass and thus $A_{d\theta}$ increases less, resulting in less packing, thus larger \mathcal{R} . In general $\mathcal{R} < 1$ because the acquisition of vortex motion by the drops makes the shell thinner since the outer cluster boundary moves less than the inner cluster boundary. For small St^0 there is strong coupling between phases and the drops move first inward and then outward. It is conjectured that at fixed ϕ^0 the minimum in \mathcal{R} is obtained when the irrotational motion is most important with respect to solid body rotation. As St^0 decreases

further [$St^0=O(10^{-1})$], a curve crossing is observed for the two values of ϕ^0 used here. This is consistent with previous findings⁽¹⁵⁾ that when $St^0=0$ and ϕ^0 decreases, there is more cooling of the gas, and for dilute mixtures \tilde{R} stays constant. For large St^0 the interaction between phases is weak and the drops do not acquire much vortex motion. Thus solid body rotation dominates resulting in shell thickening as seen in Fig. 3.

The description given above is confirmed by plots versus R^0 and also versus $A_{g\theta}^0=B_{d\theta}^0$. At fixed St^0 , both V^f/V^0 and \mathcal{R} are independent of R^0 . When R^0 is very small this conclusion slightly deteriorates due to the dominance of cooling generated contraction. When R^0 is fixed and $A_{g\theta}^0=B_{d\theta}^0$ increases, greater final expansion, larger final mass gain and fuel loss to the cluster, smaller t_{evap} and larger T_{ga} are obtained.

Figure 4 shows the dependence of t_{evap} and V^f/V^0 upon \tilde{R}^0 . When \tilde{R}^0 is small and \tilde{R}^0 decreases the surface to volume ratio of the cluster increases and thus there is more interaction with the ambient. As a result T_{ga} stays larger and t_{evap} decreases. When \tilde{R}^0 is large and \tilde{R}^0 increases, the surface to volume ratio of the cluster decreases, and thus interactions with the ambient are more difficult. However, the initial slip velocity increases with \tilde{R}^0 for given spin because it is a function of r . This results in increasing convective evaporation yielding a slight decrease in t_{evap} . A plausible explanation for V^f/V^0 increasing with decreasing \tilde{R}^0 (except when the initial shell thickness is constant) is as follows: Smaller clusters reside in the inner vortex part dominated by irrotational motion, whereas larger clusters have more mass in the outer part of the vortex dominated by spin. Since the centrifugal force is a stronger function of the irrotational motion than of spin as \tilde{R}^0 decreases, for smaller clusters there is a larger centrifugal force if there is strong coupling between $A_{g\theta}$ and $A_{d\theta}$ which is what happens for dense clusters. This results in more expansion and thus larger V^f/V^0 . When the initial shell thickness is constant, as \tilde{R}^0 increases spin becomes relatively more important than in the other cases because here there is not much liquid mass in the core.

Because larger clusters have generally more spin and thus a larger centrifugal force, the expansion is larger and V^f/V^0 increases.

In Fig. 5, \mathcal{R} is plotted versus \tilde{R}^0 . As explained above, when \tilde{R}^0 increases spin dominates, resulting in a larger drop dispersion and thus \mathcal{R} increases. In contrast, when \tilde{R}^0 decreases, irrotational motion dominates, resulting in more packing of the drops and thus \mathcal{R} decreases.

V. SUMMARY AND CONCLUSIONS

A formulation has been presented which describes the evaporation of clusters of drops in large, coherent, vortices. The model takes into account the dynamic and thermodynamic interactions between drops and gas and is valid for both dense and dilute clusters of drops.

The results show the importance of both $B_{d\theta}^0$ and $B_{g\theta}^0$ for achieving complete evaporation in the dense cluster regime. By increasing $B_{d\theta}^0$ and $B_{g\theta}^0$, complete evaporation is achieved in cases where saturation would be obtained otherwise. It was also found that V^f/V^0 and \mathcal{R} are both decreasing functions of ϕ^0 due to the larger mass (and thus larger centrifugal force) as the mixture is richer, and also due to the complex interplay between irrotational motion and solid body rotation in affecting the fate of the drops.

Results obtained for dense clusters of drops show that t_{evap} does not correlate with St^0 . In contrast, both V^f/V^0 and \mathcal{R} correlate very well with St^0 . This result is very significant for experimentalists and designing engineers and also gives a way to qualitatively check this theory without needing a precise measurement of n providing $n^0 > 10^4 \text{ cm}^{-3}$. When St^0 is small the behavior is dominated by evaporative cooling and cluster contraction whereas when St^0 is large expansion is due either to larger initial velocities or larger evaporation time. At constant St^0 , t_{evap} increases with R^C , but both V^f/V^0 and \mathcal{R} are independent of R^0 .

The results show also that t_{evap} is a nonmonotonic, convex function of \tilde{R}^0 , although the variation when \tilde{R}^0 is large is slight. Since when \tilde{R}^0 is small t_{evap} is a strongly increasing function of \tilde{R}^0 this means that by slightly decreasing \tilde{R}^0 one

could achieve important reductions in \dot{m}_{evap} . V^f/V^0 is a decreasing function of \tilde{R}^0 , except when the initial shell thickness is constant, in which case it is an increasing function of \tilde{R}^0 . \mathcal{Q} is an increasing function of \tilde{R}^0 characterized by drop packing and shell-thinning for small \tilde{R}^0 , and drop dispersion and shell-thickening for large values of \tilde{R}^0 .

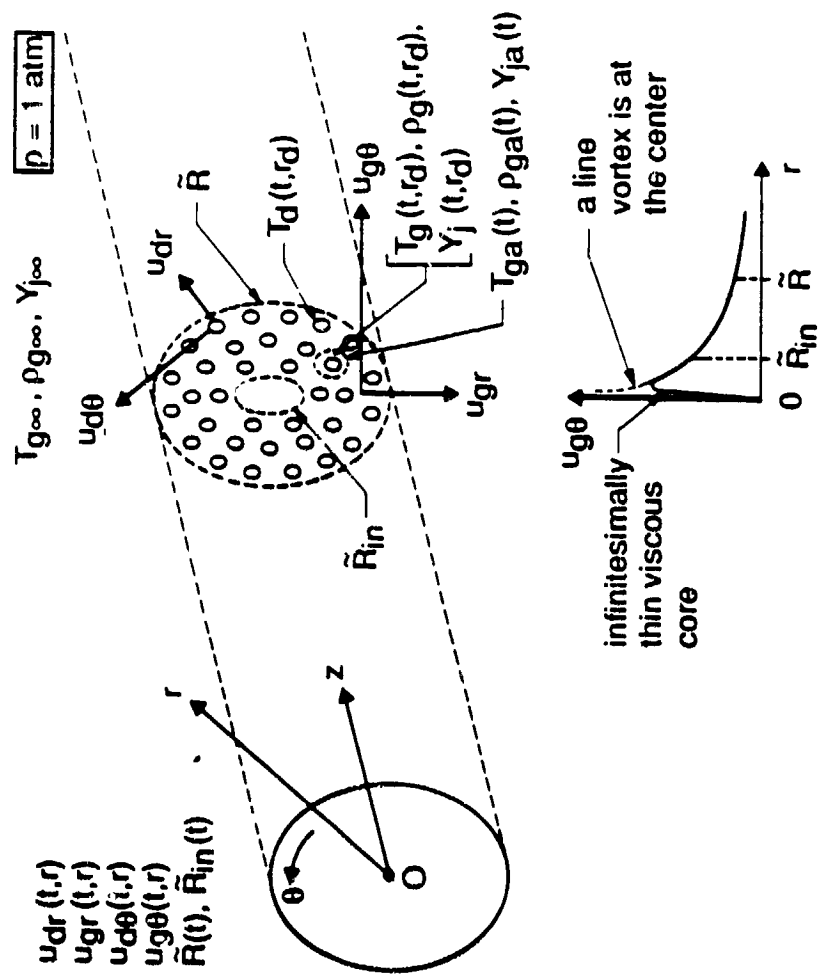
The confirmation of all the above results awaits comparison with experimental observations which so far are lacking, except for the dilute cluster regime and/or non evaporating case. In the dilute regime the present model predicts qualitatively the global observations of the experiments(1,2,3), but detailed comparisons cannot be made due to the fact that the more realistic case of the evaporating drops was treated here. In the present calculations an efficient computational procedure was developed using the drop radius as the advancing, time-like variable. This procedure precludes comparisons with the non-evaporating drops experiments.

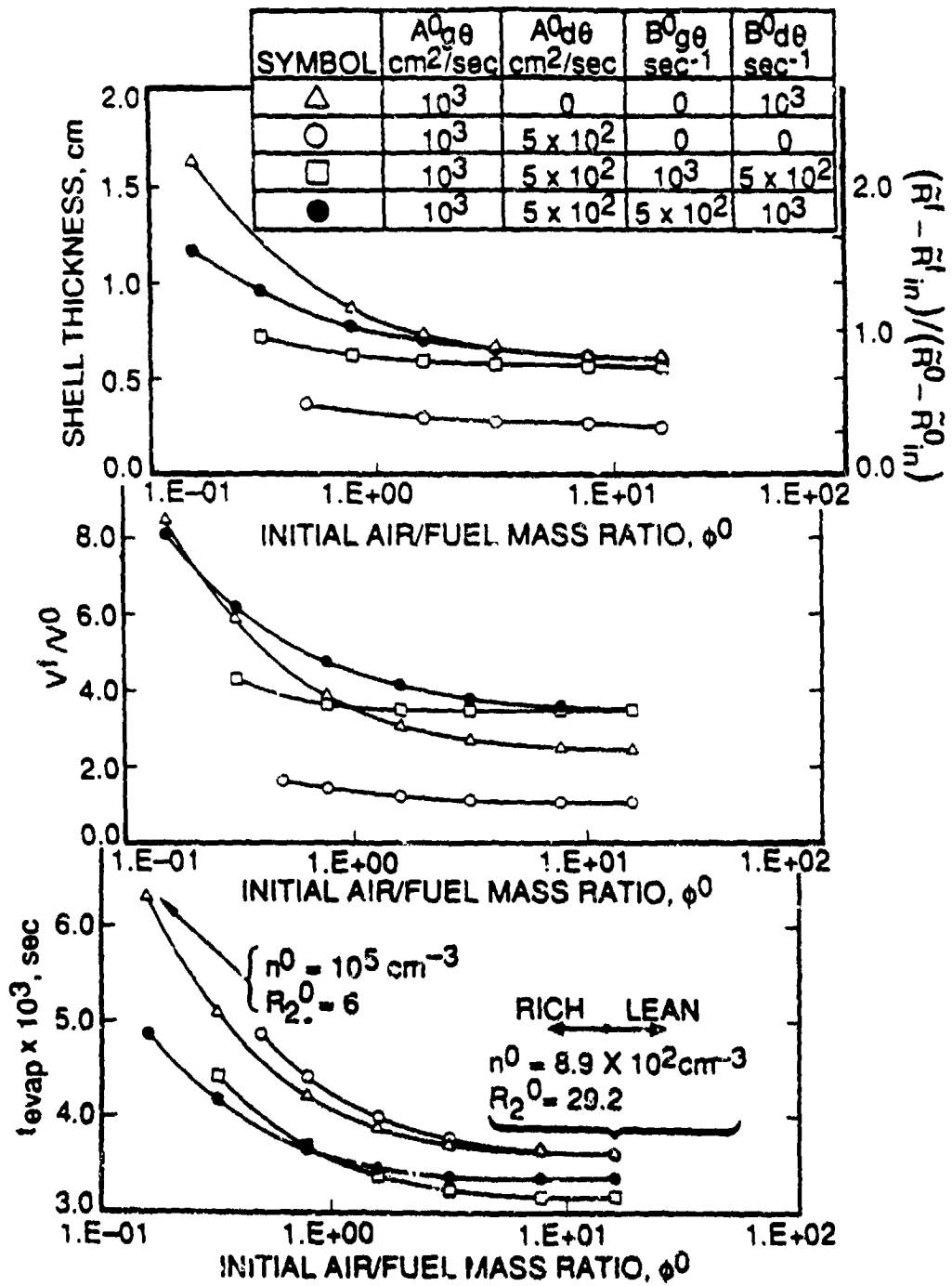
Acknowledgement

This work was supported by the Air Force Office of Scientific Research, with Dr. Julian Tishkoff acting as technical monitor through an interagency agreement with the National Aeronautics and Space Administration.

REFERENCES

1. Lazaro, B. J., and Lasheras, J. C.: 22nd Symp. (Int.) on Combustion, pp 1991-1998, (1988)
2. Lazaro, B. J., and Lasheras, J. C.: Phys. Fluids A, 1, 6, pp 1035-1044, (1989).
3. Kamalu, N., Wen, F., Troutt, T. R., and Crowe, C. T.: ASME Cavitation and Multiphase Flow Forum, FED, 64, p 150, (1988).
4. Crowe, C. T., Chung, J. N., and Troutt, T. R.: Prog. Energy Comb. Sci., 14, pp 171-194, (1988).
5. Chung, J. N., and Troutt, T. R.: J. Fluid Mech., 186, pp 199-222, (1988).
6. Yang, M. H.: Ph.D. Thesis, The University of Michigan, (1989)
7. Yang, M., and Sichel, M.: AIAA 89-0159, 27th Aerospace Sciences Meeting, Reno, Nevada, (1989).
8. Chigier, N. A., Mao, C. P. and Oechsle, V.: 7-6A, CSS/WSS/The Combustion Institute Spring Meeting, (1985); also private communication, (1989).
9. Rudoff, R. C., Brena de la Rosa, A., Sankar, S. V., and Bachalo, W. D.: AIAA-89-0052, 27th Aerospace Sciences Meeting, Reno, Nevada, (1989).
10. Allen, M. G., and Hanson, R. K.: 21st Symp. (Int.) on Combustion, pp 1755-1762, (1986).
11. Nakabe, K., Mizutani, Y., Hiro, T. and Tanimura, S.: Combust. Flame, 74, pp 39-57, (1988).
12. Bellan, J. and Cuffel, R.: Comb. Flame, 51, 1, pp 55-67, (1983).
13. Cliffe, K. A., and Lever, D. A.: Int. J. Numer. Meth. Fluids, 5, pp 709-725, (1985).
14. Bellan, J. and Harstad, K.: Int. J. Heat Mass Transfer, 30, 1, pp 125-136, (1987).
15. Bellan, J. and Harstad, K.: Int. J. Heat Mass Transfer, 31, 8, pp 1655-1668, (1988).





SYMBOL	ϕ^0	R^0	INITIAL TANGENTIAL VELOCITIES
\triangle	1.57	VARIES	VARY
\circ	0.785	VARIES	CONSTANT
\square	0.785	CONSTANT	VARY
\bullet	1.57	VARIES	CONSTANT
\blacksquare	1.57	CONSTANT	VARY

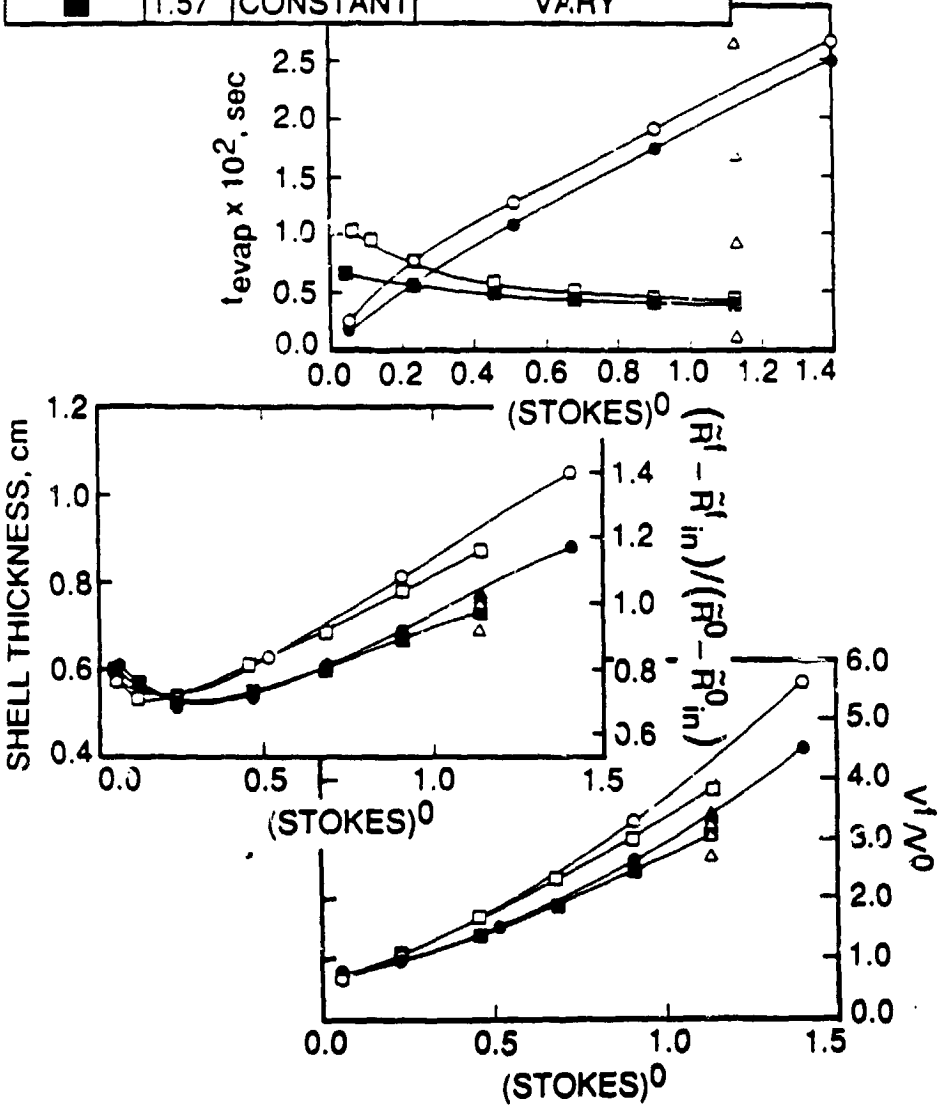
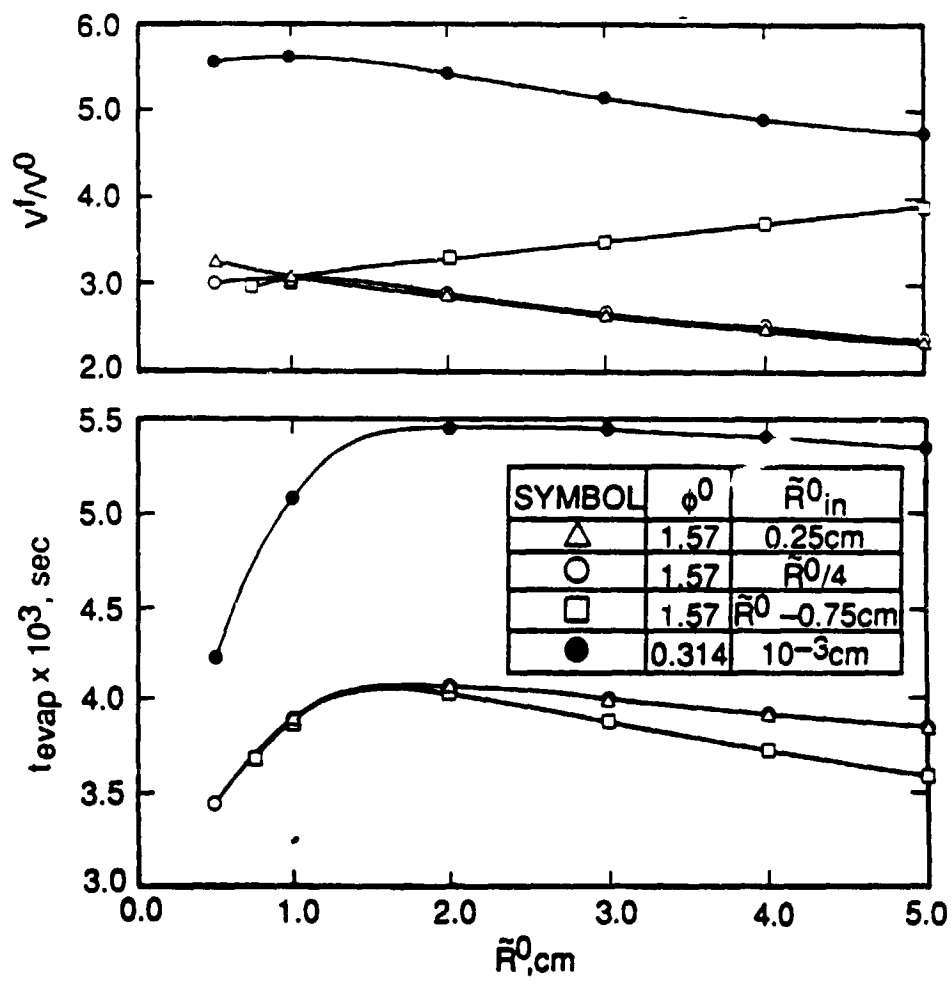


Figure 3



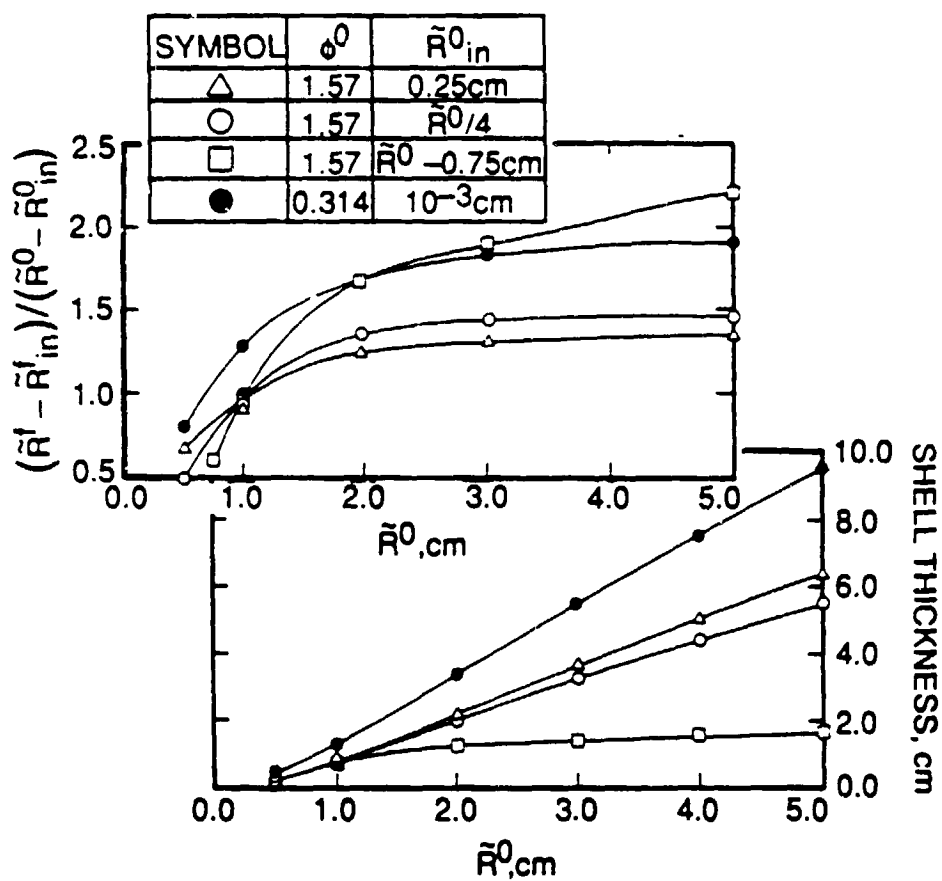


Figure 5

FIGURE CAPTIONS

- Figure 1 Physical situation studied. \tilde{R}_{in} and \tilde{R} are both located in the free vortex part of the line vortex which is located at the center of the cluster.
- Figure 2 Variation of the evaporation time, volume ratio, final shell thickness and shell thickness ratio versus the initial air/fuel mass ratio. $T_{ga}^0 = 1000K$, $T_{gs}^0 = 350K$, $Y_{Fva}^0 = 0$, $R^0 = 2 \times 10^{-3}cm$, $\tilde{R}^0 = 1.0cm$, $\tilde{R}_{in}^0 = 0.25cm$, $\rho_l = 0.734 \text{ g/cm}^3$, $C_p = 0.241 \text{ cal/gK}$, $C_{pFv} = 0.4 \text{ cal/gK}$, $L_{bn} = 73.92 \text{ cal/g}$.
- Figure 3 Variation of the evaporation time, volume ratio, final shell thickness and shell ratio with the initial Stokes number for initially dense clusters of drops. $T_{ga}^0 = 1000K$, $T_{gs}^0 = 350K$, $Y_{Fva}^0 = 0$, $\tilde{R}^0 = 1.0 \text{ cm}$, $\tilde{R}_{in}^0 = 0.25cm$, $A_{d\theta}^0 = B_{g\theta}^0 = 0$, $\rho_l = 0.734g/cm^3$, $C_p = 0.241 \text{ cal/gK}$, $C_{pFv} = 0.4 \text{ cal/gK}$, $L_{bn} = 73.92 \text{ cal/g}$.
- Figure 4 Evaporation time and volume ratio versus the initial outer radius of the cluster. $T_{ga}^0 = 1000K$, $T_{gs}^0 = 350K$, $Y_{Fva}^0 = 0$, $A_{d\theta}^0 = B_{g\theta}^0 = 0$, $A_{g\theta}^0 \text{ (cm}^2\text{/sec)} = B_{d\theta}^0 \text{ (sec}^{-1}\text{)} = 10^3$, $\rho_l = 0.734g/cm^3$, $C_p = 0.241 \text{ cal/gK}$, $C_{pFv} = 0.4 \text{ cal/gK}$, $L_{bn} = 73.92 \text{ cal/g}$, $R^0 = 2 \times 10^{-3}cm$.
- Figure 5 Variation of the final shell thickness and shell thickness ratio with the initial outer radius of the cluster. $T_{ga}^0 = 1000K$, $T_{gs}^0 = 350K$, $Y_{Fva}^0 = 0$, $A_{d\theta}^0 = B_{g\theta}^0 = 0$, $A_{g\theta}^0 \text{ (cm}^2\text{/sec)} = B_{d\theta}^0 \text{ (sec}^{-1}\text{)} = 10^3$, $\rho_l = 0.734g/cm^3$, $C_p = 0.241 \text{ cal/gK}$, $C_{pFv} = 0.4 \text{ cal/gK}$, $L_{bn} = 73.92 \text{ cal/g}$, $R^0 = 2 \times 10^{-3}cm$.